

# XMM-Newton

## XMM-Newton Users Handbook

Issue 2.18

Prepared by the XMM-Newton Community Support Team  
with contributions from the entire XMM-Newton Science Operations Centre Team

13.07.2020

Extensive contributions from the members of the Instrument Teams, the SSC  
and NASA's XMM-Newton Guest Observer Facility are gratefully acknowledged.

### Revision history

Revision number	Date	Revision editor	Comments
Issue 2.18	13.07.2020	J. Ebrero	Release for AO-20
Issue 2.17	15.07.2019	J. Ebrero	Release for AO-19
Issue 2.16	16.07.2018	J. Ebrero	Release for AO-18
Issue 2.15	17.07.2017	J. Ebrero	Release for AO-17
Issue 2.14	18.07.2016	J. Ebrero	Release for AO-16
Issue 2.13	20.07.2015	J. Ebrero	Release for AO-15
Issue 2.12	15.07.2014	A.L. Longinotti	Release for AO-14
Issue 2.11	23.07.2013	A.L. Longinotti	Release for AO-13
Issue 2.10	13.07.2012	E. Piconcelli	Release for AO-12
Issue 2.9	19.07.2011	J.-U. Ness	Release for AO-11
Issue 2.8	19.07.2010	J.-U. Ness	Release for AO-10
Issue 2.7	17.07.2009	J.-U. Ness	Release for AO-9
Issue 2.6	15.08.2008	M. Ehle	Release for AO-8
Issue 2.5	07.08.2007	M. Ehle	Release for AO-7
Issue 2.4	12.07.2006	M. Ehle	Release for AO-6
Issue 2.3	08.07.2005	M. Ehle	Release for AO-5
Issue 2.2	01.07.2004	M. Ehle	Release for AO-4
Issue 2.1	03.03.2003	M. Ehle	Release for AO-3
Issue 2.0	15.08.2001	M. Ehle	Release for AO-2
Issue 1.2	31.03.2000	M. Ehle	Minor updates
Issue 1.1	19.01.1999	M. Dahlem	Release of Cal/PV/GT target tables
Issue 1.0	23.09.1998	M. Dahlem	Official release
Draft 3.0	August 1998	M. Dahlem	Complete draft

Citation: In publishing, refer to this document as:

"XMM-Newton Users Handbook", Issue 2.18, 2020 (ESA: XMM-Newton SOC).

## Contents

<b>1</b>	<b>Glossary</b>	<b>1</b>
<b>2</b>	<b>Introduction</b>	<b>3</b>
2.1	Scope of this document . . . . .	3
2.2	Structure and contents of the Users Handbook . . . . .	3
2.3	Location . . . . .	3
2.4	Sources of information . . . . .	4
2.5	Updates on this document . . . . .	4
2.6	How to obtain further help and information . . . . .	4
2.7	Acknowledgements . . . . .	4
<b>3</b>	<b>XMM-Newton – a concise overview</b>	<b>6</b>
3.1	Basic characteristics . . . . .	7
3.2	X-ray Telescopes . . . . .	9
3.2.1	X-ray point-spread function . . . . .	10
3.2.1.1	On-axis PSF . . . . .	10
3.2.1.2	Off-axis PSF . . . . .	11
3.2.2	X-ray effective area . . . . .	17
3.2.2.1	On-axis effective area . . . . .	17
3.2.2.2	Off-axis effective area . . . . .	19
3.2.3	Response matrices used in the SAS data analysis . . . . .	21
3.2.4	Straylight rejection . . . . .	21
3.3	EUROPEAN PHOTON IMAGING CAMERA (EPIC) . . . . .	23
3.3.1	Two types of EPIC camera: MOS and pn . . . . .	25
3.3.1.1	EPIC MOS chip geometry . . . . .	26
3.3.1.2	EPIC pn chip geometry . . . . .	27
3.3.2	Science modes of the EPIC cameras . . . . .	28
3.3.3	EPIC imaging – angular resolution . . . . .	35
3.3.4	Intrinsic energy resolution of EPIC . . . . .	35
3.3.5	EPIC quantum efficiencies . . . . .	35
3.3.6	EPIC filters and effective area . . . . .	39
3.3.7	EPIC background . . . . .	43
3.3.7.1	EPIC external ‘flaring’ background . . . . .	43
3.3.7.2	EPIC internal ‘quiescent’ background . . . . .	44
3.3.7.3	EPIC Detector Noise . . . . .	45
3.3.7.4	EPIC background and its importance for extended sources . . . . .	46
3.3.8	EPIC’s sensitivity limits . . . . .	47
3.3.9	EPIC photon pile-up . . . . .	51
3.3.10	EPIC out-of-time events . . . . .	55
3.3.11	EPIC event grade selection . . . . .	60
3.3.12	EPIC-specific proposal submission information . . . . .	61
3.3.12.1	EPIC spectral quality . . . . .	61
3.3.12.2	EPIC flux to count rate conversion . . . . .	64
3.3.12.3	Count rate conversion from other X-ray satellite missions . . . . .	64
3.4	REFLECTION GRATING SPECTROMETER (RGS) . . . . .	92
3.4.1	Diffraction Geometry . . . . .	92



3.4.2	RFC chip arrays . . . . .	93
3.4.3	RGS Order Separation . . . . .	94
3.4.4	In-Flight Performance . . . . .	96
3.4.4.1	The Line Spread Function . . . . .	96
3.4.4.2	Resolving Power and Spectral Resolution . . . . .	96
3.4.4.3	RGS spectral resolution for extended sources . . . . .	99
3.4.4.4	Wavelength Scale Accuracy . . . . .	99
3.4.4.5	RGS effective area for dispersive spectroscopy . . . . .	100
3.4.4.6	The RGS Background . . . . .	103
3.4.4.7	RGS Sensitivity Limits . . . . .	105
3.4.4.8	RGS photon pile-up . . . . .	108
3.4.5	Operating Modes of the RGS . . . . .	109
3.4.5.1	RGS Small Window Mode . . . . .	110
3.4.5.2	RGS Multipointing Mode (MPM) . . . . .	111
3.4.6	RGS specific proposal submission information . . . . .	112
3.4.6.1	RGS avoidance angles . . . . .	114
3.4.6.2	RGS flux to count rate conversion . . . . .	114
3.4.6.3	RGS spectral quality . . . . .	115
3.5	OPTICAL MONITOR (OM) . . . . .	124
3.5.1	OM telescope . . . . .	124
3.5.2	OM detector . . . . .	125
3.5.2.1	Imaging with OM . . . . .	125
3.5.3	OM optical elements . . . . .	127
3.5.3.1	OM filter band passes . . . . .	127
3.5.3.2	OM grisms . . . . .	129
3.5.4	Optical/UV point spread function of the OM and tracking . . . . .	131
3.5.5	OM sensitivity and detection limits . . . . .	132
3.5.6	OM brightness and dose limits . . . . .	137
3.5.7	OM distortion . . . . .	139
3.5.8	OM Field Acquisition . . . . .	139
3.5.9	OM Operating modes and filters configuration . . . . .	140
3.5.9.1	OM operating modes . . . . .	140
3.5.9.2	OM operating configurations . . . . .	142
3.5.9.3	Integration time for exposures . . . . .	145
3.5.9.4	Filter choice . . . . .	145
3.5.9.5	Multiple rotations of the filter wheel . . . . .	146
3.5.9.6	Practical use of OM. Some examples . . . . .	146
3.5.10	OM specific proposal submission information . . . . .	148
3.5.10.1	Choice of Science User Defined non-default windows . . . . .	148
3.6	XMM-Newton support instruments . . . . .	151
3.6.1	EPIC Radiation Monitor Subsystem (ERMS) . . . . .	151
3.6.2	Attitude & Orbit Control Subsystem (AOCS) . . . . .	151
3.7	Comparison with other X-ray satellites . . . . .	153
3.7.1	A comparison of XMM-Newton vs. Chandra . . . . .	153
3.7.1.1	Effective area for dispersive spectroscopy . . . . .	154
3.7.1.2	Non-dispersive spectroscopy: an example . . . . .	154
3.7.1.3	XMM-Newton EPIC vs. Chandra ACIS-I pile-up comparison . .	155

**esa**european space agency  
agence spatiale européenne

Document No.: XMM-SOC-USR-MAN-0006

Issue/Rev.: Issue 2.18

Date: 13.07.2020

<b>4 Observing with XMM-Newton</b>	<b>158</b>
4.1 XMM-Newton orbit . . . . .	158
4.2 Observing constraints . . . . .	158
4.2.1 Radiation belts . . . . .	159
4.2.2 Celestial constraints . . . . .	160
4.2.3 Sky visibility during the XMM-Newton mission . . . . .	160
4.3 Points of concern . . . . .	161
4.3.1 Bright source avoidance . . . . .	161
4.3.2 Other considerations . . . . .	165
4.4 Field of View geometry . . . . .	169
4.4.1 Instrument alignment . . . . .	169
4.4.2 Position angle constraints and determination . . . . .	169
4.5 Observation overheads . . . . .	169
4.5.1 Operational overheads . . . . .	170
4.5.2 Instrument and setup overheads . . . . .	170
4.5.3 Special science exposures . . . . .	170
4.6 Observing modes . . . . .	171
4.6.1 Mosaic Mode . . . . .	171
4.6.2 RGS Multipointing Mode (MPM) . . . . .	173
4.6.3 Slew observations . . . . .	174
<b>5 Proposal Submission and Optimisation</b>	<b>175</b>
<b>6 Analysing XMM-Newton data</b>	<b>177</b>
6.1 XMM-Newton analysis software – the Science Analysis Subsystem . . . . .	177
6.1.1 XMM-Newton data: the Observation/Slew Data Files (ODF/SDF) . . . . .	177
6.1.2 The Science Analysis Software (SAS) . . . . .	177
6.1.3 XMM-Newton data: the Processing Pipeline Subsystem (pipeline) products (PPS) . . . . .	177
6.1.4 Time scale and Reference Time . . . . .	178
6.2 XMM-Newton Calibration data . . . . .	178
6.3 The XMM-Newton data distribution . . . . .	179
6.4 The XMM-Newton Science Archive (XSA) . . . . .	179
6.5 The XMM-Newton Serendipitous Source Catalogue . . . . .	179
6.6 The XMM-Newton OM Source Catalogue . . . . .	180
6.7 The XMM-Newton Slew Survey Catalogue . . . . .	180
<b>7 Documentation</b>	<b>181</b>
<b>A XMM-Newton Survey Science Centre (SSC)</b>	<b>185</b>
A.1 Pipeline processing of XMM-Newton science data . . . . .	186
A.2 Science analysis software development . . . . .	187
A.3 The XMM-Newton Serendipitous Source Catalogues . . . . .	187
A.3.1 4XMM-DR9 . . . . .	188
A.3.2 Upper Limit Server . . . . .	189
<b>B XMM-Newton Routine Calibration Programme</b>	<b>190</b>

**esa**european space agency  
agence spatiale européenne

## List of Figures

1	Sketch of the XMM-Newton payload. The mirror modules, two of which are equipped with Reflection Grating Arrays, are visible at the lower left. At the right end of the assembly, the focal X-ray instruments are shown: The EPIC MOS cameras with their radiators (black/green “horns”), the radiator of the EPIC pn camera (violet) and those of the (light blue) RGS detectors (in pink). The OM telescope is obscured by the lower mirror module. Figure courtesy of Dornier Satellitensysteme GmbH. . . . .	6
2	The light path in XMM-Newton’s open X-ray telescope with the pn camera in focus (not to scale). . . . .	9
3	The light path in the two XMM-Newton telescopes with grating assemblies (not to scale). Note that the actual fraction of the non-intercepted light that passes to the primary MOS focus is 44%, while 40% of the incident light is intercepted by grating plates of the RGA. . . . .	10
4	On axis point spread function (PSF) of the MOS1, MOS2 and pn X-ray telescopes (left to right) registered on the same source with each MOS camera in Small Window mode, and the pn camera in Large Window mode. The pixel size is 1.1 arcsec square for the MOS, and 4.1 arcsec square for the pn. The images are 110 arcsec wide. A square root scale has been used to visualise the wings of the PSF. The core of the PSF is piled-up for this source, with a different factor for the MOS and the pn. The star-like pattern is created by the spider which supports the 58 co-axial Wolter I mirrors of the telescope. The shape of the PSF core is slightly different for all cameras, with MOS2 having a somewhat more pronounced shape.	11
5	The MOS1 fractional encircled energy as a function of angular radius (on-axis) at different energies. The curves were calculated integrating the PSF that is currently implemented in the CCF. . . . .	12
6	The MOS2 fractional encircled energy as a function of angular radius (on-axis) at different energies. The curves were calculated integrating the PSF that is currently implemented in the CCF. . . . .	13
7	The pn fractional encircled energy as a function of angular radius (on-axis) at different energies. The curves were calculated integrating the PSF that is currently implemented in the CCF. . . . .	13
8	The dependence of the X-ray PSF’s shape on the position in the field of view. This image was made from an observation towards the Orion molecular cloud. EPIC pn, MOS1 and MOS2 exposures have been merged together and exposure corrected. The data has been slightly smoothed with a Gaussian of 10” FWHM. The intensity scale is square root. . . . .	14
9	The W90 radius of a point source observed with the MOS1 camera as a function of off-axis angle at three energies. The curves are based on early ray-trace simulations and should not be used for quantitative analysis; see text on how to obtain W90 radii in-line with the current calibration. . . . .	15
10	The W90 radius of a point source observed with the pn camera as a function of off-axis angle at three energies. The curves are based on early ray-trace simulations and should not be used for quantitative analysis; see text on how to obtain W90 radii in-line with the current calibration. . . . .	16
11	The net effective area of all XMM-Newton X-ray telescopes, EPIC and RGS (linear scale). . . . .	17



---

12	<i>The net effective area of all XMM-Newton X-ray telescopes, EPIC and RGS (logarithmic scale).</i>	18
13	<i>Vignetting function as a function of off-axis angle (<math>0'</math>–<math>15'</math>, based on simulations), at a few selected energies, of the X-ray telescope in front of the pn camera . . . . .</i>	19
14	<i>Vignetting function as a function of azimuth angle of the X-ray telescope in front of the MOS1 camera. The curves are given for an off-axis angle of 10 arcmin. Due to the presence of reflection grating assemblies in the exit beams of the X-ray telescopes, the vignetting functions measured in the MOS cameras are modulated azimuthally. . . . .</i>	20
15	<i>EPIC pn image of GRS1758-258 (a black hole candidate near the Galactic centre) observed in the large window readout mode demonstrating the effect of straylight: in the upper part of the image, sharp arcs appear that are caused by single mirror reflections of photons possibly from GX 5-1 which is <math>\sim 40</math> arcmin offaxis to the north and outside the FOV. . . . .</i>	22
16	<i>A rough sketch of the field of view of the two types of EPIC camera; MOS (left) and pn (right). The shaded circle depicts a <math>30'</math> diameter area. For the alignment of the different cameras with respect to each other in the XMM-Newton focal plane refer to the text. . . . .</i>	24
17	<i>The field of view of the EPIC MOS cameras for an observation with a position angle of <math>\sim 80^\circ</math>: MOS1 (here) and MOS2 (next figure). The two MOS cameras view the same field as displayed in sky coordinates with North to the top and East to the left. In each case the camera detector coordinate frames are noted. . . . .</i>	25
18	<i>The field of view of the EPIC MOS cameras (cntd. from previous figure): MOS2. . . . .</i>	26
19	<i>The field of view of the EPIC pn camera for an observation with a position angle of <math>\sim 80^\circ</math>. The pn camera views the same field as displayed in Figs. 17 and 18 in sky coordinates with North to the top and East to the left. Again the camera detector coordinate frame is noted. The nominal boresight is marked with a small box. Note that the approximate distance between the boresight and the nearby chip gaps is <math>\sim 40</math> arcsec, which can be of importance when observing extended sources. Position 'X' shows the preferred location to centre on an object in the pn small window mode, however, the user is advised that this requires a knowledge of the position angle of the observation, and will also place the target outside the EPIC MOS small window. . . . .</i>	27
20	<i>The layout of the MOS cameras is presented in this figure for MOS1 (above) and MOS2 (bottom). The images (in detector coordinates [DETX,DETY]) are extracted from an exposure taken with the calibration (CAL_CLOSED) filter in Rev. #80 (Obs. #0124700101). The number of the CCD where each photon has fallen is included in the CCDNR column of the calibrated event list files. The MOS cameras are orthogonally oriented. Hence, the RGS dispersion direction is aligned with the DETY direction in the MOS1 camera, while it is aligned along the DETX direction in the MOS2 camera. Users are warned that <b>scientific observations are performed with MOS1 CCD3 and CCD6 switched off</b> due to a hardware failure, probably due to a micrometeorite impact (see Sect. 3.3). . . . .</i>	28
21	<i>The layout of the EPIC MOS cameras as presented in SAS (cntd. from previous figure): MOS2. . . . .</i>	29

---

22	<i>The layout of the EPIC pn camera as presented in SAS. The orientation of the RAWX/RAWY (CCD specific) and of the DETX/DETY axes are shown, to highlight that the RGS dispersion axes are parallel within spacecraft physical coordinates. The readout CAMEX of each CCD is located at RAWY = 0, i.e. at the top (for CCDs 1 – 6) or bottom (for CCDs 7 – 12) of the displayed array. In the upper left corner, the orientation of the celestial North and East axes is displayed for an assumed position angle (PA) of 30°.</i>	30
23	<i>Operating modes for the pn-CCD camera. Top left: Full Frame and Extended Full Frame mode; top right: Large Window mode; bottom left: Small Window mode, and bottom right: Timing mode. The Burst mode is different from the Timing mode as the source position is not read out, i.e. rows 181-200 will be dark.</i>	32
24	<i>Operating modes for the MOS-CCD cameras. Top left: Full Frame mode; top right: Large Window mode; bottom left: Small Window mode, and bottom right: Timing mode. In Timing mode, the X axis of the central CCD is the projected image of the source, and has thus true spatial information; the Y axis does not carry any spatial information but is a measure of time, with roll-over of 1024 time-units in the figure shown.</i>	34
25	<i>Temporal evolution of the EPIC MOS energy resolution (FWHM) as a function of energy. The solid curve is a best fit <math>E^{0.5}</math> function to ground calibration data between 0.1 and 12 keV; all events with pattern 0-12 were included in the analysis. Below around 0.6 keV (shown by the dotted region) surface charge loss effects distort the main photo peak significantly from a Gaussian and hence the effective energy resolution. The data points represent MOS 1 in-flight measurements of the FWHM of the Al <math>K_{\alpha}</math> (1.478 keV) and Mn <math>K_{\alpha}</math> (5.893 keV) lines in five different epochs. It should be noted the rapid degradation of the resolution between the first and the second epoch, and the recovery and subsequent stability after the cooling of the MOS camera (performed between November and December 2002, i.e. between Rev.#530 and Rev.#560). In the main panel measurement error bars are smaller than the symbol size. In the insets a zoom of the spectral ranges around the nominal line positions is shown. Typical standard deviations in each epoch range between 5 and 10 eV, and 8 and 19 eV for the Al and Mn line, respectively.</i>	36
26	<i>Top panel: MOS 1 energy resolution as a function of energy for singles (blue) and singles+doubles (black) events. Bottom panel: pn energy resolution as a function of energy for: a) single events at the boresight (position "Y9" in the canned response matrices; black); b) double events at the boresight position (red); c) single events closest to the readout node (position "Y0", blue); d) double events closest to the readout node (green). Line widths are based on monochromatic line spectra, simulated with the SASv7.1 canned response matrices.</i>	37
27	<i>Quantum efficiency of the EPIC MOS1 (solid line) and MOS2 (dashed line) CCD1 chip as a function of photon energy.</i>	38
28	<i>Quantum efficiency of the EPIC pn CCD chips as a function of photon energy (Strüder et al., 2001, A&amp;A, 365, L18, Fig. 5).</i>	38
29	<i>The EPIC MOS effective area for each of the optical blocking filters.</i>	41
30	<i>The EPIC pn effective area for each of the optical blocking filters.</i>	41
31	<i>Combined effective area of all telescopes assuming that the EPIC cameras operate with the same filters, either thin, medium or thick.</i>	42
32	<i>Image from a MOS2 observation badly affected by soft proton flares.</i>	44



---

33	<i>Light curve from a MOS1 observation badly affected by soft proton flares. During the first part of the observation the background is constant. The second half, however, is heavily affected by a proton flare.</i>	45
34	<i>Background spectrum for the MOS1 camera during an observation with the filter wheel in the closed position. The prominent features around 1.5 and 1.7 keV are respectively Al-K and Si-K fluorescence lines. The rise of the spectrum below 0.5 keV is due to the detector noise.</i>	46
35	<i>Background spectrum for the pn camera during an observation with the filter wheel in the CLOSED position (top: single events, bottom: double events) in the energy range 0.2-18 keV. The prominent features around 1.5 keV are Al-K<math>\alpha</math>, at 5.5 keV Cr-K<math>\alpha</math>, at 8 keV Ni-K<math>\alpha</math>, Cu-K<math>\alpha</math>, Zn-K<math>\alpha</math> and at 17.5 keV (only in doubles) Mo-K<math>\alpha</math> fluorescence lines. The rise of the spectrum below 0.3 keV is due to the detector noise. The relative line strengths depend on the (variable) incident particle spectrum.</i>	48
36	<i>Background images for the pn camera with spatially inhomogeneous fluorescent lines: smoothed image in the Ti+V+Cr-K<math>\alpha</math> lines (top left), full resolution image in Copper (7.8 – 8.2 keV) (top right), Nickel (7.3 – 7.6 keV) (bottom left) and Molybdenum (17.1 – 17.7 keV) (bottom right). The absolute normalisation of the images can be inferred from the spectra in Fig. 35. The inhomogeneity is caused by the electronics board mounted below the CCDs; in case of the energy range 4.4 – 5.7 keV probably due to a supporting screw - however at a very low level.</i>	49
37	<i>EPIC sensitivity (<math>5\sigma</math> minimum detectable flux in <math>\text{erg cm}^{-2} \text{s}^{-1}</math> in respective bands) as a function of exposure time (from Watson et al., 2001). Sensitivity is computed for an assumed <math>\alpha = 1.7</math> powerlaw spectrum with a column density <math>N_H = 3 \times 10^{20} \text{ cm}^{-2}</math>. Solid curves are for the nominal background rates. Dashed curves are for background levels enhanced by a factor 3. The EPIC MOS curves correspond to the combination of the two cameras.</i>	50
38	<i>In-orbit observations performed with EPIC MOS showing the increase of pile-up with increasing photon count rate per frame. The panels are arranged clockwise, with the lowest count rate (and thus pile-up rate) in the upper left and the highest in the lower left. The observed count rates are 2, 5, 12 and 16 counts/frame, respectively.</i>	52
39	<i>The best-fitting power law slope, <math>\alpha</math>, for an <math>\alpha = 1.7</math> input spectrum into SciSim, with different input count rates, leading to different levels of pile-up.</i>	53
40	<i>Plot of the pn pattern distribution with energy as produced by the SAS task epatplot (see text for further details).</i>	54
41	<i>Effect of spectral broadening due to OoT events: the upper panel shows a spectrum extracted from a pn CalClosed full frame mode observation (black) together with the spectrum corrected for OoT events (green). In the lower panel the spectrum of the simulated OoT events over the whole FoV is plotted.</i>	57
42	<i>Effect of OoT events on images: The upper left panel contains a 2-10 keV band image of a pn observation of a bright source in full frame mode with the OoT events visible as a strip running from the source toward the top of the image (in detector coordinates). The upper right panel depicts the modelled (see SAS task epchain) OoT event distribution where in the lower left panel these are subtracted from the original image. The lower right panel is cleaned for the soft 0.2-2 keV band for comparison.</i>	58

**esa**european space agency  
agence spatiale européenne

43	<i>Illustration on how the EPIC-pn camera in Small Window mode works. For clarity the grid is 4x4 pixels. Left panel is the input sky image. Right panel shows the out-of-time events in the science window region. See text for details. Full animation can be found at: <a href="http://xmm-tools.cosmos.esa.int/external/xmm_user_support/documentation/uhb/">http://xmm-tools.cosmos.esa.int/external/xmm_user_support/documentation/uhb/</a>.</i>	
44	<i>Series of EPIC MOS1 model spectra of a Mekal thermal plasma with a temperature of 0.1 keV. From the bottom to the top, the total number of counts in the XMM-Newton passband (0.15–12 keV) increases from 500 to 20,000. . . . .</i>	61
45	<i>Series of EPIC MOS1 model spectra of a Mekal thermal plasma with a temperature of 0.5 keV. From the bottom to the top, the total number of counts in the XMM-Newton passband (0.15–12 keV) increases from 500 to 20,000. . . . .</i>	62
46	<i>Series of EPIC MOS1 model spectra of a Mekal thermal plasma with a temperature of 2.0 keV. From the bottom to the top, the total number of counts in the XMM-Newton passband (0.15–12 keV) increases from 500 to 20,000. . . . .</i>	62
47	<i>Series of EPIC pn model spectra of a Mekal thermal plasma with a temperature of 2.0 keV. From the bottom to the top, the total number of counts in the XMM-Newton passband (0.15–12 keV) increases from 500 to 20,000. . . . .</i>	63
48	<i>Series of EPIC MOS1 model spectra of a Mekal thermal plasma with a temperature of 10.0 keV. From the bottom to the top, the total number of counts in the XMM-Newton passband (0.15–12 keV) increases from 500 to 20,000. . . . .</i>	63
49	<i>EPIC flux to count rate conversion factors (in units of <math>10^{11}</math> counts <math>\text{erg}^{-1} \text{cm}^2</math>) for pn camera for various power law spectra and for different values of the absorbing column density, <math>N_H</math> (thin filter). . . . .</i>	65
50	<i>EPIC flux to count rate conversion factors (in units of <math>10^{11}</math> counts <math>\text{erg}^{-1} \text{cm}^2</math>) for pn camera for various power law spectra and for different values of the absorbing column density, <math>N_H</math> (medium filter). . . . .</i>	66
51	<i>EPIC flux to count rate conversion factors (in units of <math>10^{11}</math> counts <math>\text{erg}^{-1} \text{cm}^2</math>) for pn camera for various power law spectra and for different values of the absorbing column density, <math>N_H</math> (thick filter). . . . .</i>	67
52	<i>EPIC flux to count rate conversion factors (in units of <math>10^{11}</math> counts <math>\text{erg}^{-1} \text{cm}^2</math>) for MOS1 camera for various power law spectra and for different values of the absorbing column density, <math>N_H</math> (thin filter). . . . .</i>	68
53	<i>EPIC flux to count rate conversion factors (in units of <math>10^{11}</math> counts <math>\text{erg}^{-1} \text{cm}^2</math>) for MOS1 camera for various power law spectra and for different values of the absorbing column density, <math>N_H</math> (medium filter). . . . .</i>	69
54	<i>EPIC flux to count rate conversion factors (in units of <math>10^{11}</math> counts <math>\text{erg}^{-1} \text{cm}^2</math>) for MOS1 camera for various power law spectra and for different values of the absorbing column density, <math>N_H</math> (thick filter). . . . .</i>	70
55	<i>EPIC flux to count rate conversion factors (in units of <math>10^{11}</math> counts <math>\text{erg}^{-1} \text{cm}^2</math>) for MOS2 camera for various power law spectra and for different values of the absorbing column density, <math>N_H</math> (thin filter). . . . .</i>	71
56	<i>EPIC flux to count rate conversion factors (in units of <math>10^{11}</math> counts <math>\text{erg}^{-1} \text{cm}^2</math>) for MOS2 camera for various power law spectra and for different values of the absorbing column density, <math>N_H</math> (medium filter). . . . .</i>	72
57	<i>EPIC flux to count rate conversion factors (in units of <math>10^{11}</math> counts <math>\text{erg}^{-1} \text{cm}^2</math>) for MOS2 camera for various power law spectra and for different values of the absorbing column density, <math>N_H</math> (thick filter). . . . .</i>	73



XMM-Newton Science Operations Centre

---

58	<i>EPIC flux to count rate conversion factors (in units of <math>10^{11}</math> counts <math>\text{erg}^{-1} \text{ cm}^2</math>) for pn camera for various mekal spectra and for different values of the absorbing column density, <math>N_H</math> (thin filter).</i>	74
59	<i>EPIC flux to count rate conversion factors (in units of <math>10^{11}</math> counts <math>\text{erg}^{-1} \text{ cm}^2</math>) for pn camera for various mekal spectra and for different values of the absorbing column density, <math>N_H</math> (medium filter).</i>	75
60	<i>EPIC flux to count rate conversion factors (in units of <math>10^{11}</math> counts <math>\text{erg}^{-1} \text{ cm}^2</math>) for pn camera for various mekal spectra and for different values of the absorbing column density, <math>N_H</math> (thick filter).</i>	76
61	<i>EPIC flux to count rate conversion factors (in units of <math>10^{11}</math> counts <math>\text{erg}^{-1} \text{ cm}^2</math>) for MOS1 camera for various mekal spectra and for different values of the absorbing column density, <math>N_H</math> (thin filter).</i>	77
62	<i>EPIC flux to count rate conversion factors (in units of <math>10^{11}</math> counts <math>\text{erg}^{-1} \text{ cm}^2</math>) for MOS1 camera for various mekal spectra and for different values of the absorbing column density, <math>N_H</math> (medium filter).</i>	78
63	<i>EPIC flux to count rate conversion factors (in units of <math>10^{11}</math> counts <math>\text{erg}^{-1} \text{ cm}^2</math>) for MOS1 camera for various mekal spectra and for different values of the absorbing column density, <math>N_H</math> (thick filter).</i>	79
64	<i>EPIC flux to count rate conversion factors (in units of <math>10^{11}</math> counts <math>\text{erg}^{-1} \text{ cm}^2</math>) for MOS2 camera for various mekal spectra and for different values of the absorbing column density, <math>N_H</math> (thin filter).</i>	80
65	<i>EPIC flux to count rate conversion factors (in units of <math>10^{11}</math> counts <math>\text{erg}^{-1} \text{ cm}^2</math>) for MOS2 camera for various mekal spectra and for different values of the absorbing column density, <math>N_H</math> (medium filter).</i>	81
66	<i>EPIC flux to count rate conversion factors (in units of <math>10^{11}</math> counts <math>\text{erg}^{-1} \text{ cm}^2</math>) for MOS2 camera for various mekal spectra and for different values of the absorbing column density, <math>N_H</math> (thick filter).</i>	82
67	<i>EPIC flux to count rate conversion factors (in units of <math>10^{11}</math> counts <math>\text{erg}^{-1} \text{ cm}^2</math>) for pn camera for various black body spectra and for different values of the absorbing column density, <math>N_H</math> (thin filter).</i>	83
68	<i>EPIC flux to count rate conversion factors (in units of <math>10^{11}</math> counts <math>\text{erg}^{-1} \text{ cm}^2</math>) for pn camera for various black body spectra and for different values of the absorbing column density, <math>N_H</math> (medium filter).</i>	84
69	<i>EPIC flux to count rate conversion factors (in units of <math>10^{11}</math> counts <math>\text{erg}^{-1} \text{ cm}^2</math>) for pn camera for various black body spectra and for different values of the absorbing column density, <math>N_H</math> (thick filter).</i>	85
70	<i>EPIC flux to count rate conversion factors (in units of <math>10^{11}</math> counts <math>\text{erg}^{-1} \text{ cm}^2</math>) for MOS1 camera for various black body spectra and for different values of the absorbing column density, <math>N_H</math> (thin filter).</i>	86
71	<i>EPIC flux to count rate conversion factors (in units of <math>10^{11}</math> counts <math>\text{erg}^{-1} \text{ cm}^2</math>) for MOS1 camera for various black body spectra and for different values of the absorbing column density, <math>N_H</math> (medium filter).</i>	87
72	<i>EPIC flux to count rate conversion factors (in units of <math>10^{11}</math> counts <math>\text{erg}^{-1} \text{ cm}^2</math>) for MOS1 camera for various black body spectra and for different values of the absorbing column density, <math>N_H</math> (thick filter).</i>	88
73	<i>EPIC flux to count rate conversion factors (in units of <math>10^{11}</math> counts <math>\text{erg}^{-1} \text{ cm}^2</math>) for MOS2 camera for various black body spectra and for different values of the absorbing column density, <math>N_H</math> (thin filter).</i>	89



---

74	<i>EPIC flux to count rate conversion factors (in units of <math>10^{11}</math> counts <math>\text{erg}^{-1} \text{cm}^2</math>) for MOS2 camera for various black body spectra and for different values of the absorbing column density, <math>N_H</math> (medium filter).</i>	90
75	<i>EPIC flux to count rate conversion factors (in units of <math>10^{11}</math> counts <math>\text{erg}^{-1} \text{cm}^2</math>) for MOS2 camera for various black body spectra and for different values of the absorbing column density, <math>N_H</math> (thick filter).</i>	91
76	<i>Schematic drawing of a grating, including some of the key dispersion angles.</i>	93
77	<i>Sketch of an RFC chip array with 9 MOS CCDs. The half of each CCD at large camera y coordinates is exposed to the sky, the other half is used as a storage area. The dispersion direction is along the Z axis, so that higher energies (shorter wavelengths) are dispersed to higher values in Z. Using the spacecraft axis, the BETA value (dispersion direction) is antiparallel to Z, and the cross-dispersion is parallel to Y.</i>	94
78	<i>Example of RGS data for a calibration observation of Capella shown with a logarithmic intensity scale. The dispersion axis runs horizontally and increases to the right. Lower dispersion angles correspond to shorter wavelengths or higher energy. The top panel shows the image of the dispersed light in the detector. The cross dispersion is along the vertical axis. The bottom panel shows the order selection plane, with the energy, PI, on the ordinate. This also illustrates the mechanism used for separation of first, second and higher grating orders. Standard data selections are indicated by the white curves. In the bottom panel, the low and high level thresholds are visible. In the top panel, the effect of fixed pattern noise at long wavelengths is seen.</i>	97
79	<i>The three main components of the LSF: the projected mirror response (green), broadened after folding with the grating response (red), and after applying the detector energy selections (blue). All components are normalised to their maximum.</i>	98
80	<i>Measured (black) and simulated (red) RGS2 Line Spread Function for the O VIII Ly<math>\alpha</math> line in HR 1099. The assumed background is shown in green.</i>	98
81	<i>A close-up view of the O VIII Ly<math>\alpha</math> line in HR 1099 along the cross-dispersion direction.</i>	99
82	<i>The resolving power (HEW and FWHM) of RGS1 (left) and RGS2 (right) in the -1 and -2 grating orders. HEW indicates the detectability of a weak feature against a strong continuum and FWHM whether two closely spaced spectral lines can be resolved.</i>	100
83	<i>Comparison of measured and laboratory wavelengths for a number of sources and observations. Observed wavelengths have been corrected for solar angle dependence and for heliocentric velocity.</i>	101
84	<i>The effective area of both RGS units combined as a function of energy and wavelength (top and bottom horizontal scales, respectively). See text for detailed explanations.</i>	102
85	<i>The effective areas of both RGS units separately as a function of energy and wavelength (top and bottom horizontal scales, respectively). See text for detailed explanations.</i>	103
86	<i>The RGS1 effective area as a function of cross dispersion off-axis angle.</i>	104



---

87	<i>The average quiet background spectra from first (top) and second (bottom) order. RGS1 is shown in black and RGS2 in red. An enhancement of the count rate below 7 Å in each RGS is due to a change in the width of the pulse height filter at that wavelength. There is a bump around 32 Å in the RGS1 spectrum. The origin has not been fully understood but the most likely explanation is a somewhat higher dark current for CCD2 in this RGS. The lower background in the first order spectrum of RGS2 in this range seems to be related to the use of “single node readout” mode in this RGS.</i>	106
88	<i>Scheme of the position of the RGS detector defects in wavelength space.</i>	113
89	<i>RGS avoidance angles for sources brighter than 4 and between 4 and 5 optical magnitudes (left and right panel, respectively). -Z is the dispersion direction of RGS, Y is the cross-dispersion direction.</i>	114
90	<i>Coronal spectrum of the binary star Capella adapted from Audard et al. 2001, A&amp;A 365, L329. The RGS1 first order spectrum is shown with some line identifications. The total exposure time is 53 ks.</i>	115
91	<i>RGS spectra of the highly variable low-mass X-ray binary EXO 0748-67. The three panels show the spectra for three different activity states: low emission, active variation and burst. The spectra are binned to 0.035 Å per bin. The cumulative exposure time for each spectrum is indicated (Cottam et al. 2001, A&amp;A 365, L277).</i>	116
92	<i>Detail of the EXO 0748-67 RGS spectrum. The O VII He-like lines are shown overlaid with the instrument line spread function, broadened to account for a 1390 km s<sup>-1</sup> velocity field. The contributions from the resonance line (r), intercombination lines (i), and forbidden line (f) are shown with thin lines. The thick line shows the combined fit (Cottam et al. 2001, A&amp;A 365, L277).</i>	117
93	<i>The first order RGS spectrum of the SMC supernova remnant 1E 0102.2-7219. The effective exposure time is 29.7 ks for each RGS after selection of low background periods in a 37.9 ks exposure. RGS1 is plotted in black, RGS2 in red. The data are shown in both linear and logarithmic scales. This figure and the next show that almost the nominal RGS spectral resolution can be achieved even for moderately extended (<math>\approx 2'</math>) objects (Rasmussen et al., 2001, A&amp;A 365, L231).</i>	118
94	<i>Detail of the 8-20 Å region of the spectrum shown in the previous figure. First (black) and second (red) order are plotted separately. The data from the two spectrometers have been averaged for each order extraction. The higher spectral resolution and resilience to source extent is clearly seen in second order, where some line complexes blended in first order are resolved (Rasmussen et al., 2001, A&amp;A 365, L231).</i>	118
95	<i>Detail of the Oxygen line profile in the 1E 0102.2-7219 spectrum. The plot compares the point source line spread function for RGS1, the approximate monochromatic line profile based on the target’s angular distribution and a heuristic wavelength broadening function that is applied in addition to the angular distribution (Rasmussen et al., 2001, A&amp;A 365, L231).</i>	119
96	<i>RGS spectrum of the bright starburst nucleus of the nearby edge-on galaxy NGC 253, binned to 0.07 Å per bin. The effective exposure time is <math>\approx</math> 53.4 ks for each spectrograph, after selection of low background periods. The extraction region is 1' along the minor disk axis. (Pietsch et al. 2001, A&amp;A 365, L174).</i>	120
97	<i>RGS spectra of two bright, nearby, Narrow Line Seyfert 1 galaxies. MCG-6-30-15 (top) was observed for a total of 120 ks while the exposure time for Mrk 766 (bottom) was 55 ks. (Branduardi-Raymont et al. 2001, A&amp;A 365, L140).</i>	121



---

98	<i>The RGS spectrum of the rich cluster of galaxies Sérsic 159-03 (Abell S 1101). The effective exposure time is 36 ks. The plot also shows in red a fit with a two component cooling flow model. Note the redshifted O VIII Ly <math>\alpha</math> line at 20.0 Å and the Fe XXIV, Fe XXIII and Ne X lines between 11.2 and 12.8 Å (Kaastra et al. 2001, A&amp;A 365, L99).</i>	122
99	<i>First order RGS spectra of the dipping, transient low-mass X-ray binary MXB 1658-298. The upper curve is the persistent emission spectrum and the lower curve that of the dipping intervals. Narrow absorption lines of O VII and Ne X are visible in the persistent spectrum revealing the presence of a warm absorber (Sidoli et al. 2001, A&amp;A 379, 540).</i>	123
100	<i>The light path in XMM-Newton's optical/UV telescope, OM.</i>	125
101	<i>Sketch of the OM micro-channel plate intensified CCD (MIC) detector.</i>	126
102	<i>Throughput curves for the OM filters, folded with the detector sensitivity.</i>	128
103	<i>The OM grisms Inverse Sensitivity Functions</i>	130
104	<i>Flux calibrated spectrum of the white dwarf HZ 2, obtained with the OM ultraviolet (in blue) and visible (in green) grisms.</i>	130
105	<i>Optics+detector OM PSF in different filters</i>	132
106	<i>OM count rates vs. filter selection for stars of different spectral type with <math>m_v = 20</math> mag.</i>	133
107	<i>Theoretical (red line) and empirical (blue line) coincidence loss correction curves superposed to flight data</i>	135
108	<i>Out-of-focus ghost image (“smoke ring”) of a bright field star, during a 3C273 observation. Clearly visible is the strong fixed pattern noise around the bright source</i>	137
109	<i>Straylight ellipses caused by reflection of a star outside the field of view, taken from the PKS 0312 offset 6 field (V filter in use). The average background rate is 15 counts pixel<math>^{-1}</math> per exposure; in the bright straylight loop is 30 counts pixel<math>^{-1}</math>. The background is also enhanced in the central region due to reflection of the diffuse sky light from outside the field. In the centre it rises to <math>\simeq 3</math> times the average background rate.</i>	138
110	<i>Image obtained with the V filter showing the depletion patch caused by Jupiter in July 2017. The RGS and EPIC-pn boresights are marked in red.</i>	139
111	<i>Positional error of sources in a field of view, where the distortion map has been applied. The histogram was made using sources from the 3C273 field corrected for distortion</i>	140
112	<i>Setup of OM imaging mode default mode observations consisting of a sequence of 5 exposures. The science windows are indicated by solid lines, the detector windows by dashed lines. A 16 in-memory pixel margin around the science window is allocated to accommodate spacecraft drifts.</i>	143
113	<i>Example of a field imaged with the default Image Mode configuration.</i>	144
114	<i>When the boundaries of OM science windows are defined in detector pixel coordinates, the relative location of the windows with respect to each other does not change. However, different areas on the sky are imaged under different position angles.</i>	149



---

115	<i>Defining the locations of OM science windows in sky coordinates one makes sure that (approximately) the same area of the sky is imaged under different position angles. However, the OM science windows can change their relative locations. Windows 3 and 5 (which used to be in the upper left corner of window 3, see previous figure) are now partially overlapping, which is not allowed and window 4 is now partly outside the OM FOV (which is also not allowed).</i> . . . . .	150
116	<i>The effective area of both RGS units combined, compared with Chandra's ACIS-S instrument with various transmission gratings. Note that since early after the beginning of the mission, CCD7 in RGS1 and CCD4 in RGS2 are inoperative, thus the effective area in each of the mentioned CCD energy range is reduced by a factor of 2 (see Table 9).</i> . . . . .	154
117	<i>Top:</i> Comparison of a modelled 30 ks observation of a cluster with a 6 keV thermal plasma spectrum with Chandra ACIS-I (purple line) and XMM-Newton EPIC (pn: black, MOS1: red, MOS2: green). Normalised counts are counts per spectral bin. <i>Bottom:</i> Comparison of the spectral response, for several line triplets at different energies, of XMM-Newton EPIC and RGS and Chandra ACIS instruments. Colour codes are: pn: black; MOS1: red; MOS2: green; RGS1/RGS2: dark/light blue; ACIS LEG/MEG/HEG: purple/green/orange. . . . .	156
118	<i>Comparison of Chandra ACIS-I vs. XMM-Newton EPIC (pn and MOS) pile-up for different total frame count rates. The frame times are 3.3, 2.8 and 0.07 seconds for ACIS-I, MOS and pn, respectively.</i> . . . . .	157
119	<i>Comparison of Chandra ACIS-I vs. XMM-Newton EPIC (pn and MOS) pile-up for different incident source fluxes, after conversion of counts per frame to flux units, adopting an <math>\alpha = -1.7</math> power law spectrum with an absorbing hydrogen column density of <math>3 \times 10^{20} \text{ cm}^{-2}</math>.</i> . . . . .	157
120	<i>Sketch of the highly elliptical XMM-Newton orbit. Original figure provided by Dornier Satellitensysteme GmbH.</i> . . . . .	159
121	<i>Approximate sky visibility, as a fraction of the total time available for science</i> . .	161
122	<i>Maximum target visibility within a single orbit of XMM-Newton during the current AO.</i> . . . . .	162
123	<i>Evolution of maximum target visibility within a single orbit for future AOs</i> . . . . .	163
124	<i>Percentage of observations when the labelled MOS1 (top) and MOS2 (bottom) CCD count rate within the energy range 200-1000 eV is larger by a factor of 4 than the mean of the count rate in the other CCDs (noisy CCD excluded) as a function of the revolution number. In each plot the curves of a "noisy" and of a "clean" CCD are shown.</i> . . . . .	168
125	<i>Simulated EPIC-pn exposure maps for a 5×3 mosaic observation with pointing offsets of 1arcmin (top-left), 15arcmin (top-right) and 30arcmin (bottom). The colour bar at the top gives the effective exposure relative to the duration of individual pointings.</i> . . . . .	172



## List of Tables

1	<i>XMM-Newton characteristics – an overview</i>	8
2	<i>The on-axis in orbit and on ground 1.5 keV PSFs of the different X-ray telescopes</i>	11
3	<i>Basic numbers for the science modes of EPIC</i>	33
4	<i>Detection limits (i.e., minimum detectable flux at <math>4\sigma</math> in units of <math>10^{-15}</math> erg cm<math>^{-2}</math> s<math>^{-1}</math>) for different energy bands in the 1.16 Ms observation of the Lockman Hole (Hasinger et al., 2001, A&amp;A 365, L45; Brunner et al. 2008, A&amp;A, 479, 283).</i>	47
5	<i>The effect of pile-up on spectral fits</i>	51
6	<i>EPIC Out-of-Time (OoT) events. The percentage of OoT events is given by the mode dependent ratio of readout time and integration time</i>	55
7	<i>List of EPIC event patterns</i>	60
8	<i>RGS In-orbit Performance</i>	93
9	<i>Wavelength and energy ranges covered by the chips of RGS1 and RGS2 for an on-axis source in first order. Due to the scattering, the chip boundaries do not cause sharp features in the effective area. Values in brackets correspond to the non-operational chains.</i>	95
10	<i>Wavelength ranges covered by the RGS in different grating orders</i>	95
11	<i>Flux per CCD<sup>1</sup> for a &lt; 2% pile-up for point sources in Spectroscopy mode and using 8 CCDs<sup>2</sup></i>	109
12	<i>RGS science data acquisition modes</i>	110
13	<i>RGS1 detector defects and corresponding wavelengths for on-axis sources.</i>	112
14	<i>RGS2 detector defects and corresponding wavelengths for on-axis sources. Since the introduction of single-node operations, the node gap that applies between the two nodes of the RGS1 CCDs is no longer relevant in RGS2.</i>	113
15	<i>OM characteristics – an overview</i>	124
16	<i>OM optical elements</i>	128
17	<i>OM filters: effective wavelengths, widths and Zeropoints</i>	129
18	<i>OM UV grism sensitivity [detected flux: erg cm<math>^{-2}</math> s<math>^{-1}</math> Å<math>^{-1}</math>] for different detection levels. The Visible grism is one order of magnitude more sensitive than the UV one.</i>	131
19	<i>OM on-board PSF FWHM in different lenticular filters</i>	131
20	<i>OM count rates [<math>10^{-4}</math> counts s<math>^{-1}</math>] as function of spectral type for stars with <math>m_V = 20</math> mag under the assumption of a detector with zero deadtime, no coincidence loss and no time sensitivity degradation.</i>	133
21	<i>OM coincidence loss corrections for high count rates.</i>	134
22	<i>Limiting magnitudes<sup>1</sup> for a 5-<math>\sigma</math> detection in 1000 s</i>	135
23	<i>Observed limiting magnitudes<sup>1</sup> for a 5-sigma detection (scaled to 1000s)</i>	136
24	<i>Levels of different OM background contributors</i>	136
25	<i>The <math>m_V</math> brightness limits for all OM filters. An A0 type star spectrum is assumed.</i>	138
26	<i>The science data acquisition modes of OM</i>	141
27	<i>OM exposure time constraints</i>	146
28	<i>Comparison of XMM-Newton with other X-ray satellites</i>	153
29	<i>Evolution of Orbital Parameters of XMM-Newton</i>	158



## 1 Glossary

Acronym	Explanation
ACIS	<i>Chandra</i> CCD Imaging Spectrograph
AHF	Attitude History File
AMS	Archival Management Subsystem
AO	Announcement of Opportunity
AOCS	Attitude and Orbit Control and Measurement Subsystem
CAMEX	CMOS Amplifier and Multiplexer Chip
CCD	Charge Coupled Device
CCF	Current Calibration File
<i>Chandra</i>	<i>Chandra</i> X-Ray Observatory
CTE	Charge Transfer Efficiency
CTI	Charge Transfer Inefficiency
DPU	Digital Processing Unit
EPIC	European Photon Imaging Camera
ERMS	EPIC Radiation Monitor Subsystem
ESAC	European Space Astronomy Centre
FAQ	OM Field Acquisition
FITS	Flexible Image Transport System
FOV	Field Of View
<i>FWHM</i>	Full Width at Half Maximum
GO	Guest Observer
GT	Guaranteed Time
GUI	Graphical User Interface
HEASARC	(NASA) High Energy Astrophysics Science Archive Research Center
HED	High Energy Detector (of the ERMS)
HER	RGS high event rate (selectable mode)
HETG	( <i>Chandra</i> ) High Energy Transmission Grating
<i>HEW</i>	Half Energy Width
HRC	( <i>Chandra</i> ) High Resolution Camera
LED	Low Energy Detector (of the ERMS)
LETG	( <i>Chandra</i> ) Low Energy Transmission Grating
LSF	Line-spread Function
MCP	Micro-Channel Plate
MIC	Micro-Channel Plate Intensified CCD
MIP	Minimum Ionising Particle
MOS	Metal Oxide Semi-conductor
MPM	RGS Multipointing Mode
OCB	On-Chip Binning
ODF	Observation Data File
OM	Optical Monitor
OTAC	Observatory Time Allocation Committee



PHA	Pulse Height Analyser
PHS	Proposal Handling Subsystem
PI	Principal Investigator
<i>PIMMS</i>	Portable, Interactive Multi-Mission Simulator
PPS	Pipeline Processing Subsystem
PSF	Point-Spread Function
PV	Performance Verification
QE	Quantum Efficiency
RAF	Raw Attitude File
RFC	RGS Focal Camera
RFS	Refreshed Frame Store (readout mode of EPIC MOS)
RGA	Reflection Grating Assembly (of the RGS)
RGS	Reflection Grating Spectrometer
RPE	Relative Pointing Error
RPS	Remote Proposal Submission software
SAS	Science Analysis Software
SciSim	XMM-Newton Science Simulator
SDF	Slew Data File
SOC	XMM-Newton Science Operations Centre
SSC	Survey Science Centre
UHB	XMM-Newton Users Handbook
URL	Unique Resource Location
UT	Universal Time
<i>W90</i>	90% energy width
XID	X-ray source identification (by the SSC)
XMM-Newton	X-ray Multi-Mirror Mission
XRPS	XMM-Newton Remote Proposal Submission software
XSA	XMM-Newton Science Archive



## 2 Introduction

### 2.1 Scope of this document

This document is designed to be the starting point for XMM-Newton users in the search for information on the instrumentation on board the satellite. Users working with a printed (postscript or PDF) version of this document, please note that the online XMM-Newton Users Handbook (UHB) is full of links to other components of our web-based information system (and other, external, servers). Also, most of the figures are colour based and some do not reproduce well in black and white. Various appendices also provide introductions and links to other online services of the XMM-Newton Science Operations Centre (SOC) and the Survey Science Centre (SSC). The XMM-Newton UHB is primarily intended to serve as a proposal preparation document, based on which potential XMM-Newton users will be able to assess the technical feasibility of their planned observations and the expected data quality. Information about the procedure to submit proposals is given in the current version of the Policies and Procedures.

In addition, the UHB provides an overview of XMM-Newton data calibration and analysis (the Science Analysis Software, SAS) mainly specifying links to related documents for further reading. This version of the UHB represents the best *current* understanding of XMM-Newton at the time of release based on acquired experience in-orbit with the satellite and the instruments. It is therefore more complete and accurate than previous versions which should be discarded.

### 2.2 Structure and contents of the Users Handbook

This document contains, in the order listed here:

1. A concise summary of XMM-Newton's properties and the instruments onboard (§ 3) and a description of how to conduct observations with XMM-Newton (§ 4).
2. A description of the two-phase proposal submission and the technical optimisation step performed for approved XMM-Newton proposals (§ 5).
3. A brief description of the data calibration and analysis software (§ 6), which also introduces the XMM-Newton Science Analysis Software SAS (§ 6.1) and the XMM-Newton Science Archive (§ 6.4).
4. Additional sources of information on XMM-Newton (§ 7).
5. Appendices on the XMM-Newton Survey Science Centre (SSC; Appendix A) and the XMM-Newton Routine Calibration Programme (Appendix B).

The information contained in § 3 and § 4 should supply sufficient detail to enable the reader to prepare the submission of an XMM-Newton observing proposal.

### 2.3 Location

This document forms part of the online XMM-Newton SOC documentation server on the WWW, at the URL <http://www.cosmos.esa.int/web/xmm-newton/>. The URL of the interface document leading to the XMM-Newton Users Handbook is

<http://www.cosmos.esa.int/web/xmm-newton/documentation>.



## 2.4 Sources of information

Information presented in this document and related to scientific data is based on in-flight observations, except for Section 3.3.9 which discusses some effects of pile-up on spectral fits that are based on model simulations using the XMM-Newton Science Simulator (SciSim). The SciSim tool was developed before launch by the SOC for modelling XMM-Newton observations. The last version of SciSim (V4.0) was released in Jan 2005 and kept operational until July 2010, when maintenance and public distribution of SciSim was finally stopped.

## 2.5 Updates on this document

It is intended not to update this document during a call for proposals. If, however, new information which is significant for the proposal preparation becomes available, the user will be informed via the XMM-Newton News Mailing List.

## 2.6 How to obtain further help and information

The Users Handbook is an integral part of the SOC's web-based online information system and it contains lots of links to other components of the web server. All links can also always be reached via the SOC home page.

Additionally, in order to facilitate the search for more information, § 7 of this document contains a compilation of relevant links and references.

Continuously updated information on the calibration status of the XMM-Newton scientific payload can be found in the XMM-Newton Calibration Portal. The Calibration status of EPIC, RGS, and OM can be found in the respective technical notes XMM-SOC-CAL-TN-0018, XMM-SOC-CAL-TN-0030, and XMM-SOC-CAL-TN-0019.

The main point of contact for users who need help or additional information, or who want to send suggestions that may improve our system, is the XMM-Newton HelpDesk. All questions related to the current Announcement of Opportunity and observing matters, should also be sent to us using this interface. An archive of all questions with their solutions can be consulted before raising a new ticket. To avoid that the communication is visible to the public, the originator of a help ticket may select the *Private* flag, which may be of interest if requests contain, e.g., personal or confidential information.

The XMM-Newton HelpDesk interface can be accessed via:

<http://www.cosmos.esa.int/web/xmm-newton/xmm-newton-helpdesk>.

## 2.7 Acknowledgements

Extensive contributions to several sections of the Users Handbook are gratefully acknowledged, especially from

- B.Aschenbach and P.Gondoin (§ 3.2, X-ray Telescopes),
- U.Briel, A.De Luca, K.Dennerl, P.Ferrando, M.Freyberg, G.Griffiths, F.Haberl, E.Kenziolla, M.Kirsch, D.Lumb, S.Molendi, A.Read, R.Saxton and S.Sembay (§ 3.3, EUROPEAN PHOTON IMAGING CAMERA (EPIC)),
- A.Read and the whole Background Working Group (§3.3.7.4, EPIC background and its importance for extended sources)

- M.Audard, C.Erd, J.W.den Herder, C.Gabriel, F.Paerels, A.Pollock, A.Rasmussen, M.Sako and T.Tamura (§ 3.4, REFLECTION GRATING SPECTROMETER (RGS)),
- I.Antokhin, A.Breeveld, B.Chen, K.O.Mason, R.Much and A.Talavera (§ 3.5, OPTICAL MONITOR (OM)),
- M.Watson, S.Rosen (Appendix A, XMM-Newton Survey Science Centre (SSC)).



**esa**

European space agency  
agence spatiale européenne

### 3 XMM-Newton – a concise overview

XMM-Newton is the second of ESA's four “cornerstone” missions defined in the Horizon 2000 Programme. It was launched on December 10th, 1999 and carries two distinct types of telescope: three Wolter type-1 X-ray telescopes, with different X-ray detectors in their foci (which are described in this chapter), and a 30-cm optical/UV telescope with a microchannel-plate pre-amplified CCD detector in its focal plane (see also below). Thus, XMM-Newton offers simultaneous access to two windows of the electromagnetic spectrum: X-ray and optical/UV.

XMM-Newton provides the following three types of science instrument:

#### 1. European Photon Imaging Camera (EPIC)

3 CCD cameras for X-ray imaging, moderate resolution spectroscopy, and X-ray photometry; the two different types of EPIC camera, MOS and pn, are described in § 3.3. XMM-Newton carries 2 MOS cameras and one pn.

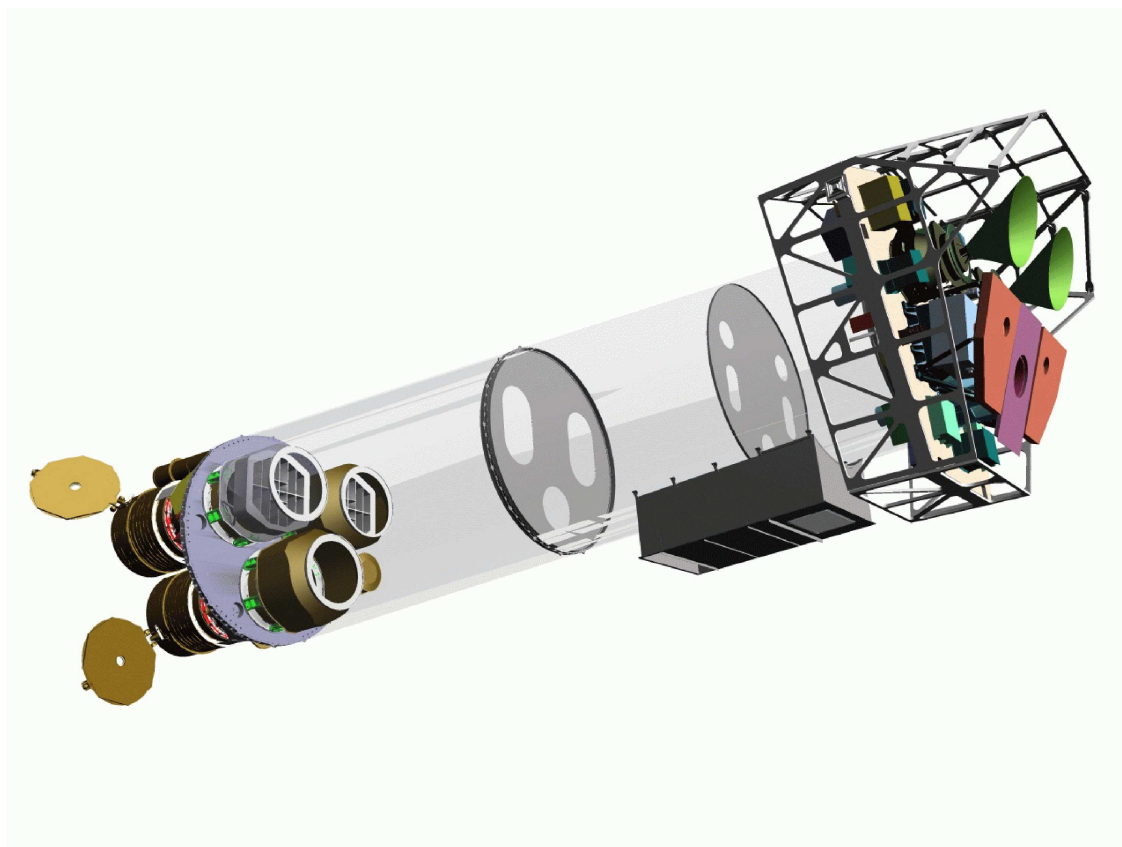


Figure 1: Sketch of the XMM-Newton payload. The mirror modules, two of which are equipped with Reflection Grating Arrays, are visible at the lower left. At the right end of the assembly, the focal X-ray instruments are shown: The EPIC MOS cameras with their radiators (black/green “horns”), the radiator of the EPIC pn camera (violet) and those of the (light blue) RGS detectors (in pink). The OM telescope is obscured by the lower mirror module. Figure courtesy of Dornier Satellitensysteme GmbH.



## 2. Reflection Grating Spectrometer (RGS)

2 essentially identical spectrometers for high-resolution X-ray spectroscopy and spectro-photometry (§ 3.4).

## 3. Optical Monitor (OM)

for optical/UV imaging and grism spectroscopy; § 3.5 provides an overview.

The three EPIC cameras and the two detectors of the RGS spectrometers reside in the focal planes of the X-ray telescopes, while the OM has its own telescope. A sketch of the XMM-Newton payload is displayed in Fig. 1. **There are in total six science instruments on board XMM-Newton, which are operated simultaneously** (unless prohibited by constraints, for example, excessive target brightness). The instruments can be operated independently and each in different modes of data acquisition. Observers will receive data from all science instruments.

### 3.1 Basic characteristics

The most important characteristics of XMM-Newton are compiled in Table 1. More detailed numbers will follow in the chapters on the individual instruments (below) and a comparison with other X-ray satellites is provided in § 3.7. The basic characteristics of XMM-Newton are:

- Simultaneous operation of all science instruments

If not prohibited, e.g. by target brightness constraints, all six XMM-Newton science instruments operate simultaneously. They work independently (i.e., exposures of the individual instruments do not necessarily start and end at the same time).

- High sensitivity

XMM-Newton carries the X-ray telescopes with the largest effective area of a focusing telescope ever: the total mirror geometric effective area at 1.5 keV energy is ca. 1550 cm<sup>2</sup> for each telescope, i.e., 4650 cm<sup>2</sup> in total.

- Good angular resolution

XMM-Newton's high sensitivity is achieved by using 58 thin nested mirror shells in each X-ray telescope. The achieved point-spread function (PSF) has a full width at half maximum (*FWHM*) on the order of 6'' and a *HEW*, at which 50% of the total energy are encircled, of ca. 15''.

- Moderate and high spectral resolution

The EPIC CCD cameras have moderate spectral resolution (with a resolving power, E/ΔE, of ca. 20–50). The RGS spectrometers offer much higher spectral resolution, with a resolving power in the range of 200–800.

- Simultaneous optical/UV observations

Observations with the co-aligned OM optical/UV telescope render possible the monitoring and identification of optical/UV counterparts of X-ray sources seen by the X-ray telescopes as well as imaging of the surrounding field.

- Long continuous target visibility

A highly elliptical orbit offers continuous target visibility of up to about 40 hours, with a minimum height for science observations of 46,000 km. This is very favourable



Table 1: *XMM-Newton characteristics – an overview*

Instrument	EPIC MOS	EPIC pn	RGS	OM
Bandpass	0.15–12 keV	0.15–12 keV	0.35–2.5 keV <sup>(1)</sup>	180–600 nm
Orbital target vis. <sup>(2)</sup>	5–135 ks	5–135 ks	5–135 ks	5–145 ks
Sensitivity <sup>(3)</sup>	$\sim 10^{-14}$ <sup>(4)</sup>	$\sim 10^{-14}$ <sup>(4)</sup>	$\sim 8 \times 10^{-5}$ <sup>(5)</sup>	20.7 mag <sup>(6)</sup>
Field of view (FOV)	30' <sup>(7)</sup>	30' <sup>(7)</sup>	~5'	17'
PSF ( <i>FWHM/HEW</i> ) <sup>(8)</sup>	5"/14"	6"/15"	N/A	1.4"-2.0"
Pixel size	40 μm (1.1")	150 μm (4.1")	81 μm ( $9 \times 10^{-3}$ Å) <sup>(9)</sup>	0.476513" <sup>(10)</sup>
Timing resolution <sup>(11)</sup>	1.75 ms	0.03 ms	0.6 s	0.5 s
Spectral resolution <sup>(12)</sup>	~70 eV	~80 eV	0.04/0.025 Å <sup>(13)</sup>	180 <sup>(14)</sup>

Notes to Table 1:

- 1) In the –1. grating order (wavelength range: 5–35 Å;  $\lambda$  [Å]  $\times$  E [keV] = 12.3984).
- 2) Total time available for science per orbit; minimum of 5 ks (excl. overheads, see § 4.5.2) in order to ensure observatory efficiency. XMM-Newton science observations can only be performed outside the Earth's radiation belts (see § 4.2.1).
- 3) After 10 ks; cf. overview tables on the individual instruments.
- 4) In the range 0.15–12.0 keV, in units of erg s<sup>-1</sup> cm<sup>-2</sup>, see § 3.3.8 for details.
- 5) O VII 0.57 keV line flux in photons cm<sup>-2</sup> s<sup>-1</sup>, for an integration time of 10 ks and a background of 10<sup>-4</sup> photons cm<sup>-2</sup> s<sup>-1</sup> keV<sup>-1</sup>. More details are provided in § 3.4.4.7.
- 6) 5- $\sigma$  detection of an A0 star in 1000 s.
- 7) See Figs. 17, 18 and 19 for the detailed shape of the FOV.
- 8) See Fig. 4 and 105 for an in-flight point source measurement for EPIC and OM, respectively. Table 2 lists in orbit and on ground PSF values for all three EPIC cameras separately.
- 9) In spectroscopy mode (standard 3 × 3 pixel on-chip binning applied).
- 10) 1" with 2 × 2 binning in default configuration mode.
- 11) In fast data acquisition mode (i.e., fast mode for OM and timing mode for EPIC, spectroscopy mode for RGS1 [1.2 s for RGS2], reading out only one of nine CCDs). The EPIC pn burst mode offers an even higher timing resolution of 7μs, but has a very low duty cycle of 3%.
- 12) At 1 keV energy. At the energy of Fe K $\alpha$  (6.4 keV), the energy resolution of both EPIC cameras is ca. 150 eV.
- 13) In –1. and –2. order, resp.; at 1 keV, this corresponds to 3.2/2.0 eV (*HEW*).
- 14) Resolving power ( $\lambda/\Delta\lambda$ ) with UV and optical grism.

for studies of source variability and also in order to achieve a high overall observatory efficiency.

For a comparison of these basic characteristics with those of other past or contemporaneous X-ray satellite missions, see § 3.7.

More detailed information on the mirrors and on the instruments listed in Table 1 and their observing modes is provided in the following sections (§ 3.2 – § 3.5).



**esa**

European space agency  
agence spatiale européenne

### 3.2 X-ray Telescopes

**XMM-Newton's three X-ray telescopes** are co-aligned with a relative astrometry between the three EPIC cameras calibrated to better than 1–2" across the full FOV. One telescope has a light path as shown in Fig. 2; the two others have grating assemblies in their light paths, diffracting part of the incoming radiation onto their secondary focus. Fig. 3 shows the light path in the latter two X-ray telescopes on board XMM-Newton. Ca. 44% of the incoming light focused by the multi-shell grazing incidence mirrors is directed onto the camera at the prime focus, while 40% of the radiation is dispersed by a grating array onto a linear strip of CCDs. The remaining light is absorbed by the support structures of the RGAs.

The focal instruments are described in §§ 3.3, 3.4 and 3.5. First we explain the most important properties of the mirror assemblies.

The performance of each X-ray telescope is characterised by:

1. the image quality,
2. the effective area, and
3. the straylight rejection efficiency,

which will be described in the following sections.

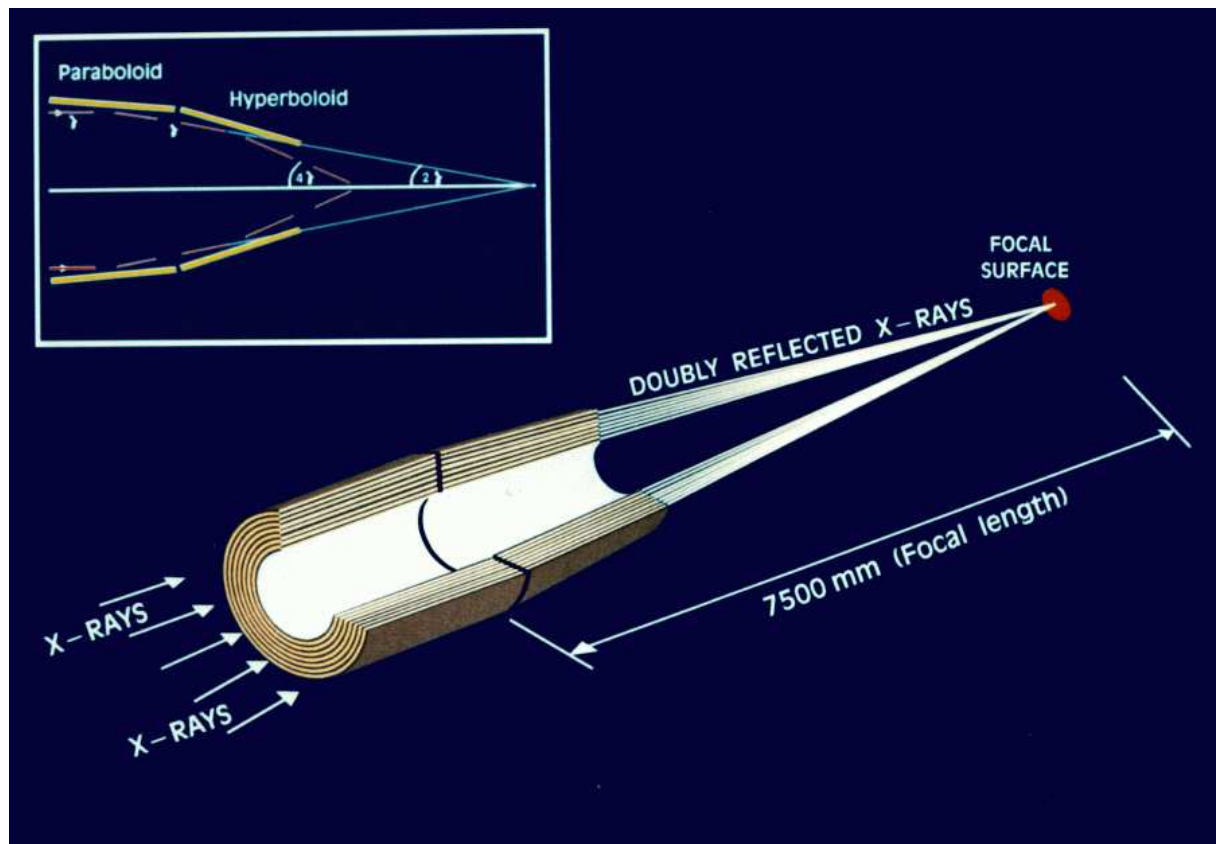


Figure 2: The light path in XMM-Newton's open X-ray telescope with the pn camera in focus (not to scale).



**esa**

european space agency  
agence spatiale européenne

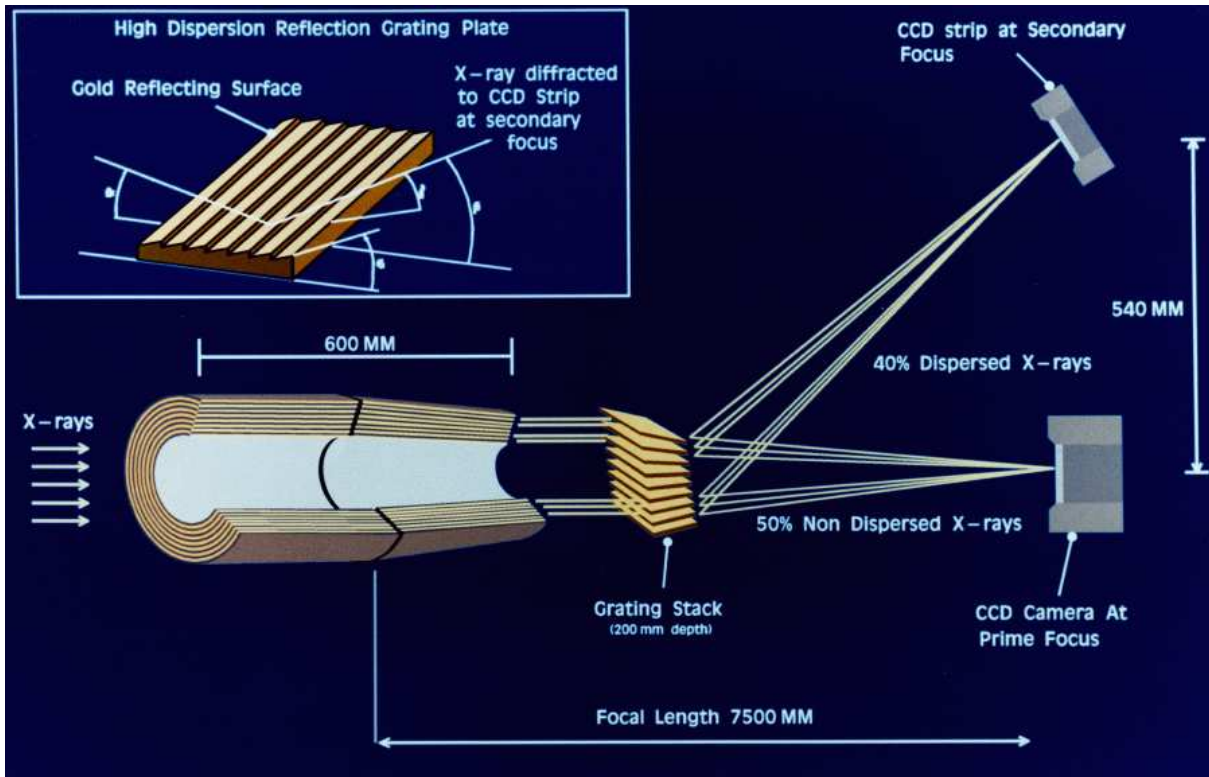


Figure 3: *The light path in the two XMM-Newton telescopes with grating assemblies (not to scale). Note that the actual fraction of the non-intercepted light that passes to the primary MOS focus is 44%, while 40% of the incident light is intercepted by grating plates of the RGA.*

### 3.2.1 X-ray point-spread function

The first critical parameter determining the quality of an X-ray mirror module is its ability to focus photons. Here lies one of XMM-Newton's major strong points: the core of its on-axis point-spread function (PSF) is narrow and varies little over a wide energy range (0.1–6 keV). Above 6 keV, the PSF becomes only slightly more energy dependent.

#### 3.2.1.1 On-axis PSF

Each of the three Wolter-type X-ray telescopes on board XMM-Newton has its own point-spread function (PSF). As an example, Fig. 4 shows the in orbit on-axis PSF of the MOS1, MOS2 and pn X-ray telescopes, registered on the same source. This figure is primarily provided to show the shape of the PSF, with for example the radial substructures caused by the spiders holding the mirror shells. Values for the full width at half maximum (*FWHM*) and half energy width (*HEW*) of the PSFs (both in-orbit and ground measurements) are listed in Table 2.

Figs. 5, 6 and 7 show the fractional encircled energy as a function of radius from the centre of the PSF for several different energies as it is currently implemented in the current calibration file (CCF, ELLBETA mode).

Please note that the PSF measurements by the EPIC cameras might depend on the instrument readout mode, through combinations of out-of-time event smearing and/or pile-up. The PSF can be severely affected by pile-up effects when the count rate exceeds a few counts per frame.



**esa**

european space agency  
agence spatiale européenne

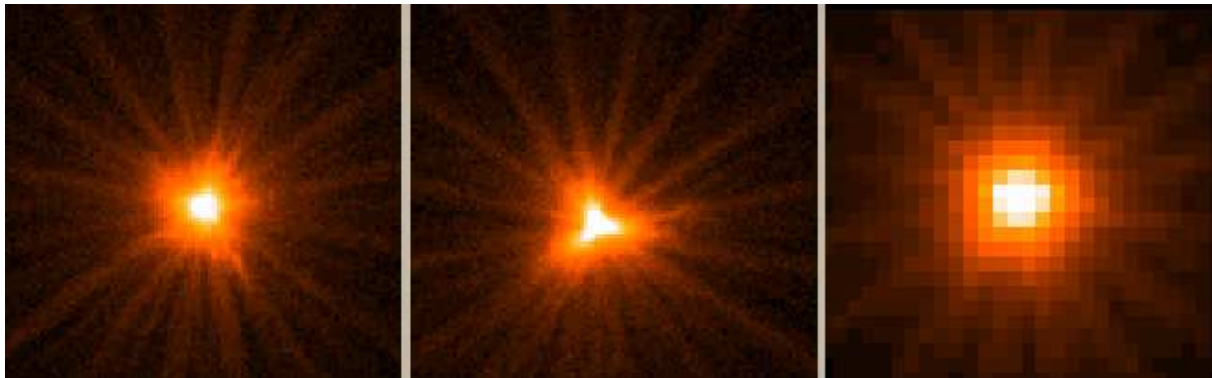


Figure 4: *On axis point spread function (PSF) of the MOS1, MOS2 and pn X-ray telescopes (left to right) registered on the same source with each MOS camera in Small Window mode, and the pn camera in Large Window mode. The pixel size is 1.1 arcsec square for the MOS, and 4.1 arcsec square for the pn. The images are 110 arcsec wide. A square root scale has been used to visualise the wings of the PSF. The core of the PSF is piled-up for this source, with a different factor for the MOS and the pn. The star-like pattern is created by the spider which supports the 58 co-axial Wolter I mirrors of the telescope. The shape of the PSF core is slightly different for all cameras, with MOS2 having a somewhat more pronounced shape.*

Depending on the selection of event types in the EPIC event analysis process, a hole can even appear in the core of the PSF due to the lack of events whose reconstructed energy is above the onboard high-energy rejection threshold (see § 3.3.9).

### 3.2.1.2 Off-axis PSF

The PSF of the X-ray telescopes depends on the source off-axis angle, i.e., its distance from the centre of the field of view (FOV). It also depends slightly on the source azimuth within the FOV. In Fig. 8 the dependence of the shape of the XMM-Newton X-ray PSF on the position within the FOV is presented. One can see that the PSF at large off-axis angles is elongated due to off-axis aberration (astigmatism). The reader is also referred to Figs. 17, 18 and 19 for additional impressions of the off-axis PSF.

For the two EPIC MOS cameras, the PSF is also affected at a level of a few times  $10^{-4}$  (integral

Table 2: *The on-axis in orbit and on ground 1.5 keV PSFs of the different X-ray telescopes*

Mirror module	2	3	4
Instr. chain <sup>a</sup>	pn	MOS-1+RGS-1	MOS-2+RGS-2
	orbit/ground	orbit/ground	orbit/ground
FWHM ["]	< 12.5 <sup>b</sup> /6.6	4.3/6.0	4.4/4.5
HEW ["]	16.6/15.1	16.8/13.6	17.0/12.8

Notes to Table 2:

a) The instruments located behind the mirror module.

b) The core of mirror module 2 cannot be better resolved in orbit because of the large pn-CCD pixel size.

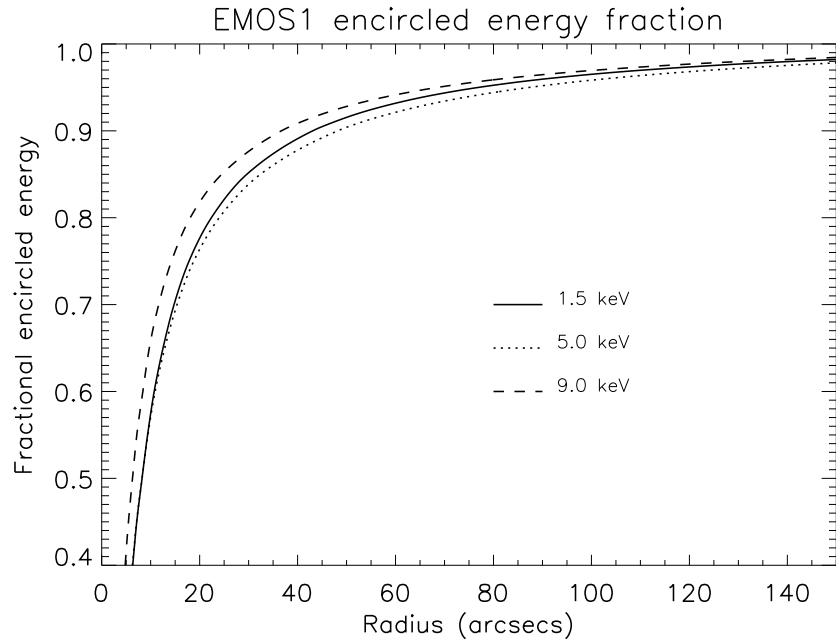


Figure 5: The MOS1 fractional encircled energy as a function of angular radius (on-axis) at different energies. The curves were calculated integrating the PSF that is currently implemented in the CCF.

relative intensity) by scattering off the RGA rib structures. This contribution, however, is negligible in the vast majority of cases.

Figs. 9 and 10 show the off-axis angle dependence of the radius at which 90% of the total energy is encircled ( $W90$ ). As the off-axis angle increases the energy dependence of the PSF changes as focusing of high energy photons is no longer confined to the inner shells. A substantial fraction of these high energy photons are redistributed into the wings of the PSF by X-ray scattering; hence  $W90$  is larger at high energies than at soft energies for large off-axis angles. Note that these data are based on early ray-trace simulations at three discrete energies, and assume a fractional encircled energy of 100% at a radial distance of 5 arcmin, independent of the off-axis angle. For a more precise estimate based on the currently implemented PSF calibration, the user may use the SAS task calview to obtain the encircled energy fraction at a given energy and off-axis angle (note that the "Accuracy Level" should be set to "ELLBETA" through the task interface <http://xmm-tools.cosmos.esa.int/external/sas/current/doc/calview/node3.html>). Also note that encircled energy correction of point sources is performed by default through the respective SAS tasks (see Section 3.2.3).

Users are referred to Read et al. 2011, A&A, 534, 34 for a comprehensive description of the EPIC PSF, as well as for an empirical characterization as a function of off-axis angle and energy.



**esa**

European space agency  
agence spatiale européenne

Document No.: XMM-SOC-USR-MAN-0006

Issue/Rev.: Issue 2.18

Date: 13.07.2020

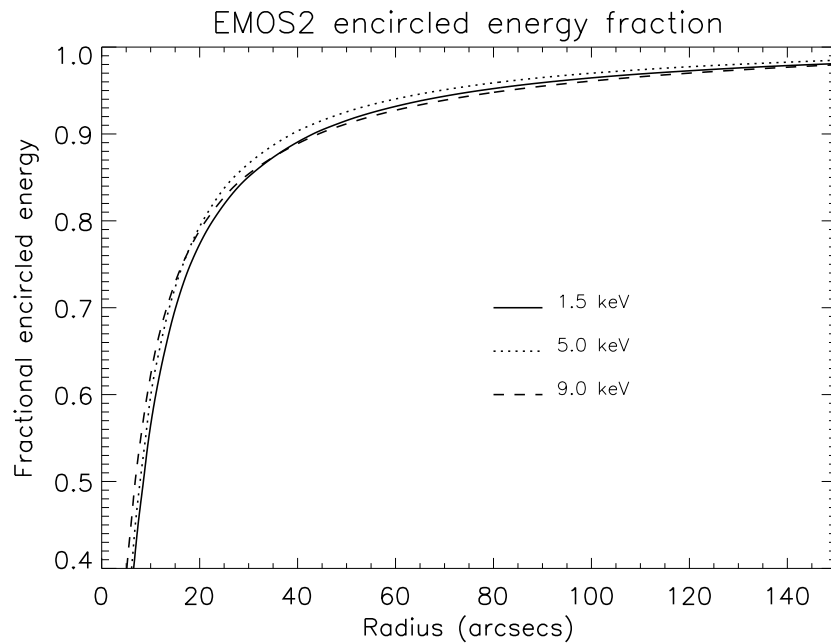


Figure 6: The MOS2 fractional encircled energy as a function of angular radius (on-axis) at different energies. The curves were calculated integrating the PSF that is currently implemented in the CCF.

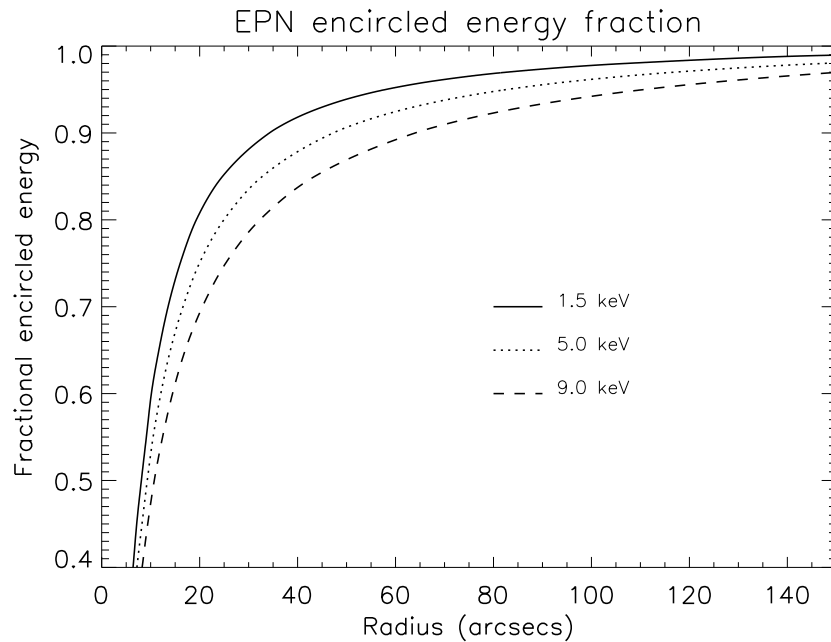


Figure 7: The pn fractional encircled energy as a function of angular radius (on-axis) at different energies. The curves were calculated integrating the PSF that is currently implemented in the CCF.



**esa**

european space agency  
agence spatiale européenne

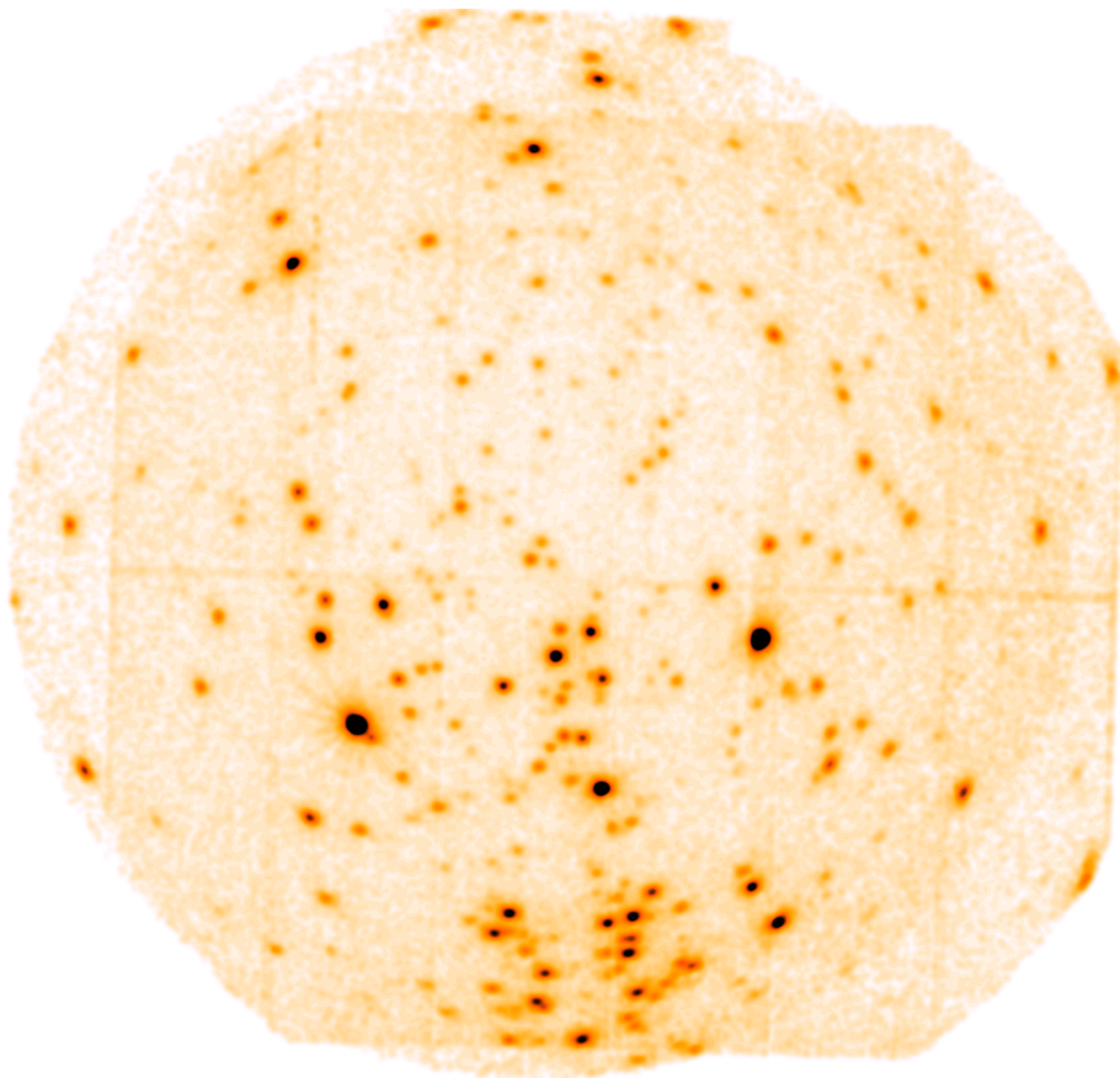


Figure 8: *The dependence of the X-ray PSF's shape on the position in the field of view. This image was made from an observation towards the Orion molecular cloud. EPIC pn, MOS1 and MOS2 exposures have been merged together and exposure corrected. The data has been slightly smoothed with a Gaussian of 10" FWHM. The intensity scale is square root.*

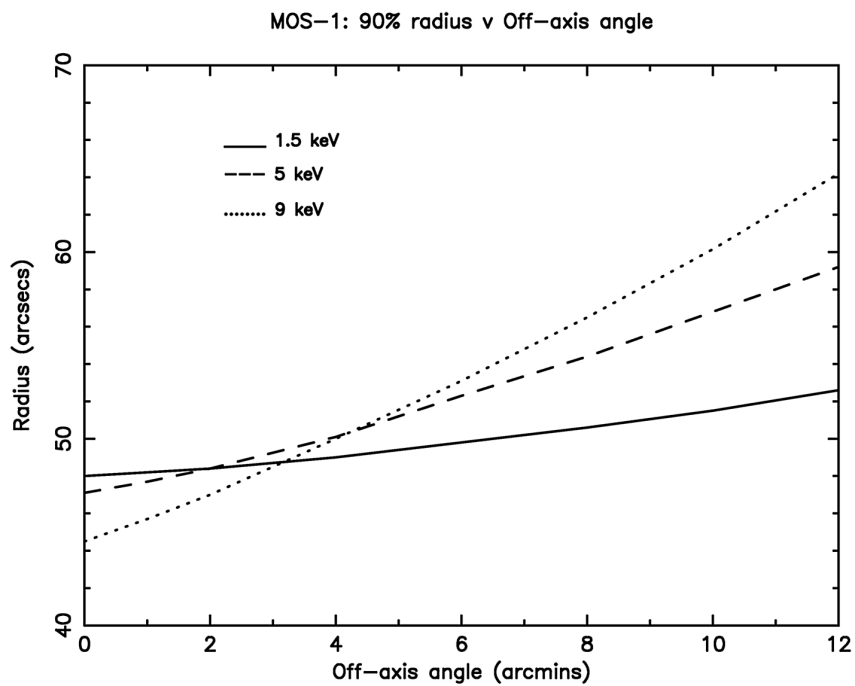


Figure 9: The W90 radius of a point source observed with the MOS1 camera as a function of off-axis angle at three energies. The curves are based on early ray-trace simulations and should not be used for quantitative analysis; see text on how to obtain W90 radii in-line with the current calibration.

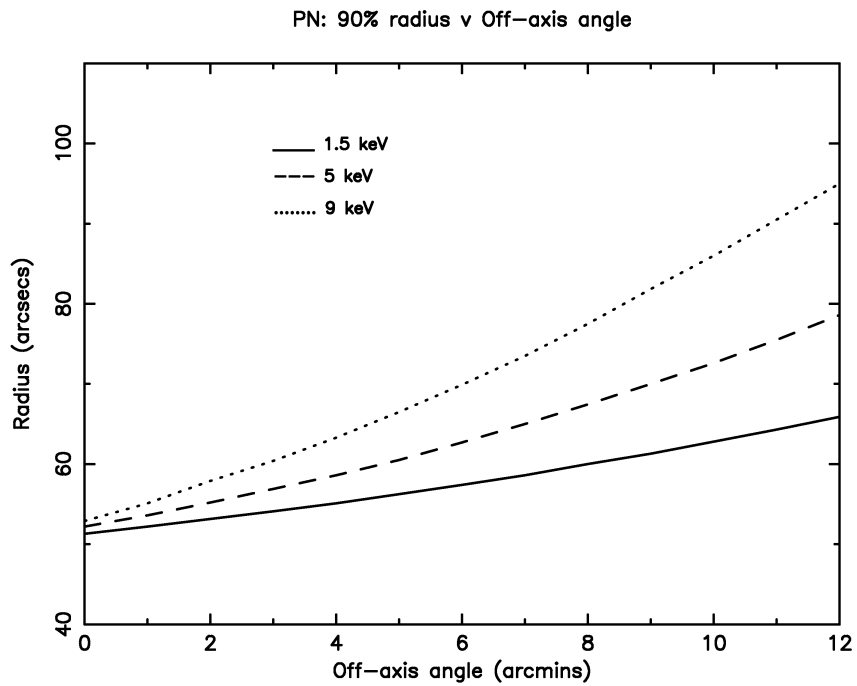


Figure 10: The W90 radius of a point source observed with the pn camera as a function of off-axis angle at three energies. The curves are based on early ray-trace simulations and should not be used for quantitative analysis; see text on how to obtain W90 radii in-line with the current calibration.



### 3.2.2 X-ray effective area

The second important characteristic of the mirror performance is their effective area,  $A_e$ , which reflects the ability of the mirrors to collect radiation at different photon energies.

#### 3.2.2.1 On-axis effective area

The most important information to XMM-Newton users is the mirror effective area, folded through the response of the different focal instruments. These are shown in Figs. 11 and 12. The effective areas have been extracted from the ready-made EPIC response matrices (full-frame mode, thin filter) and from response matrices created with the SAS task rgsrmfgen in case of the RGS's. Being the product of the effective area of the X-ray telescopes and the quantum efficiency of the detectors ( $XRT \star QE$ ), they correspond to the open filter positions (cf. Figs. 29, 30 and 31 for effective area plots of the EPIC cameras in case of other filter positions).

One can see that the XMM-Newton mirrors are most efficient in the energy range from 0.1 to 10 keV, with a maximum at about 1.5 keV and a pronounced edge near 2 keV (the Au M edge). The effective areas of the two MOS cameras are lower than that of the pn, because only part of the incoming radiation falls onto these detectors, which are partially obscured by the RGAs (Fig. 3).

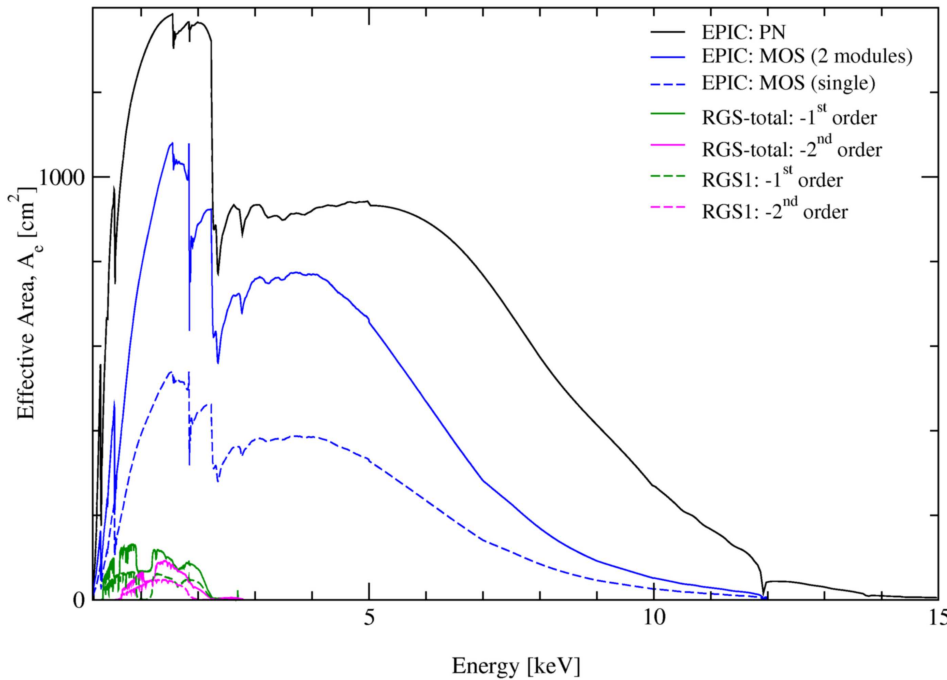


Figure 11: The net effective area of all XMM-Newton X-ray telescopes, EPIC and RGS (linear scale).



**esa**

european space agency  
agence spatiale européenne

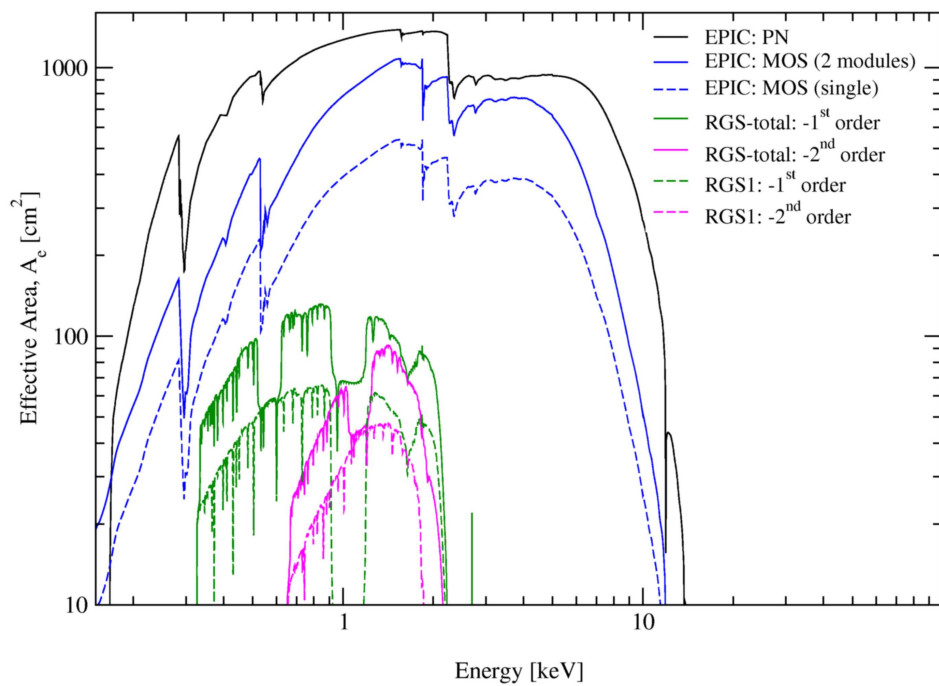


Figure 12: The net effective area of all XMM-Newton X-ray telescopes, EPIC and RGS (logarithmic scale).



### 3.2.2.2 Off-axis effective area

Not only the shape of the X-ray PSF, but also the effective area of the mirrors is a function of off-axis angle within the mirrors' 30' FOV. With increasing off-axis angle, less of the photons entering the telescopes actually reach the focal plane. This effect is called "vignetting". The vignetting of the XMM-Newton telescopes, which is reflected by the decline of the X-ray telescope's effective area as a function of off-axis angle, is displayed for a few energies for the X-ray telescope in Fig. 13.

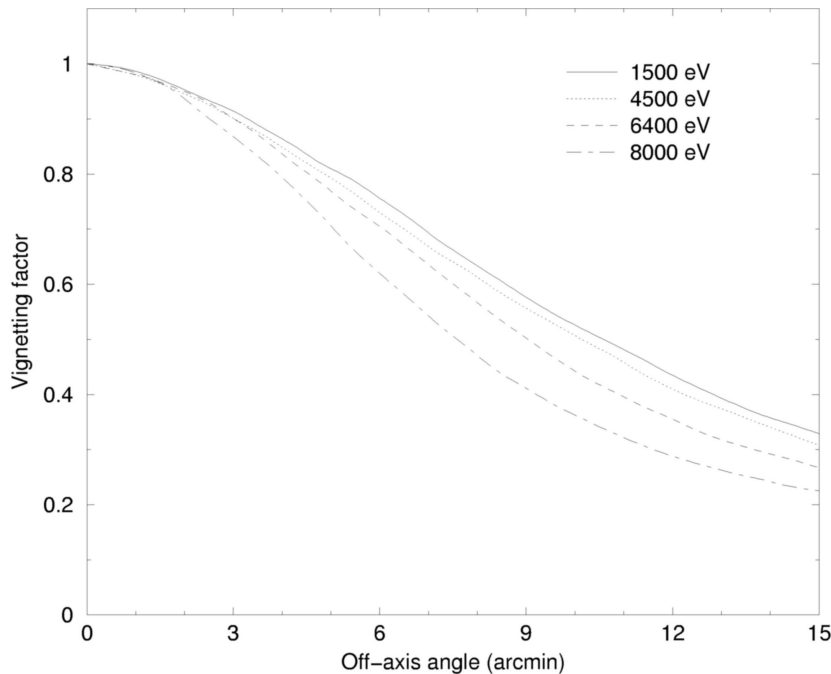


Figure 13: *Vignetting function as a function of off-axis angle ( $\theta=15'$ , based on simulations), at a few selected energies, of the X-ray telescope in front of the pn camera*

The off-axis vignetting in the two telescopes with an RGA has a dependence on angle with respect to the RGAs' dispersion direction. A source at an off-axis position perpendicular to the dispersion direction will be vignetted by a different amount to one at a position parallel to the dispersion direction. This azimuthal dependency of the vignetting is shown in Fig. 14. Readers are referred to Mateos et al. 2009, A&A, 496, 879 for a discussion on the calibration of this azimuthal dependency.

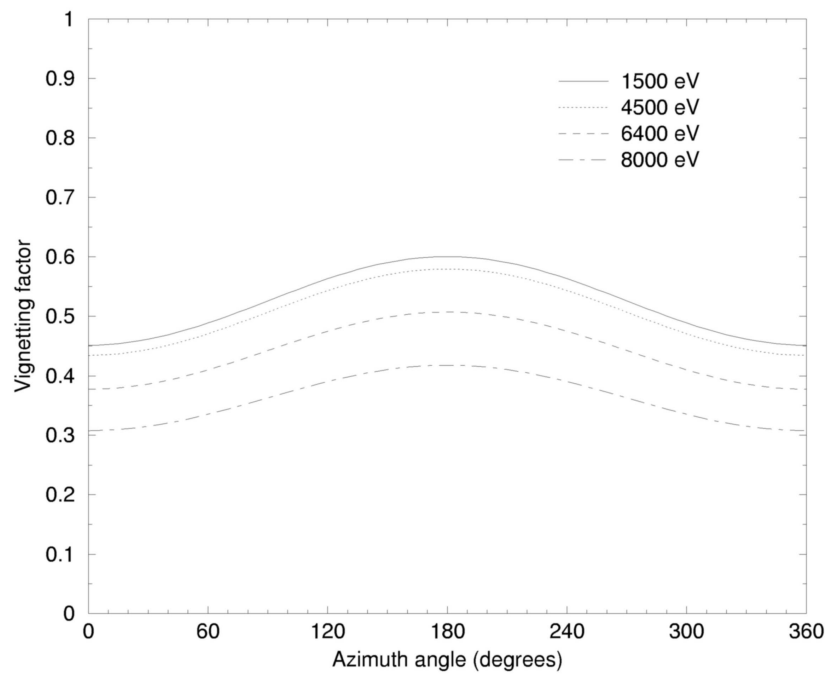


Figure 14: Vignetting function as a function of azimuth angle of the X-ray telescope in front of the MOS1 camera. The curves are given for an off-axis angle of 10 arcmin. Due to the presence of reflection grating assemblies in the exit beams of the X-ray telescopes, the vignetting functions measured in the MOS cameras are modulated azimuthally.



### 3.2.3 Response matrices used in the SAS data analysis

The EPIC and RGS response matrices generated by the SAS tasks ‘arfgen’ and ‘rmfgen’, and ‘rgsrdfgen’ respectively, already include the effective area of the telescopes together with the vignetting or the diffraction efficiency of the gratings, the transmissions of the filters and the quantum efficiency of the detectors.

Depending on the selected source extraction window in EPIC and on the spectrum extraction region in RGS, the SAS tasks ‘rmfgen’ and ‘rgsrdfgen’ apply additional corrections for count losses out of these windows. In the case of EPIC, this is performed using encircled energy fractions of the point spread function calibrated for the different telescopes. The illustration of telescopes effective area (Figs. 11 and 12) and encircled energy (Figs. 5, 6 and 7) functions are provided in this section only for general information. These graphs should not be used for the purpose of effective area correction. This is normally done by the SAS tasks by the generation of the RGS and EPIC instrument response matrices. The user could produce tabulated values of the telescope effective area and encircled energy fraction using the SAS task ‘calview’. Should this be the case, the XMM-Newton SAS Users Guide should be consulted.

### 3.2.4 Straylight rejection

The third important performance characteristic of the X-ray telescope, as listed above, is the efficiency of the straylight rejection.

X-ray straylight in EPIC is produced by rays which are singly reflected by the mirror hyperbolae and which reach the sensitive area of the camera. An X-ray baffle was implemented to shadow those singly reflected rays. It consists of two sieve plates made of concentric annular aperture stops located in front of the mirrors at 85 mm and 145 mm, respectively. The design is such that the entrance annular aperture of each mirror remains unobstructed for on-axis rays. Most of the rays with large off-axis angle are vigneted and cannot reach the detectors anymore via a single hyperbola reflection.

The straylight collecting area in the EPIC detector as a function of off-axis angle for a point source is about  $3 \text{ cm}^2$  for stray sources located between  $20'$  and  $1.4^\circ$  from the optical axis. At higher off-axis angles it is completely negligible. The ratio of the X-ray straylight collecting area to the on-axis effective area is smaller than 0.2% at 1.5 keV for a point source located at off-axis angles of  $0.4$ – $1.4^\circ$  and negligible at higher off-axis angles. This ratio, expressed in surface brightness values, is even smaller since the stray-image is unfocused at the detector position.

Assuming a 10 counts/s source, for EPIC MOS on-axis observations half of the incoming photon flux is distributed over about 150 pixels (adopting a  $15''$  HEW), with a central peak. The light of the same source, observed at a large off-axis angle, is distributed over about 1/4 or 1/5 of the total EPIC FOV (of order  $10^6$  pixels), leading to a *mean* count rate of  $10^{-5} \text{ counts s}^{-1} \text{ pixel}^{-1}$  of diffuse straylight. However, this is only a rough approximation, because the stray radiation due to an off-axis point source is not uniformly distributed in the EPIC FOV, but produces near-annular structures in the image, as for example seen in Fig. 15.

This illustrates the high straylight rejection efficiency of the XMM-Newton mirror modules. EPIC observations of isolated sources and RGS spectra are hardly affected. For bright extended sources (which are larger than the EPIC FOV, such as some supernova remnants, clusters of galaxies, stellar clusters and star forming regions), on the contrary, there might be a degradation in the ability to perform spatially resolved spectroscopy.

These limitations could play a role in the consideration of proposing observations of targets that are located within  $1.5^\circ$  of a bright X-ray source, or in cases when imaging an extended object that is larger than the EPIC  $30'$  FOV. Whether or not straylight is an issue depends largely



**esa**

european space agency  
agence spatiale européenne

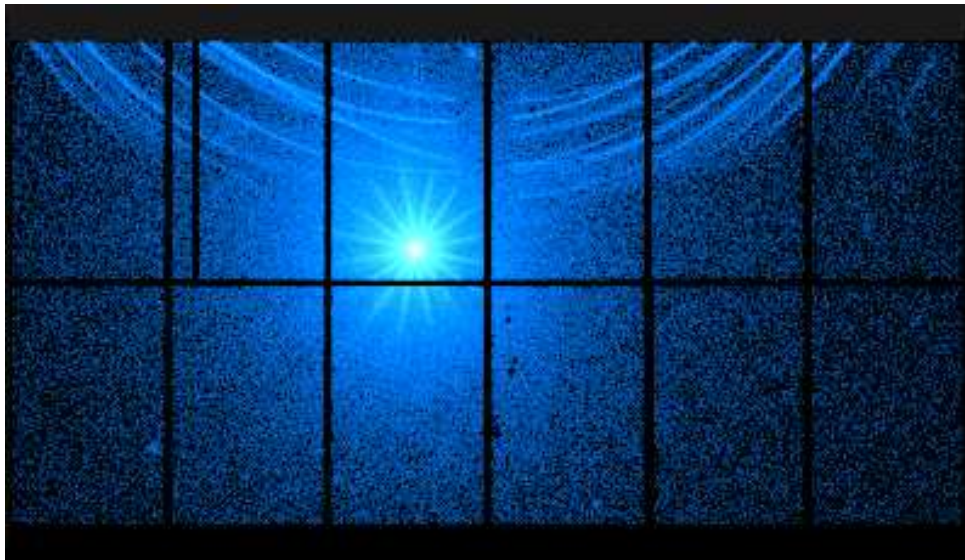


Figure 15: *EPIC pn image of GRS1758-258 (a black hole candidate near the Galactic centre) observed in the large window readout mode demonstrating the effect of straylight: in the upper part of the image, sharp arcs appear that are caused by single mirror reflections of photons possibly from GX 5-1 which is  $\sim 40$  arcmin offaxis to the north and outside the FOV.*

on the scientific objectives and on the ratio of the flux of the off-axis source and the required minimum detectable source flux within the FOV.

Further information on the XMM-Newton EPIC straylight (which in fact is one of the background components listed in a summarising table available from the Background Analysis page or directly at <http://www.cosmos.esa.int/web/xmm-newton/background>) can be obtained from an on-line presentation at

[http://www2.le.ac.uk/departments/physics/research/src/Missions/xmm-newton/technical/mpe-2006-05/MFreyberg\\_slewcal.pdf](http://www2.le.ac.uk/departments/physics/research/src/Missions/xmm-newton/technical/mpe-2006-05/MFreyberg_slewcal.pdf) at download/file.



### 3.3 EUROPEAN PHOTON IMAGING CAMERA (EPIC)

Two of XMM-Newton's X-ray telescopes are equipped with EPIC MOS (Metal Oxide Semiconductor) CCD arrays, the third carries a different CCD camera called EPIC pn. In a nutshell, the XMM-Newton EPIC cameras offer the possibility to perform extremely sensitive imaging observations over a field of view of 30' and the energy range from 0.2 to 12 keV, with moderate spectral ( $E/\Delta E \sim 20 - 50$ ) and angular resolution ( $\sim 6'' FWHM; \sim 15'' HEW$ ). The pn type camera can be operated with very high time resolution down to 0.03 ms in the timing mode and 0.007 ms (but with a very low duty cycle of 3%) in the burst mode. Note however that the absolute timing accuracy is determined by the process that correlates the on-board time to the universal time. The accuracy of the absolute and relative timing reconstruction in the EPIC-pn camera is regularly monitored through observations of the Crab Pulsar. Regularly updated results of this monitoring are published in the EPIC Calibration Status Document (XMM-SOC-CAL-TN-0018).

The detector layout and the baffled X-ray telescope FOV of both types of EPIC camera are shown in Figs. 16 (which is just a rough sketch), 17, 18 and 19. For all cameras the sensitive area of the detector is about 30' across. The following details should be noted:

- The pn chip array is slightly offset with respect to the optical axis of its X-ray telescope so that the nominal, on-axis observing position does not fall on the central chip boundary (see approximate boresight position for pn marked in Fig. 19). This ensures that  $\geq 90\%$  of the energy of an on-axis point source are collected on one pn CCD chip.
- The two EPIC MOS cameras are rotated by 90° with respect to each other.
- The dead spaces between the MOS chips are not gaps, but unusable areas due to detector edges (the MOS chips physically overlap each other, the central one being located slightly behind the ones in the outer ring).
- At about 01:30 hrs. UT on 09 March, 2005, during XMM-Newton revolution 961, an event was registered in the focal plane of the EPIC MOS1 instrument. The characteristics of the event might be attributed to a micrometeorite impact scattering debris into the focal plane. In the period immediately following a light flash it became apparent that MOS1 CCD6 was no longer recording events, and that all CCD6 pixels were, in effect, returning signal at the saturation level raising the possibility that CCD6 had sustained significant damage. Scientific observations are continuing normally with XMM-Newton, including MOS1, but with the peripheral CCD6 (see Fig. 20) switched off.

Observers are invited to read a dedicated web page, available at  
<http://www.cosmos.esa.int/web/xmm-newton/mos1-ccd6>.

- At about 06:51 hrs. UT on 11 December 2012, during XMM-Newton revolution 2382, an event was registered in the focal plane of the EPIC MOS1 instrument. The characteristics of the event were reminiscent of the aforementioned March 2005 event, and therefore tentatively attributed to micro-meteoroid impacts scattering debris into the focal plane. After this event, MOS1-CCD3 has been significantly damaged, and declared not usable for science. Scientific observations are continuing normally



with MOS1, but now without data from CCD3 as well. The event has also increased the noise level in CCD4.

For a complete assessment of the scientific impact of this event, readers are referred to the following web page:

[http://www.cosmos.esa.int/web/xmm-newton/mos1-ccd3.](http://www.cosmos.esa.int/web/xmm-newton/mos1-ccd3)

### Comparison of focal plane organisation of EPIC MOS and pn cameras

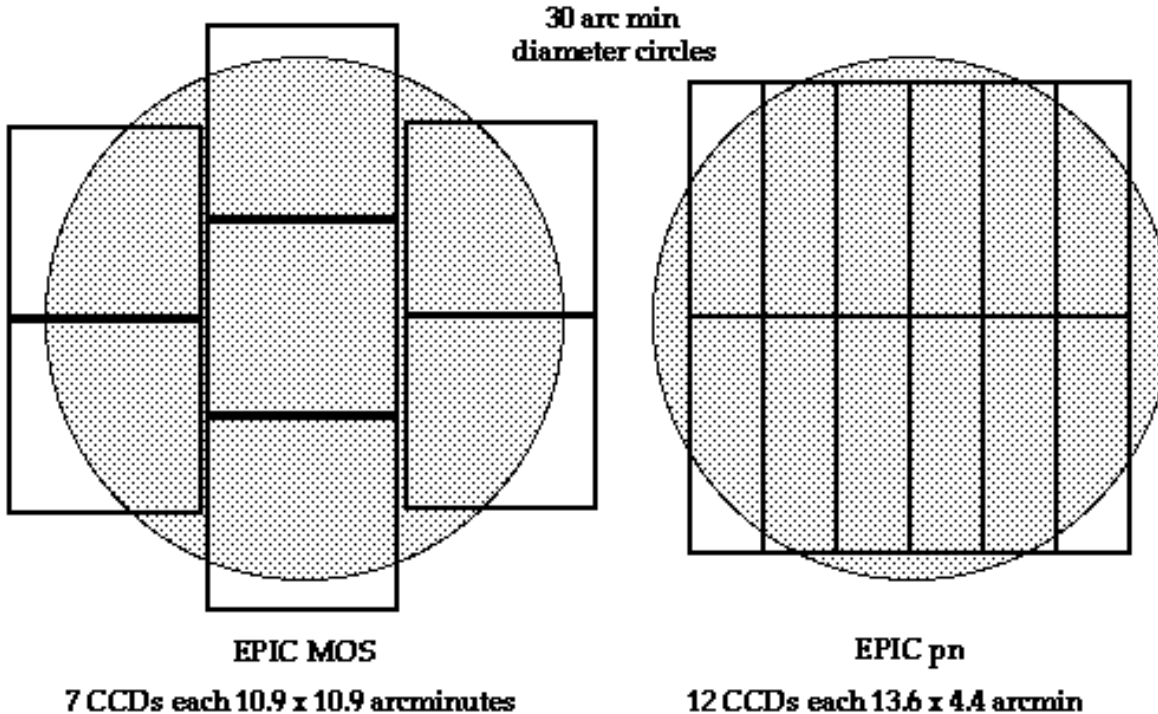


Figure 16: A rough sketch of the field of view of the two types of EPIC camera; MOS (left) and pn (right). The shaded circle depicts a 30' diameter area. For the alignment of the different cameras with respect to each other in the XMM-Newton focal plane refer to the text.

All EPIC CCDs operate in photon counting mode with a fixed, mode dependent frame read-out frequency, producing event lists.<sup>1</sup> This allows for simultaneous imaging and non-dispersive spectroscopy due to the intrinsic energy resolution of the pixels.

**Note:** If for any reason a user should decide to observe a target with EPIC **not on-axis**, **but instead off-axis**, then for off-axis angles in excess of 2.5' the grating spectrum might slip off the RGS detector array (because the RGS FOV is about 5' across in the cross-dispersion direction). Observing off-axis can be complicated if the observer wants to avoid all the MOS and pn inter-chip gaps – very careful position angle and off axis angle compromises should be made.

Users are encouraged to be familiar with the EPIC Calibration Status Document, XMM-SOC-CAL-TN-0018, that is regularly updated to reflect any changes in the instrument calibrations. Additionally, spe-

<sup>1</sup>An event list is a table with one line per received event, listing (among others) attributes of the events such as the x and y position at which they were registered, their arrival time and their energy.



**esa**

European space agency  
agence spatiale européenne

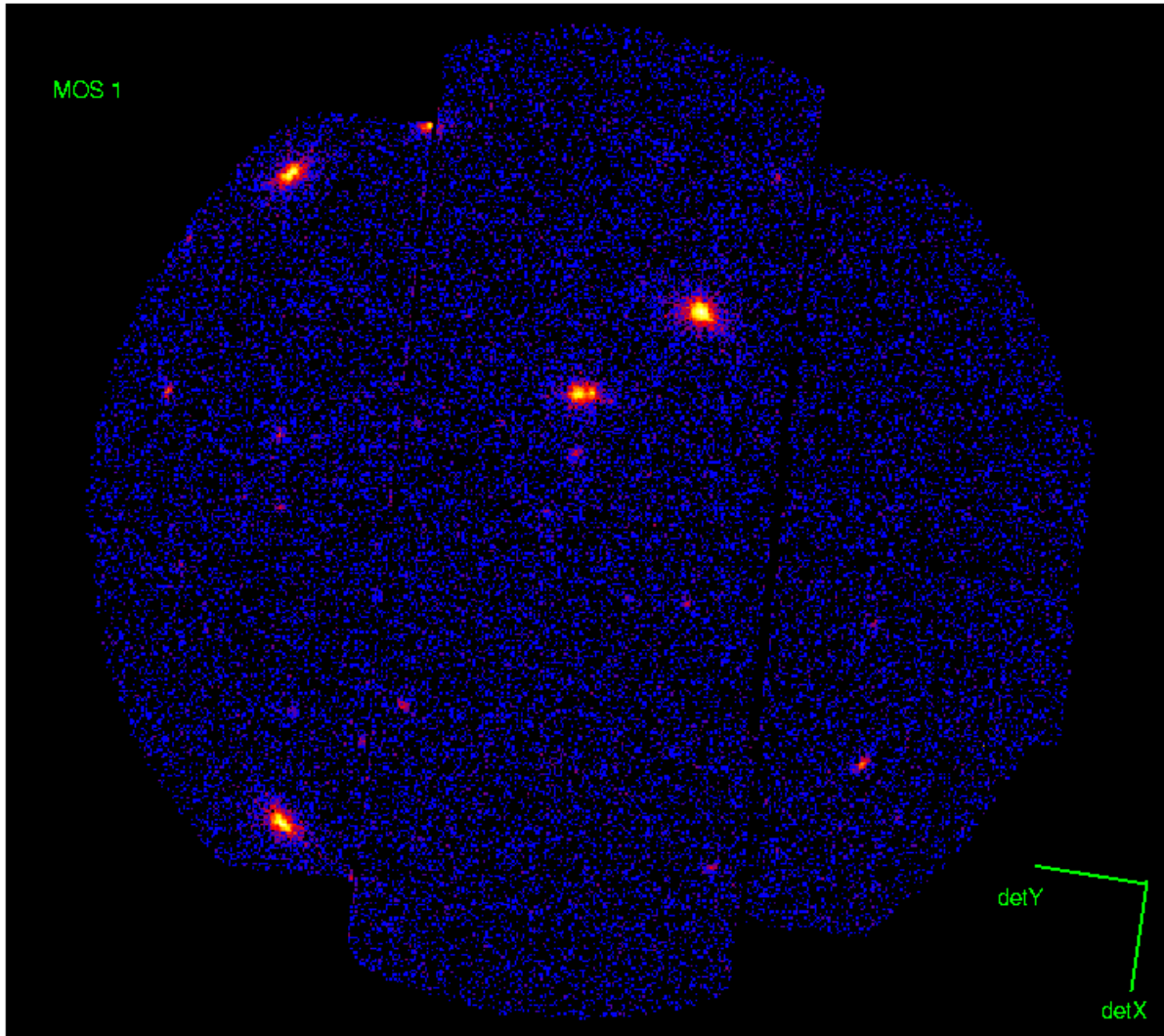


Figure 17: The field of view of the EPIC MOS cameras for an observation with a position angle of  $\sim 80^\circ$ : MOS1 (here) and MOS2 (next figure). The two MOS cameras view the same field as displayed in sky coordinates with North to the top and East to the left. In each case the camera detector coordinate frames are noted.

cific documents deal with the calibration status of fast modes in EPIC-MOS (<http://xmmweb.esac.esa.int/docs/documents/CAL-TN-0082.pdf>) and EPIC-pn (<http://xmmweb.esac.esa.int/docs/documents/CAL-TN-0083.pdf>). They are also updated whenever new calibration results are available.

### 3.3.1 Two types of EPIC camera: MOS and pn

The two types of EPIC camera are fundamentally different. This does not only hold for the geometry of the MOS chip array and the pn chip array (Figs. 17, 18 and 19), but other properties as well, like e.g., their readout times. The readout of the pn chips is much faster than that of the MOS cameras, because each pixel column has its own readout node. Another important difference is that the MOS chips are front-illuminated, while the pn CCDs are back-illuminated,



**esa**

european space agency  
agence spatiale européenne

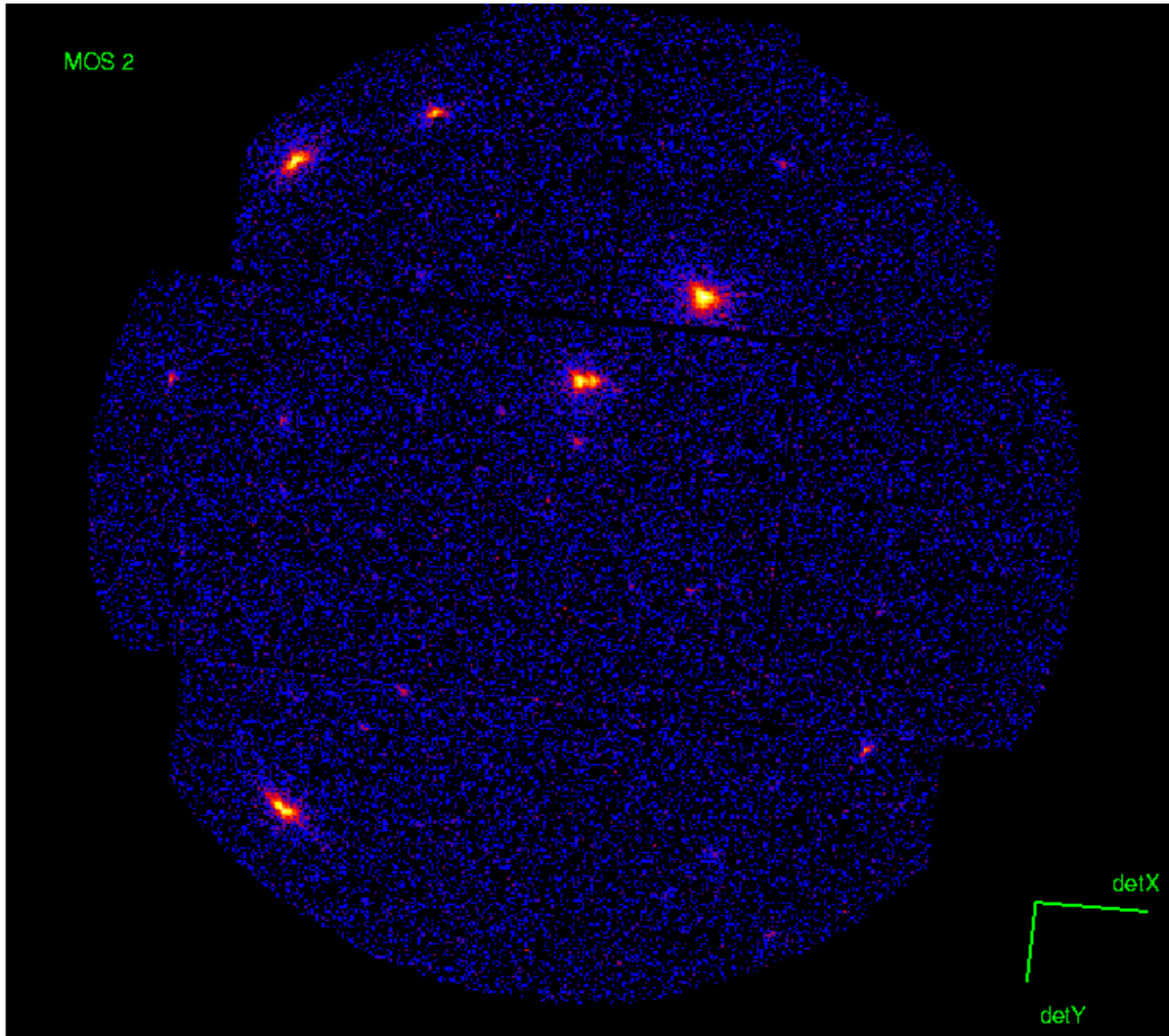


Figure 18: *The field of view of the EPIC MOS cameras (cntd. from previous figure): MOS2.*

which affects the detector quantum efficiencies decisively (§ 3.3.5).

#### 3.3.1.1 EPIC MOS chip geometry

The MOS chip arrays consist of 7 individual identical, front-illuminated chips. The individual CCDs are not co-planar, but offset with respect to each other, following closely the slight curvature of the focal surface of the Wolter telescopes. Technically, this leaves space for the connections to the central CCD. The numbering scheme for the EPIC MOS chip array, the individual chip coordinate frames and the directions of the detector coordinates are displayed in Figs. 20 and 21. Not visible in the figures is that the MOS chips have a frame store region which serves as a data buffer for storage before they are read out through the readout nodes, while the rest of the chip is obtaining the next exposure.

As indicated above, the MOS cameras are mounted on those X-ray telescopes that also carry RGS instruments. Therefore, they receive only 44% of the reflected light.



**esa**

European space agency  
agence spatiale européenne

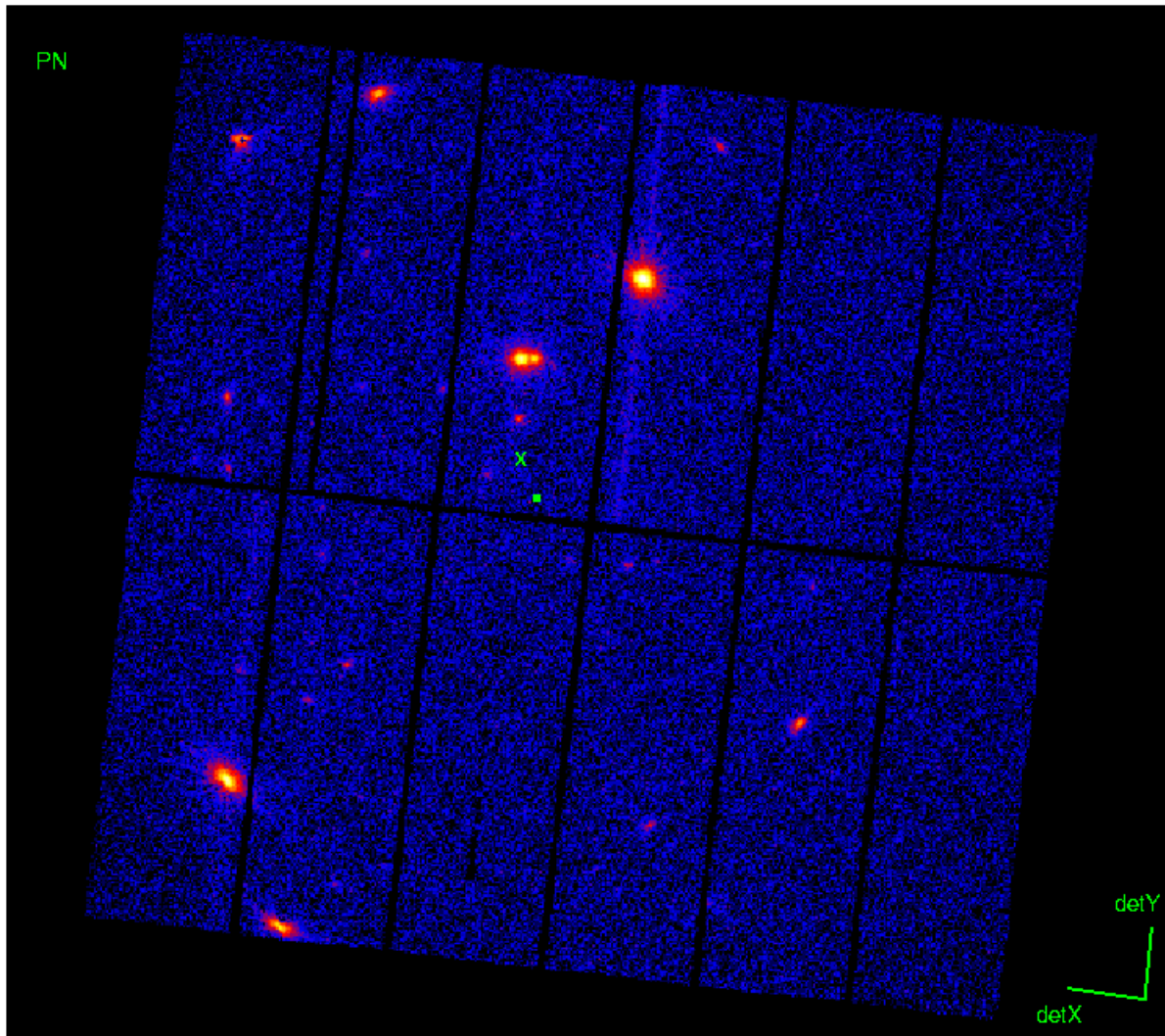


Figure 19: The field of view of the EPIC pn camera for an observation with a position angle of  $\sim 80^\circ$ . The pn camera views the same field as displayed in Figs. 17 and 18 in sky coordinates with North to the top and East to the left. Again the camera detector coordinate frame is noted. The nominal boresight is marked with a small box. Note that the approximate distance between the boresight and the nearby chip gaps is  $\sim 40$  arcsec, which can be of importance when observing extended sources. Position 'X' shows the preferred location to centre on an object in the pn small window mode, however, the user is advised that this requires a knowledge of the position angle of the observation, and will also place the target outside the EPIC MOS small window.

### 3.3.1.2 EPIC pn chip geometry

The heart of the pn camera is a single Silicon wafer with 12 CCD chips integrated. The pn chip array numbering scheme, the individual chip coordinate frames and the directions of the detector coordinates are displayed in Fig. 22.



**esa**

euopean space agency  
agence spatiale europ  ne

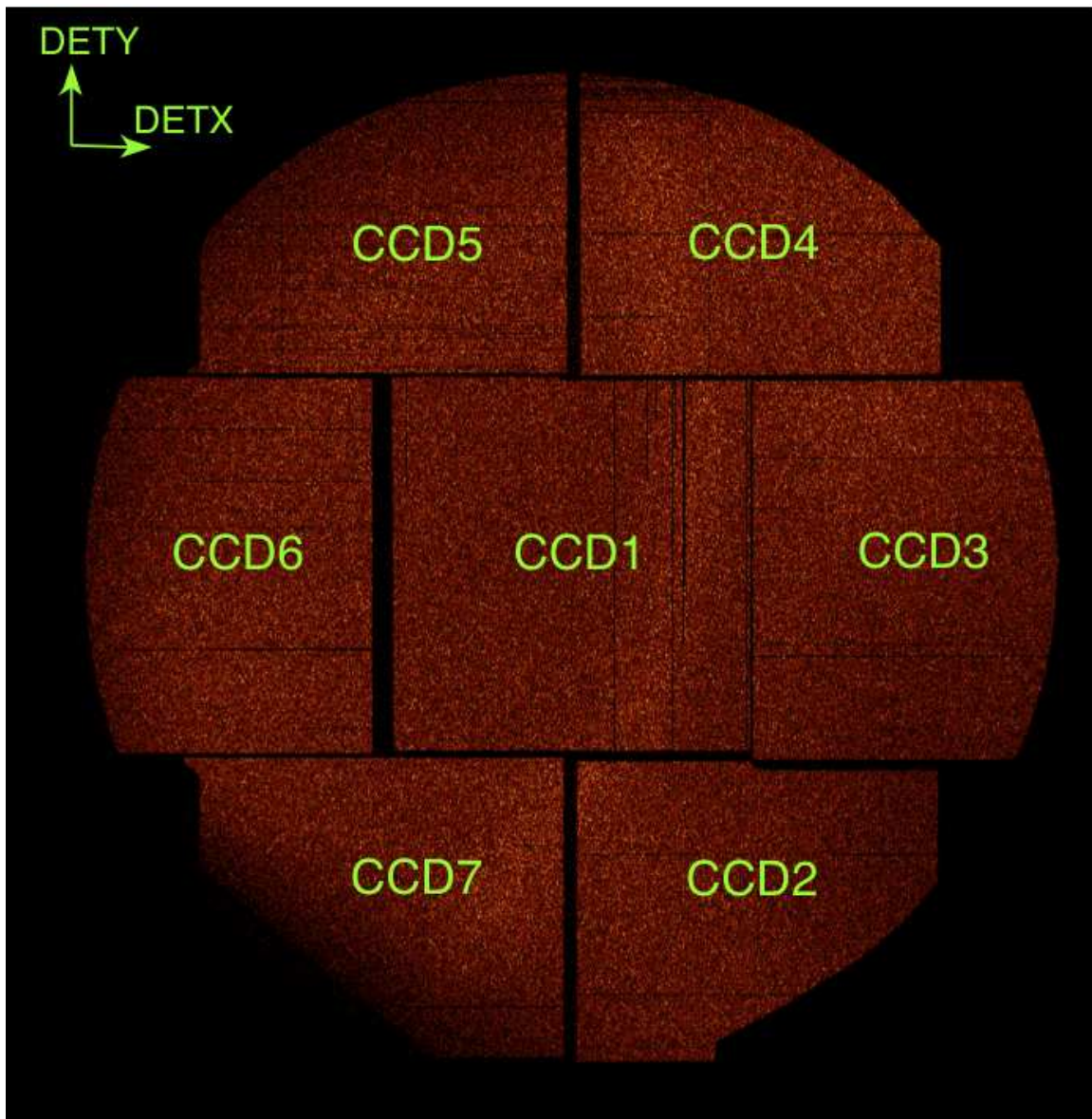


Figure 20: The layout of the MOS cameras is presented in this figure for MOS1 (above) and MOS2 (bottom). The images (in detector coordinates [DETX,DETY]) are extracted from an exposure taken with the calibration (CAL\_CLOSED) filter in Rev.#80 (Obs.#0124700101). The number of the CCD where each photon has fallen is included in the CCDNR column of the calibrated event list files. The MOS cameras are orthogonally oriented. Hence, the RGS dispersion direction is aligned with the DETY direction in the MOS1 camera, while it is aligned along the DETX direction in the MOS2 camera. Users are warned that **scientific observations are performed with MOS1 CCD3 and CCD6 switched off due to a hardware failure, probably due to a micrometeorite impact (see Sect. 3.3)**.

### 3.3.2 Science modes of the EPIC cameras

The EPIC cameras allow several modes of data acquisition. Note that in the case of MOS the outer ring of 6 CCDs remain in standard imaging mode while the central MOS CCD can be

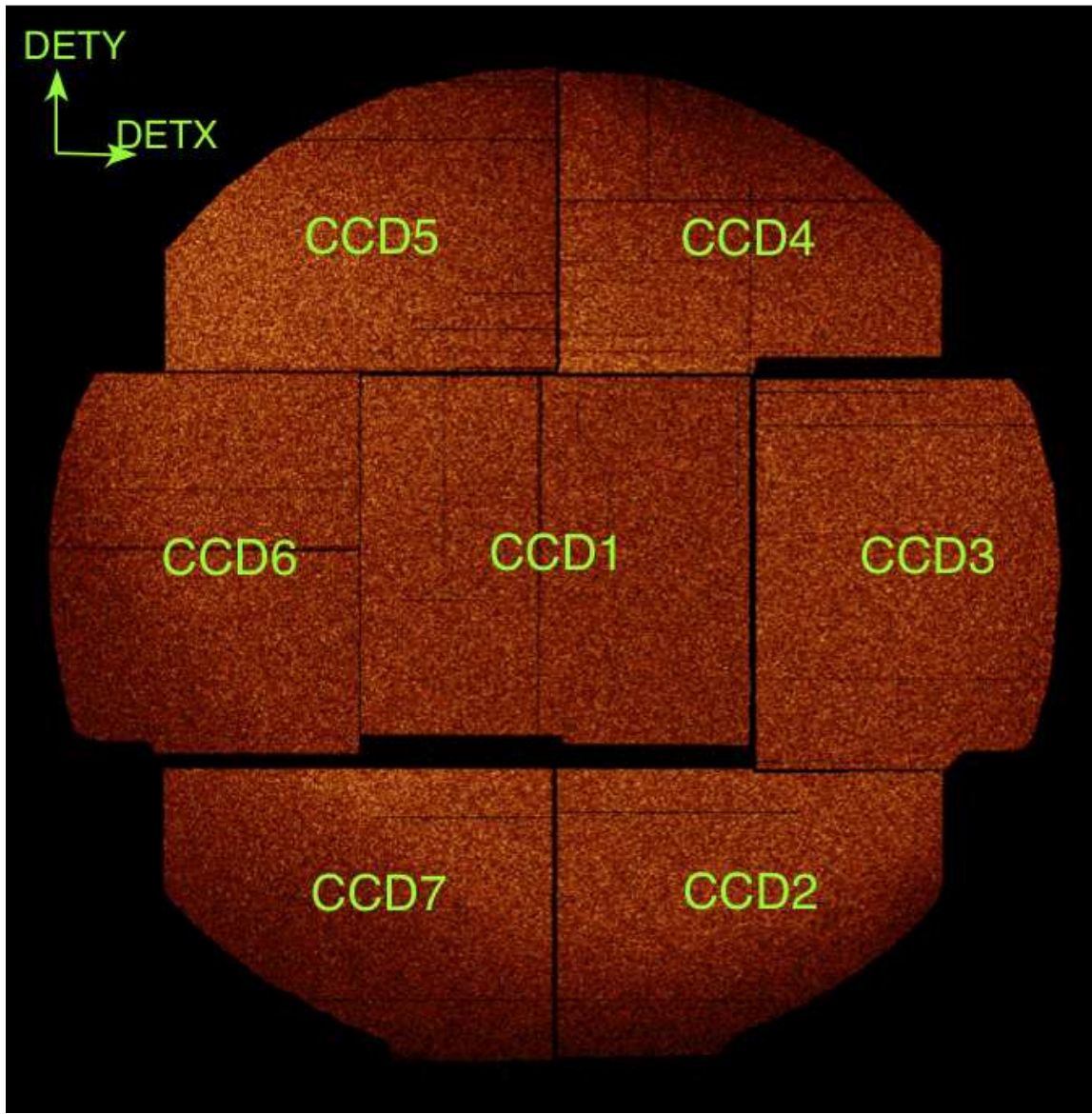


Figure 21: *The layout of the EPIC MOS cameras as presented in SAS (cntd. from previous figure): MOS2.*

operated separately. Thus all CCDs are gathering data at all times, independent of the choice of operating mode. The pn camera CCDs can be operated in common modes in all quadrants for Full Frame, Extended Full Frame and Large Window mode, or just with one single CCD (CCD number 4 in Fig. 22) for Small Window, Timing and Burst mode.

1. “Full Frame” and “Extended Full Frame” (pn only)

In this mode, all pixels of all CCDs are read out and thus the full FOV is covered.

2. “Partial Window”

- a) MOS

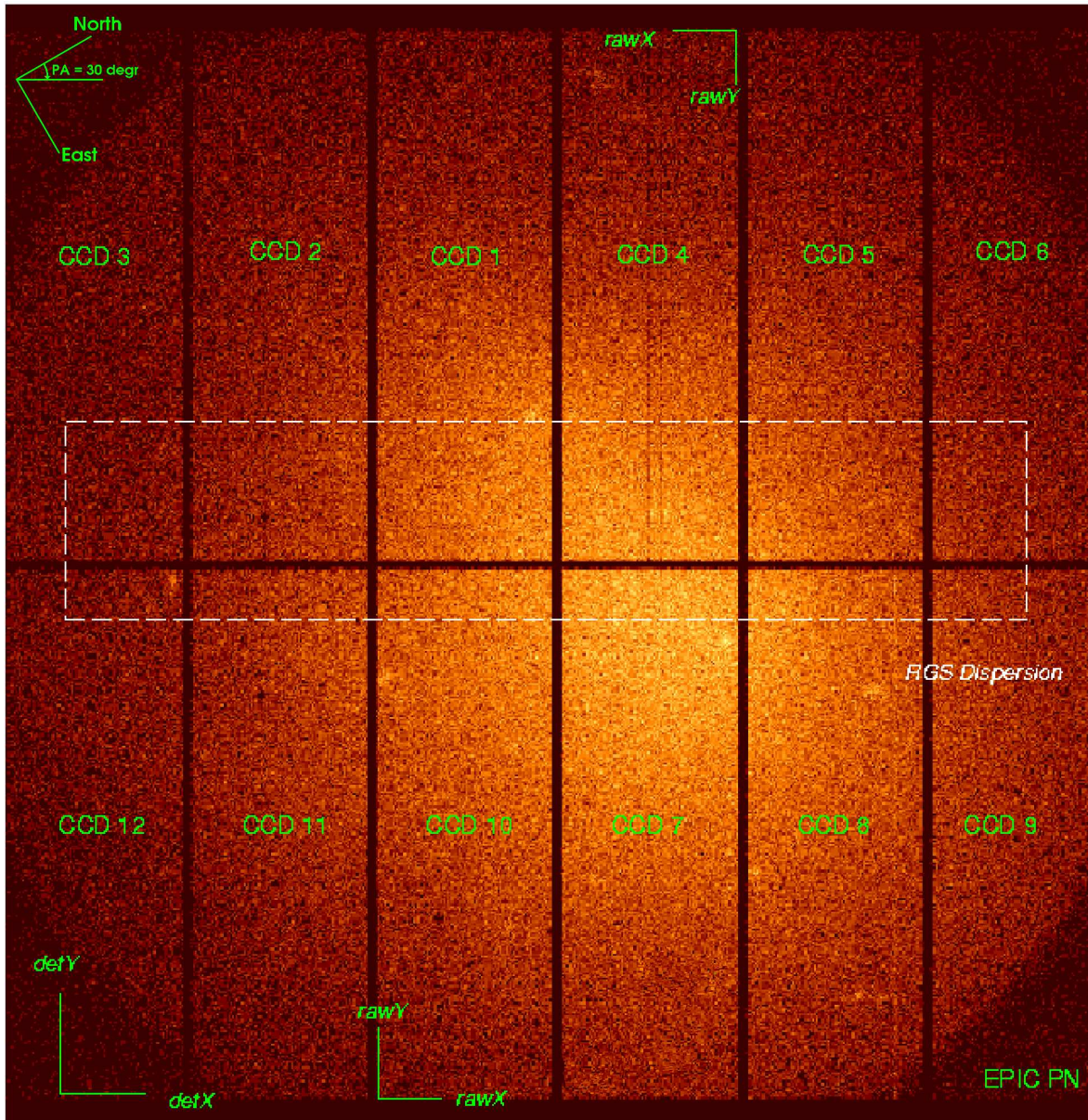


Figure 22: The layout of the EPIC pn camera as presented in SAS. The orientation of the RAWX/RAWY (CCD specific) and of the DETX/DETY axes are shown, to highlight that the RGS dispersion axes are parallel within spacecraft physical coordinates. The readout CAMEX of each CCD is located at RAWY = 0, i.e. at the top (for CCDs 1 – 6) or bottom (for CCDs 7 – 12) of the displayed array. In the upper left corner, the orientation of the celestial North and East axes is displayed for an assumed position angle (PA) of 30°.

In a Partial Window mode the central CCD of both MOS cameras can be operated in a different mode of science data acquisition, reading out only part of the CCD chip.

b) pn



In Large Window mode only half of the area in all 12 CCDs is read out, whereas in Small Window mode only a part of CCD number 4 is used to collect data. Note that the pn camera in these windowed modes is operated in such a way that non-read regions of the CCDs are exposed to the sky so that bright sources in these "dark" areas might still affect the observation.

### 3. "Timing"

#### a) MOS + pn

In the Timing mode, spatial information is maintained only in one dimension, along the column (RAWX) axis. For pn, the full width of CCD4 is active, whereas for MOS the active area is reduced to about 100 columns around the boresight. Along the row direction (RAWY axis), spatial information is lost due to continuous shifting and collapsing of rows to be read out at high speed. Since the 2 MOS cameras orientations differ by 90 degrees, the "imaging" direction in the 2 MOS are perpendicular to each other.

#### b) pn only

A special flavour of the Timing mode of the EPIC pn camera is the "Burst" mode, which offers very high time resolution, but has a very low duty cycle of 3%.

The most important characteristics of the EPIC science modes (time resolution and count rate capability) are tabulated in Table 3. Fig. 23 and Fig. 24 show the active CCD areas for the different pn and MOS readout modes, respectively.

The count rate limitations are defined for a 2.5% flux loss (see § 3.3.9 and XMM-SOC-CAL-TN-0200 for details on pile-up) in point like sources. This level entails a <1% spectral distortion, which in this case is defined as the complement to 1 of the ratio between two measured count rates: the count rate of good patterns originated exclusively by one individual photon and the count rate of good patterns originated by all events. Early estimates of spectral fitting errors without any response matrix corrections show that a doubling of these count rates could lead to systematic errors greater than the nominal calibration accuracies. The Pile-up can be alleviated by excising the PSF core at the penalty of losing overall flux, but retaining spectral fitting integrity, modulo the accuracy in the calibration of the Point Spread Function wings.

For sources with very soft spectra, a factor of 2–3 lower maximum incident flux limits are recommended, while maximum count rates remain unchanged, see § 3.3.9. For the pn camera also for point sources with hard spectra (power law photon index  $\alpha < 2$ ) lower count rate limits should be applied, in order to avoid X-ray loading (see XMM-SOC-CAL-TN-0050, available from <http://www.cosmos.esa.int/web/xmm-newton/calibration-documentation>). For  $\alpha=1.5$  and 1.0 the maximum count rate limits given in Table 3 should be reduced by factors 2 and 4, respectively.

One of the major differences between the two types of camera is the high time resolution of the pn. With this camera high-speed photometry of rapidly variable targets can be conducted, down to a minimum integration time of 30 (7)  $\mu$ s in the Timing (Burst) mode.

The SAS task `epatplot` allows users to have a qualitative estimate of the level of pile-up affecting an input event list by comparing the observed and expected distributions of event PATTERNS. Users are referred to the description of this task in the SAS documentation (see also § 3.3.9 for details on pile-up).



**esa**

European space agency  
agence spatiale européenne

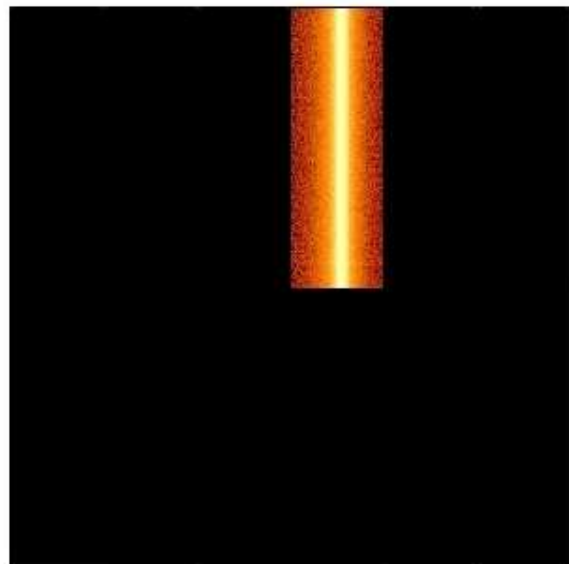
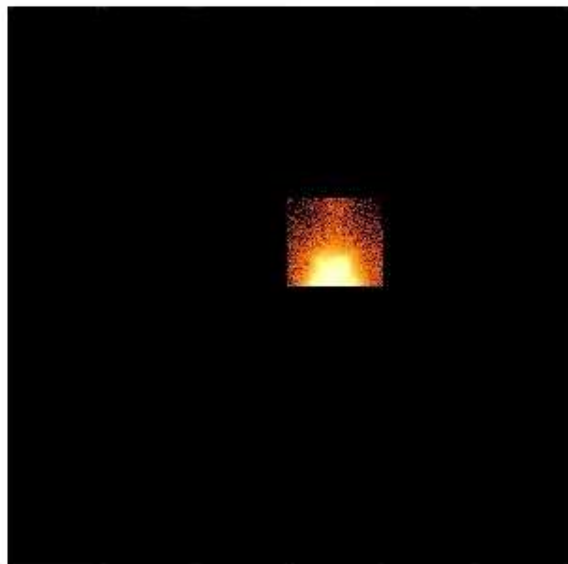
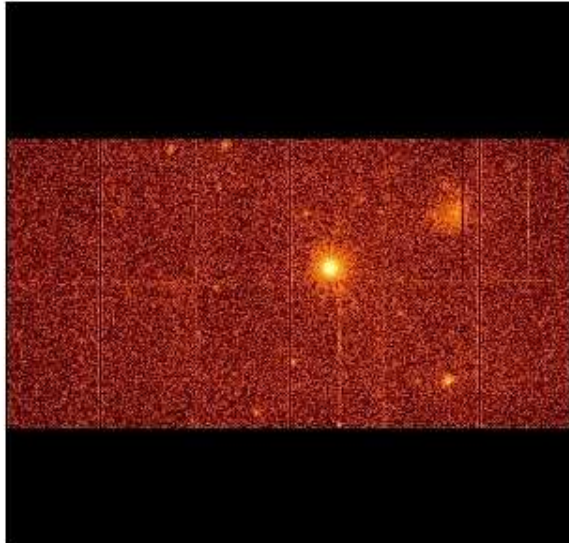
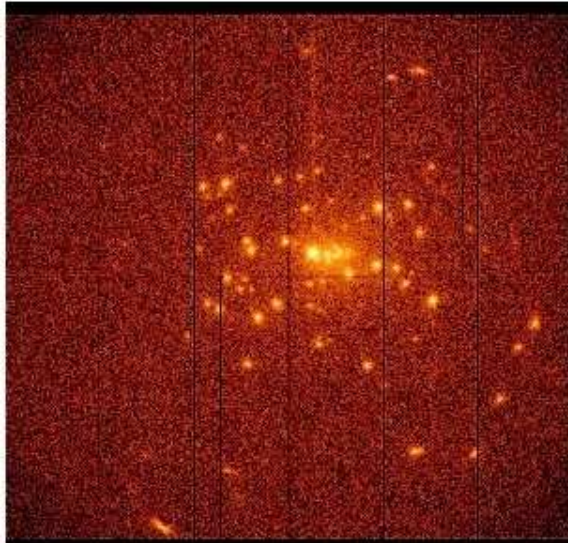


Figure 23: Operating modes for the pn-CCD camera. Top left: Full Frame and Extended Full Frame mode; top right: Large Window mode; bottom left: Small Window mode, and bottom right: Timing mode. The Burst mode is different from the Timing mode as the source position is not read out, i.e. rows 181-200 will be dark.



Table 3: Basic numbers for the science modes of EPIC

MOS (central CCD; pixels) [1 pixel = 1.1"]	Time resolution	Live time <sup>1</sup> [%]	Max. rate <sup>2</sup> (total)	count diffuse <sup>3</sup> [s <sup>-1</sup> ]	Max. count rate <sup>2</sup> (flux) point source [s <sup>-1</sup> ] ([mCrab] <sup>4</sup> )
Full frame (600×600)	2.6 s	100.0	150		0.50 (0.17)
Large window (300×300)	0.9 s	99.5	110		1.5 (0.49)
Small window (100×100)	0.3 s	97.5	37		4.5 (1.53)
Timing uncompressed (100×600)	1.75 ms	100.0	N/A		100 (35)
pn (array or 1 CCD; pixels) [1 pixel = 4.1"]	Time resolution	Live time <sup>1</sup> [%]	Max. rate <sup>2</sup> (total)	count diffuse <sup>3</sup> [s <sup>-1</sup> ]	Max. count rate <sup>2</sup> (flux) point source [s <sup>-1</sup> ] ([mCrab] <sup>4</sup> )
Full frame <sup>5</sup> (376×384)	73.4 ms	99.9	1000 (total)		2 (0.23)
Extended full frame <sup>5,6</sup> (376×384)	199.1 ms	100.0	370		0.3 (0.04)
Large window (198×384)	47.7 ms	94.9	1500		3 (0.35)
Small window (63×64)	5.7 ms	71.0	12000		25 (3.25)
Timing (64×200)	0.03 ms	99.5	N/A		800 (85)
Burst (64×180)	7 μs	3.0	N/A		60000 (6300)

Notes to Table 3:

1) Ratio between the time interval during which the CCD is collecting X-ray events (integration time, including time needed to shift events towards the readout) and the frame time (which in addition includes time needed for the readout of the events).

2) “Maximum” to avoid deteriorated response due to photon pile-up (see § 3.3.9 and XMM-SOC-CAL-TN-0200, available at <http://www.cosmos.esa.int/web/xmm-newton/calibration-documentation>) and X-ray loading (see 2nd point in § 3.3.6). These count rates include background. Note that telemetry limitations are in some cases more stringent than the pile-up constraints. For the MOS cameras the maximum count rates are about 115 counts/s for Full Window and Partial Window imaging modes and 230 counts/s for Timing mode. The pn telemetry limit is approximately 600 counts/s for the imaging modes and approximately 450 counts/s for the Timing mode. If the rate is higher, then the so-called counting mode is triggered and for some time the science data are lost. See also § 4.3.1 on the EPIC bright source avoidance. For sources with very soft spectra a factor of 2–3 lower maximum incident flux limits are recommended, while maximum count rates remain unchanged, see § 3.3.9. Despite the pile-up threshold being very similar in EPIC-pn Full Frame and Large Window modes, there are two intrinsic advantages of the latter which may compensate the loss of field-of-view: a) the significantly lower level of out-of-time events (0.16% versus >6%); b) the larger dynamical range in optical magnitude within which optical loading does not affect the data.

3) Values are representative of bright objects that are extended on scales much larger than the PSF core. In case of assumed homogeneous illumination on the CCD, a 1% pile-up limit for MOS is reached for a flux of 1 event per 900 pixels per frame.

4) Conventionally, it is assumed that  $1 \text{ mCrab} = 2.4 \times 10^{-11} \text{ erg s}^{-1} \text{ cm}^{-2}$  (in the energy range 2–10 keV).

5) The first 12 rows at the readout-node are not transmitted to ground (are set to “bad”, equivalent to “bad pixels”).

6) “Extended” means that the image collection time (i.e. the frame time) is longer than in the normal Full Frame mode.



**esa**

European space agency  
agence spatiale européenne

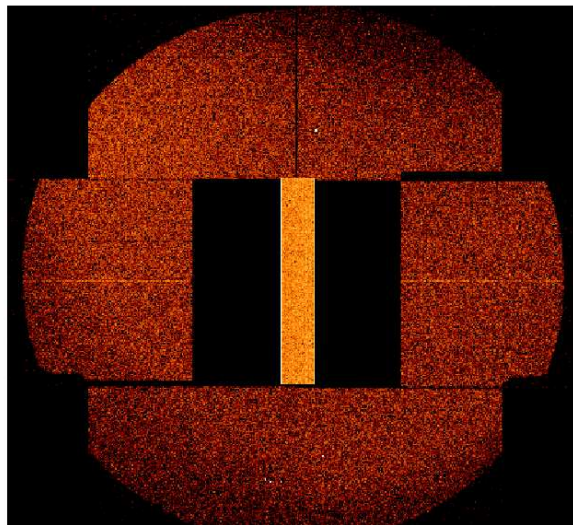
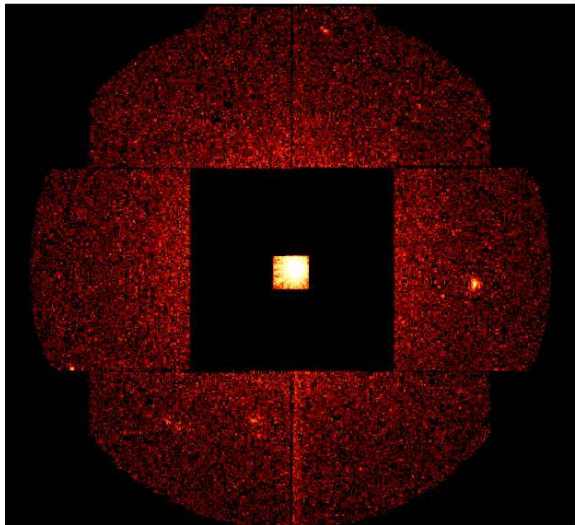
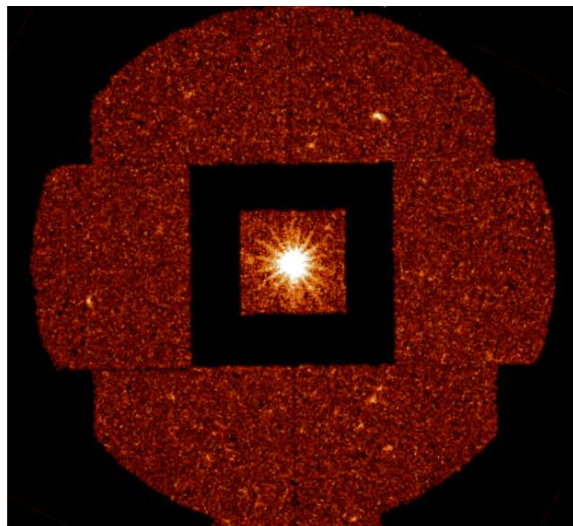
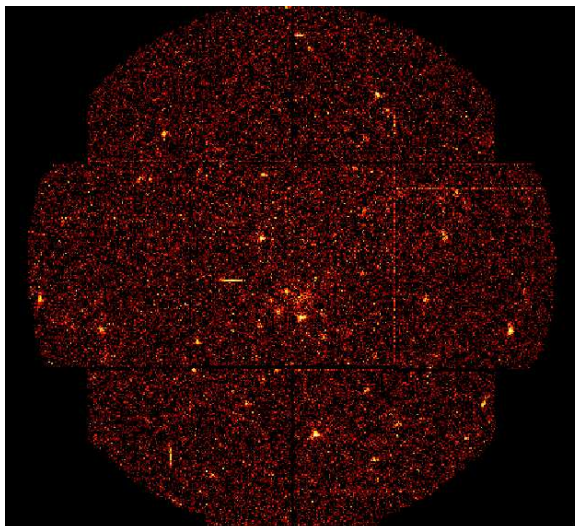


Figure 24: Operating modes for the MOS-CCD cameras. Top left: Full Frame mode; top right: Large Window mode; bottom left: Small Window mode, and bottom right: Timing mode. In Timing mode, the X axis of the central CCD is the projected image of the source, and has thus true spatial information; the Y axis does not carry any spatial information but is a measure of time, with roll-over of 1024 time-units in the figure shown.



### 3.3.3 EPIC imaging – angular resolution

EPIC’s angular resolution is basically determined by the PSF of the mirror modules. This is due to the fact that the EPIC MOS and pn cameras have pixels with sizes of 40 and 150  $\mu\text{m}$ , respectively. For the focal length of the X-ray telescopes (7.5 m), this corresponds to 1.1'' (4.1'') on the sky. Given the *FWHM* of the PSF (see Table 2), the Nyquist theorem is thus fulfilled for the MOS cameras and images are fully sampled. The pixel size of the pn camera slightly undersamples the core of the PSF.

There is one notable exception to the above, namely when the count rate of an X-ray source is so high that photon pile-up on the EPIC chips plays an important role. This is described in § 3.3.9.

### 3.3.4 Intrinsic energy resolution of EPIC

The CCD pixels of the EPIC cameras are energy sensitive, enabling non-dispersive spectroscopy. The resolving power of these cameras is determined by the intrinsic energy resolution of the individual pixels. The spectral resolution for a point source located at the nominal pointing position of both the EPIC MOS and pn CCDs, as a function of energy, is displayed in Figs. 25 and 26. Also plotted in Fig. 25 are the measured in-flight *FWHM* of the Al K $\alpha$  and Mn K $\alpha$  on-board calibration lines, after correction for charge transfer inefficiency (CTI) by the SAS, obtained in five different orbit ranges. The energy resolution of the MOS camera suffered a rapid degradation by  $\simeq 10\%$  during the early mission. The resolution was brought back to pre-launch values by decreasing the operational temperature. This “cooling” was performed between November and December 2002 (Rev.#530 to #560). Since then, the energy resolution of the MOS cameras is basically constant (Fig. 25). For the pn camera, a constant degradation of the energy resolution with a rate of  $\simeq 2.5 \text{ eV yr}^{-1}$  is measured.

### 3.3.5 EPIC quantum efficiencies

One of the factors to be taken into account when determining the effective area of the EPIC cameras is their quantum efficiency (QE). The QE of both types of EPIC CCD chip as a function of photon energy is displayed in Fig. 27 and 28. It is the QE of the EPIC MOS chips that in practice limits the energy passband at its high end, while the pn camera can detect photons with high efficiency up to 12 keV. The event selection strategies can be important in modifying the overall detection efficiency.

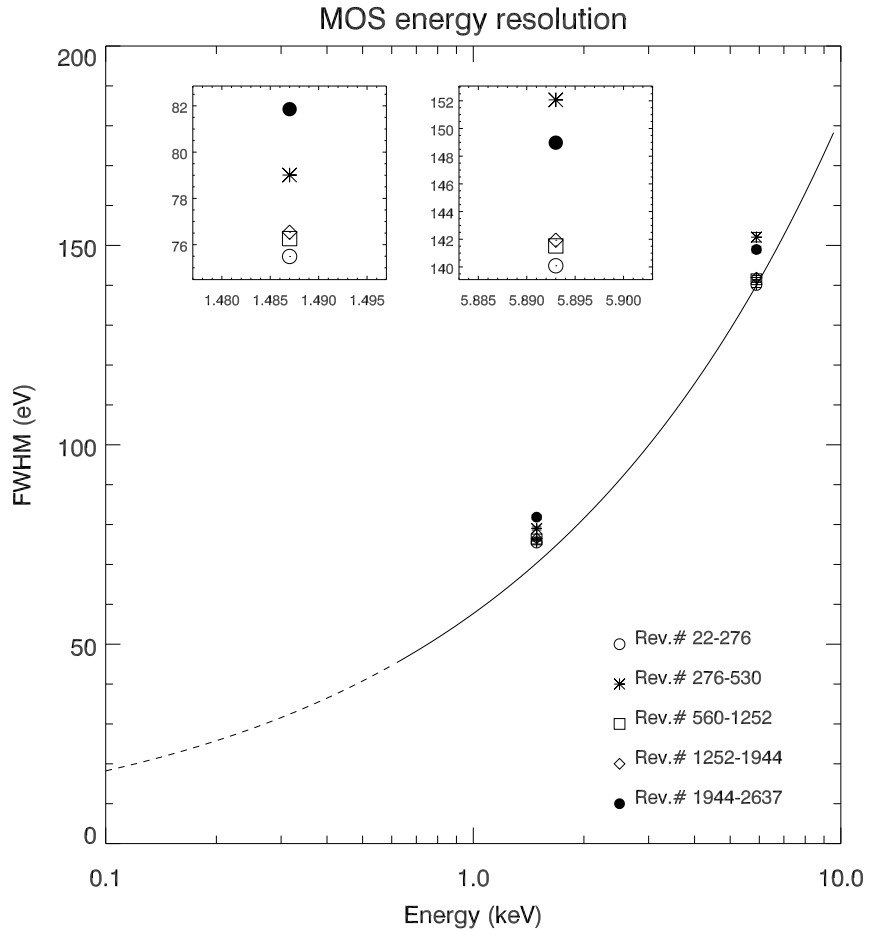


Figure 25: Temporal evolution of the EPIC MOS energy resolution (FWHM) as a function of energy. The solid curve is a best fit  $E^{0.5}$  function to ground calibration data between 0.1 and 12 keV; all events with pattern 0-12 were included in the analysis. Below around 0.6 keV (shown by the dotted region) surface charge loss effects distort the main photo peak significantly from a Gaussian and hence the effective energy resolution. The data points represent MOS 1 in-flight measurements of the FWHM of the Al  $K_{\alpha}$  (1.478 keV) and Mn  $K_{\alpha}$  (5.893 keV) lines in five different epochs. It should be noted the rapid degradation of the resolution between the first and the second epoch, and the recovery and subsequent stability after the cooling of the MOS camera (performed between November and December 2002, i.e. between Rev.#530 and Rev.#560). In the main panel measurement error bars are smaller than the symbol size. In the insets a zoom of the spectral ranges around the nominal line positions is shown. Typical standard deviations in each epoch range between 5 and 10 eV, and 8 and 19 eV for the Al and Mn line, respectively.

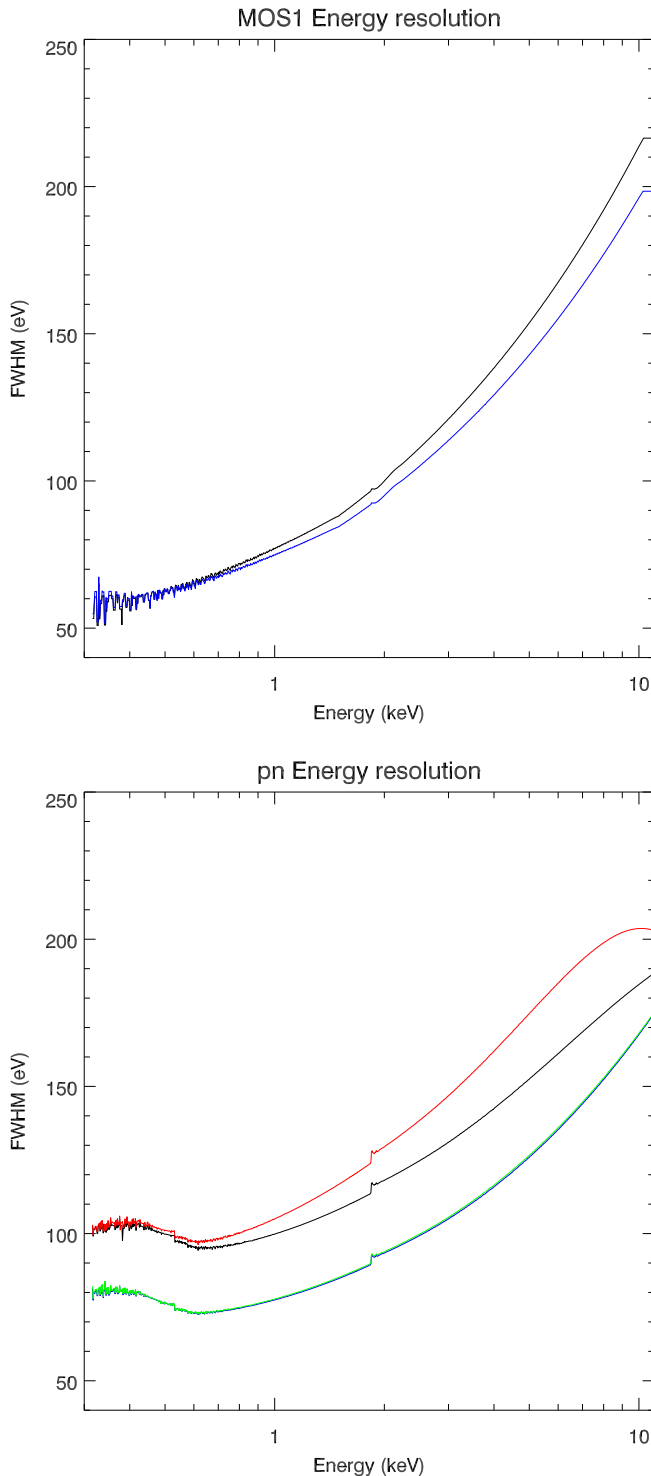


Figure 26: Top panel: MOS 1 energy resolution as a function of energy for singles (blue) and singles+doubles (black) events. Bottom panel: pn energy resolution as a function of energy for: a) single events at the boresight (position "Y9" in the canned response matrices; black); b) double events at the boresight position (red); c) single events closest to the readout node (position "Y0", blue); d) double events closest to the readout node (green). Line widths are based on monochromatic line spectra, simulated with the SASv7.1 canned response matrices.

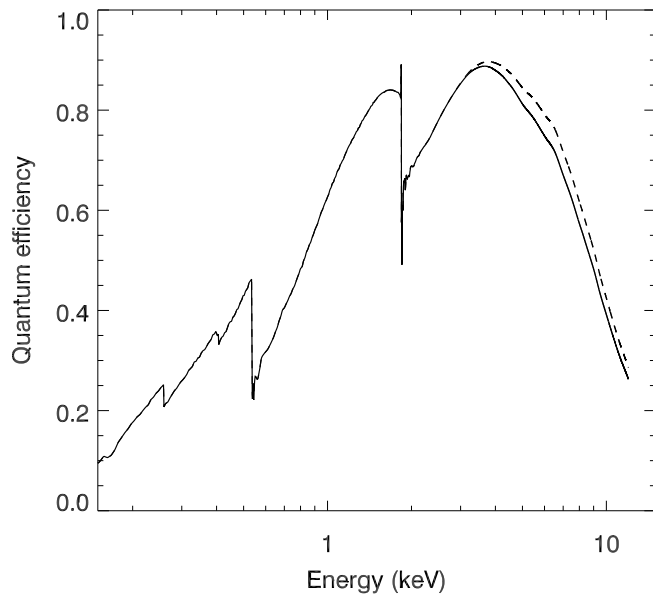


Figure 27: *Quantum efficiency of the EPIC MOS1 (solid line) and MOS2 (dashed line) CCD1 chip as a function of photon energy.*

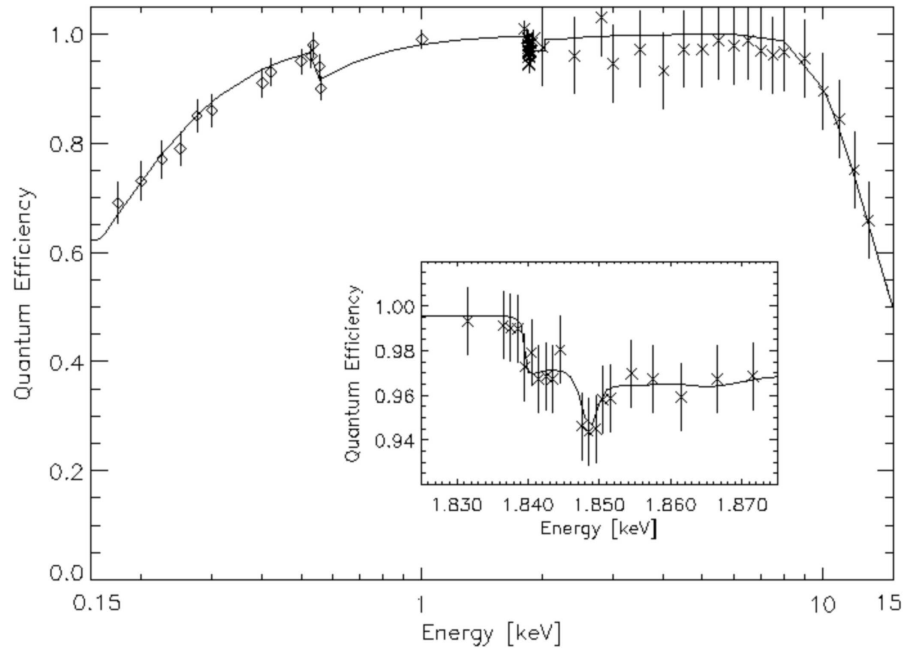


Figure 28: *Quantum efficiency of the EPIC pn CCD chips as a function of photon energy (Strüder et al., 2001, A&A, 365, L18, Fig. 5).*

**esa**european space agency  
agence spatiale européenne

### 3.3.6 EPIC filters and effective area

The next factor influencing the EPIC effective area, specifically in the low energy part of the passband, is the choice of the optical blocking filter. These filters are used, because the EPIC CCDs are not only sensitive to X-ray photons, but also to IR, visible and UV light. Therefore, if an astronomical target has a high optical flux, there is a possibility that the X-ray signal becomes contaminated by those photons. The resulting analysis of data would be impeded in four ways:

1. Shot noise on the optically-generated photo electrons will increase the overall system noise, and hence lower the energy resolution. Spectral fitting will be inaccurate, because the calibration files will assume narrower spectral lines than observed.
2. The energy scale will be incorrectly registered, because a nominally zero signal pixel will have a finite offset. For each optically generated photo electron that is registered, the energy scale shifts by about 3.6 eV. This is comparable with the accuracy with which brightest emission line features can be centred. Consequently, contamination by visible light plays a crucial role in defining the proper energy scale.
3. Excess signal and noise fluctuations can affect the detection efficiency as well, by disguising single pixel X-ray events as events split between pixels.
4. Optically-generated photo electrons can lead to a saturation of electron traps, changing (i.e. reducing) the charge transfer losses. Note that unlike items 1 to 3, this effect may be caused also by unrelated optically bright sources, which happen to irradiate the region on the detector between the X-ray source of interest and the readout node.

To prevent this, the EPIC cameras include aluminised optical blocking filters, and also an internal “offset table” to subtract the constant level of (optical) light or other systematic shifts of the zero level of charge measurements. For MOS the offset table values are fixed and the SAS task emchain/emproc are used to calculate the local changes in offset. For the pn, an offset map is computed before the beginning of each observation. This map contains also the shifts in the energy scale caused by optical photons. During the observation, the energy of each event is reduced by the value of the corresponding pixel in the offset map, before being transmitted to the ground. By this technique, the original energy scale is restored. Note, however, that very bright X-ray sources may contaminate the pn offset map; cf. § 3.3.2. The inclusion of such X-ray events in the offset map calculation, the so-called ‘X-ray loading’, is discussed in the SOC document XMM-SOC-CAL-TN-0050 (available from <http://www.cosmos.esa.int/web/xmm-newton/calibration-documentation>).

If these measures work perfectly, the above problems are minimised. The use of a thick blocking filter capable of minimising the optical light contamination for *all* scenarios will necessarily limit the softest X-ray energy response. Each EPIC camera is therefore equipped with a set of three separate filters, named **thick**, **medium** and **thin**. It is necessary for the observer to select the filter which maximises the scientific return, by choosing the optimum optical blocking required for the target of interest. At the GO’s discretion a thinner filter could be used. In theory, due to the peaked optical response, a similar PSF core excising as used in pile-up cases (see § 3.3.9) might be applied to recover the desired spectra, even if with significant count losses. Note, however, that the optical PSF is smoother than the X-ray PSF due to diffraction of optical light at the gaps between the XMM-Newton mirror shells. This analysis method has never been



**esa**

European space agency  
agence spatiale européenne

tested and in any case will only work for pn observations where related offset tables have been calculated prior to the start of the pn exposure.

It should be noted that also an off-axis bright optical object will leak through the filters generating false X-ray events, which could contribute to degrading the effective telemetry bandwidth (see § 4.3.1).

The following guidelines apply to optical point sources (extended optical objects are not expected to be a significant problem). The optical loading is only important where a bright source is within  $< 2$  arcmin of the target or along the EPIC CCD read-out direction.

The calculations below have been performed for a worst case, i.e., for the brightest pixel within the core of the PSF. Therefore, averaging the brightness of an extended object over a scale of one PSF (say,  $20''$ ) should provide a corresponding estimate with a significant margin of safety. Note that these data apply to full frame modes only, and that a change to a partial window mode with an order of magnitude faster readout rate can allow suppression of optical contamination at 2–3 visible magnitudes brighter for *ALL* filters. The GO can make an estimate on optical contamination improvement based on the mode time resolution compared with full window mode (Table 3).

- Thick filter

This filter should be used if the expected visible brightness of the target would degrade the energy scale and resolution of EPIC. It should be able to suppress efficiently the optical contamination for all point source targets up to  $m_V$  of 1–4 (MOS) or  $m_V$  of -2–1 (pn). The range depends on the spectral type, with only extremely red (M stars for example) or blue colours causing the change to 3 magnitudes fainter level.

- Medium filter

The optical blocking is expected to be about  $10^3$  less efficient than the thick filter, so it is expected that this filter will be useful for preventing optical contamination from point sources as bright as  $m_V = 6$ –9.

- Thin filter

The optical blocking is expected to be about  $10^5$  less efficient than the thick filter, so the use of this filter will be limited to point sources with optical magnitudes about 12 magnitudes fainter than the corresponding thick filter limitations.

Figs. 29 and 30 display the impact of the different filters on the soft X-ray response of both types of EPIC camera, whereas Fig. 31 displays the combined effective area of all XMM-Newton X-ray telescopes.

The user might also want to take note of the SOC document XMM-SOC-CAL-TN-0001 (available from <http://www.cosmos.esa.int/web/xmm-newton/calibration-documentation>) which explains in detail the PHS (Proposal Handling Subsystem) software tools, used during the technical evaluation and enhancement of a proposal to determine if the correct optical blocking filter has been chosen for a particular exposure. Technical notes on the assessment of optical loading for EPIC pn and MOS are available from the same URL as XMM-SOC-CAL-TN-0051 and XMM-SOC-CAL-TN-0043, respectively.



**esa**

European space agency  
agence spatiale européenne

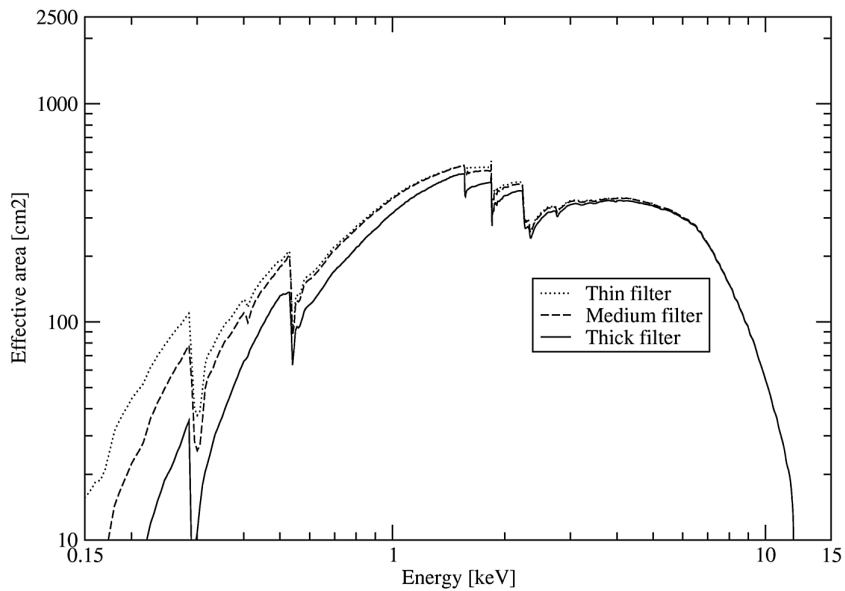


Figure 29: The EPIC MOS effective area for each of the optical blocking filters.

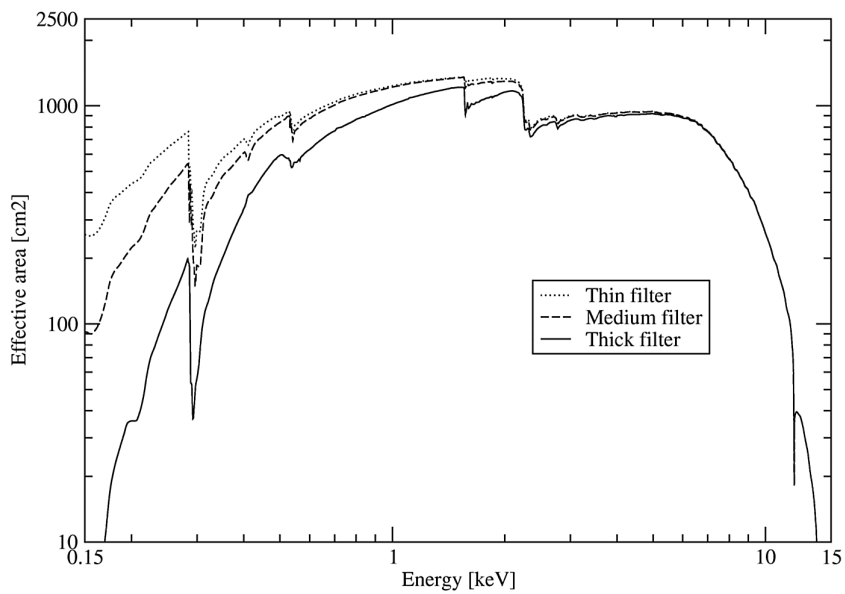


Figure 30: The EPIC pn effective area for each of the optical blocking filters.



**esa**

European space agency  
agence spatiale européenne

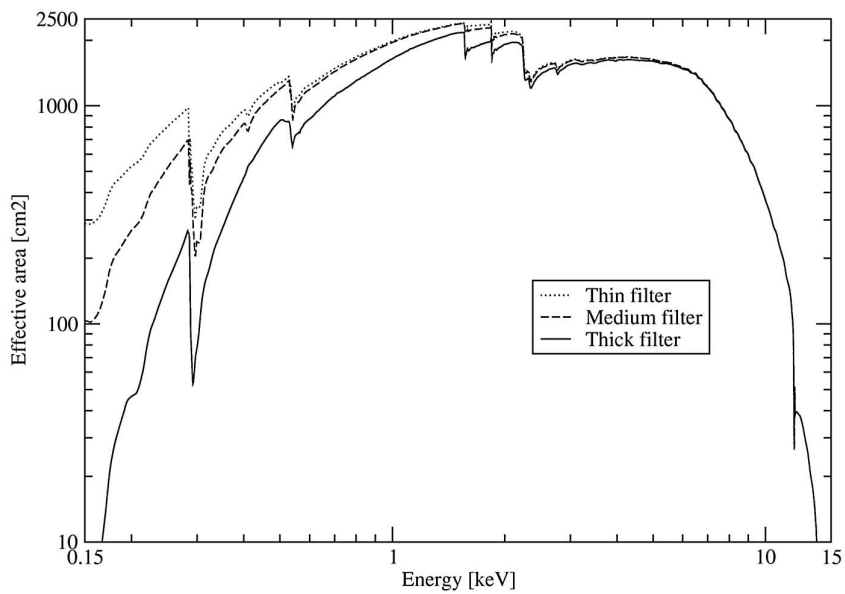


Figure 31: *Combined effective area of all telescopes assuming that the EPIC cameras operate with the same filters, either thin, medium or thick.*



### 3.3.7 EPIC background

The EPIC background can be divided into two parts: a cosmic X-ray background (CXB), and an instrumental background. The latter component may be further divided into a detector noise component, which becomes important at low energies (i.e. below 300 eV) and a second component which is due to the interaction of particles with the structure surrounding the detectors and the detectors themselves. This component is characterised by a flat spectrum and is particularly important at high energies (i.e. above a few keV).

The particle induced background can be divided into 2 components: an external ‘flaring’ component, characterised by strong and rapid variability, which is often totally absent and a second more stable internal component. The flaring component is currently attributed to soft protons ( $E_p$  smaller than a few 100 keV), which are presumably funnelled towards the detectors by the X-ray mirrors. The stable component is due to the interaction of high-energy particles ( $E$  larger than some 100 MeV) with the structure surrounding the detectors and possibly the detectors themselves.

A table summarising the temporal, spectral and spatial properties of the EPIC background components mentioned above is available at <http://www.cosmos.esa.int/web/xmm-newton/background>. The SOC has performed an analysis of the seasonal and long-term behaviour of the XMM-Newton background from the beginning of the mission (available as XMM-SOC-GEN-TN-0014). Main conclusions are:

- The data clearly show that the distance to the Earth is the dominant parameter (as expected, the background is lower close to apogee). There are quite often differences of about one order of magnitude or even more, between the background at the end of the science window of the revolution and at apogee.
- In addition to this:
  - There is a marked asymmetry in the behaviour of the background when moving away from perigee and when approaching to it (the ascending and descending parts of the orbit).
  - The background reaches higher values at the end of the revolution than at the beginning. The high background time does not extend usually beyond orbital phase  $\sim 0.2$  (i.e. 9–10 hours after perigee passage)<sup>2</sup>. There are however epochs of the year in which the background starts to rise a few hours after apogee.
  - The behaviour of the background presents a pronounced seasonal effect, but it has long-term changes from year to year, due to the XMM-Newton orbit evolution and/or the solar cycle.
  - Around solar maximum, the probability of solar flaring activity increases, whereas the level of quiescent background decreases.

#### 3.3.7.1 EPIC external ‘flaring’ background

This component is produced by protons with energies less than a few 100 keV which are funnelled towards the detectors by the X-ray mirrors. In Fig. 32 we show an image of the MOS2 detector during an observation which was badly affected by soft proton flares. The intensity of the background within the field of view is much larger than outside because of the soft proton component.

---

<sup>2</sup>The Target Visibility Checker, a tool to check the visibility of any target in the sky for XMM-Newton, provides also information on the orbital phase when the target visibility starts and ends.

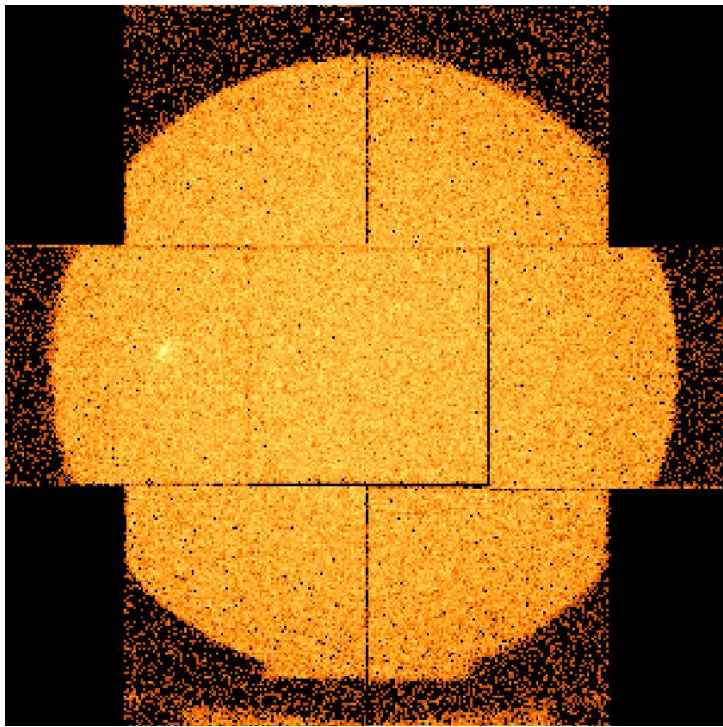


Figure 32: *Image from a MOS2 observation badly affected by soft proton flares.*

In Fig. 33 we show the background light-curve for the MOS1 unit for another observation (one of the Lockman Hole observations in 2000) where rapid and strong variability is clearly present. While the MOS1 and MOS2 cameras show almost identical light-curves the pn camera can yield substantially different results, in the sense that some flares appear to be much more intense in the pn than in the MOS cameras.

The spectra of soft proton flares are variable and no clear correlation is found between intensity and spectral shape. The current understanding is that soft protons are most likely organised in clouds populating the Earth's magneto-sphere. The number of such clouds encountered by XMM-Newton in its orbit depends upon many factors, such as the altitude of the satellite, its position with respect to the magneto-sphere, and the amount of solar activity.

Plots showing the radiation levels reported by the spacecraft Radiation Monitor (§ 3.6.1) in quasi real time on a range of time scales spanning the preceding 48 hours together with an archive of daily plots are available from the Live Radiation Monitor web page.

### 3.3.7.2 EPIC internal ‘quiescent’ background

This quiescent component is associated with high energy particles interacting with the structure surrounding the detectors and the detectors themselves. The intensity of the quiescent component is monitored regularly for both MOS and PN cameras during CLOSED filter observations. The component shows only small intensity variations in time which are typically observed on long time-scales. The intensity of this component during any given observation is within  $\sim 10\%$  of the mean. The intensity observed in one MOS camera is usually well correlated with the intensity measured in the other, although some exceptions have been observed. In Figs. 34 and 35 we show the spectrum of the quiescent component for the MOS1 and PN camera, respectively.

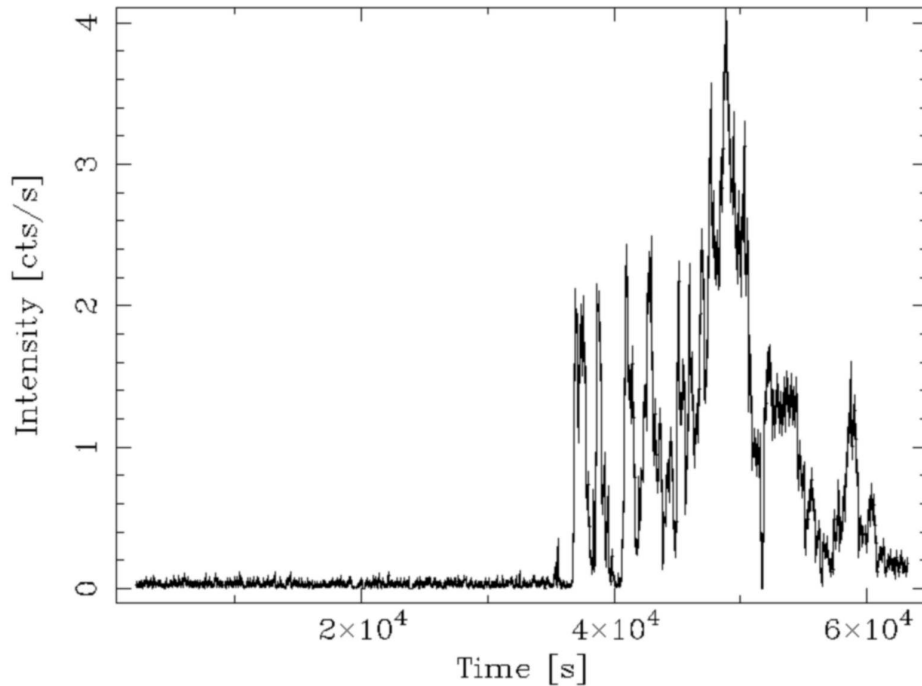


Figure 33: *Light curve from a MOS1 observation badly affected by soft proton flares. During the first part of the observation the background is constant. The second half, however, is heavily affected by a proton flare.*

The spectra are quite flat and present a number of spectral features due to fluorescence from the detectors and the structure surrounding them. Al-K $\alpha$  and Si-K $\alpha$  lines are clearly visible in the MOS spectrum. In case of the PN Al-K $\alpha$  and an intense complex due to Cu-K $\alpha$ , Ni-K $\alpha$  and Z-K $\alpha$  lines around 8 keV is visible. An important point is that the intensity of this complex is not constant over the PN detector. More specifically there exists a central circular region (see Fig. 36) where the complex is virtually absent.

Average count rates due to the internal "quiescent" background, for both MOS and PN, in different modes and filters, as well as energy ranges and pattern selection, can be found at:  
<http://www.cosmos.esa.int/web/xmm-newton/bs-countrate>.

These count rates have been worked out using out-of-field events from Blank Sky event files.

### 3.3.7.3 EPIC Detector Noise

The dark currents of both types of EPIC CCD are negligible sources of background noise under nominal operating conditions (especially above 250 eV for the pn camera).

In MOS there are low level 'flickerings' of a small number of pixels at an occurrence rate < 1%. Two peripheral CCDs of the MOS cameras (CCD4 on MOS1, and CCD5 on MOS2) are frequently affected by a low-energy ( $E < 1$  keV) noise plateau, see Section 4.3.2 "EPIC-MOS low energy noise in two peripheral CCDs" for details. Noisy features appeared on MOS1 CCD4 after the event leading to the loss of CCD3 (see Sect. 3.3). In pn occasionally (mainly during high particle background) the offset calculation leads in some pixels to a slight underestimate of the

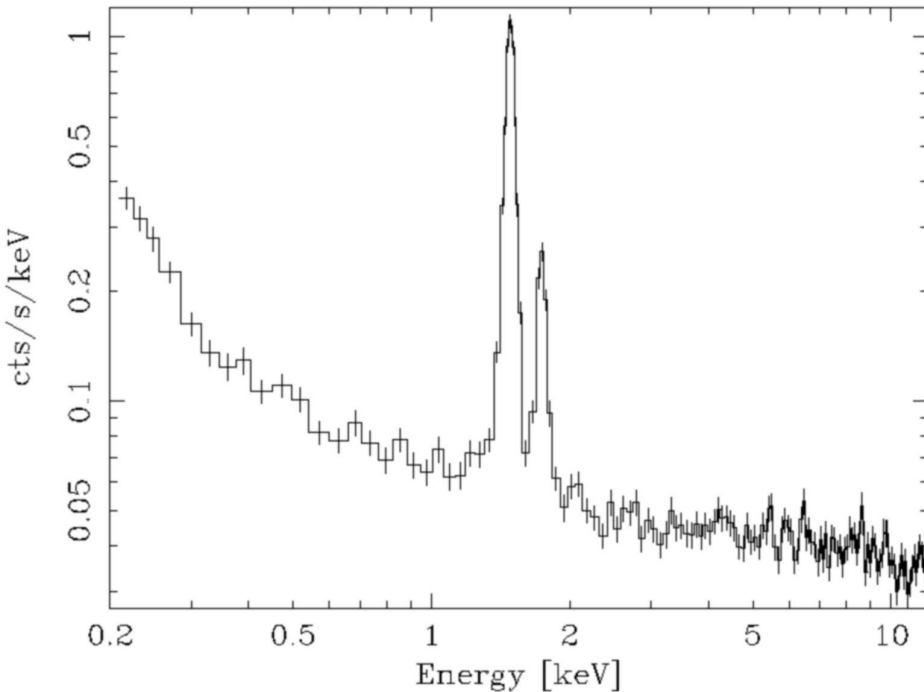


Figure 34: *Background spectrum for the MOS1 camera during an observation with the filter wheel in the closed position. The prominent features around 1.5 and 1.7 keV are respectively Al-K and Si-K fluorescence lines. The rise of the spectrum below 0.5 keV is due to the detector noise.*

offset, which can result in blocks of approx.  $4 \times 4$  pixels with enhanced low energy signal.

#### 3.3.7.4 EPIC background and its importance for extended sources

As the variable EPIC background is especially important for extended sources, the user is strongly advised to make use of previous XMM-Newton observations to estimate the ratio between expected target emission and EPIC background. The discussion of the background effects on the analysis of extended sources that even might fill the whole EPIC field of view is critical. The Background Analysis page provides an overview on all sources of background analysis and modelling, pointing out the recommended guideline for background treatment by the EPIC consortium. It also lists products aimed at helping the user in the analysis of extended sources. Currently available products are

- XMM-Newton Extended Source Analysis Software package, XMM-ESAS, allowing the user to model the quiescent particle background both spectrally and spatially for the EPIC detectors. XMM-ESAS is part of the Science Analysis Software (SAS).
- XMM-Newton blank sky background event files for the 3 EPIC instruments, in Full Frame and Extended Full Frame (PN only) modes, constructed using a superposition of pipeline product data from the 3XMM (see § A.3.1) reprocessing of many pointed observations.



- Filter Wheel Closed data:

The stacked collections of Filter Wheel Closed (FWC) data are available for the MOS and pn cameras.

Suggestions and caveats on the analysis of extended sources with the EPIC cameras have also been addressed in a SAS workshop presentation (available from the SAS Workshop page). Readers are referred to the EPIC Background Analysis page for an extensive description of the properties of the EPIC background, links to blank field and filter wheel CLOSED data, and data reduction and analysis tools.

### 3.3.8 EPIC's sensitivity limits

The EPIC sensitivity limits depend on the sky area, i.e. the true X-ray background and on the ‘space weather’ as described in §§ 3.3.7.1 and 3.3.7.2.

As the sensitivity limits also depend on the angular structure and the spectral characteristics of the source that is observed, it is strongly recommended to use simulations to get an estimate of the signal to noise which can be achieved with a certain instrument setup and exposure time. Currently the best statistical results on the EPIC sensitivity limits are based on the Lockman Hole data (Hasinger et al., 2001, A&A 365, L45; Brunner et al. 2008, A&A, 479, 283). In Table 4 the sensitivity limits in the “soft”, “hard”, and “very hard” energy band are reported

Table 4: *Detection limits (i.e., minimum detectable flux at  $4\sigma$  in units of  $10^{-15}$  erg cm $^{-2}$  s $^{-1}$ ) for different energy bands in the 1.16 Ms observation of the Lockman Hole (Hasinger et al., 2001, A&A 365, L45; Brunner et al. 2008, A&A, 479, 283).*

Band	Lockman Hole
“Soft” (0.5–2 keV)	0.19
“Hard” (2–10 keV)	0.9
“Very hard” (5–10 keV)	1.8

Watson et al., 2001, A&A, 365, L51 used the nominal quiescent background values together with the measured XMM-Newton PSF to compute an EPIC point source sensitivity based on a simple  $5\sigma$  source detection criterion against assumed purely Poissonian background fluctuations, as shown in Fig. 37<sup>3</sup>. These estimates are in reasonable agreement with the flux distribution of sources in the EPIC Serendipitous Source Catalogue (Watson et al., 2009, A&A, 493, 339).

The actual background in an observation depends critically on the fraction of background flares removed, i.e. the trade off between net background levels and net exposure time.

At very faint fluxes the effective sensitivity is potentially limited by confusion effects. However, recent estimates indicate that the confusion limit in the hard X-ray band (2-10 keV) is only reached after 2 Ms of observing time and will probably never be reachable in the 5-10 keV band.

<sup>3</sup>The  $5\sigma$  value represents a relatively conservative limit. For the effective beam area of XMM-Newton, the appropriate limit for purely Poissonian background fluctuations to yield  $\leq 1$  spurious source per field is about  $3.5 - 4\sigma$ .

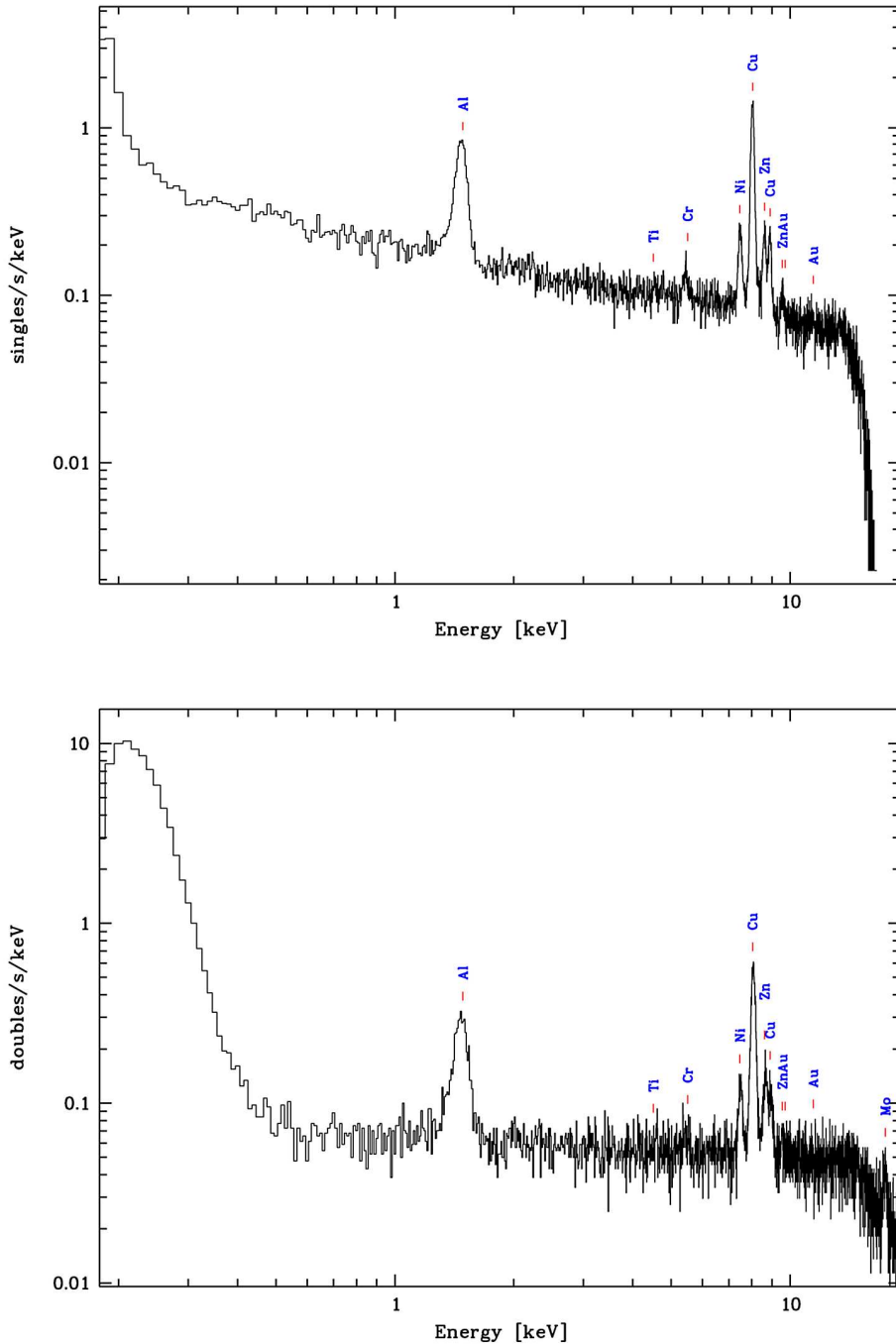


Figure 35: Background spectrum for the pn camera during an observation with the filter wheel in the CLOSED position (top: single events, bottom: double events) in the energy range 0.2-18 keV. The prominent features around 1.5 keV are Al-K $\alpha$ , at 5.5 keV Cr-K $\alpha$ , at 8 keV Ni-K $\alpha$ , Cu-K $\alpha$ , Zn-K $\alpha$  and at 17.5 keV (only in doubles) Mo-K $\alpha$  fluorescence lines. The rise of the spectrum below 0.3 keV is due to the detector noise. The relative line strengths depend on the (variable) incident particle spectrum.



**esa**

European space agency  
agence spatiale européenne

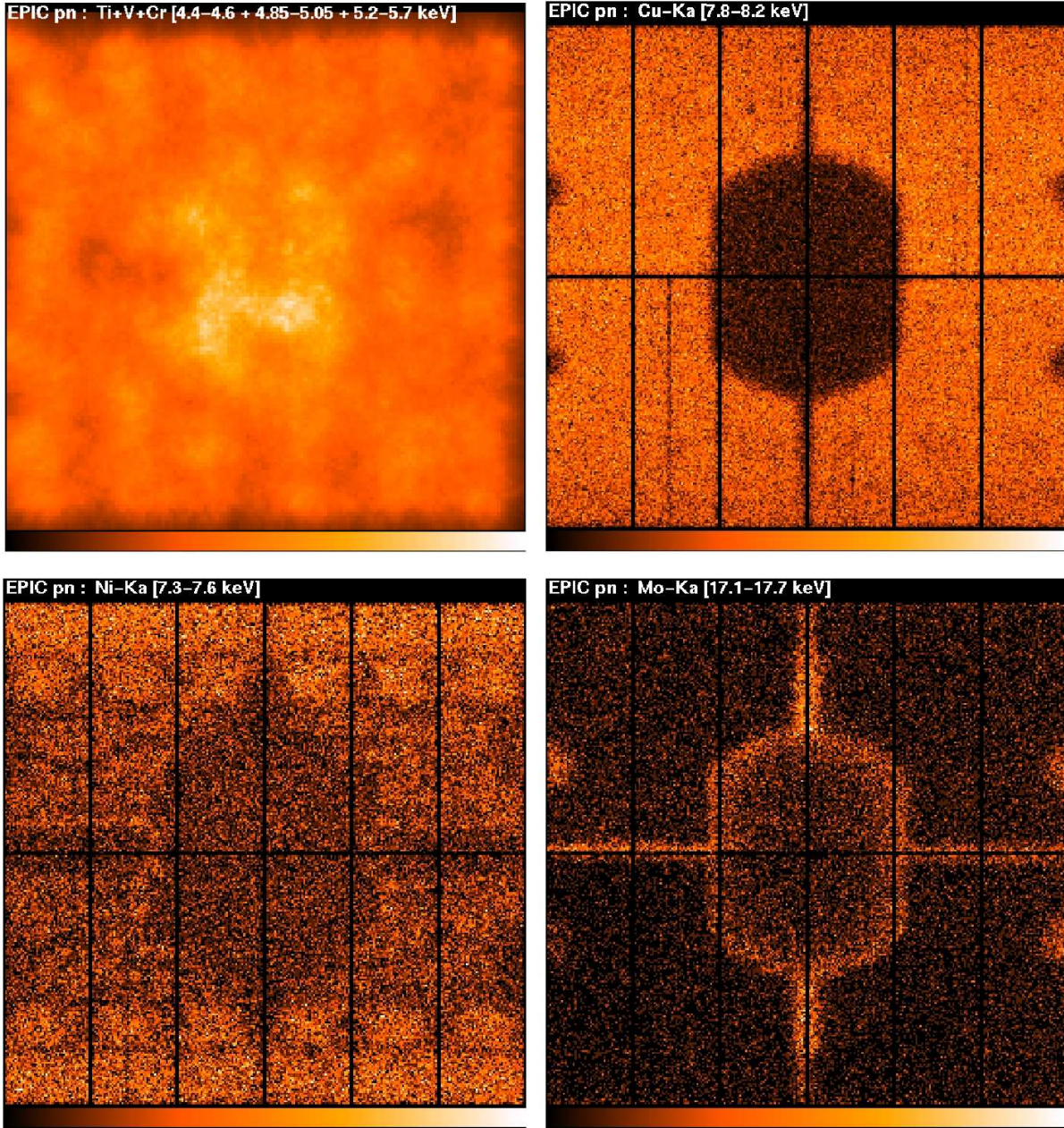


Figure 36: Background images for the pn camera with spatially inhomogeneous fluorescent lines: smoothed image in the Ti+V+Cr-K $\alpha$  lines (top left), full resolution image in Copper (7.8 – 8.2 keV) (top right), Nickel (7.3 – 7.6 keV) (bottom left) and Molybdenum (17.1 – 17.7 keV) (bottom right). The absolute normalisation of the images can be inferred from the spectra in Fig. 35. The inhomogeneity is caused by the electronics board mounted below the CCDs; in case of the energy range 4.4 – 5.7 keV probably due to a supporting screw - however at a very low level.

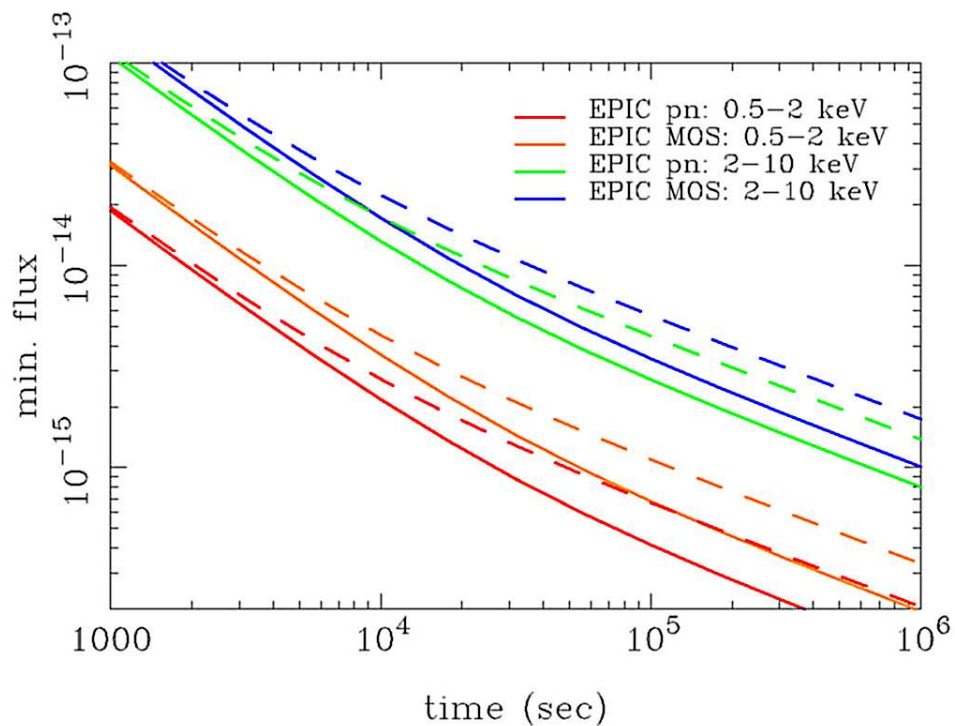


Figure 37: EPIC sensitivity ( $5\sigma$  minimum detectable flux in  $\text{erg cm}^{-2} \text{ s}^{-1}$  in respective bands) as a function of exposure time (from Watson et al., 2001). Sensitivity is computed for an assumed  $\alpha = 1.7$  powerlaw spectrum with a column density  $N_H = 3 \times 10^{20} \text{ cm}^{-2}$ . Solid curves are for the nominal background rates. Dashed curves are for background levels enhanced by a factor 3. The EPIC MOS curves correspond to the combination of the two cameras.



### 3.3.9 EPIC photon pile-up

Photon pile-up, i.e., the arrival of more than one X-ray photon in one camera pixel or in adjacent pixels before it is read out, can affect both the PSF and the spectral response of EPIC.

Table 3 provides estimates of count rates and approximate incident fluxes for the different EPIC instrument modes for which pile-up should not be a problem. For the MOS full imaging mode, e.g., ca. 0.5 counts/s should not be exceeded. Note that the provided incident fluxes depend on the source spectrum and pile-up can become an important effect at even lower incident fluxes for sources with very steep (i.e. soft) spectra. This is because the expected count rates for a given incident flux are higher for soft than for hard spectra. On the other hand at larger off-axis position pile-up is less likely.

The PSF is influenced by pile-up, because in the core of the PSF many photons arrive at almost the same time (within one readout frame), creating multi-pixel photon patterns which, for the MOS camera, are then rejected by the onboard event reconstruction software (which suppresses large size events, such as that induced by most of the cosmic rays). For the pn camera, event reconstruction is performed offline in the SAS. The pile-up effect leads, in the most extreme case, to a PSF with an artificial “hole” at its centre, as displayed in Fig. 38.

The spectral response is compromised, because the charge deposited by more than one photon is added up before being read out, thus creating artificial “hard” photons where there have actually been two or more soft photons.

Pile-up effects on the spectral shape are very much reduced by selection of mono-pixel events. The effect of pile-up in this case is then essentially a loss of flux. Also, in case of very strong pile-up, building spectra and calculating absolute fluxes is still possible with a good accuracy by excising the heavily piled-up core (see below) from the analysis.

To get an idea on how important the pile-up effect can be for spectral analyses, a  $kT = 1$  keV Raymond-Smith model spectrum with  $N_H = 3 \times 10^{20}$  cm $^{-2}$  was simulated using a ray-tracing code and the fit to the resulting “observed” spectrum was compared with the input for EPIC MOS observations in the full window mode (Table 5).

Table 5: *The effect of pile-up on spectral fits*

Input flux <sup>1</sup>	Output count rate [s $^{-1}$ ]	Counts per MOS frame	$N_H$ [10 $^{20}$ cm $^{-2}$ ]	kT [keV]	Norm./expect
4.05	1.08	0.22	3.0	0.967	1
13.4	3.56	0.71	3.05	0.972	1
40.5	10.5	2.1	3.2	0.979	0.98
134	33.3	6.65	3.5	1.010	0.95
405	85.4	17.1	4.1	1.022	0.80

Notes to Table 5:

1) 0.15–10 keV flux in units of [10 $^{-12}$  erg s $^{-1}$  cm $^{-2}$ ].

One can see how the best-fitting  $N_H$ , kT and normalisation vary as a function of input source flux (and thus count rate per frame). Note that, because of the photon pile-up, one apparently loses soft photons (whose charge combines and is then seen at higher energies), thus requiring a higher  $N_H$  and also a higher kT to reach the minimum  $\chi^2$  for the fit. The peculiarity that for low

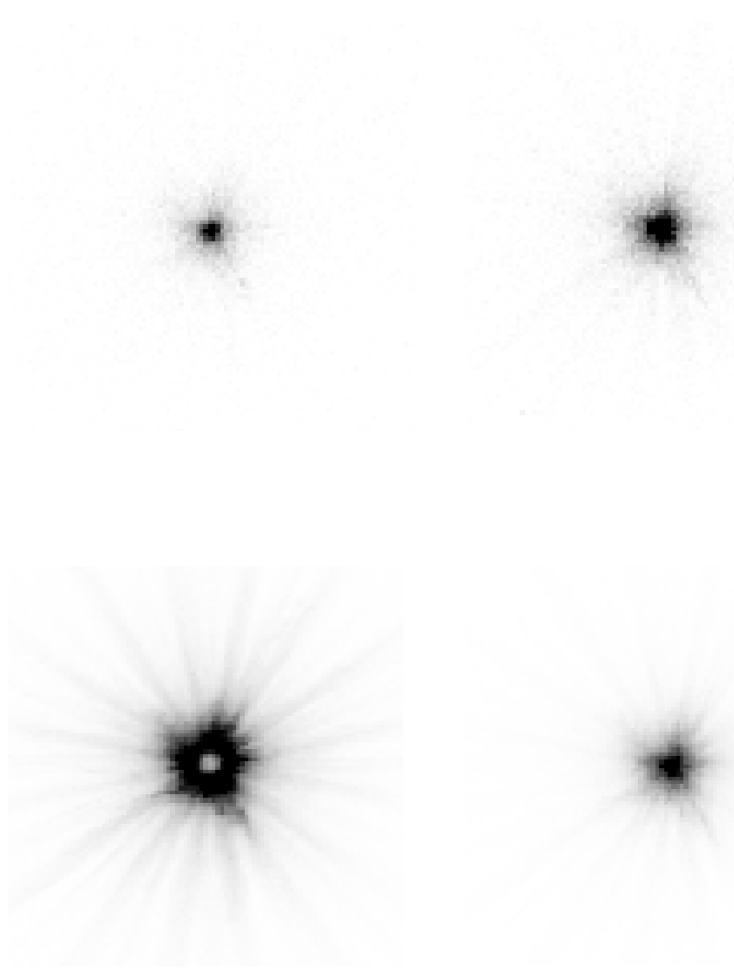


Figure 38: *In-orbit observations performed with EPIC MOS showing the increase of pile-up with increasing photon count rate per frame. The panels are arranged clockwise, with the lowest count rate (and thus pile-up rate) in the upper left and the highest in the lower left. The observed count rates are 2, 5, 12 and 16 counts/frame, respectively.*

fluxes the fitted  $kT$  is a bit lower than the input value is explained by the fact that the simulation was performed without event reconstruction. What is important to note is the relative change in  $kT$ . A similar change is also caused in the best-fitting slope of a power law, as displayed in Fig. 39. The effect of pile-up on the PSF has been taken into account in these simulations by choosing an appropriately large photon extraction region for the spectral analysis.

**Note:** No error bars are provided in Table 5, because the input spectrum is a numerical model spectrum without noise. For up to 2 counts per MOS frame, the typical error on  $N_H$  stays below 10%, those on  $kT$  and the normalisation stay at a level of 2%.

The SAS task `epatplot` can be used as a diagnostic tool for pile-up in the EPIC cameras. It utilises the relative ratios of single- and double-pixel events which deviate from standard values in case of pile-up. Fig. 40 shows the produced plot for a source with a count rate of  $\sim 14$  counts/s in pn full frame mode. As input an eventfile was used which contains all events extracted from



**esa**

european space agency  
agence spatiale européenne

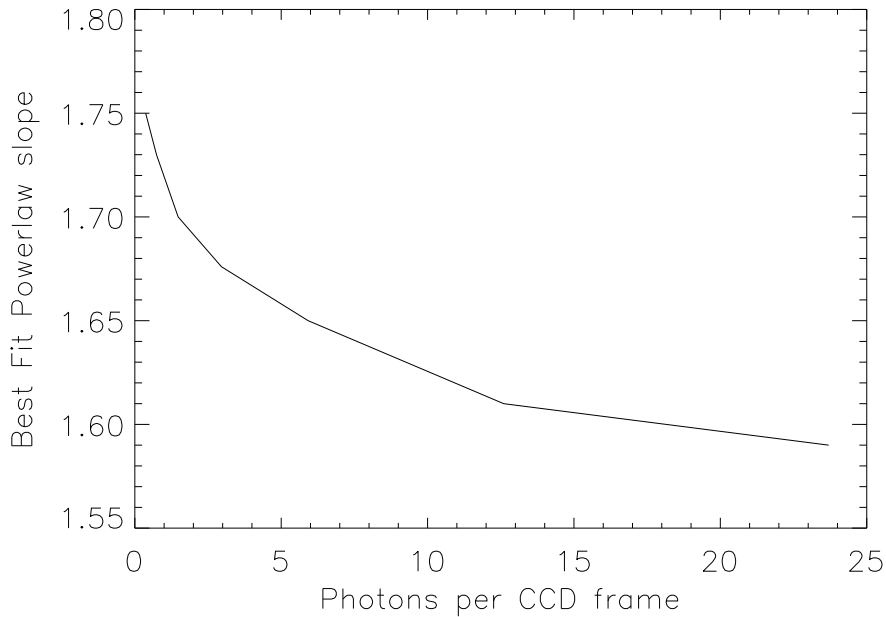


Figure 39: The best-fitting power law slope,  $\alpha$ , for an  $\alpha = 1.7$  input spectrum into SciSim, with different input count rates, leading to different levels of pile-up.

a circle with radius 1 arcmin around the source position. In the upper panel, the spectral distributions as function of PI channel for single-, double-, triple- and quadruple-events (these are the four types of valid events which can be created by an X-ray photon) are plotted. Invalid patterns are also shown to indicate how much energy is lost by pattern pile-up (refer to the pile up thread at How to evaluate pile-up for additional details).

Doubles can only be produced when the energy of both events is above the event threshold. Similarly triples and quadruples start at 3 and 4 times the threshold, respectively. In the lower panel the fraction of the four valid event types are plotted (relative to the sum). The ratios are energy dependent with higher energy photons producing less singles due to the increasing size of the electron cloud. As long as the count rate is below the pile-up limit the energy dependence follows standard curves. These are plotted for singles (1.0 at energies below twice the threshold and then decreasing with energy), doubles and singles+doubles. The curves are also used in the detector response matrices to correct for the pattern selection used in the spectrum to be analysed. In the case of pile-up, the ratios deviate from the standard curves as the example shows. Due to ‘pattern pile-up’ more doubles (which are actually two neighbouring singles) are produced.

A quantitative comparison of both types of EPIC camera with the *Chandra* ACIS-I instrument in this respect is provided in § 3.7.1.3.

Estimates of the pile-up fraction as a function of pattern, and of the associated flux loss for single events are presented by Ballet (1999, A&ASS, 135, 371); the treatment is extended to double pixels in Ballet (2003, AdSpR, 32, 2077). Empirical methods to estimate and partly to correct pile-up based on single-event spectra in EPIC-MOS are discussed in Molendi & Sembay, (2003; <http://xmmweb.esac.esa.int/docs/documents/CAL-TN-0036-1-0.ps.gz>).

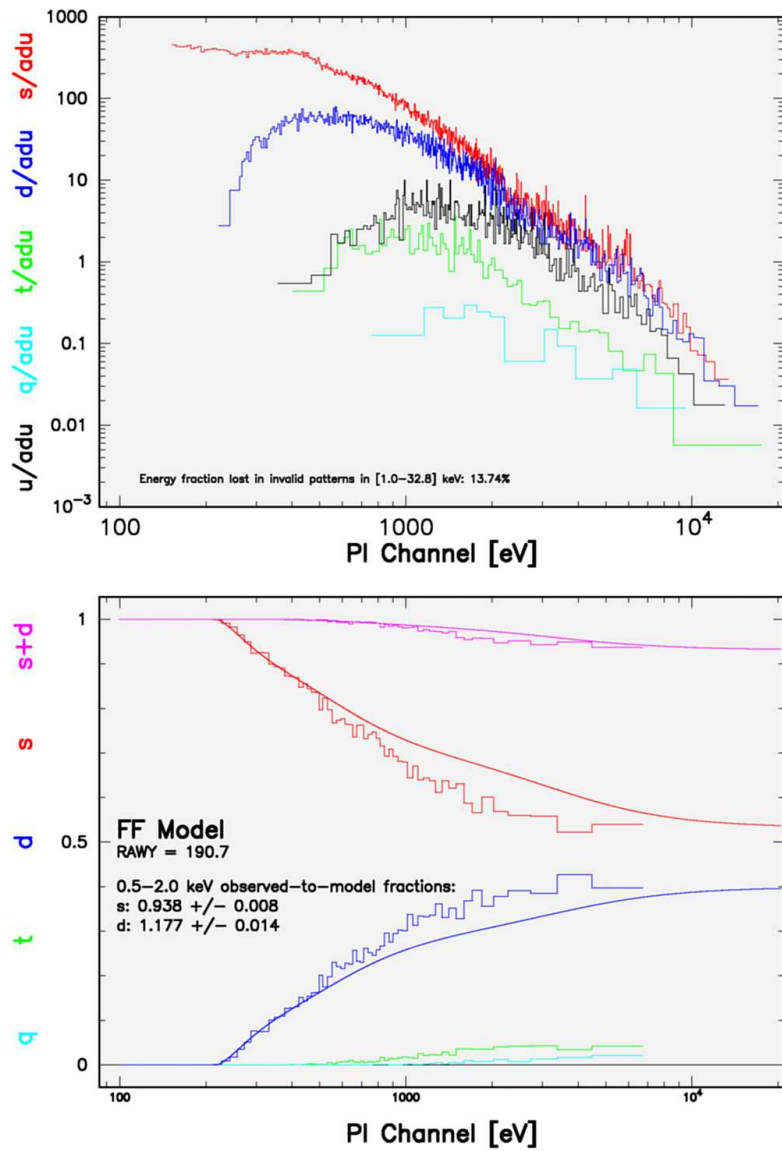


Figure 40: Plot of the *pn* pattern distribution with energy as produced by the SAS task *epatplot* (see text for further details).

**esa**european space agency  
agence spatiale européenne

### 3.3.10 EPIC out-of-time events

For the EPIC imaging modes, photons are not only registered during the actual integration interval but also during the readout of the CCD (shift of charges along a column towards the readout node). These so called Out-of-Time (OoT) events get a wrong RAWY value assigned and thus finally a wrong CTI correction. The magnitude of this effect scales with the ratio of readout time and integration time. Table 6 summarises the relevant parameters.

Table 6: *EPIC Out-of-Time (OoT) events. The percentage of OoT events is given by the mode dependent ratio of readout time and integration time*

MOS Mode	Life time with OoT events [%]	Fraction OoT [%]
Full frame	100.0	0.35
Large window	99.5	0.5
Small window	97.5	0.5

pn Mode	Life time with OoT events [%]	Fraction OoT [%]
Full frame	99.9	6.3
Ext. full frame	100.0	2.3
Large window	94.9	0.16
Small window	71.0	1.1

The effect of OoT events broadens spectral features in a systematic way: assume a bright point-like source above CCD pixel RAWY\_S then the OoT events with  $\text{RAWY} < \text{RAWY}_S$  will be undercorrected (and thus get a too low energy) while the ones for  $\text{RAWY} > \text{RAWY}_S$  will become overcorrected (too high energy).

This effect is illustrated in Fig. 41 using the internal calibration source (CalClosed filter position) as a quasi example of a bright extended source with a line spectrum. Note the significantly broadened features in the OoT spectrum.

The effect on images is shown in Fig. 42 (also note the arc-like structures due to single mirror reflections at the top left of the FoV; see § 3.2.4).

The OoT events are not only affecting the central source itself but also the region between the source and the readout node. In Fig. 42 for example a source is located close to the upper edge just along the readout direction of the bright central source. Also the spatial and spectral analysis of any extended emission (as visible e.g. in the lower right panel of Fig. 42) can significantly be hampered by OoT events.

If a performed EPIC-pn observation is affected by OoT events, the SAS task epchain can be used to create a simulated OoT events list. Images and spectra extracted from this OoT events list should be subtracted from images and spectra produced from the original events list to clean these products from the effects of OoT events.

In Fig. 43 we show an example on how the EPIC-pn camera works in Small Window mode. The process is as follows:

1. Immediately after a readout is completed the top 64 rows of the CCD (the ones



downlinked to the ground) are fast shifted downwards by 64 rows. This takes 0.046 ms (64x720 ns).

2. A nominal integration of 4.028 ms follows.
3. There is another fast shift of the top 64 rows but now they are moved to the readout node (i.e. they are shifted 136 rows). This takes 0.098 ms (136x720 ms).
4. The 64 rows of the science window are finally readout. This takes 1.518 ms (66x0.023 ms, as two additional lines are read to start the pipeline).
5. Then, the contribution of out-of-time events to the background within the science window can be divided in three parts:
  - The top 64 rows contribute during the two fast shifts.
  - The rows in the middle contribute only during the second fast shift.
  - Finally, the bottom part of the CCD contributes during the second fast shift AND during the readout, so that the out-of-time events from the lower part of the detector may become noticeable in the upper region of the science window.

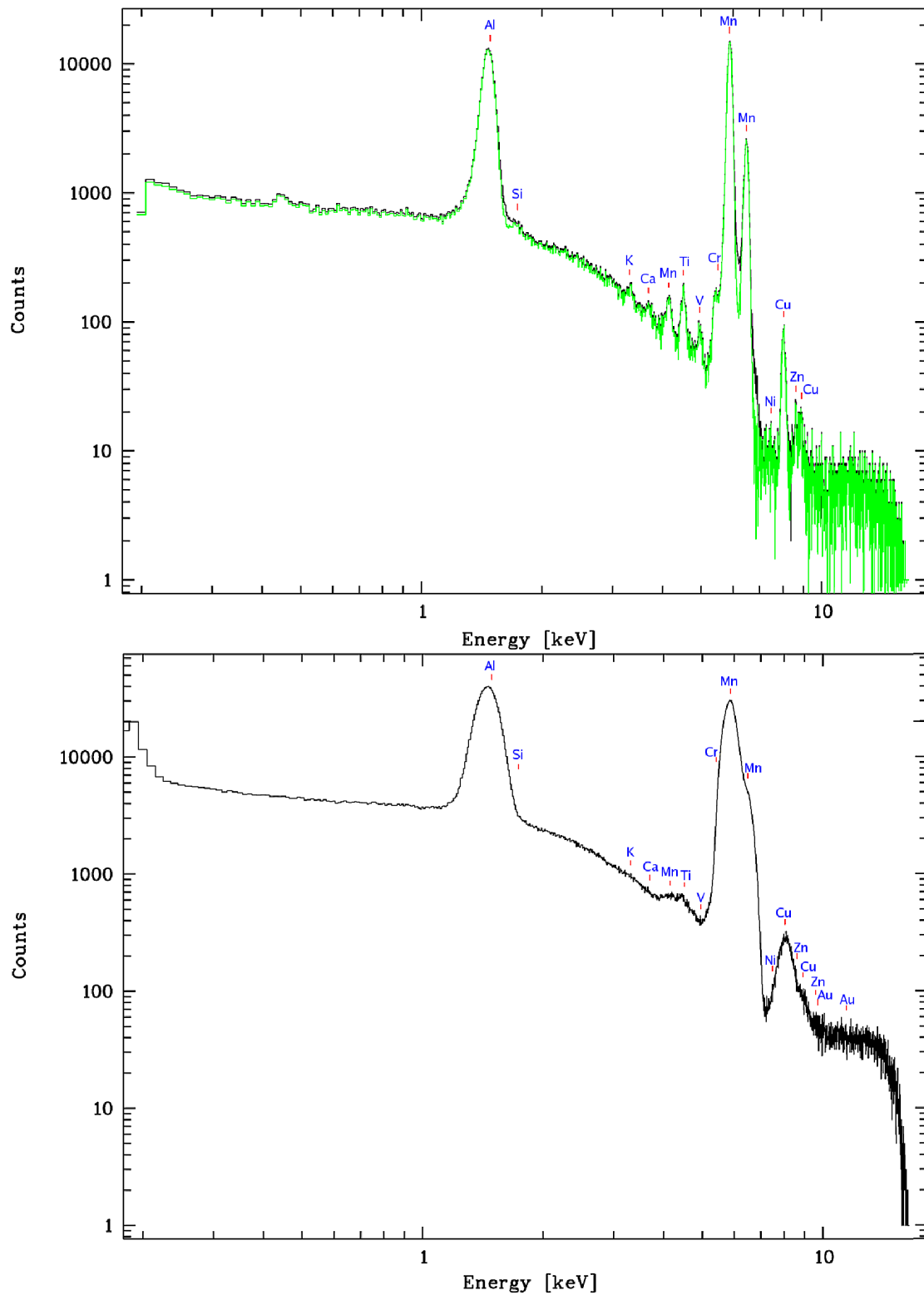


Figure 41: Effect of spectral broadening due to Oot events: the upper panel shows a spectrum extracted from a pn CalClosed full frame mode observation (black) together with the spectrum corrected for Oot events (green). In the lower panel the spectrum of the simulated Oot events over the whole FoV is plotted.

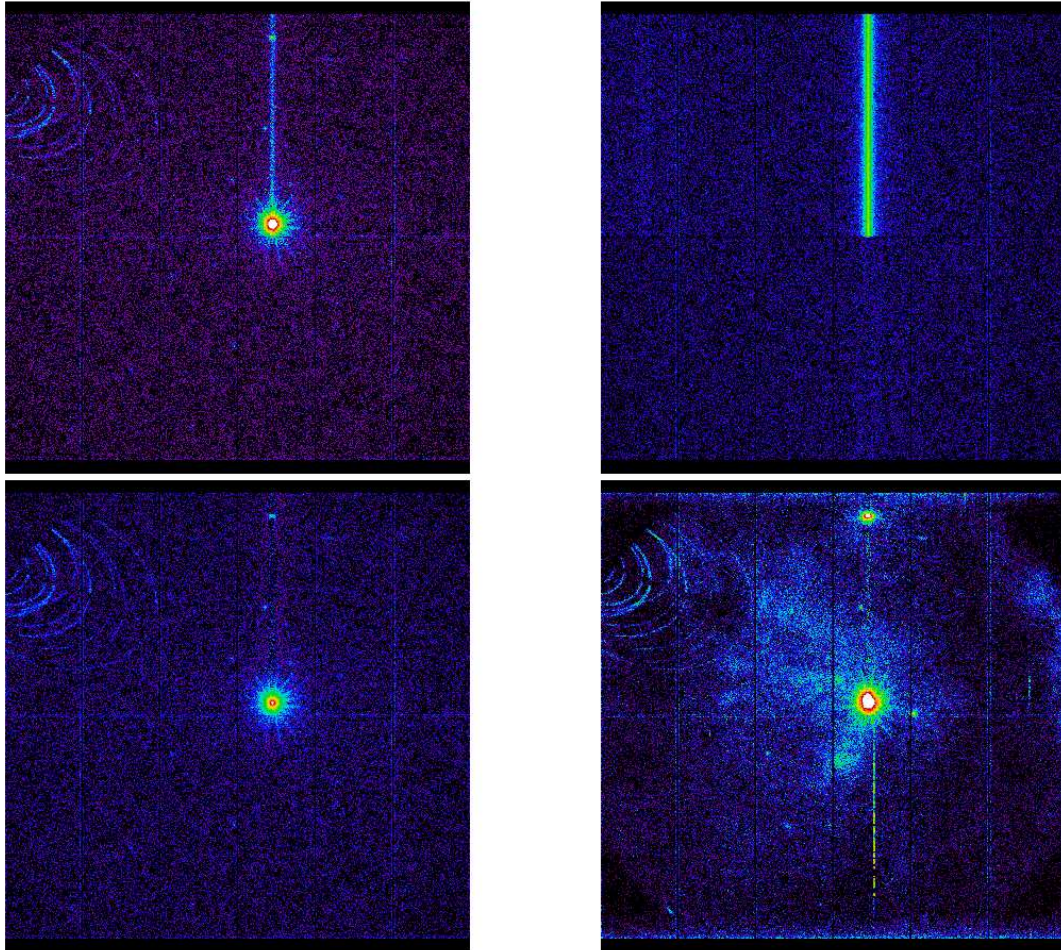


Figure 42: *Effect of OoT events on images:* The upper left panel contains a 2-10 keV band image of a pn observation of a bright source in full frame mode with the OoT-events visible as a strip running from the source toward the top of the image (in detector coordinates). The upper right panel depicts the modelled (see SAS task epchain) OoT event distribution where in the lower left panel these are subtracted from the original image. The lower right panel is cleaned for the soft 0.2-2 keV band for comparison.

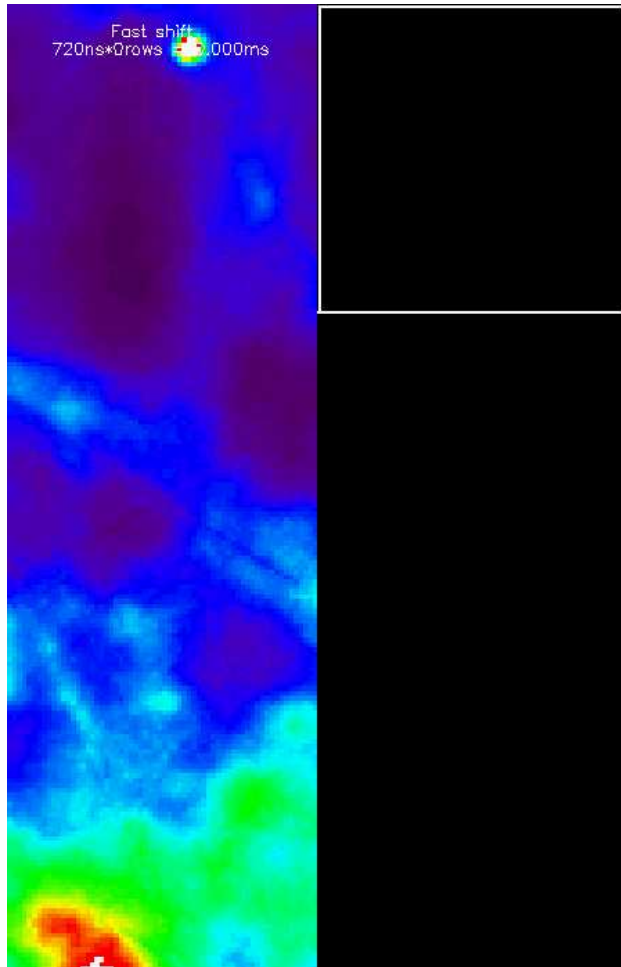


Figure 43: Illustration on how the EPIC-pn camera in Small Window mode works. For clarity the grid is 4x4 pixels. Left panel is the input sky image. Right panel shows the out-of-time events in the science window region. See text for details. Full animation can be found at: [http://xmm-tools.cosmos.esa.int/external/xmm\\_user\\_support/documentation/uhb/epicoot.html#uhb:fig:oot\\_animation](http://xmm-tools.cosmos.esa.int/external/xmm_user_support/documentation/uhb/epicoot.html#uhb:fig:oot_animation).



### 3.3.11 EPIC event grade selection

Event selection is performed on-board in order to allow transmission of useful data only (i.e., removal of empty pixels from the data stream). Also a significant number of X-ray events are expected to be split between pixels, and these must be recognised as such. The Science Analysis Subsystem (SAS) software allows these data to be reconstructed to a single energy value in an event list. Recommendations on pattern (similar to the *Chandra* or ASCA “event grade”) selections for the spatial and spectral analysis of XMM-Newton event lists are given in the document XMM-SOC-CAL-TN-0018. Users must choose carefully the data sub-set for the science of interest, and further beware that not all pattern combinations may be calibrated as well as some default sets (see Table 7. Further details about EPIC patterns are available e.g. from the descriptions of the SAS tasks emevents and epevents).

Table 7: List of EPIC event patterns

Camera	Mode	X-ray generated pattern					no X-ray <sup>1</sup>
		singles	doubles	triples	quadruples	higher	
MOS	imaging	<b>0</b>	<b>1-4</b>	<b>5-8</b>	<b>9-12</b>	13-25	26-31 <sup>2</sup> 2,3
	timing	0	1				
pn	imaging	<b>0</b>	<b>1-4</b>	5-8	9-12		> 12
	timing	<b>0</b>	<b>1-4</b>			5-12	> 12

Notes to Table 7:

Calibrated patterns are flagged by bold text font.

1) no genuine X-ray events.

2) 26-29: diagonal pattern due to Si-fluorescence or pileup of two monopixel events; 30-31: cosmic rays extended tracks.

Users should also be aware of the different methods of processing events that are present in the EPIC MOS and pn cameras. The MOS camera uses an event pattern recognition scheme and all detected events are transmitted to ground with a pattern identification already attached to them. The pn camera conversely telemeters all pixels above a certain threshold, and the X-ray event selection and processing is performed wholly on-ground, i.e., through the use of the SAS.



### 3.3.12 EPIC-specific proposal submission information

In the preparation of EPIC observing proposals, the following information should be taken into account in order to assess the technical feasibility of intended XMM-Newton observations; see § 4 for additional, more general information.

#### 3.3.12.1 EPIC spectral quality

In Figs. 44–48 we display a series of Mekal model spectra at different energies, ranging from 0.1 to 10.0 keV, with successively increasing total photon numbers (from 500 to 20,000 counts). Although these figures have been created using on-ground calibrations, they can be still used as a qualitative reference for the expected spectral quality. These show which data quality can be reached for a given total number of counts. All model spectra have been produced with *XSPEC*, faking a Mekal model spectrum and using the ready-made response matrices for MOS1 and pn for the thin filter and full window mode. Photon statistics was allowed and the faked spectra were rebinned in a way such that the 5 sigma significance criterion is fulfilled. For the 2.0 keV model, the MOS1 and pn cameras are compared directly (Figs. 46 and 47), while for all other energies only the MOS1 model spectra are displayed.

**Note:** These simulated spectra have been produced with a particular set of response matrices for MOS1 and pn. Users are strongly recommended to perform simulations of the expected spectrum, using the most updated calibration files. Fig. 44 to 48 provide only a guideline of the expected overall spectral quality and *should not be used for any quantitative estimates*.

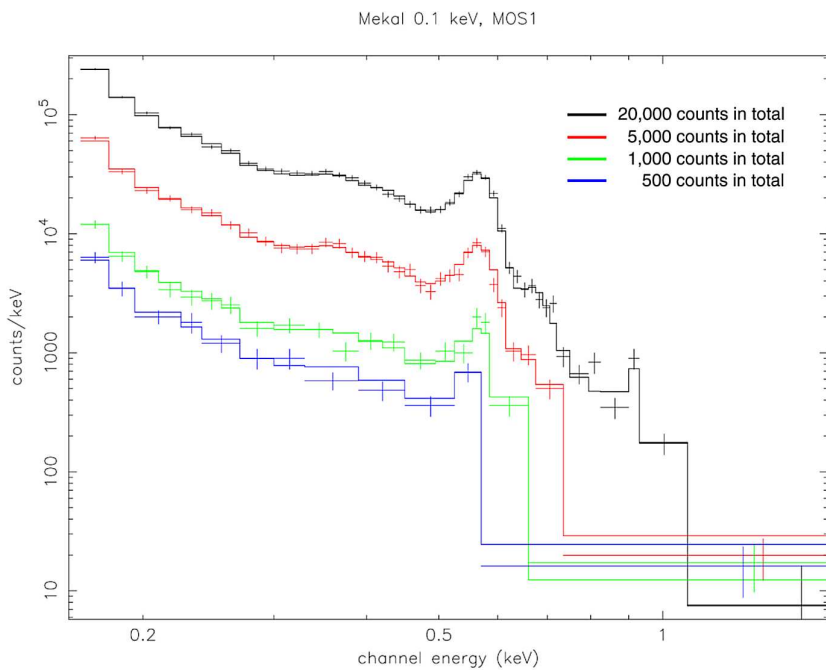


Figure 44: Series of EPIC MOS1 model spectra of a Mekal thermal plasma with a temperature of 0.1 keV. From the bottom to the top, the total number of counts in the XMM-Newton passband (0.15–12 keV) increases from 500 to 20,000.

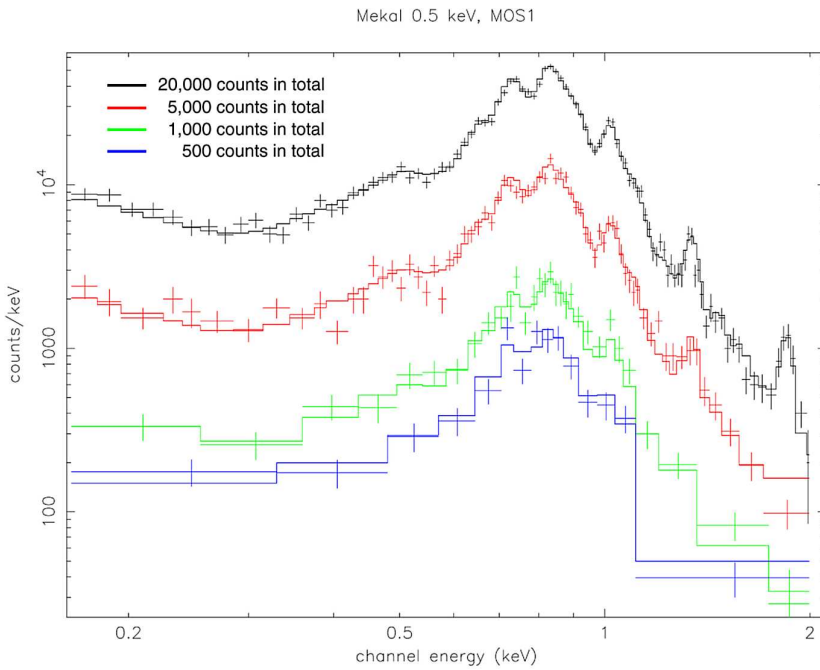


Figure 45: Series of EPIC MOS1 model spectra of a Mekal thermal plasma with a temperature of 0.5 keV. From the bottom to the top, the total number of counts in the XMM-Newton passband (0.15–12 keV) increases from 500 to 20,000.

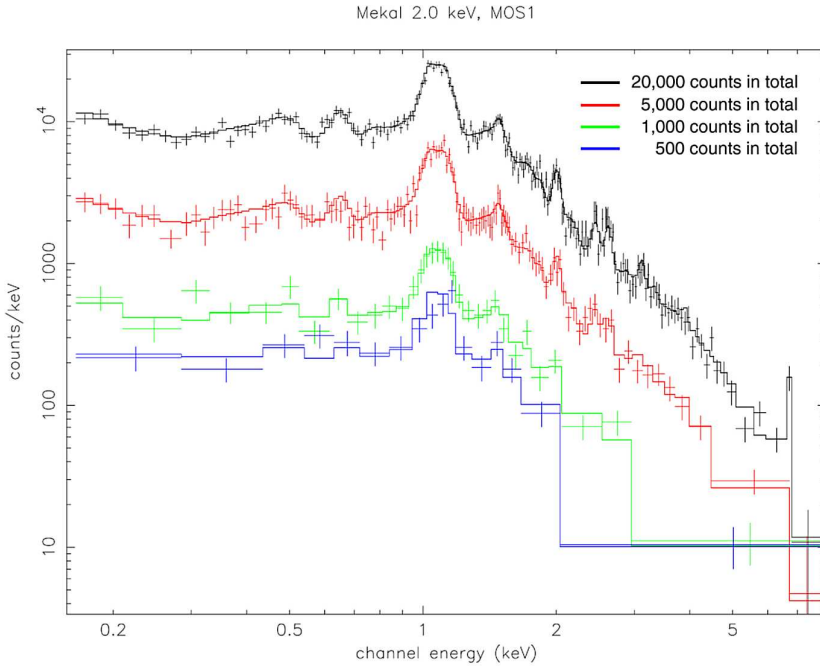


Figure 46: Series of EPIC MOS1 model spectra of a Mekal thermal plasma with a temperature of 2.0 keV. From the bottom to the top, the total number of counts in the XMM-Newton passband (0.15–12 keV) increases from 500 to 20,000.

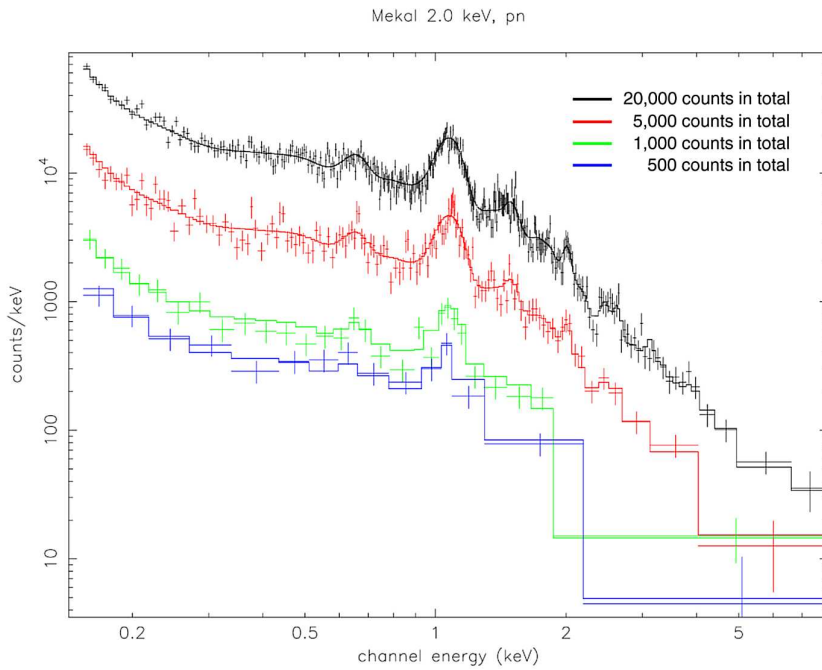


Figure 47: Series of EPIC pn model spectra of a Mekal thermal plasma with a temperature of 2.0 keV. From the bottom to the top, the total number of counts in the XMM-Newton passband (0.15–12 keV) increases from 500 to 20,000.

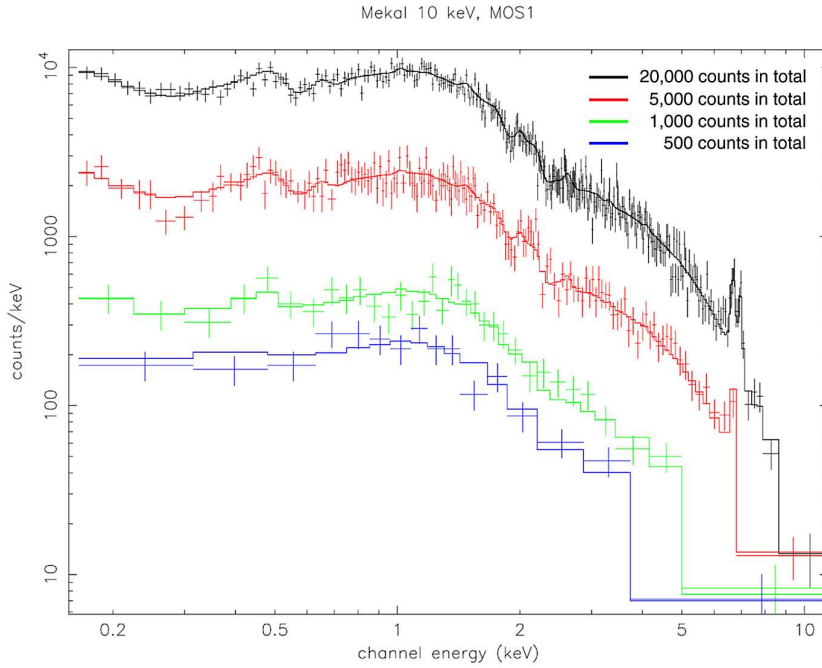


Figure 48: Series of EPIC MOS1 model spectra of a Mekal thermal plasma with a temperature of 10.0 keV. From the bottom to the top, the total number of counts in the XMM-Newton passband (0.15–12 keV) increases from 500 to 20,000.



### 3.3.12.2 EPIC flux to count rate conversion

The following set of figures (Figs. 49–75) provides EPIC flux to count rate conversion factors for a variety of standard spectral models, for each camera type (pn and MOS), with the thin, medium and thick optical blocking filters. Families of curves for various values of the foreground absorbing column density,  $N_H$ , are plotted. Both the (unabsorbed) fluxes (i.e., after taking into account the attenuation by the foreground gas) and the count rates are calculated for the 0.2–12 keV band.

Note that these plots are based on the most recent canned response matrices and effective area files using SAS 17.0.

The order of the plots is:

1. Power law models
2. Thermal plasma (mekal) models with solar metallicities
3. Black body models

For each model type, three pn camera plots are shown first (thin, medium and thick filter, in that order), then six MOS plots.

**Note:** Plots in the previous and in this section are presented only as a quick-look reference. Users are strongly advised to estimate the expected count rates and spectra for their sources through proper simulations via, *e.g.* the command `fakeit` in XSPEC. The most updated EPIC response matrices should be used for this purpose.

### 3.3.12.3 Count rate conversion from other X-ray satellite missions

For the conversion of count rates from other X-ray satellites to count rates expected for the different XMM-Newton detectors, we recommend the use of the *PIMMS* software from NASA’s HEASARC (at the URL <http://heasarc.gsfc.nasa.gov/Tools/w3pimms.html>). HEASARC updates XMM-Newton response matrices in *PIMMS* regularly before each AO, using the publicly available SAS.

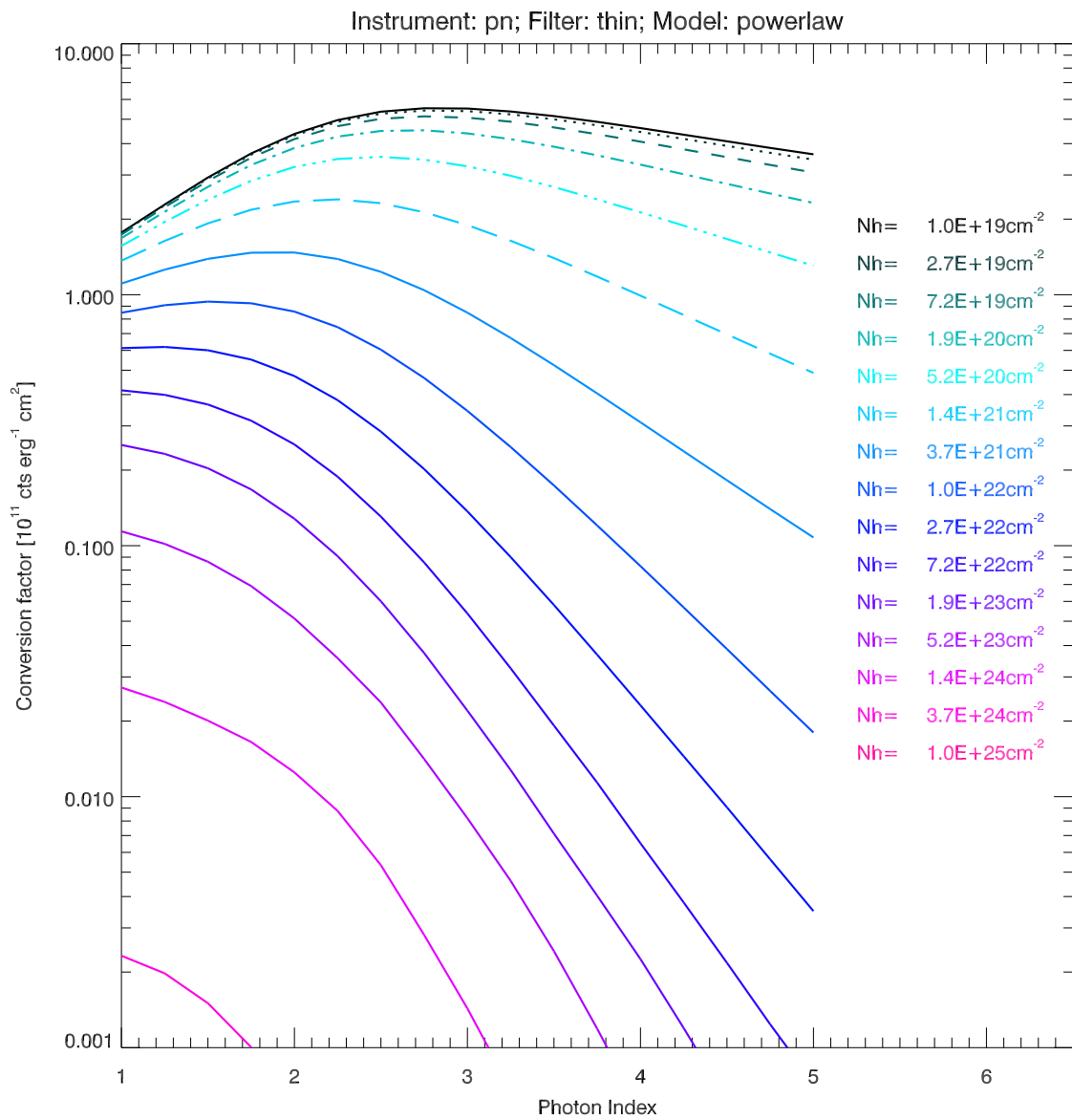


Figure 49: EPIC flux to count rate conversion factors (in units of  $10^{11}$  counts  $\text{erg}^{-1} \text{cm}^2$ ) for pn camera for various power law spectra and for different values of the absorbing column density,  $N_H$  (thin filter).

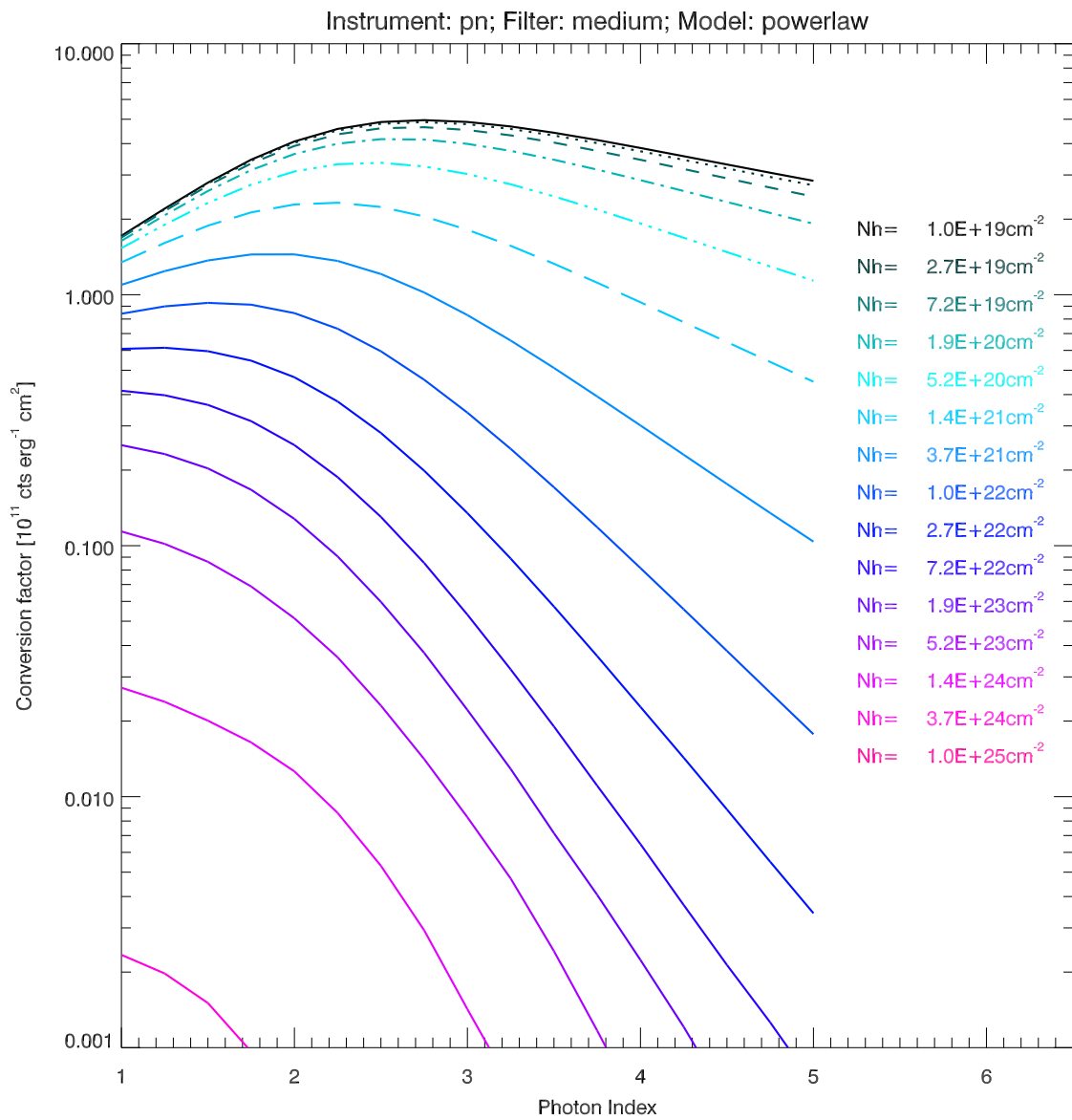


Figure 50: EPIC flux to count rate conversion factors (in units of  $10^{11}$  counts  $\text{erg}^{-1}$   $\text{cm}^2$ ) for pn camera for various power law spectra and for different values of the absorbing column density,  $N_H$  (medium filter).

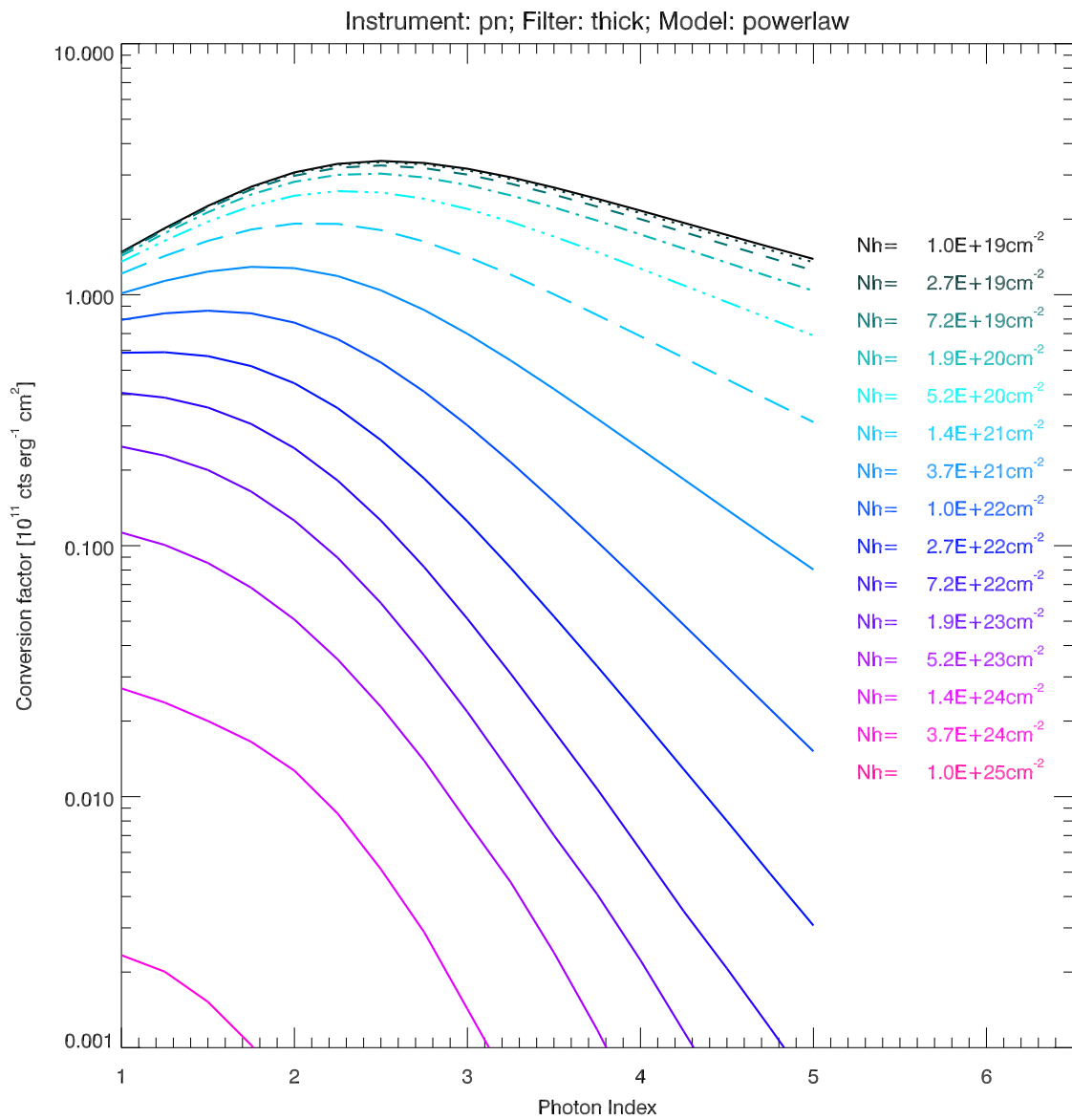


Figure 51: EPIC flux to count rate conversion factors (in units of  $10^{11}$  counts  $\text{erg}^{-1} \text{cm}^2$ ) for pn camera for various power law spectra and for different values of the absorbing column density,  $N_H$  (thick filter).

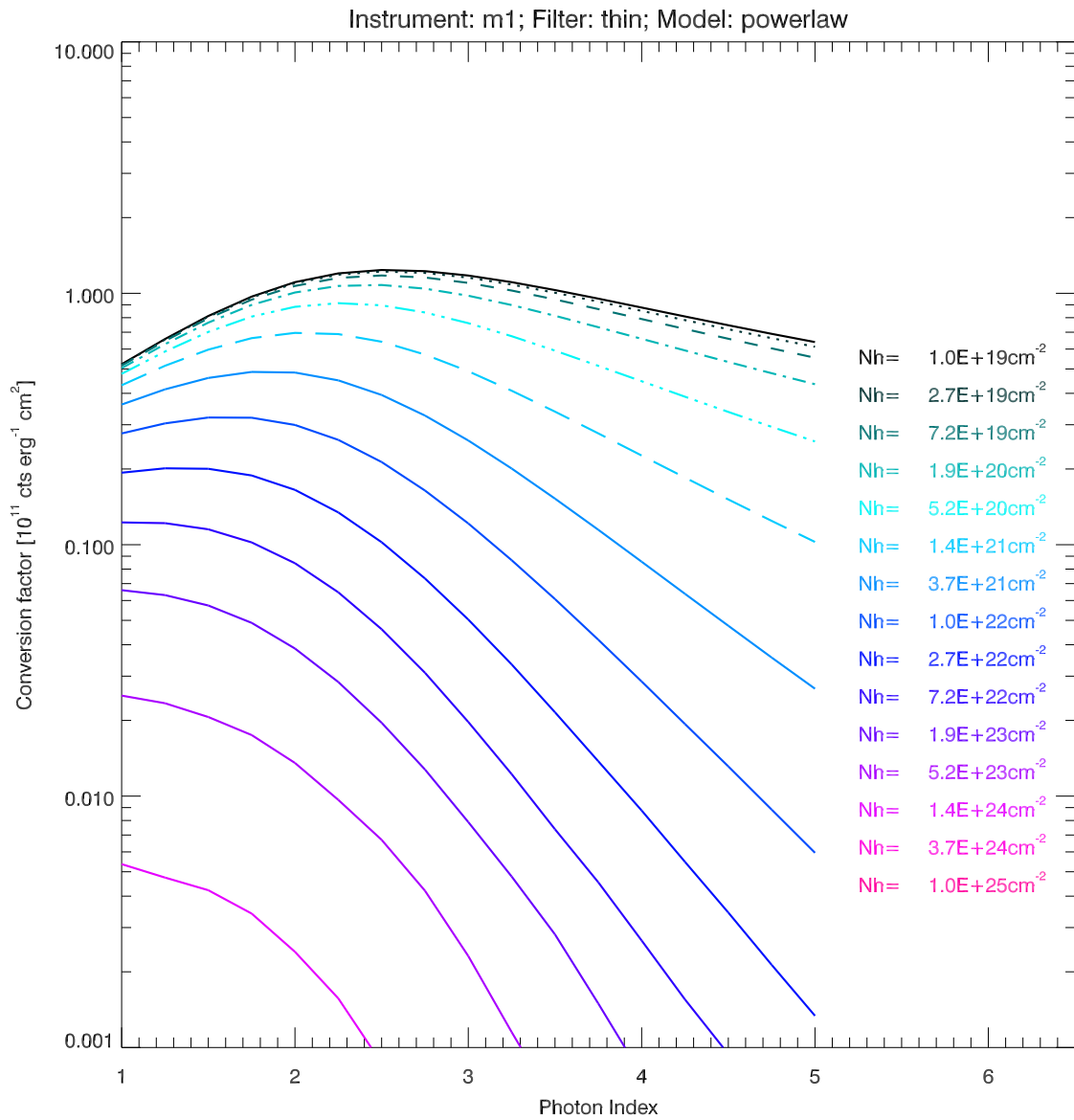


Figure 52: EPIC flux to count rate conversion factors (in units of  $10^{11}$  counts  $\text{erg}^{-1}$   $\text{cm}^2$ ) for MOS1 camera for various power law spectra and for different values of the absorbing column density,  $N_H$  (thin filter).



**esa**

European space agency  
agence spatiale européenne

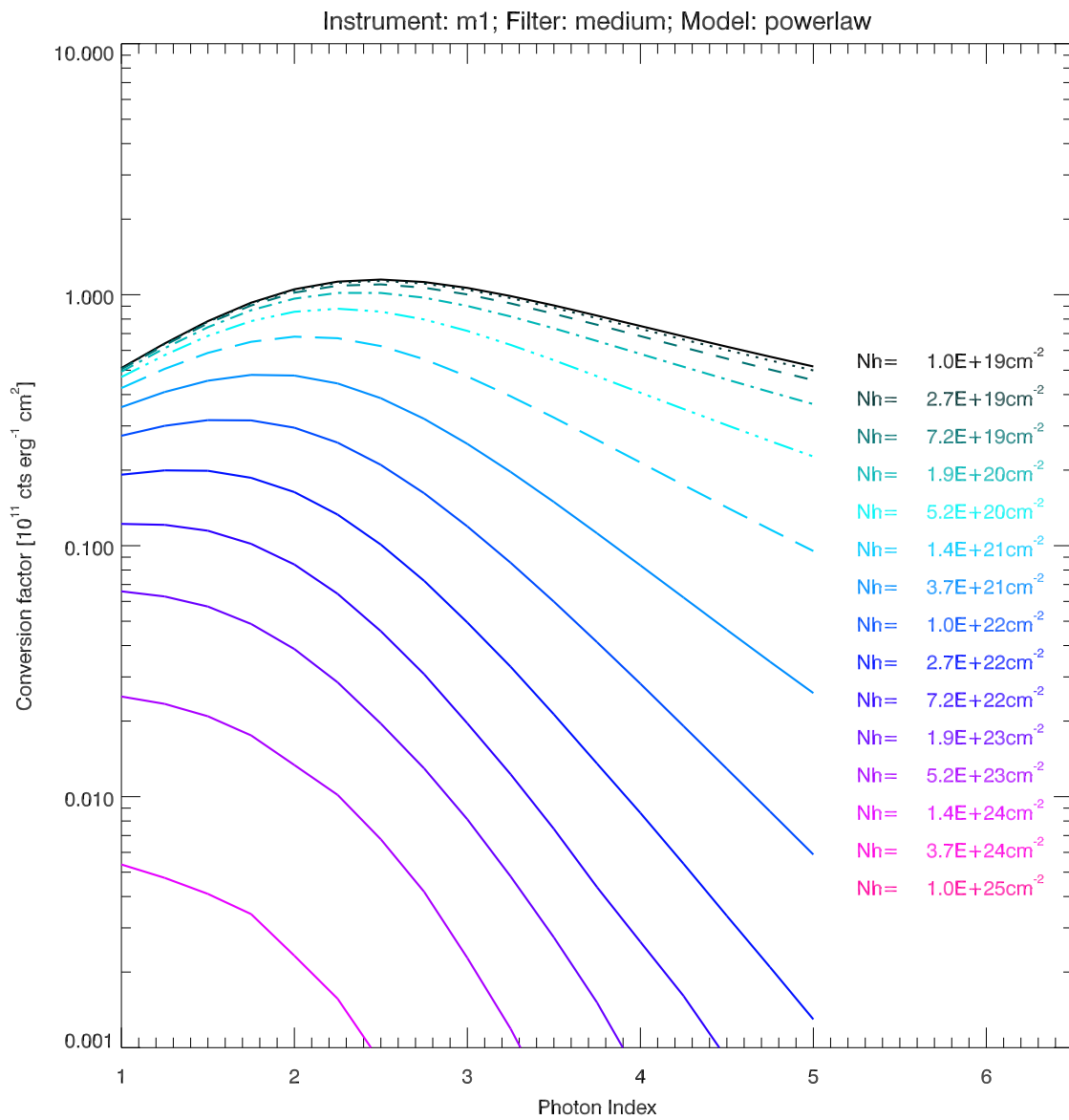


Figure 53: EPIC flux to count rate conversion factors (in units of  $10^{11}$  counts  $\text{erg}^{-1}$   $\text{cm}^2$ ) for MOS1 camera for various power law spectra and for different values of the absorbing column density,  $N_H$  (medium filter).

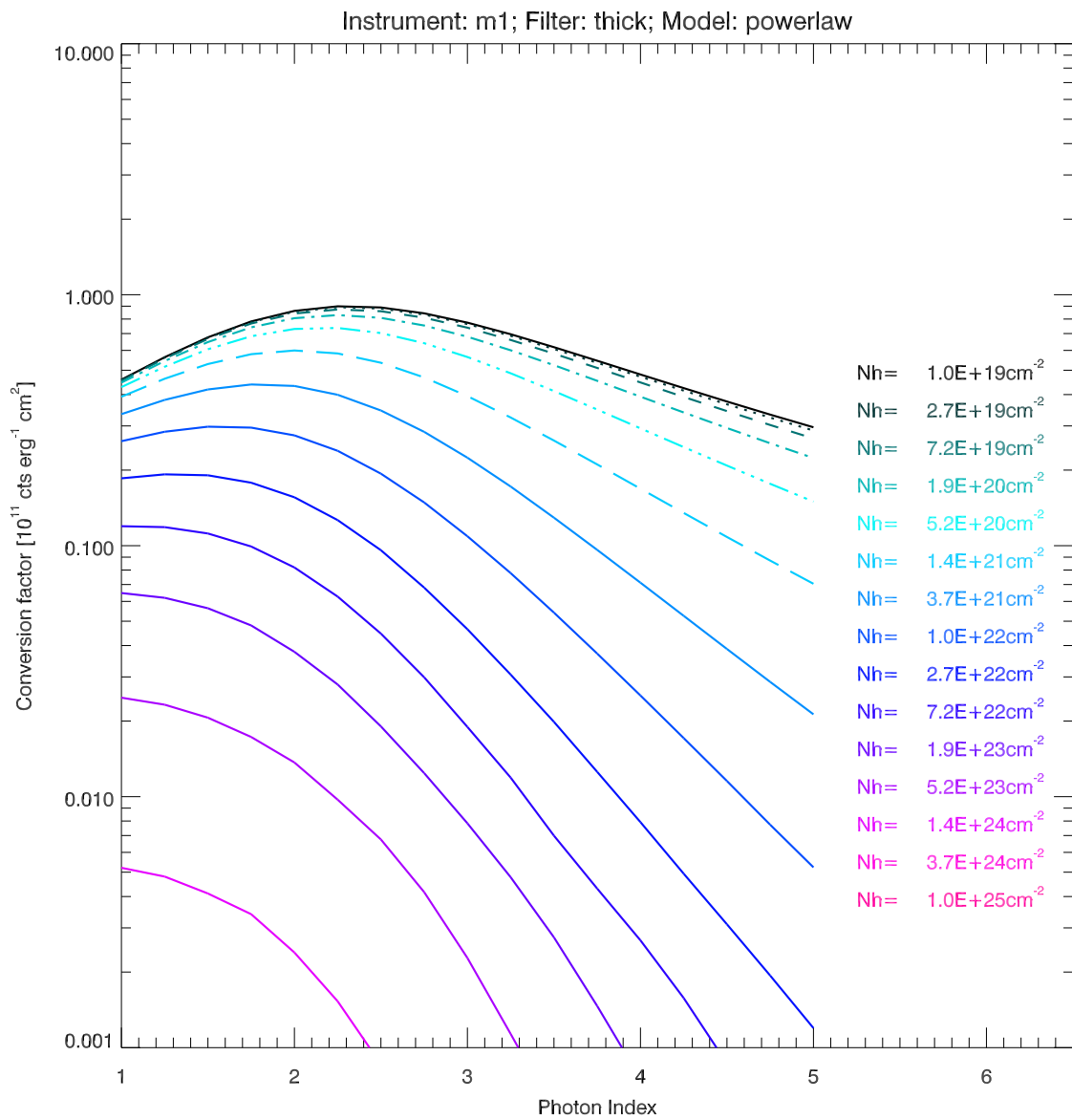


Figure 54: EPIC flux to count rate conversion factors (in units of  $10^{11}$  counts  $\text{erg}^{-1}$   $\text{cm}^2$ ) for MOS1 camera for various power law spectra and for different values of the absorbing column density,  $N_H$  (thick filter).

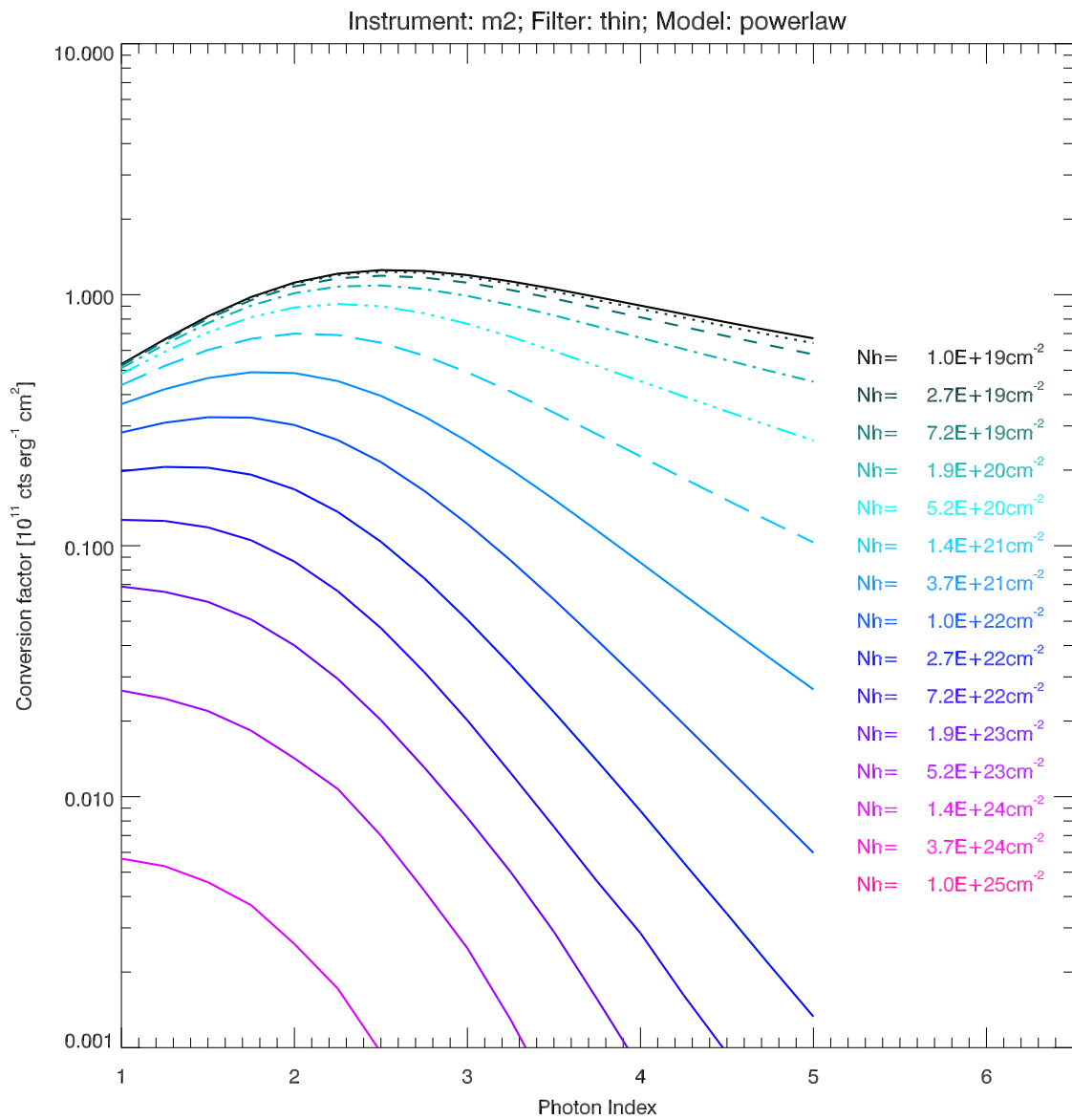


Figure 55: EPIC flux to count rate conversion factors (in units of  $10^{11}$  counts  $\text{erg}^{-1}$   $\text{cm}^2$ ) for MOS2 camera for various power law spectra and for different values of the absorbing column density,  $N_H$  (thin filter).

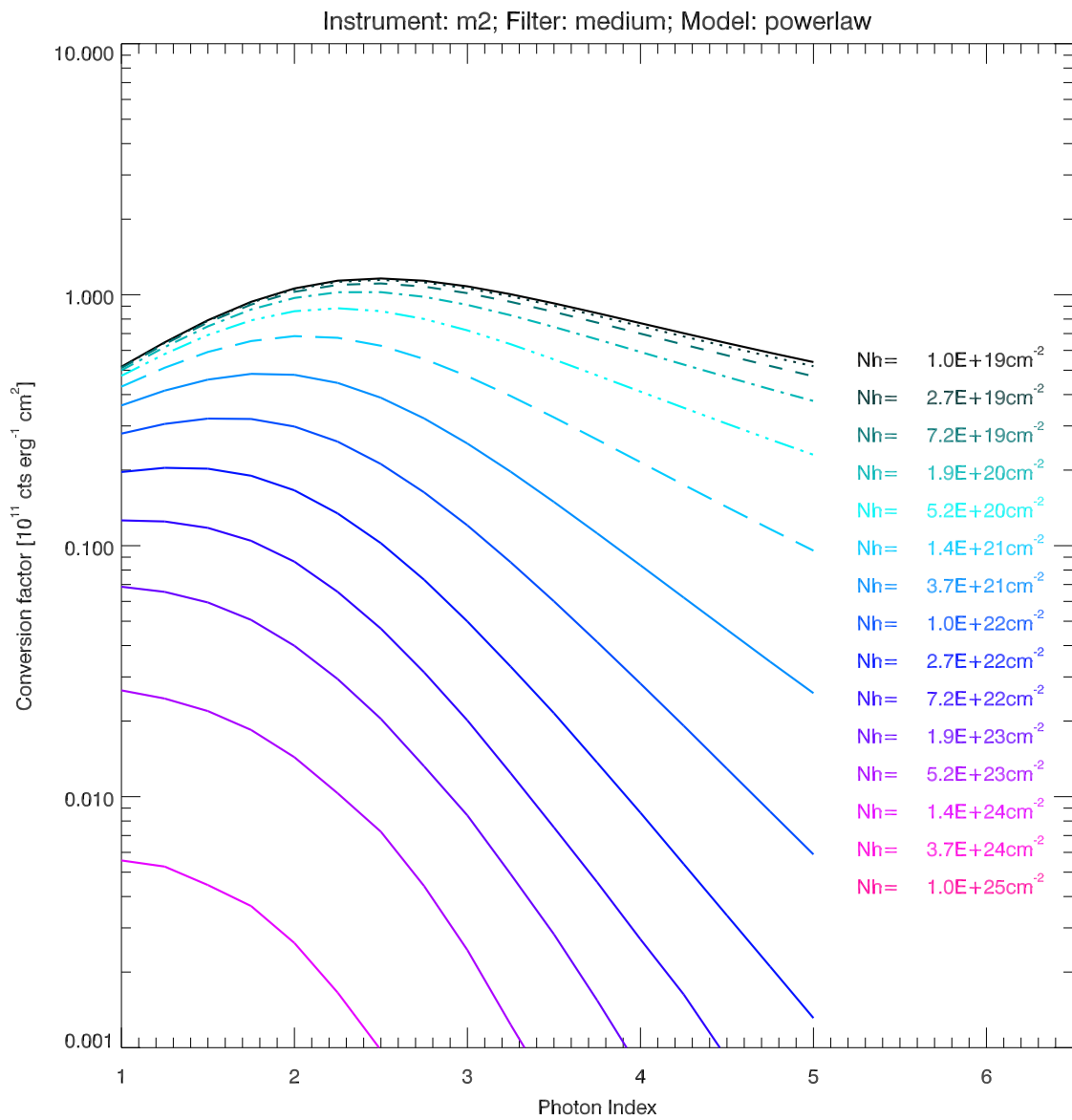


Figure 56: EPIC flux to count rate conversion factors (in units of  $10^{11}$  counts  $\text{erg}^{-1}$   $\text{cm}^2$ ) for MOS2 camera for various power law spectra and for different values of the absorbing column density,  $N_H$  (medium filter).

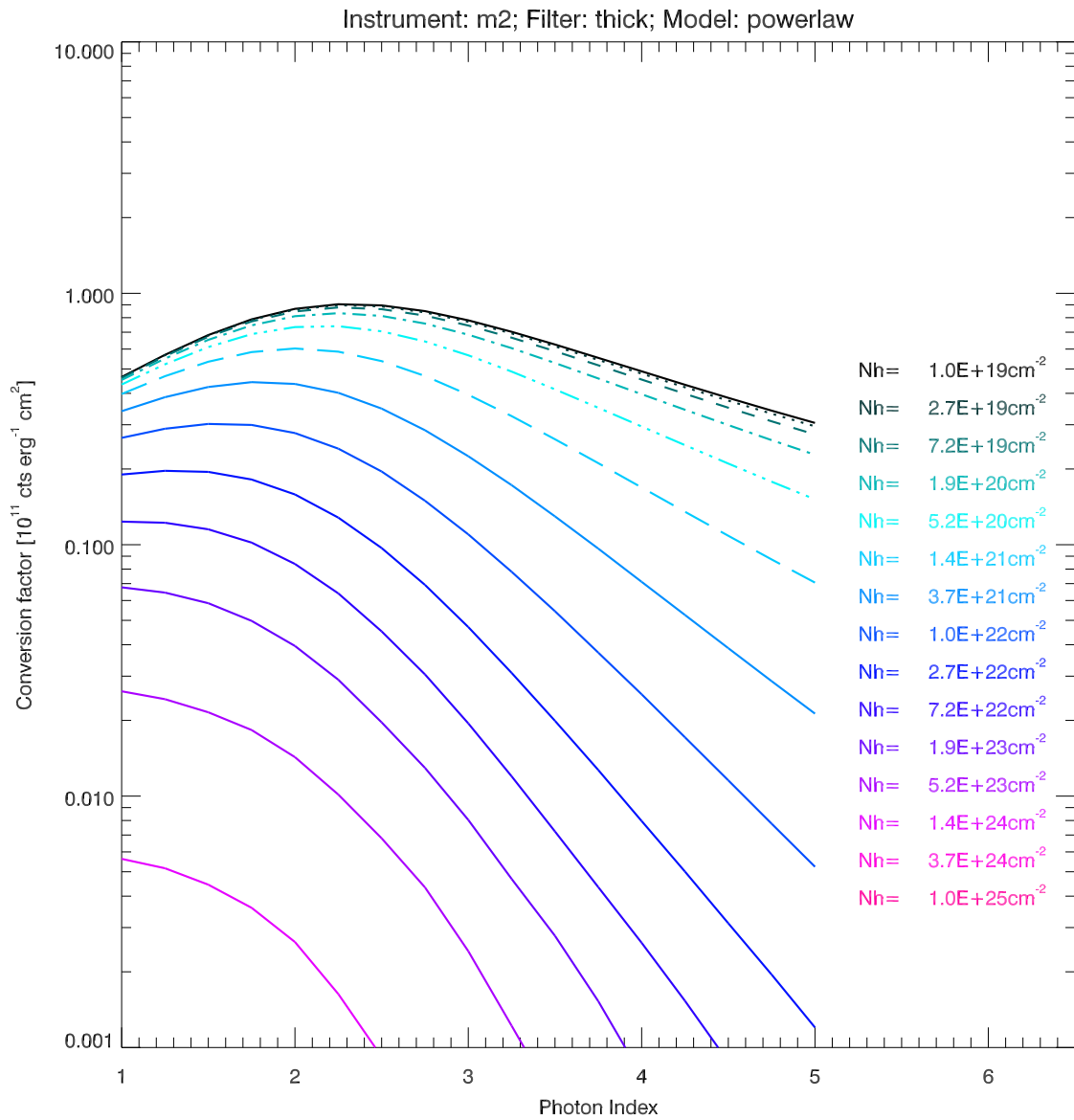


Figure 57: EPIC flux to count rate conversion factors (in units of  $10^{11}$  counts  $\text{erg}^{-1}$   $\text{cm}^2$ ) for MOS2 camera for various power law spectra and for different values of the absorbing column density,  $N_H$  (thick filter).

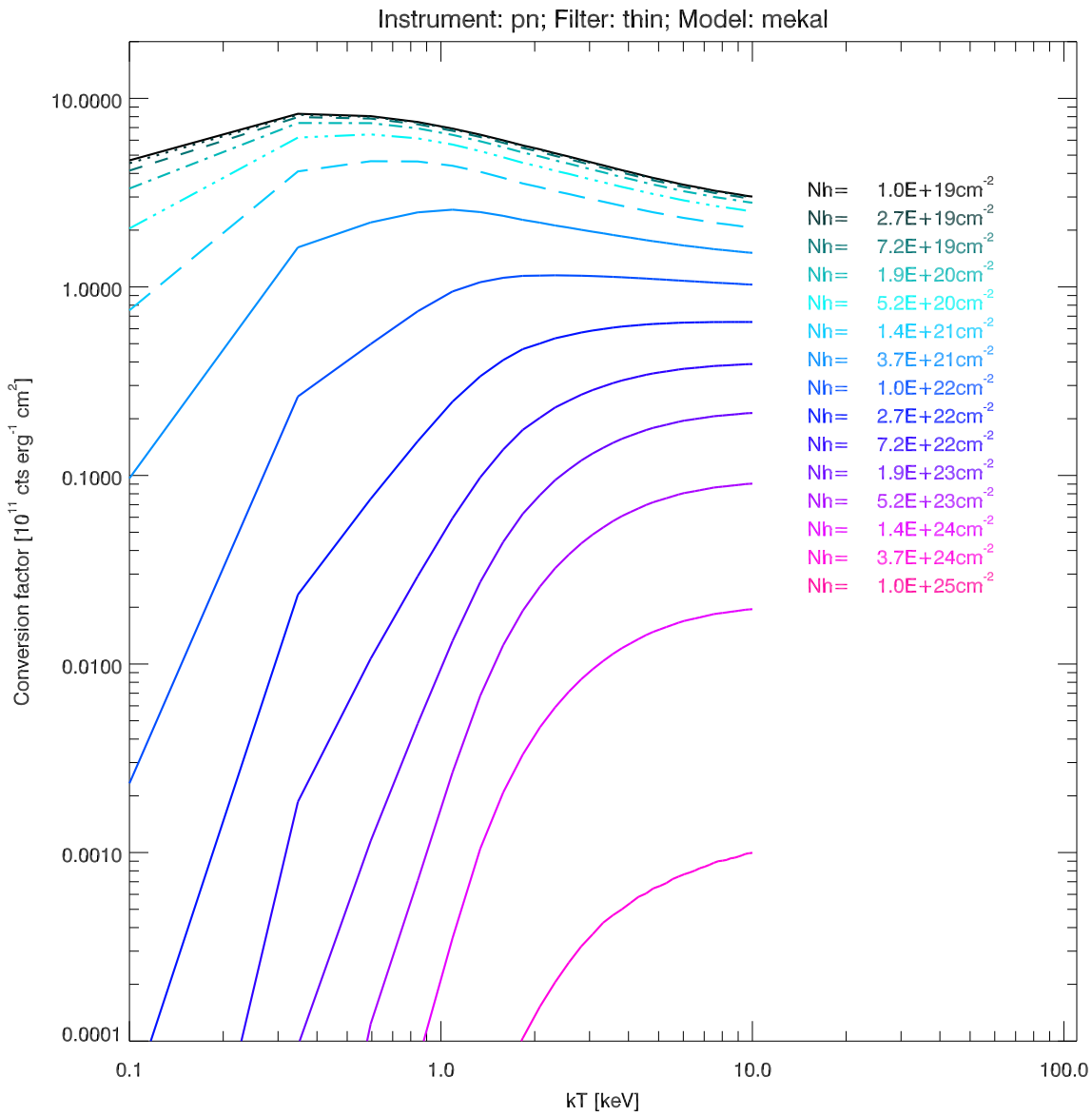


Figure 58: EPIC flux to count rate conversion factors (in units of  $10^{11}$  counts  $\text{erg}^{-1}$   $\text{cm}^2$ ) for pn camera for various mekal spectra and for different values of the absorbing column density,  $N_H$  (thin filter).

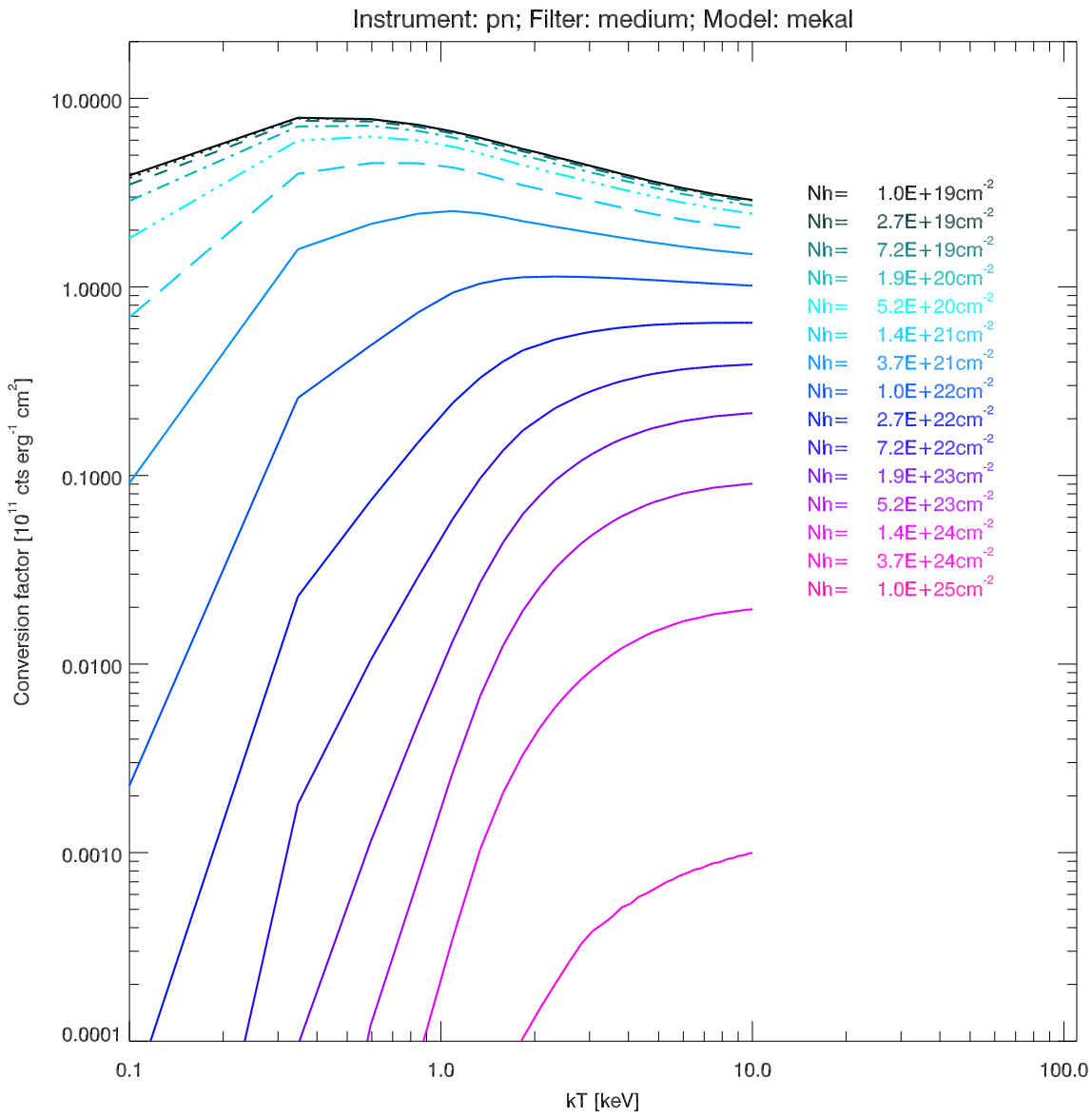


Figure 59: EPIC flux to count rate conversion factors (in units of  $10^{11}$  counts  $\text{erg}^{-1}$   $\text{cm}^2$ ) for pn camera for various mekal spectra and for different values of the absorbing column density,  $N_H$  (medium filter).

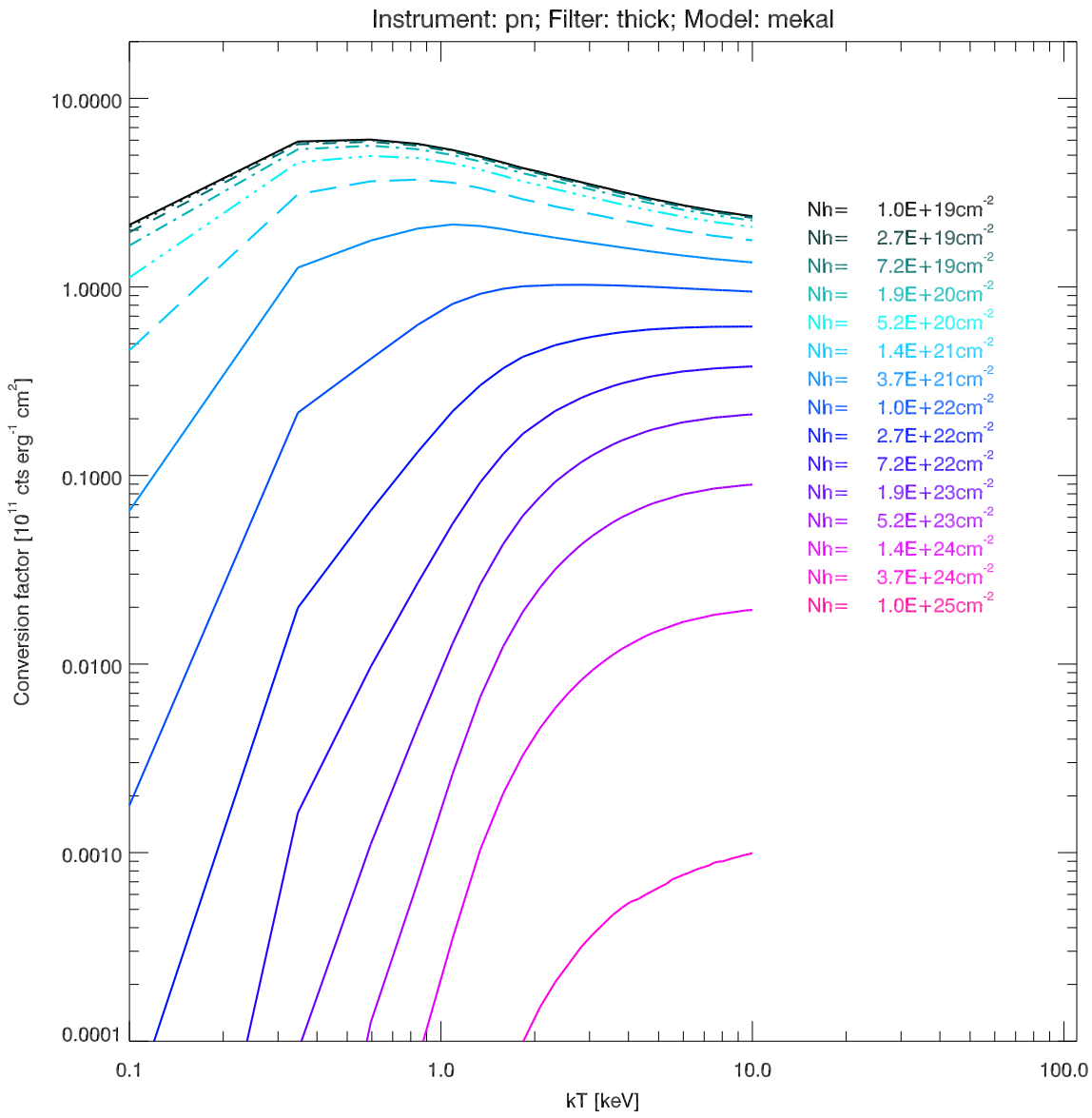


Figure 60: EPIC flux to count rate conversion factors (in units of  $10^{11}$  counts  $\text{erg}^{-1}$   $\text{cm}^2$ ) for pn camera for various mekal spectra and for different values of the absorbing column density,  $N_H$  (thick filter).

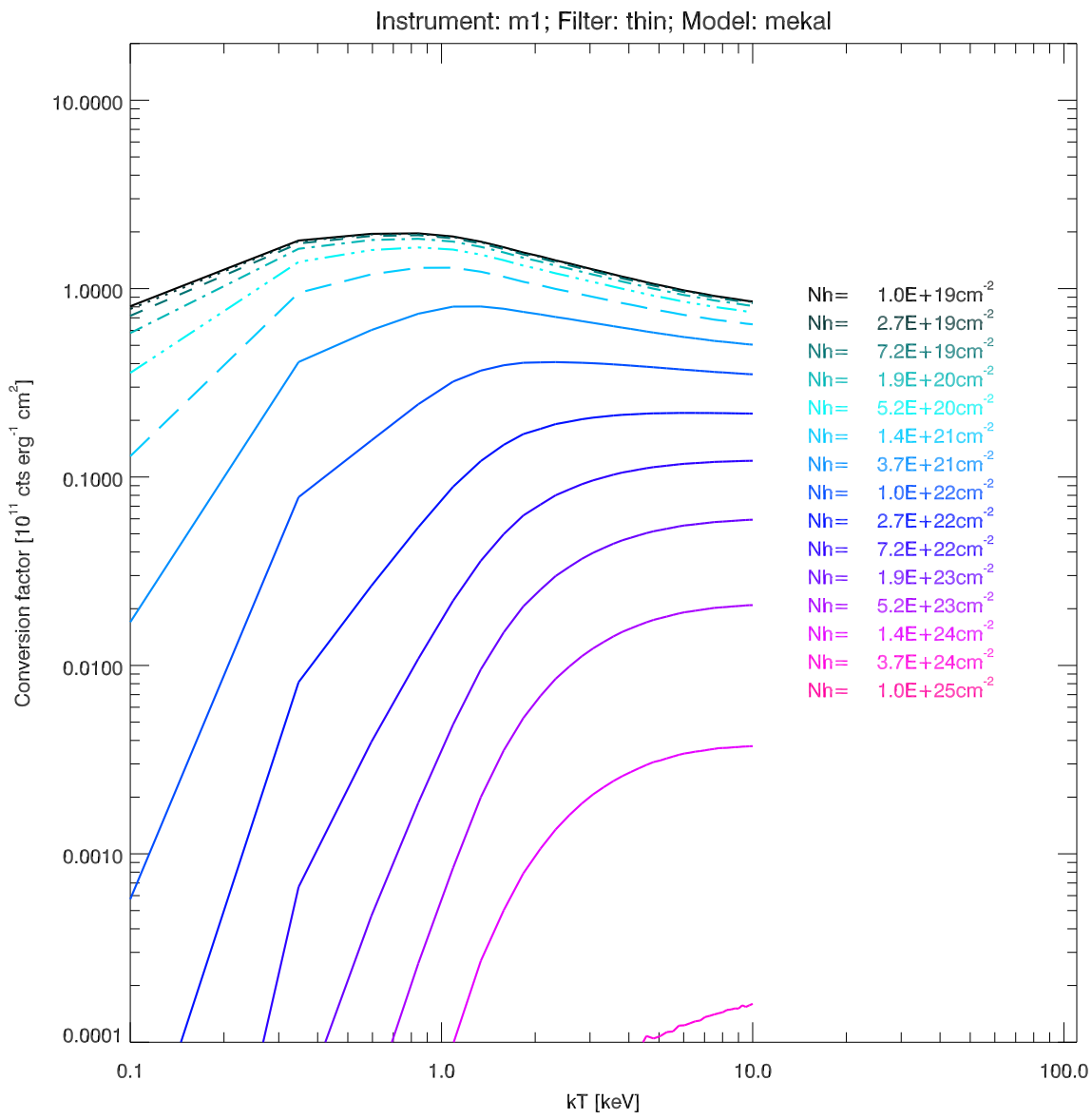


Figure 61: EPIC flux to count rate conversion factors (in units of  $10^{11}$  counts  $\text{erg}^{-1}$   $\text{cm}^2$ ) for MOS1 camera for various mekal spectra and for different values of the absorbing column density,  $N_H$  (thin filter).

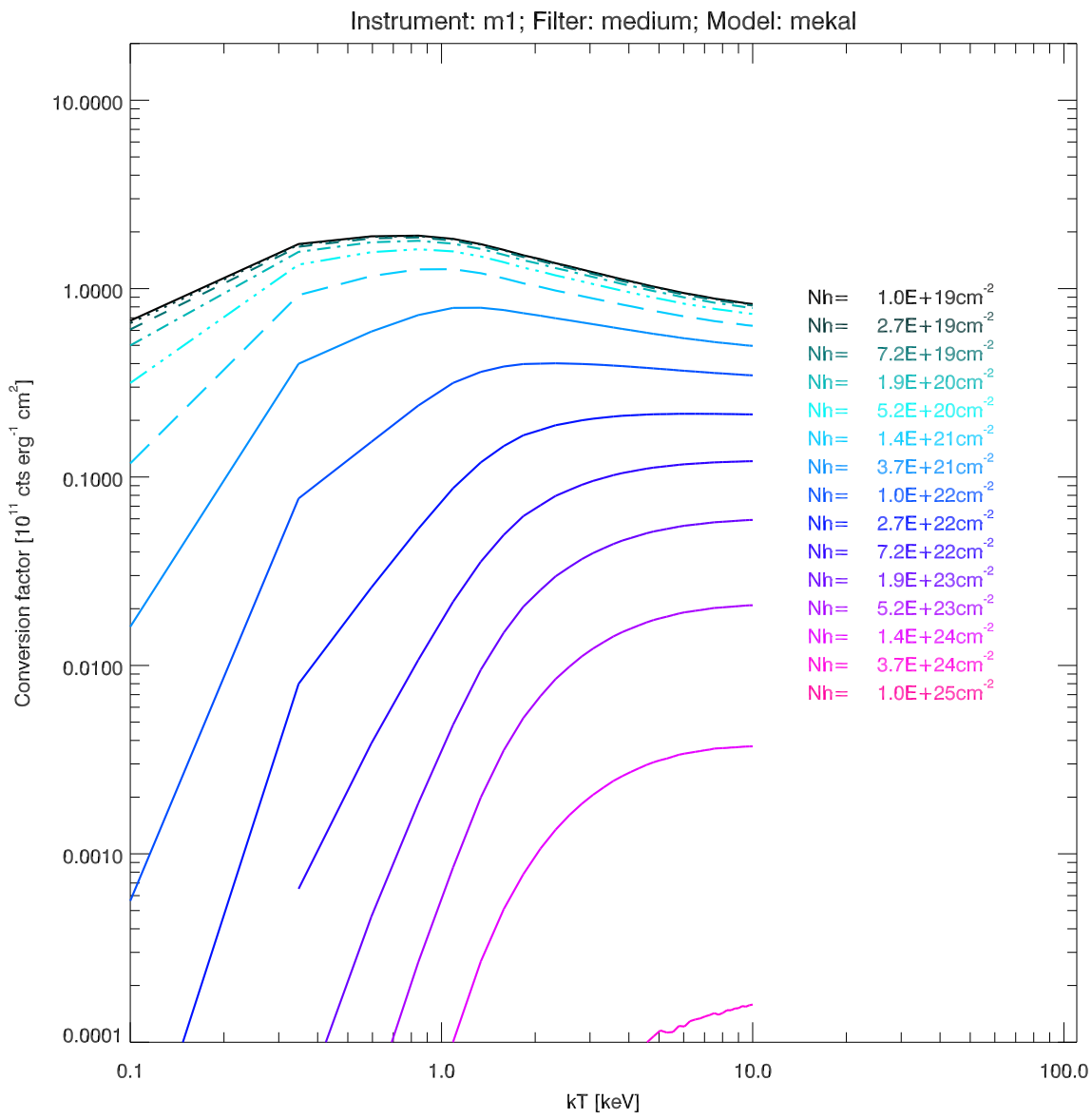


Figure 62: EPIC flux to count rate conversion factors (in units of  $10^{11}$  counts  $\text{erg}^{-1}$   $\text{cm}^{-2}$ ) for MOS1 camera for various mekal spectra and for different values of the absorbing column density,  $N_H$  (medium filter).

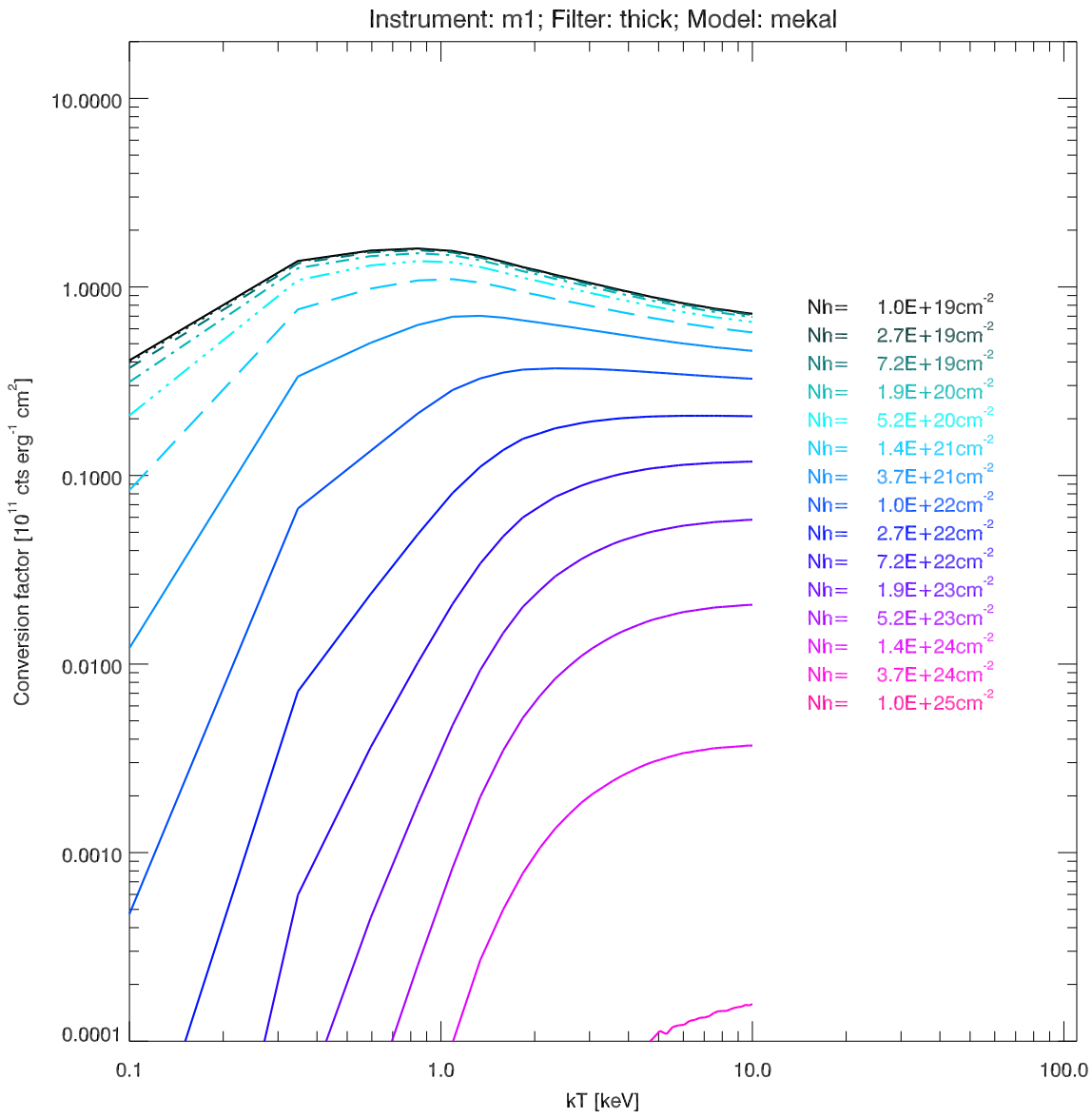


Figure 63: EPIC flux to count rate conversion factors (in units of  $10^{11}$  counts  $\text{erg}^{-1}$   $\text{cm}^2$ ) for MOS1 camera for various mekal spectra and for different values of the absorbing column density,  $N_H$  (thick filter).

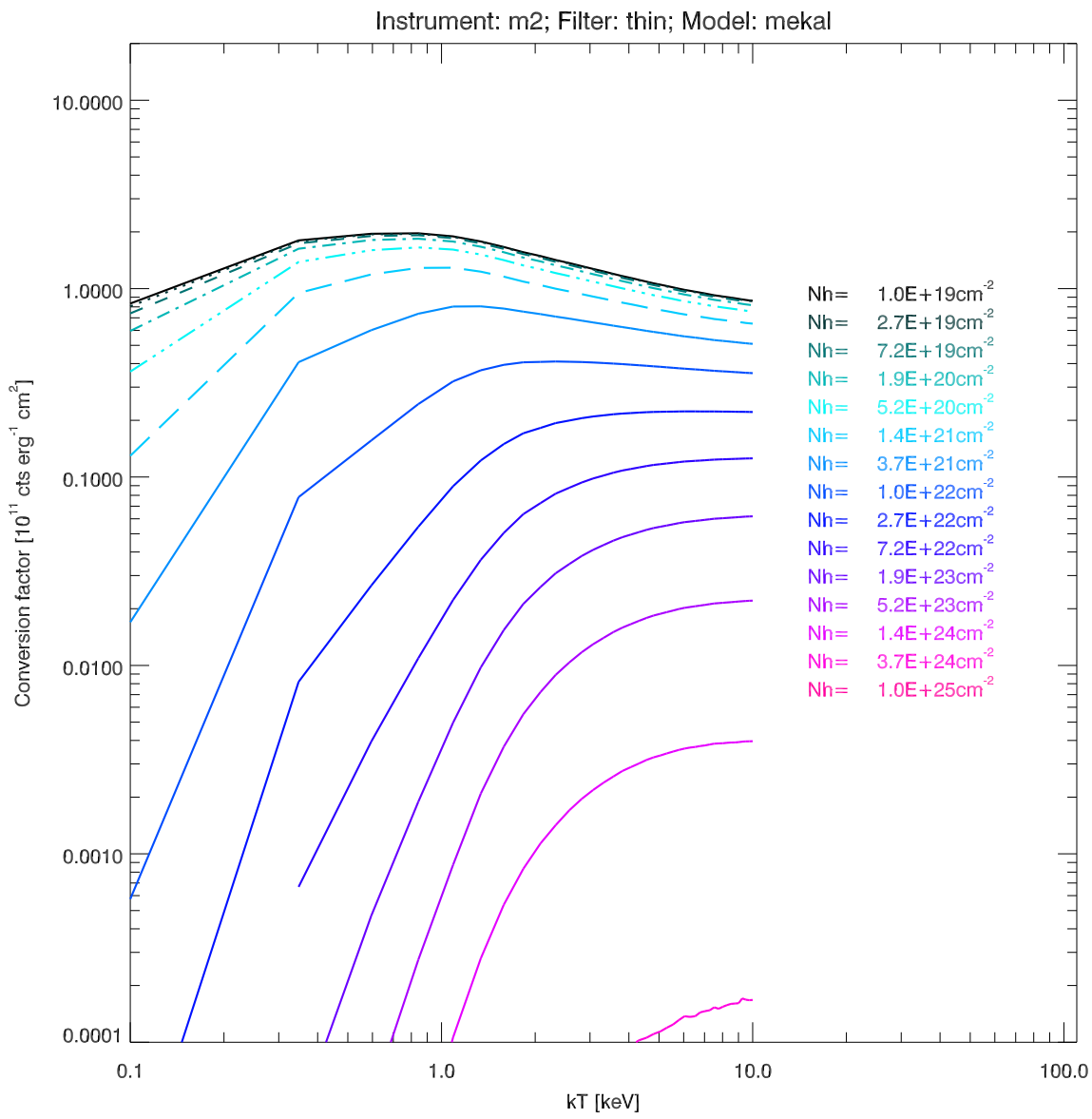


Figure 64: EPIC flux to count rate conversion factors (in units of  $10^{11}$  counts  $\text{erg}^{-1}$   $\text{cm}^2$ ) for MOS2 camera for various mekal spectra and for different values of the absorbing column density,  $N_H$  (thin filter).

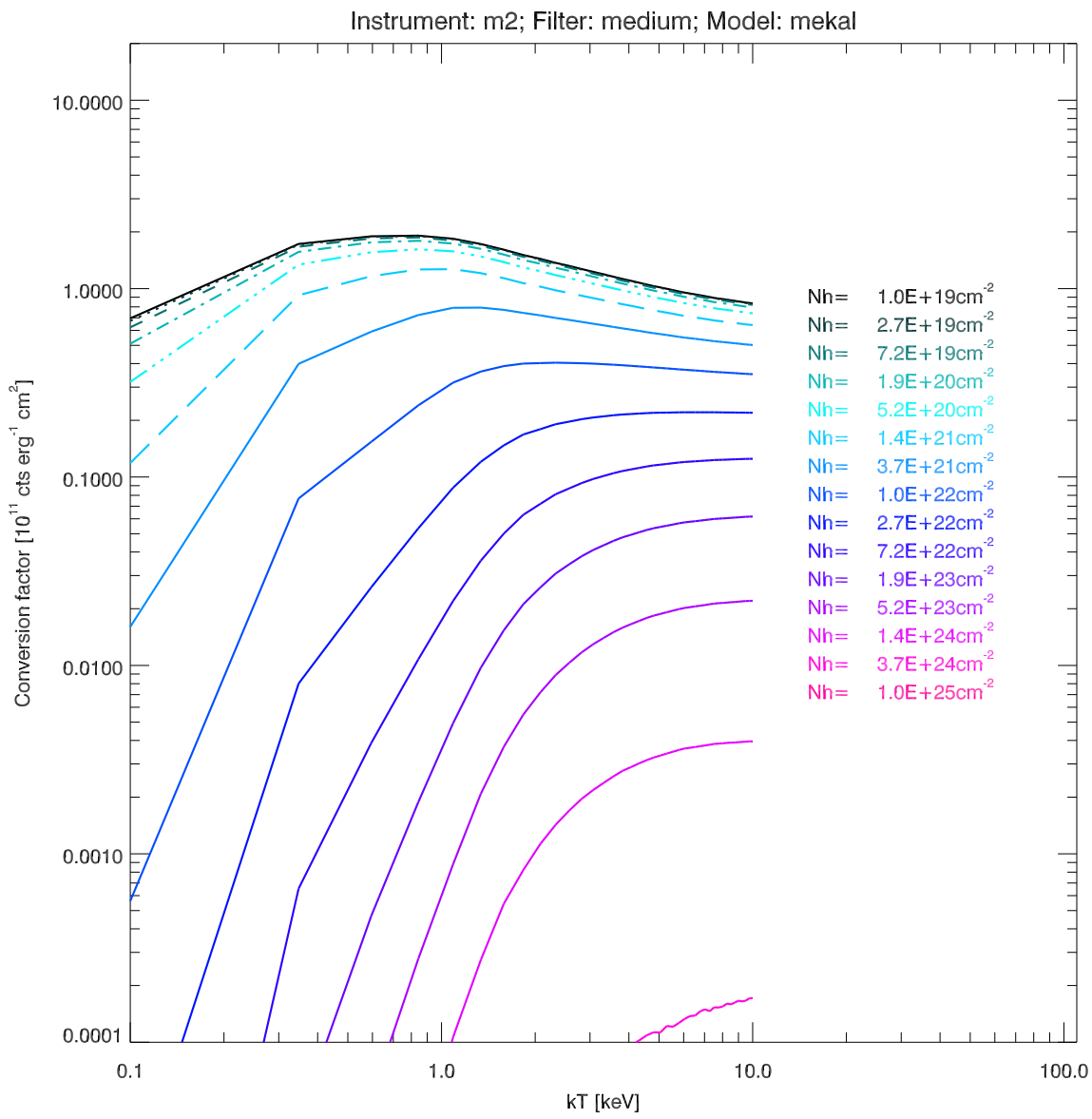


Figure 65: EPIC flux to count rate conversion factors (in units of  $10^{11}$  counts  $\text{erg}^{-1}$   $\text{cm}^{-2}$ ) for MOS2 camera for various mekal spectra and for different values of the absorbing column density,  $N_H$  (medium filter).

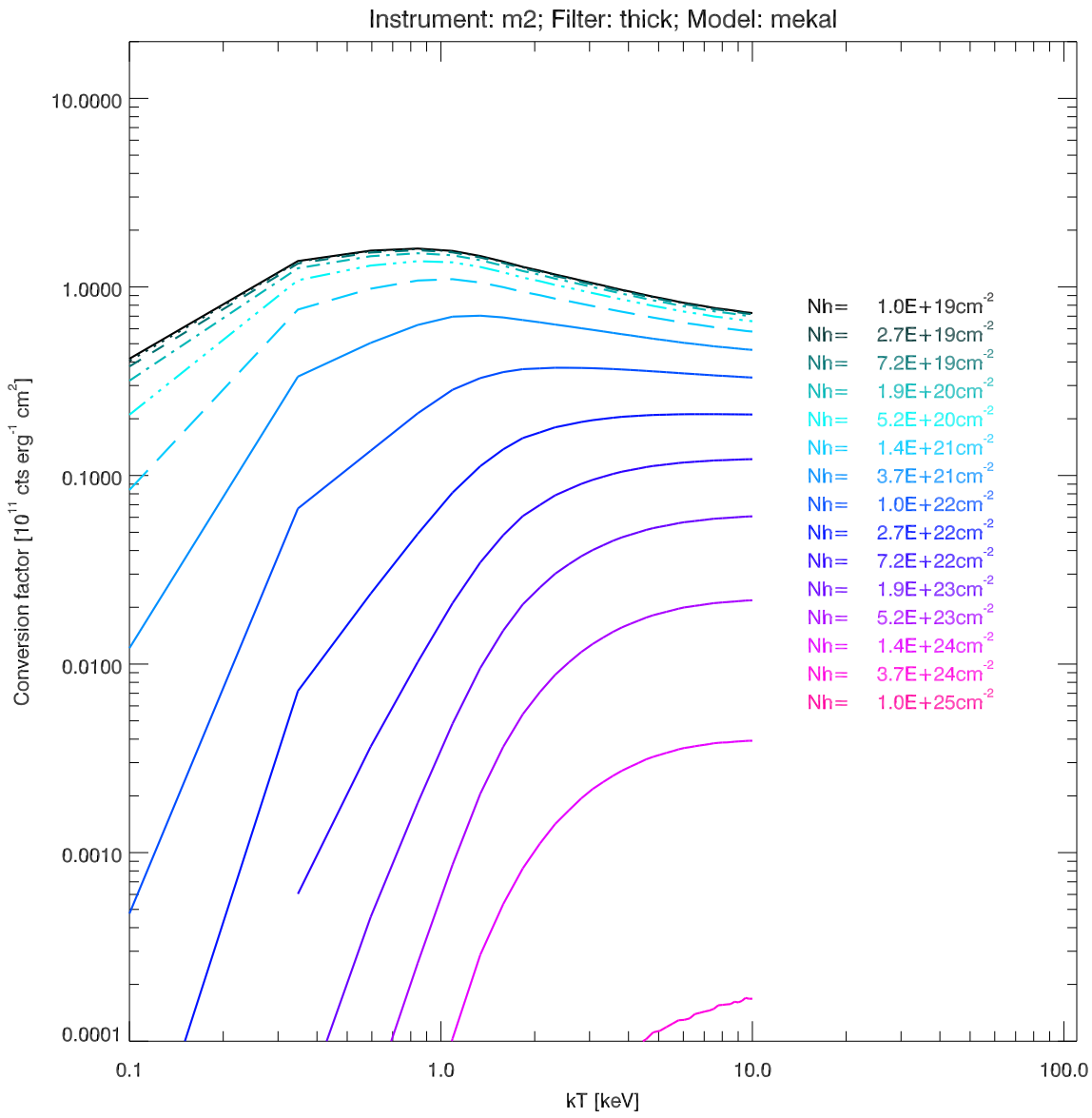


Figure 66: EPIC flux to count rate conversion factors (in units of  $10^{11}$  counts  $\text{erg}^{-1}$   $\text{cm}^2$ ) for MOS2 camera for various mekal spectra and for different values of the absorbing column density,  $N_H$  (thick filter).

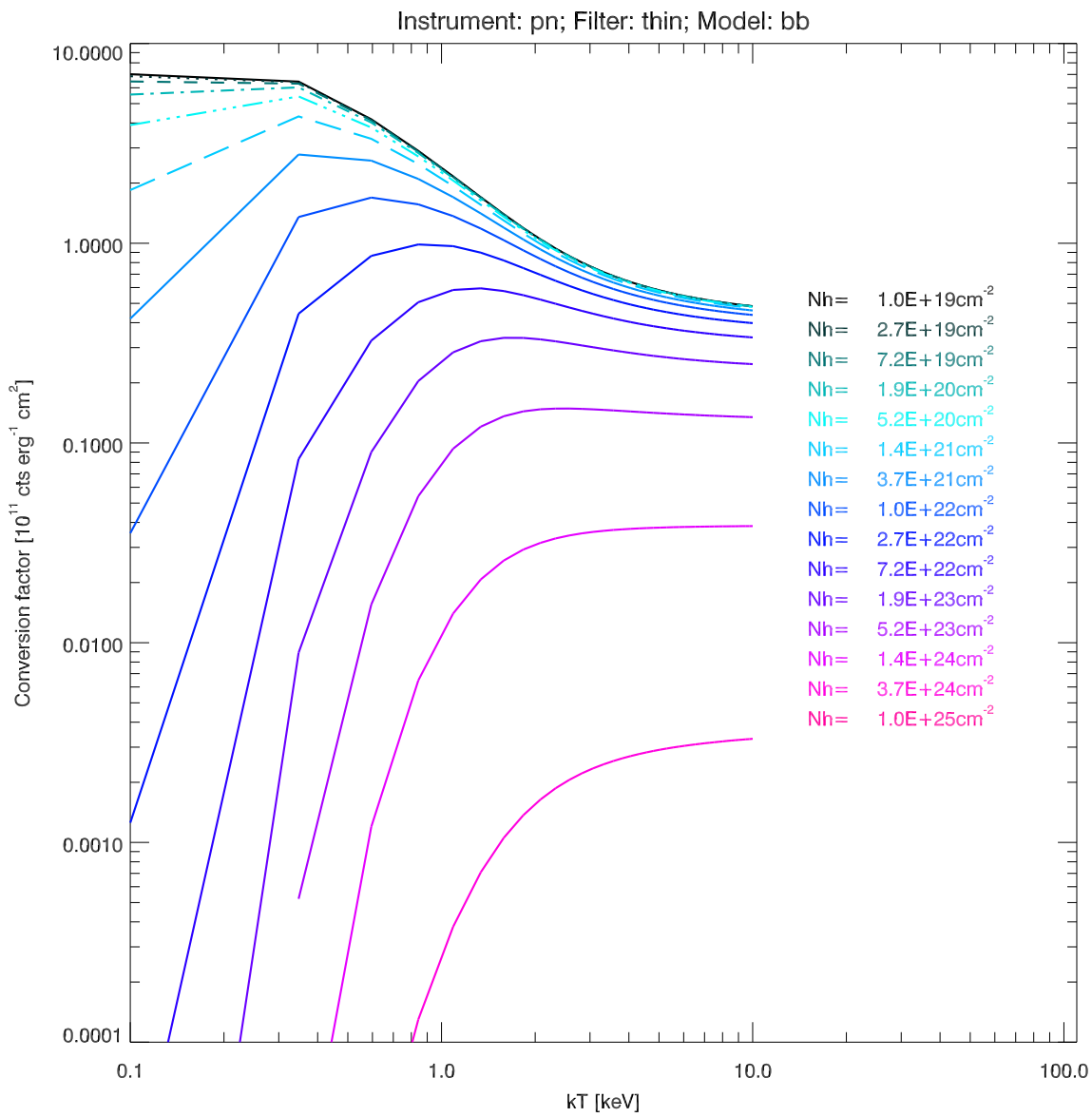


Figure 67: EPIC flux to count rate conversion factors (in units of  $10^{11}$  counts  $\text{erg}^{-1}$   $\text{cm}^2$ ) for pn camera for various black body spectra and for different values of the absorbing column density,  $N_H$  (thin filter).

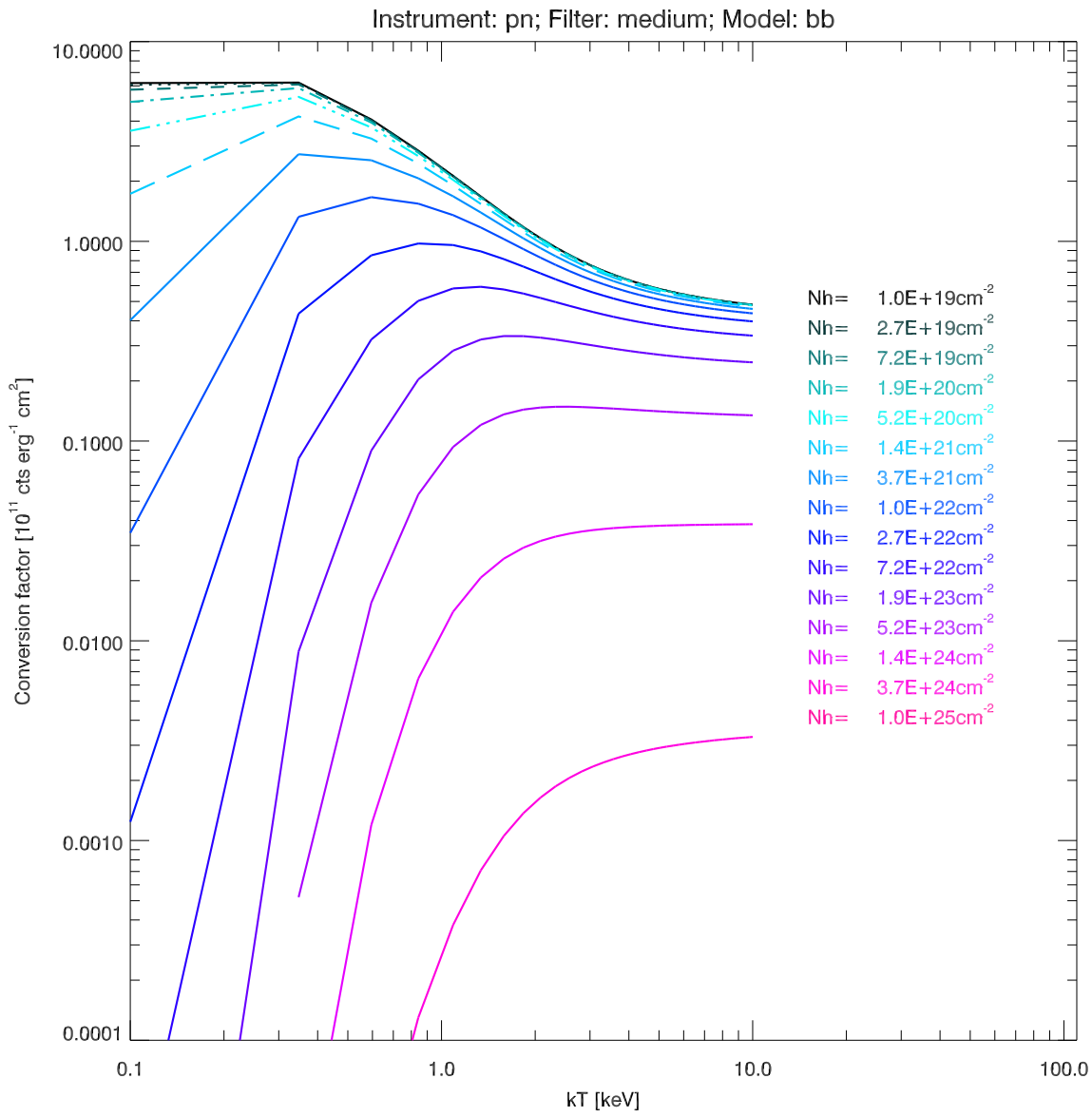


Figure 68: EPIC flux to count rate conversion factors (in units of  $10^{11}$  counts  $\text{erg}^{-1}$   $\text{cm}^2$ ) for pn camera for various black body spectra and for different values of the absorbing column density,  $N_H$  (medium filter).

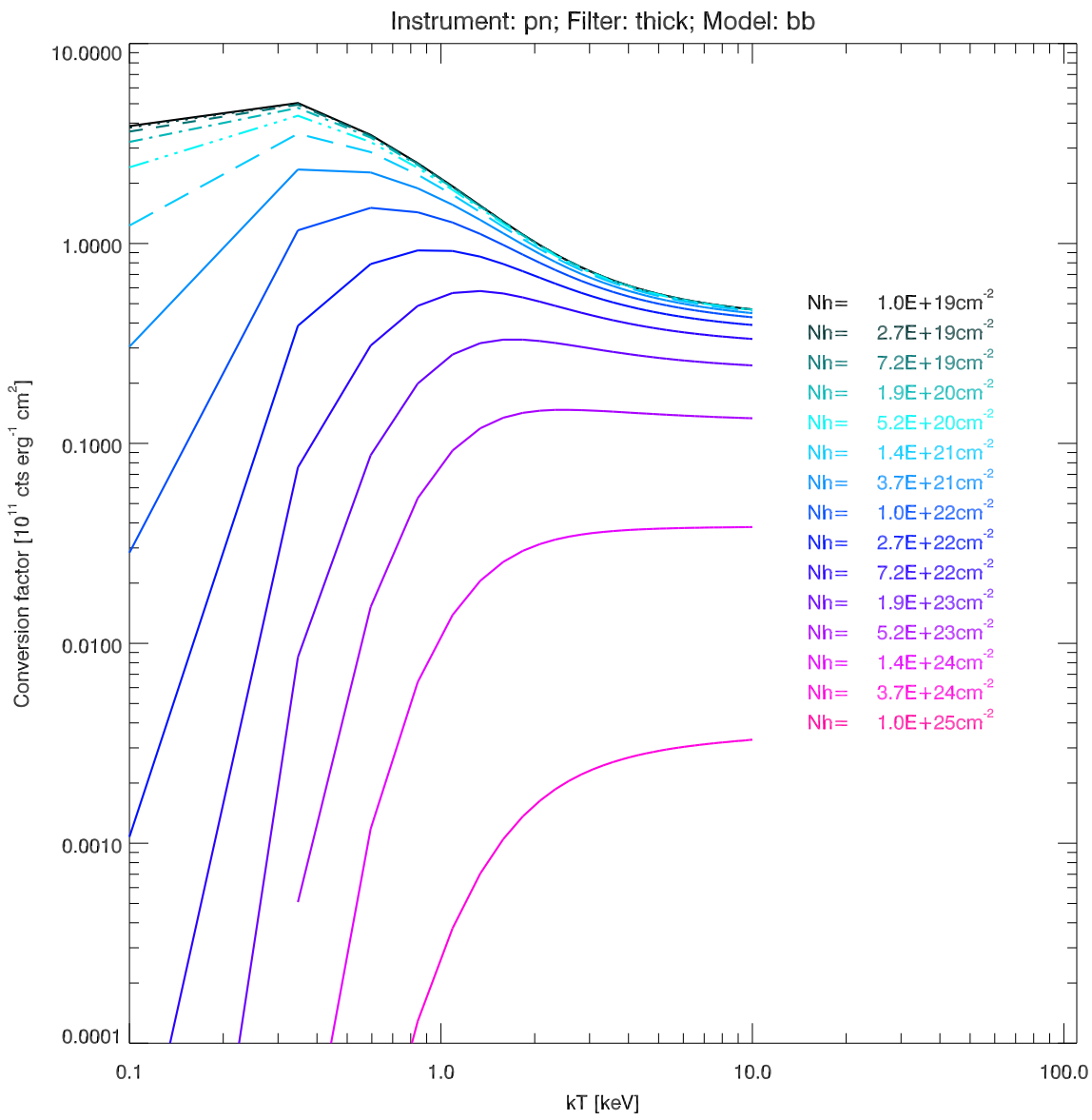


Figure 69: EPIC flux to count rate conversion factors (in units of  $10^{11}$  counts  $\text{erg}^{-1}$   $\text{cm}^2$ ) for pn camera for various black body spectra and for different values of the absorbing column density,  $N_H$  (thick filter).

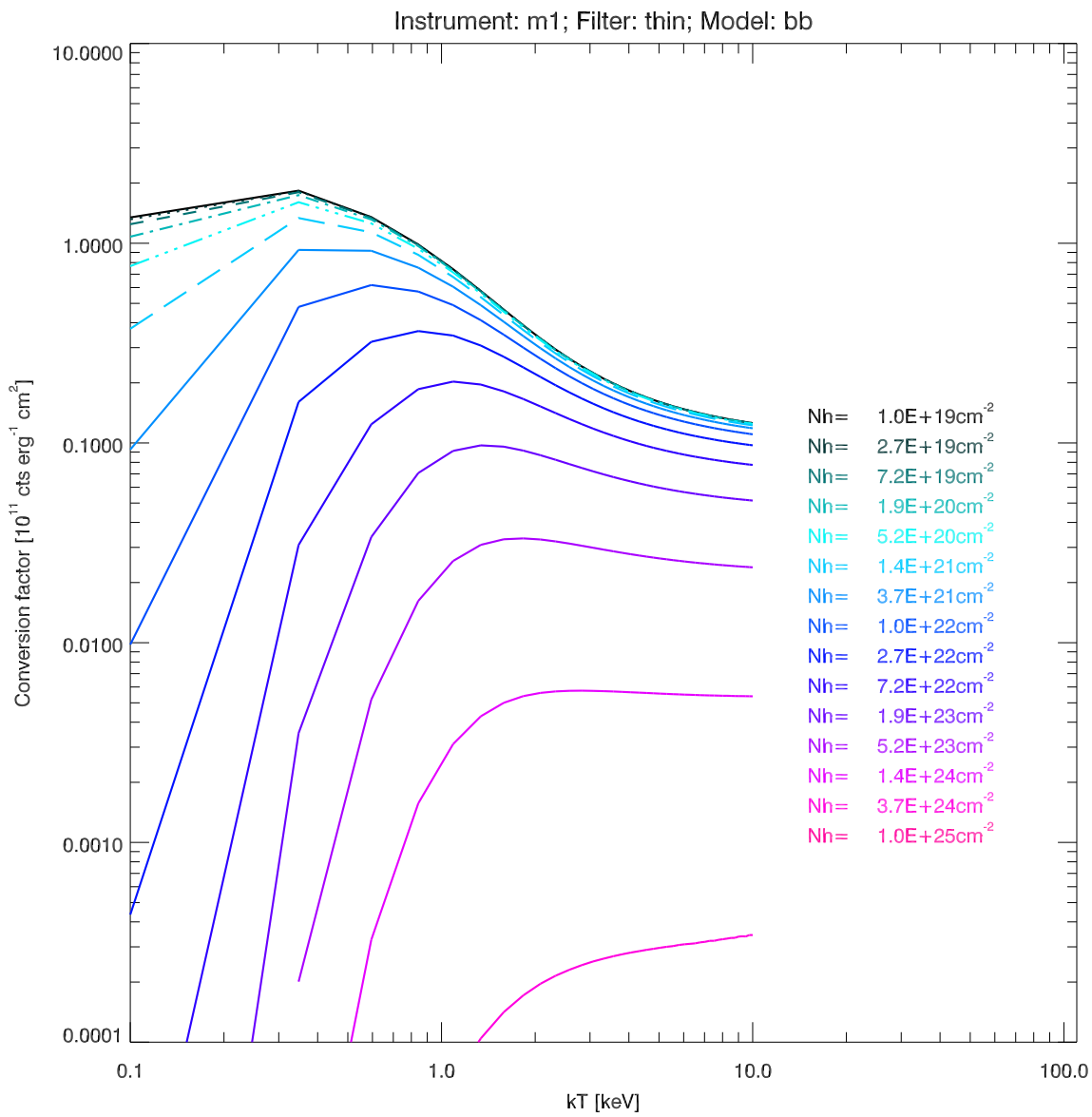


Figure 70: EPIC flux to count rate conversion factors (in units of  $10^{11}$  counts  $\text{erg}^{-1}$   $\text{cm}^2$ ) for MOS1 camera for various black body spectra and for different values of the absorbing column density,  $N_H$  (thin filter).

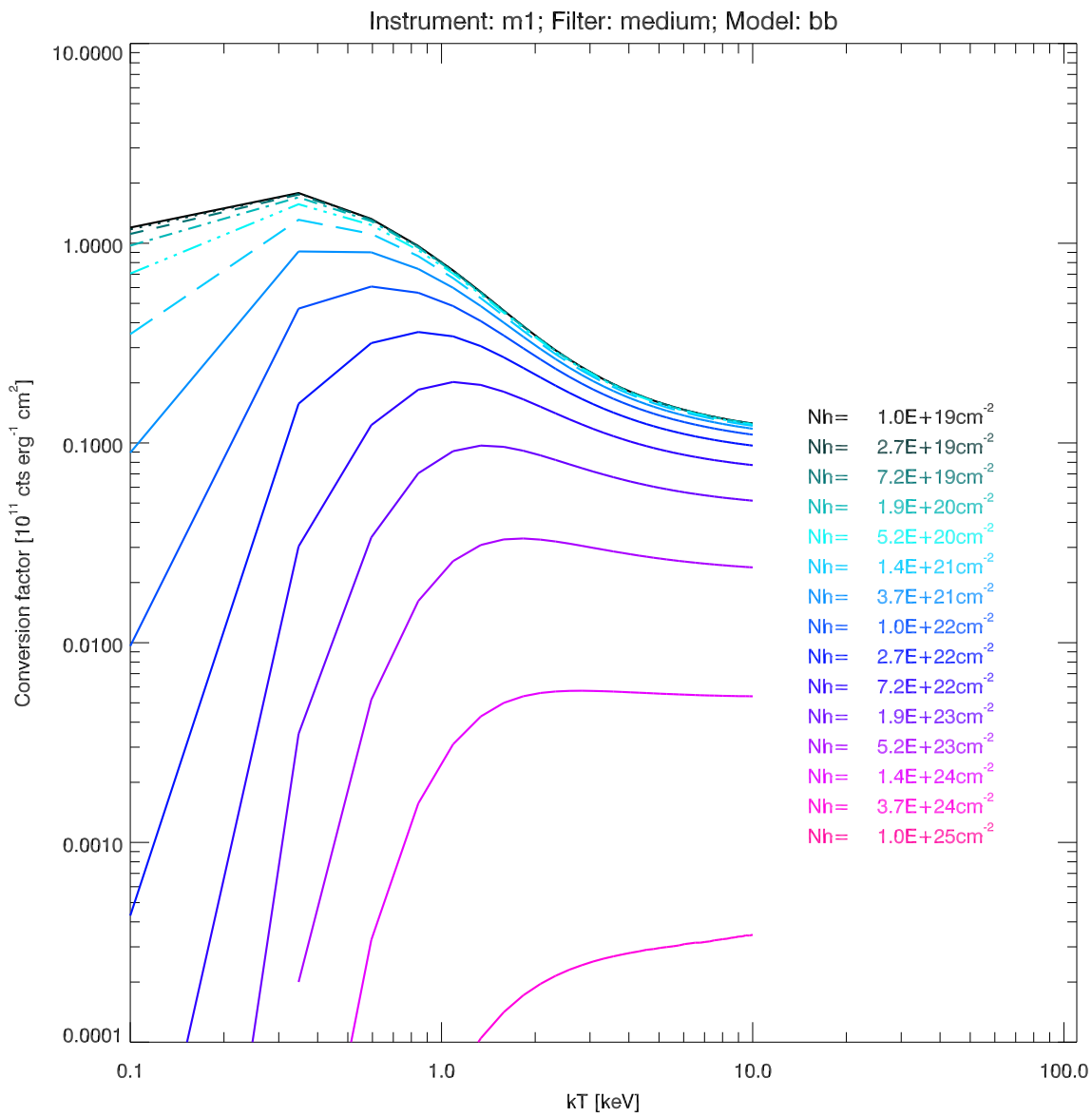


Figure 71: EPIC flux to count rate conversion factors (in units of  $10^{11}$  counts  $\text{erg}^{-1}$   $\text{cm}^{-2}$ ) for MOS1 camera for various black body spectra and for different values of the absorbing column density,  $N_H$  (medium filter).

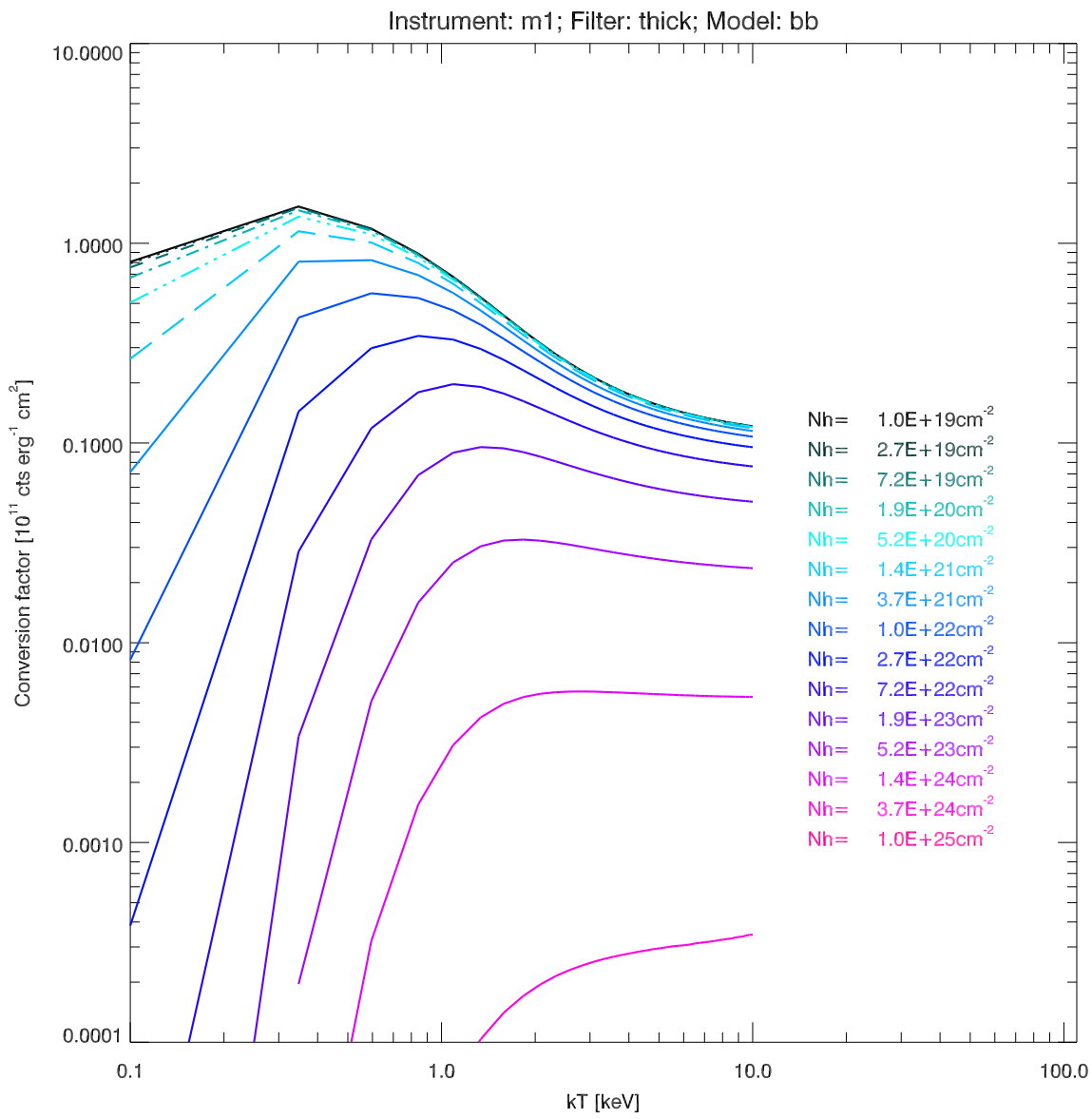


Figure 72: EPIC flux to count rate conversion factors (in units of  $10^{11}$  counts  $\text{erg}^{-1}$   $\text{cm}^{-2}$ ) for MOS1 camera for various black body spectra and for different values of the absorbing column density,  $N_H$  (thick filter).

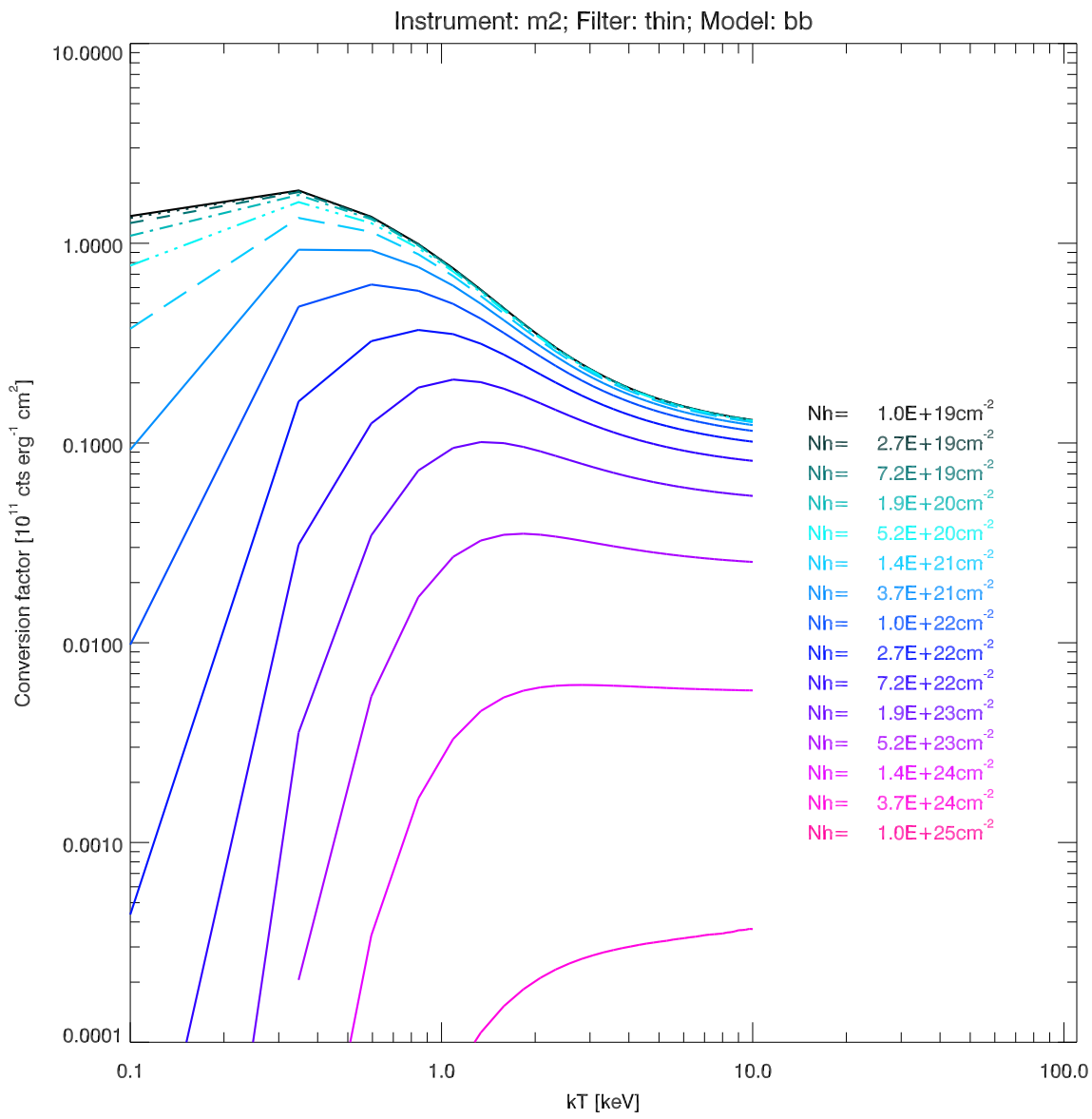


Figure 73: EPIC flux to count rate conversion factors (in units of  $10^{11}$  counts  $\text{erg}^{-1}$   $\text{cm}^2$ ) for MOS2 camera for various black body spectra and for different values of the absorbing column density,  $N_H$  (thin filter).

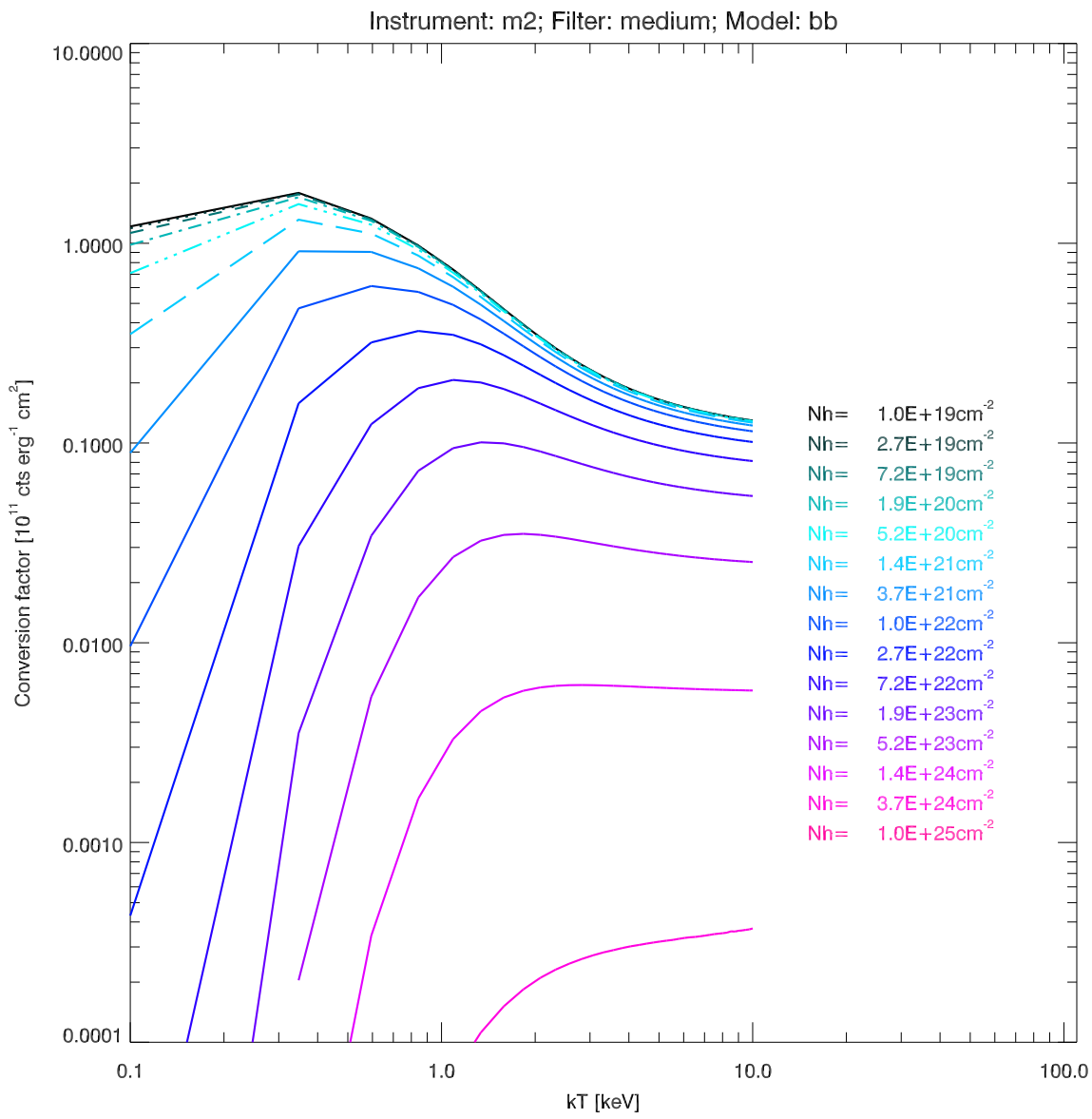


Figure 74: EPIC flux to count rate conversion factors (in units of  $10^{11}$  counts  $\text{erg}^{-1}$   $\text{cm}^2$ ) for MOS2 camera for various black body spectra and for different values of the absorbing column density,  $N_H$  (medium filter).

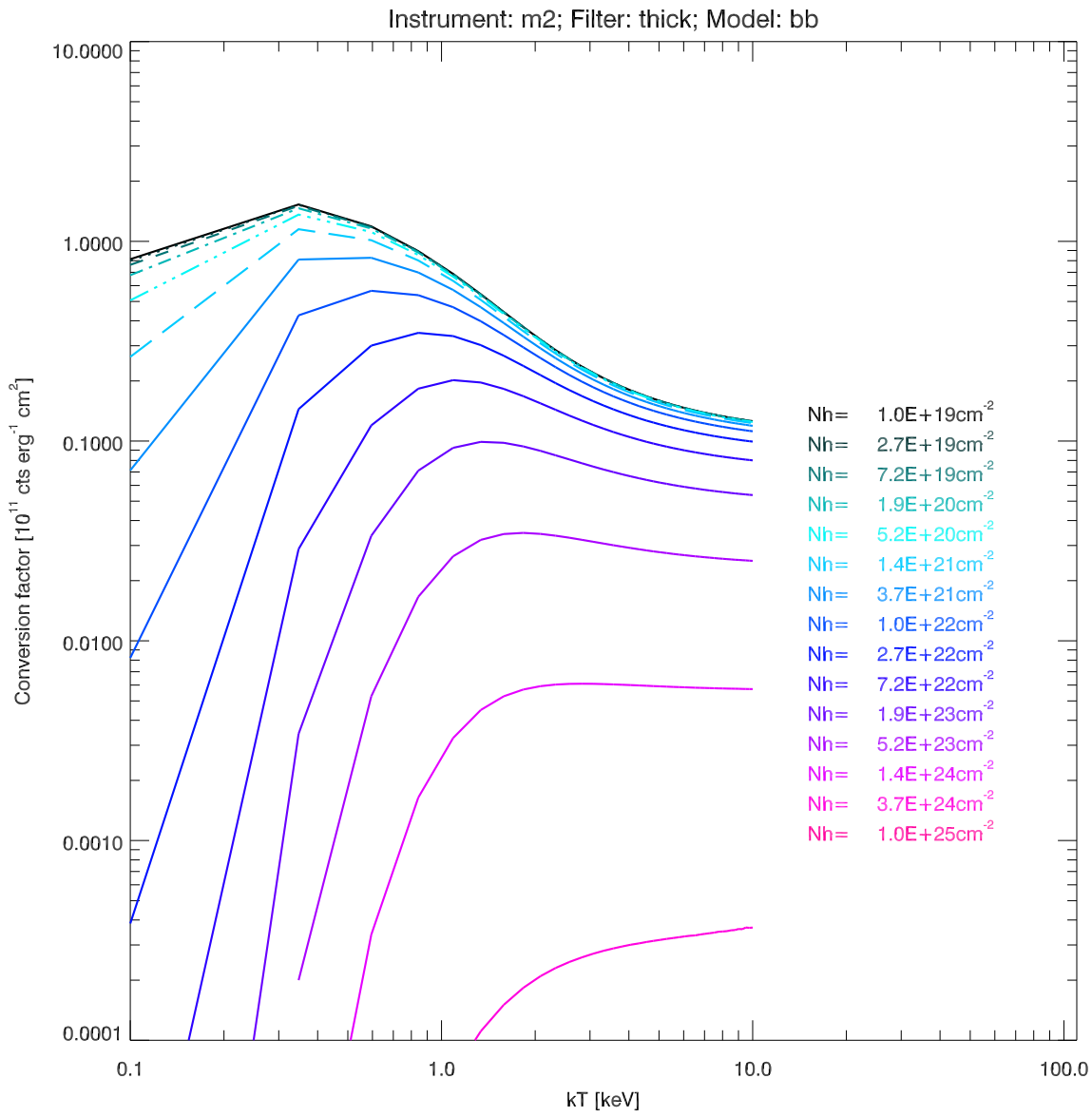


Figure 75: EPIC flux to count rate conversion factors (in units of  $10^{11}$  counts  $\text{erg}^{-1}$   $\text{cm}^2$ ) for MOS2 camera for various black body spectra and for different values of the absorbing column density,  $N_H$  (thick filter).



### 3.4 REFLECTION GRATING SPECTROMETER (RGS)

Among the science instruments of XMM-Newton, the RGS is best suited for high spectral resolution (from 100 to 500, FWHM) X-ray spectroscopy in the energy range 0.33-2.5 keV or 5-38 Å<sup>4</sup>. The energy range covered by the RGS has a particularly high density of X-ray emission lines including the K-shell transitions and He-like triplets of light elements, such as C, N, O, Ne, Mg and Si; and the L-shell transitions of heavier elements like Fe and Ni; thus offering a large number of diagnostic tools to investigate the physical conditions and chemical composition of the emitting material.

Two of the three XMM-Newton X-ray telescopes are equipped with RGS units. These consist of Reflection Grating Assemblies (RGAs) and RGS Focal Cameras (RFCs), see Fig. 3. The RGAs are mounted in the light path of the two X-ray telescopes with EPIC MOS cameras at their primary focus. Each RGA intercepts about 58% of the total light focused by the mirror module. The grating plates in the RGAs have mean groove densities of about 645.6 lines mm<sup>-1</sup>. The dispersion of the instrument is a slowly varying function of dispersion angle, and is equal to approximately 8.3 and 12.7 mm Å<sup>-1</sup> at 15 Å in first and second order, respectively.

The RFCs consist of linear arrays of 9 MOS CCD chips similar to those in the EPIC MOS cameras, which are located along the dispersion direction of the RGAs. The RGS MOS chips are back-illuminated in order to maximise the soft energy response and aluminium-coated on the exposed side in order to suppress optical and UV light. Each has 1024x768 (27μ)<sup>2</sup> pixels, half (1024x384) exposed to the sky and half used as a storage area. During readout, pixel on-chip binning (OCB) is performed in the default spectroscopy mode, leading to a bin size of (81μ)<sup>2</sup>, which is sufficient to fully sample the RGS line spread function (LSF). In the dispersion direction one bin corresponds to about 7, 10, and 14 mÅ in first order, and about 4, 6, and 10 mÅ in second order for wavelengths of 5, 15 and 38 Å, respectively. The size of one bin projected onto the sky is about 2".5 in the cross-dispersion direction, and roughly 3, 5 and 7" and 4, 6, and 9" in the dispersion direction at 5, 15 and 38 Å in first and second order, respectively.

Both spectrometers cover the same field of view, with the dispersion direction along the space-craft -Z axis. In the cross-dispersion direction, the size of the field of view is determined by the width of the CCDs (5'), and the spatial resolution in this direction is largely determined by the imaging properties of the mirror. In the dispersion direction, the aperture of RGS covers the entire FOV of the mirrors, although the effective area decreases significantly for off-axis sources. For an on-axis source, the zero-order image of the gratings is not visible on the detector array. After the first week of operations, an electronic component in the clock driver of CCD4 in RGS2 failed, affecting the wavelength range from 20.0 to 24.1 Å that includes, in particular, the O VII He-like triplet. A similar problem occurred in early September 2000 with CCD7 of RGS1 covering 10.6 to 13.8 Å, where important Ne lines are to be found. The total effective area is thus reduced by a factor of 2 in these wavelength bands. Observers should make any necessary adjustments to ensure the viability of measurements of any important spectral features that may fall in the bands covered by the two RGS CCD chain failures.

The performance of the RGS instruments is explained in detail in the following sections. Key performance parameters are summarised in Table 8.

#### 3.4.1 Diffraction Geometry

The diffraction geometry of the reflection gratings is illustrated in Fig. 76. Light strikes the gratings at an angle of incidence  $\alpha$  with respect to the plane of the grating, and emerges at

<sup>4</sup>The formula for conversion of wavelengths into energies is  $\lambda(\text{\AA}) \times E(\text{keV}) = 12.3985$



Table 8: *RGS In-orbit Performance*

		RGS1			RGS2		
		10 Å	15 Å	35 Å	10 Å	15 Å	35 Å
Effective area (cm <sup>2</sup> )	1st order	51	61	21	53	68	25
	2nd order	29	15	—	31	19	—
Resolution (km s <sup>-1</sup> )	1st order	1700	1200	600	1900	1400	700
	2nd order	1000	700	—	1200	800	—
Wavelength range	1st order	5 – 38 Å (0.35 – 2.5 keV)			5 – 20 Å (0.62 – 2.5 keV)		
	2nd order						
Wavelength accuracy	1st order	$\pm 5$ mÅ		$\pm 6$ mÅ		$\pm 6$ mÅ	
	2nd order	$\pm 5$ mÅ		$\pm 6$ mÅ		$\pm 6$ mÅ	
Bin size [3x3 (27 $\mu$ ) <sup>2</sup> pixels]		2.5 arcsec (cross dispersion direction)			7 – 14 mÅ (dispersion direction, first order)		

angle  $\beta$  given by the dispersion equation

$$\cos \beta = \cos \alpha + m\lambda/d \quad (1)$$

where  $\lambda$  is the radiation wavelength,  $d$  the grating spacing, and  $m$  the spectral order. The RGS is designed for use with negative orders,  $\beta > \alpha$ .

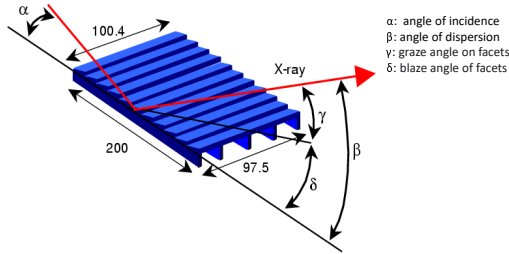


Figure 76: *Schematic drawing of a grating, including some of the key dispersion angles.*

### 3.4.2 RFC chip arrays

Fig. 77 displays a sketch of the chip geometry in an RFC. The two RFCs are offset with respect to each other along the dispersion direction so as to fill the gaps in each other's in order to provide continuous coverage along the dispersion direction. The interchip gap between adjacent CCDs is about 0.5 mm corresponding to 85 mÅ and 45 mÅ at short and long wavelengths, respectively. The dispersion direction is along the spacecraft -Z axis. Higher energies, shorter wavelengths, are dispersed to higher values in Z and to lower dispersion angles.

The chip on the right of Fig. 77 has number 1 (the low Z end of the coordinate scale), and the one on the left is number 9 (largest Z value, smallest dispersion angle and highest energy or smallest wavelength). The user is referred to the XMM-Newton Calibration Access and Data Handbook for details of the coordinate systems.



**esa**

european space agency  
agence spatiale européenne

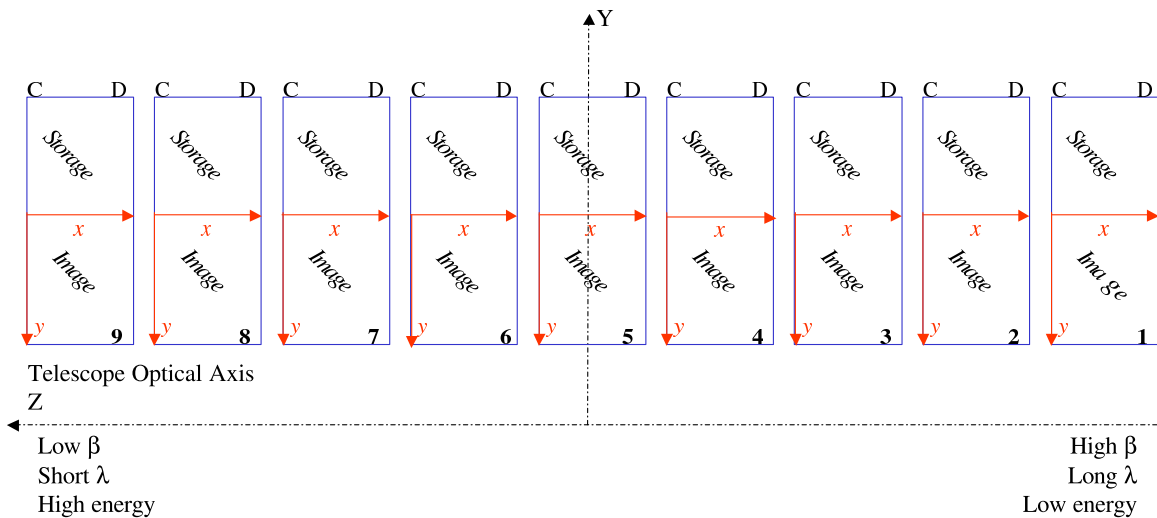


Figure 77: Sketch of an RFC chip array with 9 MOS CCDs. The half of each CCD at large camera  $y$  coordinates is exposed to the sky, the other half is used as a storage area. The dispersion direction is along the  $Z$  axis, so that higher energies (shorter wavelengths) are dispersed to higher values in  $Z$ . Using the spacecraft axis, the BETA value (dispersion direction) is antiparallel to  $Z$ , and the cross-dispersion is parallel to  $Y$ .

For an on-axis source, the individual chips cover approximately the energy ranges listed in Table 9. Simulations should be performed in case the user is interested in lines that could fall close to the chip boundaries. To shift important lines away from chip boundaries or inoperative CCDs, users may want to consider changing the diffraction geometry by moving the spacecraft pointing away from the usual boresight through explicit control of the incidence angle. For this purpose the task 'rgslinepos', provided as part of the XMM-Newton Science Analysis System SAS, computes the position of a given wavelength in CCD coordinates. Large offsets in the dispersion direction are not recommended as this reduces the overall effective area significantly. Care also has to be taken to ensure that the source does not fall on or close to an EPIC CCD gap. Last, the fact that offset pointing requires a particular position angle implies a smaller visibility window for the observation.

The exact location of a source spectrum on the RGS CCD chips depends on the source's location within the field of view of the X-ray telescopes. For a target on-axis the observed spectrum is centred on the RFC chips in the cross-dispersion direction. The wavelength scale for sources off-axis in the cross-dispersion direction is the same as for those on-axis, but is offset for sources off-axis in the dispersion direction. The offline data analysis with SAS takes care of the source position.

### 3.4.3 RGS Order Separation

X-rays are reflected into first and second spectral orders with the highest efficiency, and thus produce the most useful data. Count rates in the third order are about 8 times lower than in second order. Depending on grating order, the RGS covers the energy ranges listed in Table 10.



Table 9: *Wavelength and energy ranges covered by the chips of RGS1 and RGS2 for an on-axis source in first order. Due to the scattering, the chip boundaries do not cause sharp features in the effective area. Values in brackets correspond to the non-operational chains.*

Chip	RGS1		RGS2	
	Energy [keV]	Wavelength [ $\text{\AA}$ ]	Energy [keV]	Wavelength [ $\text{\AA}$ ]
1	0.32 – 0.37	33.6 – 38.2	0.33 – 0.38	32.7 – 37.3
2	0.37 – 0.43	29.0 – 33.5	0.38 – 0.44	28.2 – 32.6
3	0.43 – 0.50	24.8 – 28.9	0.44 – 0.52	24.1 – 28.1
4	0.50 – 0.59	20.9 – 24.7	(0.52 – 0.62)	(20.0 – 24.1)
5	0.60 – 0.72	17.2 – 20.8	0.62 – 0.75	16.5 – 20.0
6	0.73 – 0.90	13.8 – 17.1	0.76 – 0.94	13.2 – 16.4
7	(0.90 – 1.18)	(10.6 – 13.8)	0.95 – 1.23	10.0 – 13.1
8	1.18 – 1.60	7.8 – 10.6	1.24 – 1.71	7.2 – 10.0
9	1.61 – 2.41	5.2 – 7.7	1.73 – 2.64	4.7 – 7.2

Table 10: *Wavelength ranges covered by the RGS in different grating orders*

Order	Wavelength range [ $\text{\AA}$ ]
-1	$6^1$ – 38
-2	$6^1$ – 20
-3	$6^1$ – 10

<sup>1</sup> Practical limitation due to very low effective area below 6  $\text{\AA}$ . The theoretical lower limit is  $-5/m \text{\AA}$ , where m is the order number.



A consequence of the diffraction equation (1) is that orders overlap on the CCD detectors of the RFC (see Fig. 78, top panel). Separation of the spectral orders is achieved by using the intrinsic energy resolution of the CCDs, which is about 160 eV FWHM at 2 keV. The dispersion of a spectrum on an RFC array is shown in the bottom panel of Fig. 78. First and second orders are very prominent and are clearly separated in the vertical direction (i.e. in CCD energy, or PI, space). Photons of higher orders are also visible for brighter sources. The calibration sources can also be seen in the bottom panel as short horizontal features.

### 3.4.4 In-Flight Performance

#### 3.4.4.1 The Line Spread Function

The Line Spread Function (LSF) is a convolution of the response functions of the mirror and the grating, followed by convolution with the detector response. The mirror response is approximated by a Lorentzian profile, which has been calibrated against observations of PKS 0312-770. The grating response depends on the accuracy of the variable line density of the gratings, the figure errors of the gratings, their alignment, and the scattering of X-rays due to surface roughness, this latter seen as the horizontal distribution of events in the bottom panel of Fig. 78. Two scattering components have been identified: a small angle scale Gaussian component, and a large scale Lorentzian component. The wings in the LSF are reduced by applying an energy selection in the CCD response. The effect of this selection is asymmetric, as shown in Fig. 79. The LSF has been verified in several stellar sources. An example for an individual line, the first order O VIII Ly $\alpha$  (18.97 Å) emission line in HR 1099, is shown in Fig. 80.

The measured data are compared with simulations. There is excellent agreement between the measured performance of the LSF and the predicted one, which is based on pre-flight calibrations. This proves that the predicted resolving power can be achieved.

The profile of this same line in the cross-dispersion direction is presented in Fig. 81.

#### 3.4.4.2 Resolving Power and Spectral Resolution

Although the built differences between the two RGS units are small, the energy resolutions of the two instruments are slightly different due to their slightly different focusing as shown in Fig. 82.

The shape of the LSF core largely determines the ability of the spectrometer to separate closely spaced emission lines. The various components scale differently with wavelength, giving rise to a composite line shape which cannot easily be characterised in terms of a simple analytical function. The telescope blur contributes a constant term to the spectrometer line width, while misalignments and flatness errors of the gratings contribute a term which slowly increases with increasing wavelength. The broadening due to pointing instability, which affects the resolving power through variations of the angle of incidence on the gratings has proved to be negligible. The scattering component is most significant at the shortest wavelengths and the highest diffraction orders. This is illustrated in Fig. 82 where the predicted resolution (the FWHM of the LSF) for the two RGSs is shown in the second and fourth panels. The steep rise below 7 Å is due to the scattering component of the gratings. Also shown are the measurements, which are deduced from narrow, bright emission lines in HR 1099 (Ly $\alpha$  lines of Ne, O, N and C). Fig. 82 demonstrates that the instrument resolving power is close to expectations.

The ability to detect weak emission lines above the background or the continuum is better measured by the half energy width (HEW) of the profile. This width, especially at short wavelengths, is more dependent on the amplitude and width of the scattering wings. Again, the data agree



DATE-OBS 2001-03-15T19:19:40 DATE-END 2001-03-16T03:51:24  
OBS-ID 0134720101

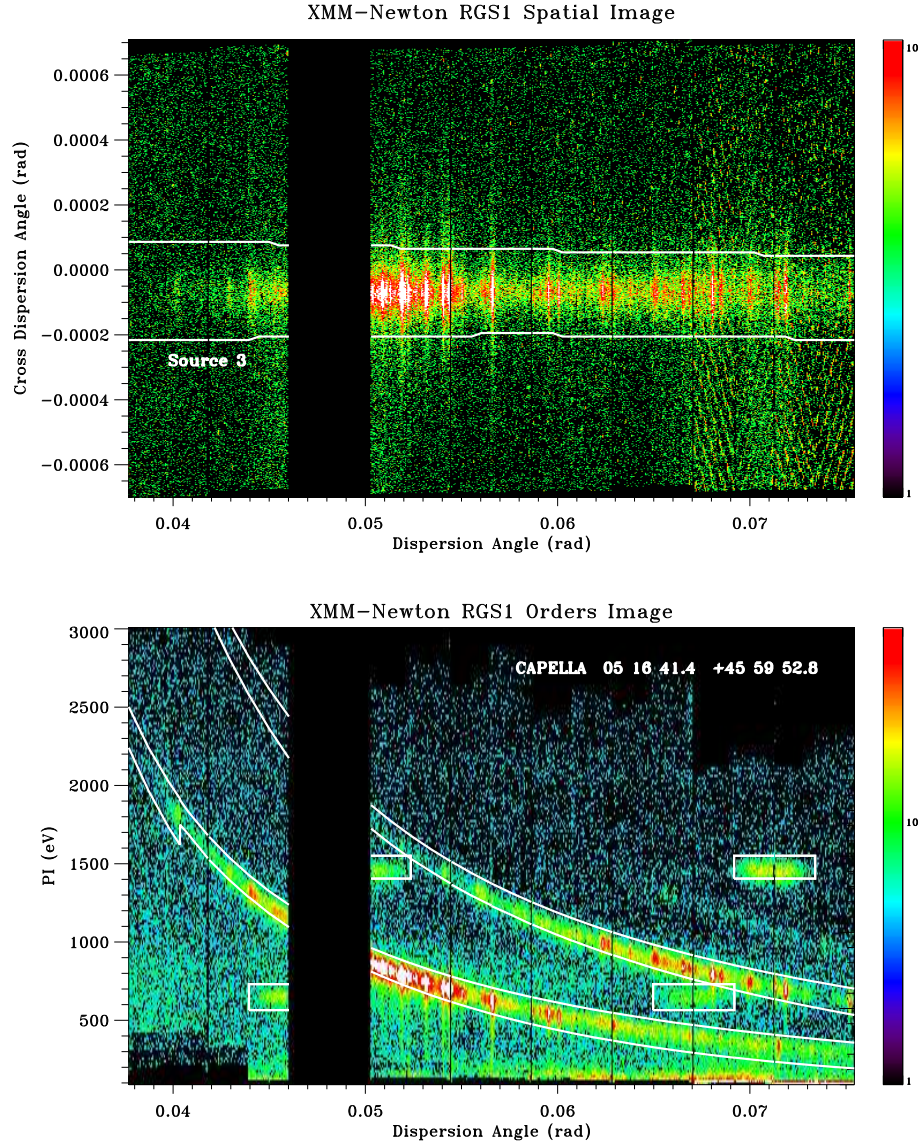


Figure 78: Example of RGS data for a calibration observation of Capella shown with a logarithmic intensity scale. The dispersion axis runs horizontally and increases to the right. Lower dispersion angles correspond to shorter wavelengths or higher energy. The top panel shows the image of the dispersed light in the detector. The cross dispersion is along the vertical axis. The bottom panel shows the order selection plane, with the energy, PI, on the ordinate. This also illustrates the mechanism used for separation of first, second and higher grating orders. Standard data selections are indicated by the white curves. In the bottom panel, the low and high level thresholds are visible. In the top panel, the effect of fixed pattern noise at long wavelengths is seen.

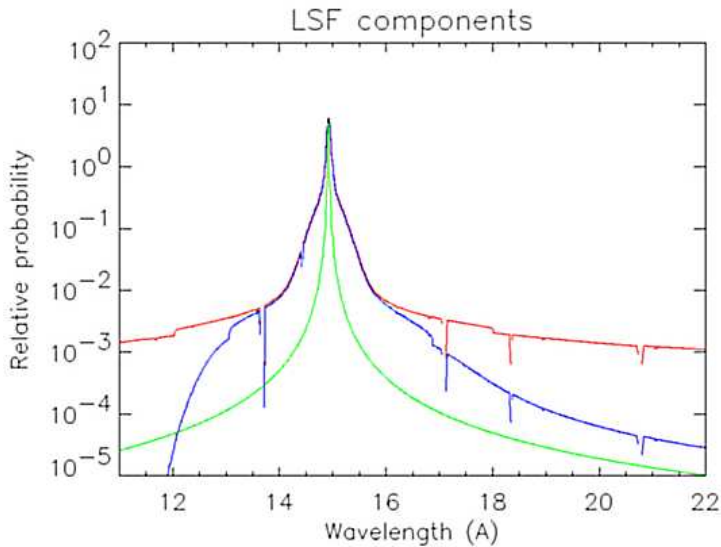


Figure 79: The three main components of the LSF: the projected mirror response (green), broadened after folding with the grating response (red), and after applying the detector energy selections (blue). All components are normalised to their maximum.

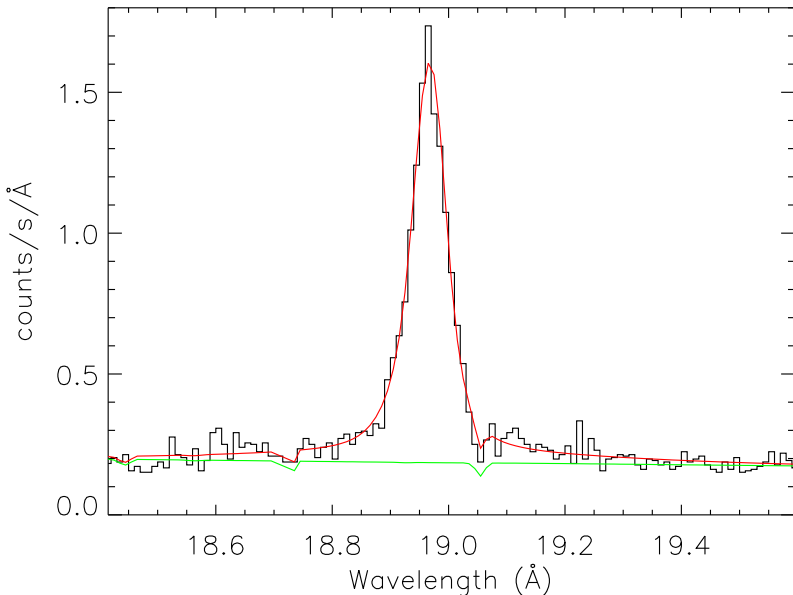


Figure 80: Measured (black) and simulated (red) RGS2 Line Spread Function for the O VIII Ly $\alpha$  line in HR 1099. The assumed background is shown in green.

with the predictions and, in the HEW sense, the resolving power goes to  $\sim 800$  at the longest wavelengths. The first and third panels of Fig. 82 display the HEW as a function of wavelength, for both RGS units separately.

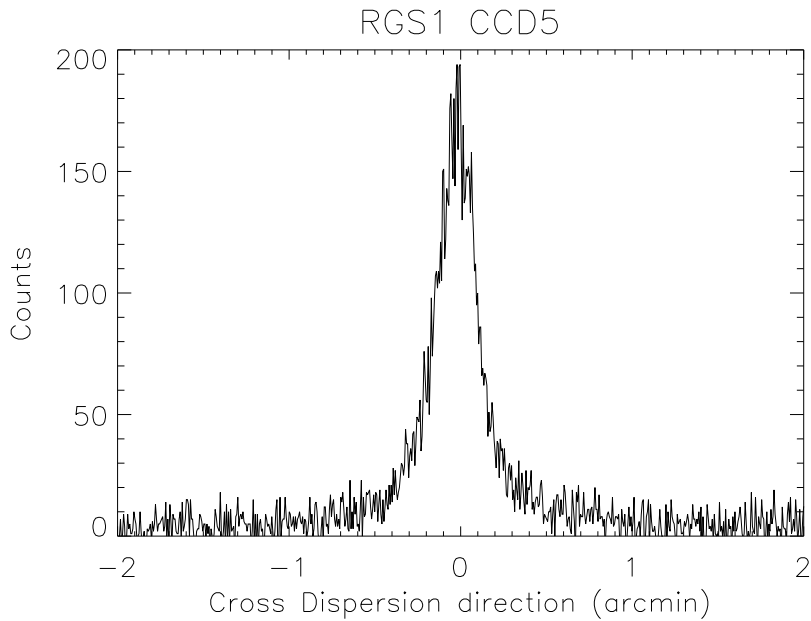


Figure 81: A close-up view of the O VIII Ly $\alpha$  line in HR 1099 along the cross-dispersion direction.

#### 3.4.4.3 RGS spectral resolution for extended sources

The RGS spectral resolution depends on the angular extent of the observed source. For extended sources, emission lines are broadened according to the relation

$$\Delta\lambda(\text{ext}) = 0.138 \theta(\text{ext})/\text{m} \quad (2)$$

where  $\Delta\lambda(\text{ext})$  is the resolution in Å in case of an extended source, for the spectral order m and a source extent of  $\theta(\text{ext})$ , in arcmin. This illustrates that, for a source extent of order 1', RGS still clearly outperforms EPIC in terms of spectral resolution. This is demonstrated for example by the observed spectra of a moderately extended source like 1E 0102.2-7219. This target is a supernova remnant in the Small Magellanic Cloud with an angular extent of 2'. The first and second order spectra of 1E 0102.2-7219 are shown in Figs. 93, 94 and 95.

#### 3.4.4.4 Wavelength Scale Accuracy

The RGS wavelength scale is determined by the relative alignment of the various instruments and their structural stability. Studies of spectra of emission line sources have shown that line positions are systematically shifted with respect to laboratory wavelengths. These shifts have been found to be correlated with the angular distance between the spacecraft pointing direction and the Sun (“solar angle”). The correction of this dependence aligns the wavelength scales of both spectrographs and orders, and improves substantially their accuracy. Fig. 83 shows the residuals of the RGS measured versus nominal positions for certain emission lines and a set of observations of coronal sources. For an on-axis source, the wavelength scale accuracy is 6 mÅ, after application of the heliocentric velocity correction and removal of the solar angle dependence. It has been verified that the wavelength scale is stable over a long timescale.

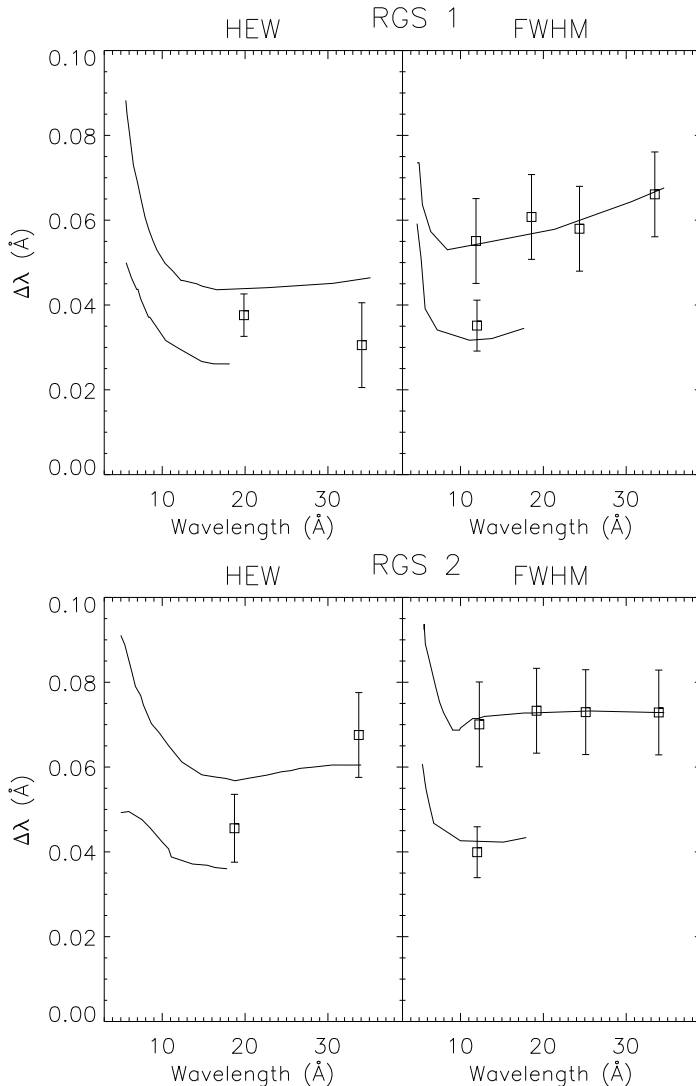


Figure 82: The resolving power (HEW and FWHM) of RGS1 (left) and RGS2 (right) in the -1 and -2 grating orders. HEW indicates the detectability of a weak feature against a strong continuum and FWHM whether two closely spaced spectral lines can be resolved.

#### 3.4.4.5 RGS effective area for dispersive spectroscopy

Several parameters determine the RGS effective area per dispersion order: the properties of all optical components in the light path, the CCD quantum efficiency and the source and order filtering criteria.

The following optical components contribute:

- The effective area of the mirror modules (see § 3.2.2.1).
- The Reflection Grating Arrays: how much of the light from the mirrors is diffracted to the different spectral orders and then absorbed on the RFCs. This is determined by the amount of collimated light that is intercepted by the grating arrays, the reflectivity of the gratings into the dispersion order and the effective surface of



**esa**

european space agency  
agence spatiale européenne

Document No.: XMM-SOC-USR-MAN-0006

Issue/Rev.: Issue 2.18

Date: 13.07.2020

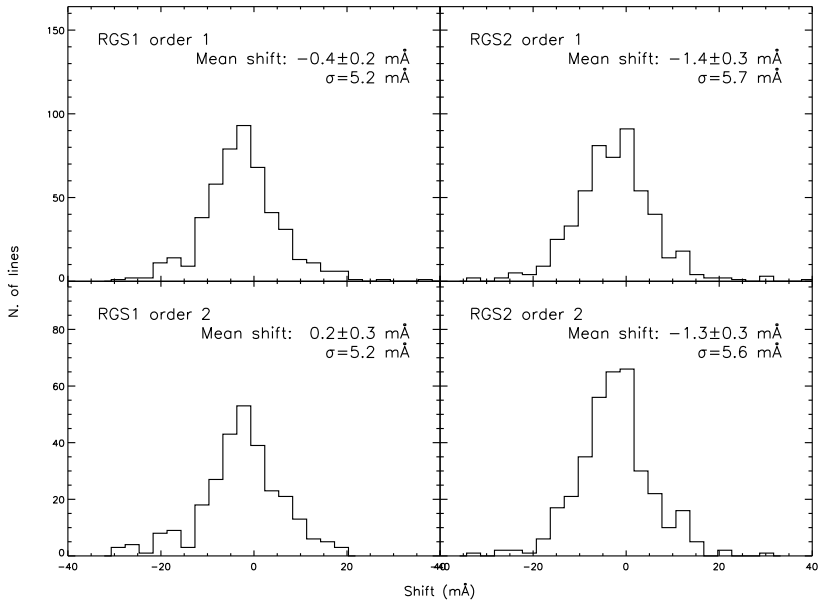


Figure 83: Comparison of measured and laboratory wavelengths for a number of sources and observations. Observed wavelengths have been corrected for solar angle dependence and for heliocentric velocity.

the gratings that provides useful dispersed light. Since the gratings are mounted relatively close together, about 1 cm spacing, light with large dispersion angles is vignetted by the back of the neighbouring grating, thus reducing the surface area that provides useful intensity to the camera at these dispersion angles.

- The quantum efficiency of the RGS focal camera CCDs, which varies from 70% to 95% over the RGS passband from 0.35 to 2.5 keV.

These three components are functions of wavelength and source position angle. Finally, data selections in the RFC, used to separate orders and to suppress scattering, will determine the effective area.

To assess the total efficiency of the RGS instrument per spectral order, the efficiency with which the background is rejected and the different spectral orders can be selected must also be taken into account. This is performed by filtering in the imaging domain (cross-dispersion versus dispersion angles) and in the domain CCD-PI versus dispersion angle. Standard data selections are indicated by the white curves in Fig. 78. In the cross-dispersion direction a filter is applied which includes typically 90-97% of the total intensity. Default masks for the spatial extraction of photons from the different orders using PHA or PI-energy channel vs. dispersion coordinate plots, as in Fig. 78, are created by the offline analysis SAS tasks for each RGS . The user can also modify the extraction masks as described in the SAS User's Guide. In addition the exposure time per wavelength bin is calculated taking into account the data selections, rejected columns and pixels and the dead space between CCDs. The expected efficiency in the post-observation RGS order selection with the SAS is about 90% (0.95x0.95). This is a function of wavelength and is less at shorter wavelengths, due to additional loss of scatter outside of the extracted



(dispersion-PI) region.

Fig. 84 displays the calculated effective area of both RGS units together, and Fig. 85 the individual RGS1 and RGS2 effective areas overlaid one on top of the other. The calculations have been performed taking into account all the factors listed above.

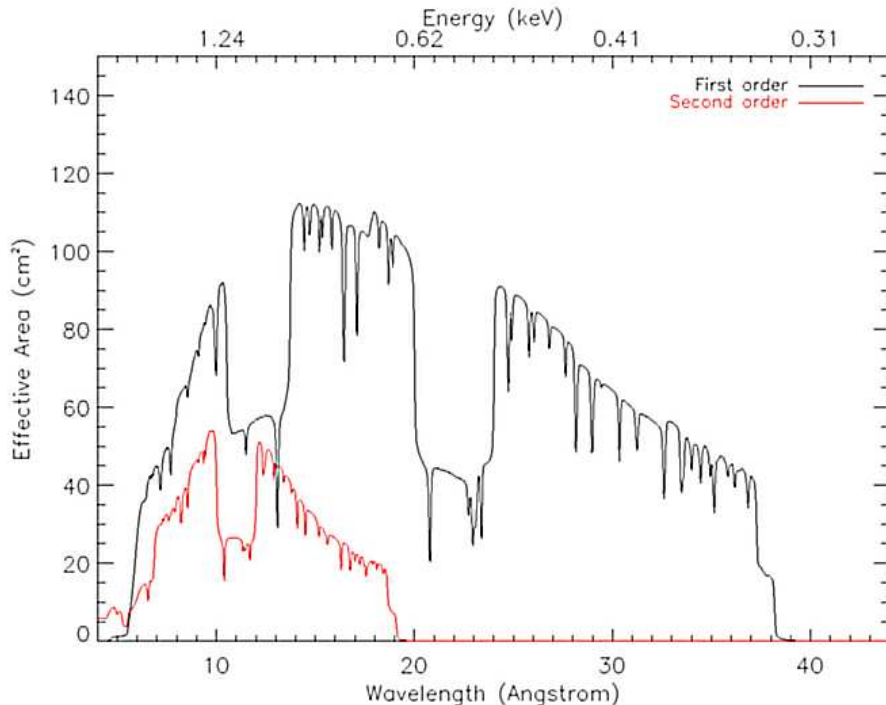


Figure 84: *The effective area of both RGS units combined as a function of energy and wavelength (top and bottom horizontal scales, respectively). See text for detailed explanations.*

Some clear features can be identified from these figures:

- the effective area has broad gaps due to the inoperative CCDs.
- the efficiency around chip boundaries does not drop sharply nor completely decreases to zero. This is due to the scattering causing photons with wavelengths corresponding to the passive areas being redistributed into non-passive areas. The amplitude of this sensitivity is strongly dependent on the selection mask in CCD PI versus dispersion coordinate space.
- the total effective area of both RGS added in Fig. 84 shows several of these chip boundaries, as the alignment of the RGS cameras is such that the inter-chip gaps do not coincide in wavelength.
- a similar effect of lower area as with the inter-chip gaps can be seen at wavelengths equivalent to bad columns, but there it is less pronounced.
- absorption edges are due to the existence of passive layers in the X-ray path consisting of the following atoms: Si (6.74 Å), Al (7.95 Å), Mg (9.51 Å), F (17.80 Å) and O (22.83 Å)



**esa**

european space agency  
agence spatiale européenne

Document No.: XMM-SOC-USR-MAN-0006

Issue/Rev.: Issue 2.18

Date: 13.07.2020

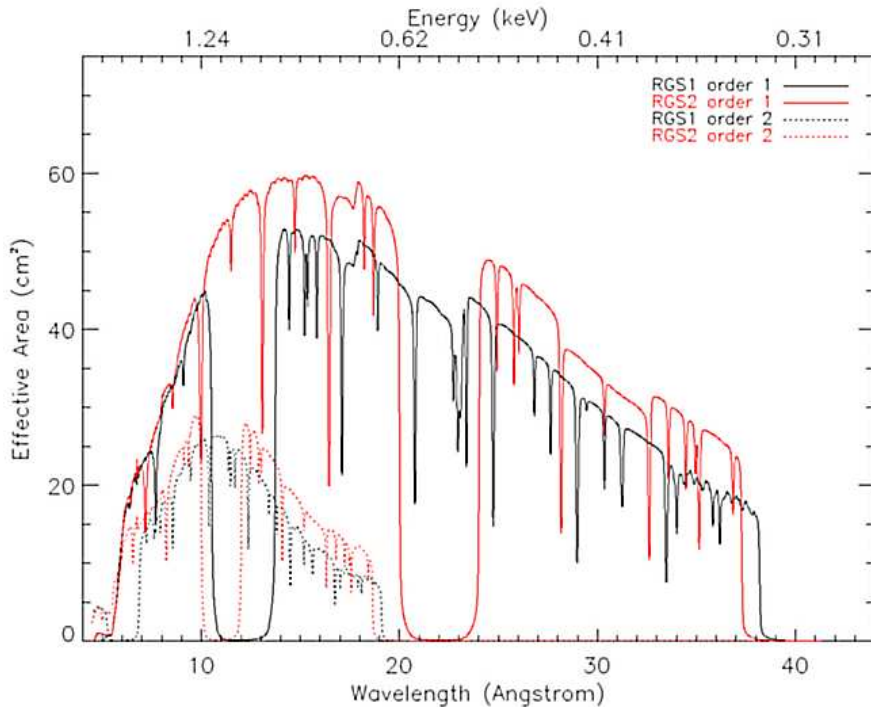


Figure 85: The effective areas of both RGS units separately as a function of energy and wavelength (top and bottom horizontal scales, respectively). See text for detailed explanations.

- apparent oscillations with small amplitude of the effective area are due to data selections by regions that are defined as polygons across the surface of binned two dimensional data (cross dispersion versus dispersion angle and CCD energy versus dispersion angle). The fact that pixels of these binned images are selected discretely, gives rise to small scale variations of the selected area within the region. This is seen as oscillations of the detection efficiency. This is not a problem, nor is it an additional uncertainty of the response, as these data selection effects are properly included in the response generation.

Fig. 86 shows the effective area as a function of the off-axis cross dispersion angle. The ratio of the median off-axis effective area to the on-axis values decreases from 0.994 at  $\pm 0'.5$  to 0.83 and 0.60 at  $-2'.2$  and  $+2'.2$ , respectively.

#### 3.4.4.6 The RGS Background

The RGS instrumental background has different components, each with its own characteristics and time dependency. The main components are listed below. The background characterisation has been performed with in-flight data by analysing clear sky images (where there is no source emission) and fitting a model.

- Particle background (minimum ionising particles, protons and ions). These particles deposit most of their energy outside the 0.35 to 2.5 keV energy band and can thus mostly be rejected by the on-board software. There is an additional on-board



**esa**

european space agency  
agence spatiale européenne

Document No.: XMM-SOC-USR-MAN-0006

Issue/Rev.: Issue 2.18

Date: 13.07.2020

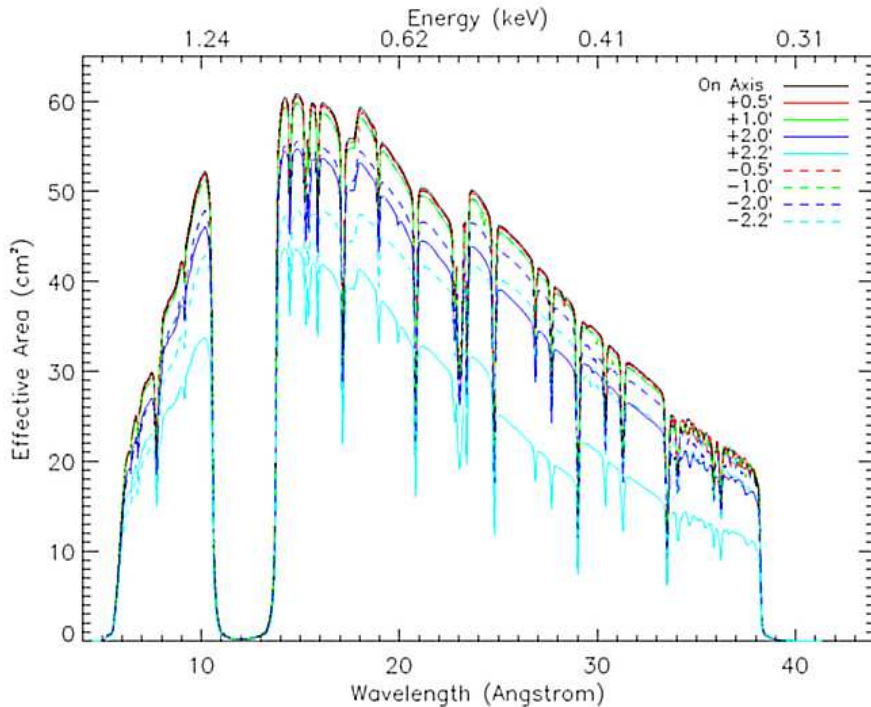


Figure 86: The RGS1 effective area as a function of cross dispersion off-axis angle.

rejection based on the spatial shape of the events. Except for the period when the spacecraft is passing through the radiation belts (i.e. for spacecraft elevation below 46000 km) and occasional solar storms, the in-flight measured particle background is quite stable. Typically it produces  $2.7 \pm 1$  events  $\text{cm}^{-2} \text{ s}^{-1}$ , which is a factor 2 higher than expected pre-launch. This number applies for event rates before any on-board selection and across the whole field of view. The quoted variation is larger than the statistical one and is due to variations in solar background.

- Low energy electrons which enter through the telescope. Electrons with energies up to 20 keV are rejected by the electron deflector at the exit plane of the mirrors. Higher energy electrons create secondary radiation in the spacecraft and detector shielding.
- Fluorescence lines in the detector housing due to interactions with the electron and other minimum ionising particles. The expected strong fluence from the detector housing material, Al, is strongly suppressed by a Au coating. One still expects to see Al K $\alpha$  and Au-M emission in the RGS energy band. These lines are indeed observed at a very low intensity ( $\leq 10^{-3}$  counts  $\text{cm}^{-2} \text{ s}^{-1}$ ).
- Calibration sources. They can easily be modelled. Nevertheless, the fraction spilling into the standard event selection regions is very small, since these are offset in the cross dispersion direction and additionally placed at locations where their energy signal is outside the order selection regions.
- Readout noise. Although strictly speaking this is not a background component, the



noise characteristics of each CCD has a tail which cannot be distinguished from proper X rays. It is roughly constant in dispersion and cross dispersion directions (with the whole detector, i.e. before any spectral extraction), and can be modelled by an exponential pulse height dependency. The typical detector noise count rate is  $10^{-3}$  counts  $s^{-1} \text{ \AA}^{-1}$ , for the background in the extracted spectrum.

- Soft protons entering through the mirrors. It has been found to be consistent with distributions coming from two different components, one distribution originating from protons being reflected off the grating array that results in a beam centred on the zero-order position and the other distribution having a much larger angular spread consistent with a diffuse non-scattered component. While the widths of these two distributions appear to be fixed, the overall count rate and shape are clearly variable with time. Overall particle count rates variations by a factor 20 have been measured for similar length observations. The changes in the background shape are related, according to the models, to changes in the input particle energy spectrum and on the fraction of protons that are reflected by the gratings. It is found that this fraction is correlated with the overall count rate. Quiescent background periods seem to be dominated by the diffuse component. The count rate in quiet periods is  $1-5 \times 10^{-3}$  counts  $s^{-1} \text{ \AA}^{-1}$ . It should also be noted that background fluence is generally higher on the CCDs that are closer to the primary focus (CCDs 8 and 9).

The average background spectrum has been analysed for quiet-time periods. This has been performed using clear sky images (or “blank” images) and selecting low background periods (after inspection of the light curves). The average first and second order RGS1 and RGS2 background spectra are shown in Fig. 87. The total exposure time is about 170 ks. The spectra have been extracted in a standard way for the energy, and with the full field-of-view in the cross-dispersion direction. The background count rate in the quiet period corresponds to  $1-5 \times 10^{-5}$  counts  $s^{-1}$  per RGS resolution element for a point source.

The fraction of the total exposure time which corresponds to quiet background periods is unpredictable, as it is basically linked to the solar activity itself. During the first years of XMM-Newton operations there have been both “active” and “quiet” background epochs, during which about 50% and nearly 100% (respectively) of most exposures were taken with quiet background. A significant fraction of the data collected so far has much higher background than the one shown in Fig. 87. This should be taken into account for exposure time estimates, specially if detection of weak features is the main objective of the observations.

Each of the background components described above has a very different impact on the RGS sensitivity. The first four are either rejected on board or have low intensity. The major constituents are therefore a tail on the CCD response due to readout noise, and the soft proton radiation.

#### 3.4.4.7 RGS Sensitivity Limits

The main point of the RGS sensitivity is the emission line detection threshold. To get an estimate of the exposure time necessary to detect a line above a certain underlying continuum (at a given significance level) detailed simulations should be performed. Then the line flux integrated over the HEW of the line profile should be evaluated. For such an estimate, four contributing components must be considered:

- the flux of the line,

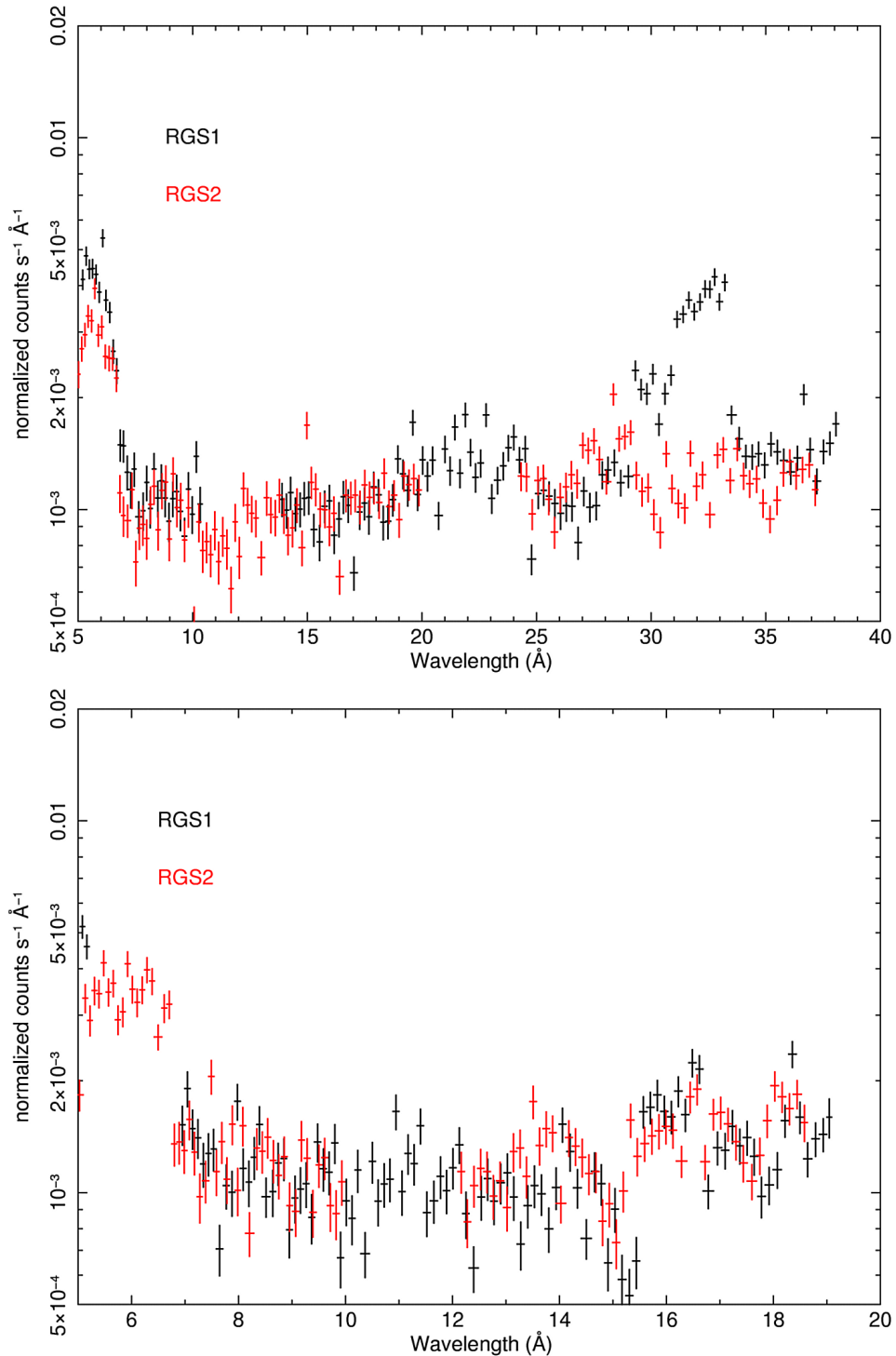


Figure 87: The average quiet background spectra from first (top) and second (bottom) order. RGS1 is shown in black and RGS2 in red. An enhancement of the count rate below 7 Å in each RGS is due to a change in the width of the pulse height filter at that wavelength. There is a bump around 32 Å in the RGS1 spectrum. The origin has not been fully understood but the most likely explanation is a somewhat higher dark current for CCD2 in this RGS. The lower background in the first order spectrum of RGS2 in this range seems to be related to the use of “single node readout” mode in this RGS.



- the flux of the underlying continuum of the source,
- the X-ray background, and
- the particle background (see § 3.4.4.6).

At the discussed energies the extragalactic X-ray background can be well reproduced by a power-law spectrum. This allows us to consider the X-ray background simply by adding an additional component to the continuum flux of the source.

Various components may feature in the data from RGS observations, such as:

- Internal X-ray calibration sources. Four calibration sources permanently illuminate the CCDs of the RFC. The emission is primarily of F-K and Al-K. They are evident as four horizontal distributions in the bottom panel of Fig. 78. The source intensity is  $0.1 \text{ counts cm}^{-2} \text{ s}^{-1}$ . Using both spatial and energy information, their contribution to the celestial spectra can be estimated.
- Optical load on the CCDs. This is caused by optical straylight. Detected optical photons will modify the gain calibration of the CCDs through an introduction of an additional energy offset. Using diagnostic mode data, these offsets can be measured.
- Background. This component is explained in detail in § 3.4.4.6. The diffuse cosmic X-ray background can be modelled assuming an isotropic spatial distribution. The soft-protons induced background is more difficult to remove. For point sources, it can be estimated by selecting a region on the CCDs in the cross dispersion direction and using the same windows in the CCD pulse height as for the source. The background estimation for spatially extended sources or low surface brightness sources (like galaxy clusters) is more problematic as it is not so simple to select an acceptable “empty” region in the cross dispersion direction. The average background described in § 3.4.4.6 could be used for quiet periods, however, as some of the components (or model parameters) are clearly variable, this is not a trivial task. The uncertainty of this method is estimated comparing the different “blank-sky” exposures used to obtain the average spectrum and it is about 30%. In some cases, EPIC data could be used to directly measure the background. As a different alternative, for extended, irregular, sources the user may consider the need for a particular position angle that could guarantee an “empty” background region in the cross dispersion direction.
- Apparent cross-talk between orders. The CCD response includes a low energy tail due to a finite number of photons producing anomalously low energy signatures. In the case of bright emission feature being measured in the second order spectrum, the intensity of this tail may become significant, as it may produce counts in the co-located first order spectrum. These effects can be easily identified in PHA or PI energy versus dispersion plane. (cf. Fig. 78).
- Effects of scattering by the gratings. Due to X-ray scattering off the gratings (about 20% at mid band), there is an additional tail of the LSF. While true source continuum emission follows the dispersion equation (the inverse relation between photon energy and wavelength), scattered light appears as an horizontal distribution in the pulse height versus dispersion plot (cf. Fig. 78). This effect can be modelled and is included in the response generator of the SAS.



### 3.4.4.7.1 Detectability of weak absorption lines

Long integrations should in principle allow the detection of weak absorption lines, but do expose systematic instrumental features that can be confused with real astrophysical lines. The ultimate sensitivity for detection of weak absorption lines is estimated at  $\approx 1.5\%$  of the continuum. This limit is reached at signal-to-noise ratios of around 70, when the statistical and the systematic uncertainties are of the same order.

### 3.4.4.8 RGS photon pile-up

RGS observations of very bright sources may show the effects of pile-up, the arrival of more than one X-ray photon in one camera pixel before it is read out, in their spectra. The potential for pile-up in the RGS spectra is discussed in this section. It is shown that pile-up is not likely to be a problem for the greatest majority of the X-ray cosmic sources. As a rule-of-thumb, pile-up effects in bright continuum sources should only be considered if integrated fluxes within one RGS CCD exceed  $\sim 1.5\text{-}3 \times 10^{-10}$  erg cm $^{-2}$  s $^{-1}$ . This level of flux integrated over the 17-21 Å (0.6-0.7 keV) range, where the RGS effective area is nearly highest, can give rise to a  $\sim 2\%$  pile-up. Only some two dozens of objects with fluxes higher than that are identified in the ROSAT All Sky Survey.

The effects of pile-up on spectra are two-fold: migration of photons from first to second order, in particular, and to higher orders generally, and rejection of events with complicated patterns by the on-board processing.

The characteristics of pile-up are likely to differ between RGS1 and RGS2 and even between CCD locations due to event-pattern variations over the detectors. Since August 2007, RGS2 is operated in single-node readout, and hence from that date on the effects of pile-up are more acute in RGS2, with double the readout time of RGS1, which is read out via two nodes.

#### 3.4.4.8.1 Pile-up prediction

For the normal spectroscopy modes listed in Table 8, it is estimated that in rough terms, any individual CCD with a total count rate in all orders of 12 counts s $^{-1}$  in RGS1 (6 counts s $^{-1}$  in RGS2) may suffer from pile-up of about 2%. It should also be borne in mind that lower limits apply for emission-line-rich sources in which some pixels are much more brightly illuminated than others.

Table 11 provides estimates of the fluxes in the individual RGS1 and RGS2 CCDs for which pile-up of the order of 2% is expected in point sources with a smooth continuum.

Pile-up on bright, narrow, emission lines should not be a major point of concern. The brightest emission lines in Capella (Fig. 90) suffer from pile-up of about 5% in RGS2 (with  $\sim 0.04$  counts per pixel per frame) and half that value in RGS1. Only two other active stars (HR 1099 and AB Dor) have occasionally reached count rates of this order during flares.

#### 3.4.4.8.2 Pile-up mitigation

The effects of pile-up can be mitigated by reducing the accumulation time. The main methods to achieve this are reading fewer CCDs, reading the most brightly illuminated CCDs more often or using the RGS Small Window mode, or even a combination of these. The XMM-SOC document XMM-SOC-CAL-TN-0075, available from

<http://www.cosmos.esa.int/web/xmm-newton/calibration-documentation>, gives more details about pile-up in RGS.

**esa**european space agency  
agence spatiale européenne

Document No.: XMM-SOC-USR-MAN-0006

Issue/Rev.: Issue 2.18

Date: 13.07.2020

Table 11: *Flux per CCD<sup>1</sup> for  $a < 2\%$  pile-up for point sources in Spectroscopy mode and using 8 CCDs<sup>2</sup>*

Instrument	CCD	Max. Flux erg cm <sup>-2</sup> s <sup>-1</sup>	Instrument	CCD	Max. Flux erg cm <sup>-2</sup> s <sup>-1</sup>
RGS1	1	$7.1 \times 10^{-10}$	RGS2	1	$3.1 \times 10^{-10}$
RGS1	2	$5.0 \times 10^{-10}$	RGS2	2	$2.1 \times 10^{-10}$
RGS1	3	$3.8 \times 10^{-10}$	RGS2	3	$1.6 \times 10^{-10}$
RGS1	4	$3.3 \times 10^{-10}$	RGS2	4	–
RGS1	5	$2.9 \times 10^{-10}$	RGS2	5	$1.5 \times 10^{-10}$
RGS1	6	$3.2 \times 10^{-10}$	RGS2	6	$1.4 \times 10^{-10}$
RGS1	7	–	RGS2	7	$1.9 \times 10^{-10}$
RGS1	8	$7.1 \times 10^{-10}$	RGS2	8	$3.7 \times 10^{-10}$
RGS1	9	$20.0 \times 10^{-10}$	RGS2	9	$14.1 \times 10^{-10}$
Double-node readout			Single-node readout		

<sup>1</sup> An estimate of which energies are sampled for a given CCD is provided in Table 9.<sup>2</sup> Limits for normal Spectroscopy mode reading 8 CCDs per exposure.If n CCDs are read, the limits increase by a factor of  $\approx 8/n$ .In Small Window mode the limits increase by a factor  $\approx 4 \times 8/n$ , see § 3.4.5.1.

#### 3.4.4.8.3 Pile-up assessment

Since pile-up most often results in the combination of two first-order events to become a single apparent second order event, a useful technique to assess its importance is the comparison of first and second order fluxed spectra. In the absence of pile-up, the effective area calibration ensures that first and second order fluxes at a given wavelength agree within a few percent. Hence, examining the ratio between first and second order can help determine whether pile-up has played a role.

Details about pile-up in RGS and the relevant methods for the assessment and management of this effect are given in the XMM-SOC Technical Note XMM-SOC-CAL-TN-0075, available from <http://www.cosmos.esa.int/web/xmm-newton/calibration-documentation>.

#### 3.4.5 Operating Modes of the RGS

All RGS CCDs are operated in the so-called “frame store” mode, in which half of each CCD is exposed to the sky. The contents of this half are transferred to the second shielded half, which works as a storage area before readout, while the first half is acquiring the next frame. Thereby, the two-dimensional dispersed photon distribution is stored.

The standard science mode of operation of the RGS instrument is called “Spectroscopy”. It consists of a two-dimensional readout of one or more CCDs over the full energy range. Each RGS1 CCD is read via two nodes, resulting in an accumulation time of 4.8 s when reading the eight CCDs. Starting in August 2007, RGS2 CCDs are read via a single node. RGS2 frame times are therefore twice as long as RGS1 frame times (accumulation time is 9.6 s when reading the eight CCDs).

The on-chip binning (OCB) factor in this mode is 3x3 pixels, after which other operations are performed on board to reduce the data rates to within the RGS telemetry bandwidth. After applying a low signal threshold, hot columns and hot pixels defined by a look-up table are



Table 12: *RGS science data acquisition modes*

Mode	Description
Spectroscopy	2-D readout of up to all CCDs over the full energy range with 4.8 s accumulation time for RGS1, 9.6 s for RGS2, for eight CCDs. Each CCD readout takes 0.6 s in RGS1 and 1.2 s in RGS2. Diagnostic images are taken in parallel.
Small Window	Similar to Spectroscopy, but only the central $\frac{1}{4}$ of the CCD rows in the cross-dispersion direction is read. Each CCD readout takes 0.15 s in RGS1 and 0.30 s in RGS2.

rejected. The remaining pixels are treated by a programmable processor (DPP). Pixels exceeding an upper signal threshold and pixels with complex structures due to cosmic rays are rejected, and only events which fit in a pattern are transferred to the ground including information on their shape.

Each individual chip or any combination of chips can be read out. The energy range covered depends on which CCDs are read out and on the positioning of the source within the field of view. A rough estimate of which energies are sampled if a given CCD is read out is provided in Table 9.

In parallel to the recording of science data, diagnostic images are transferred to the ground. One complete CCD of each RGS is read in this way every 1500 s. The on-board data processing is bypassed and the entire CCD image or “Q-dump” is transferred to ground. These data are used by the instrument and calibration teams for dark current and system noise level verification with the aim to identify possible instrument degradation with time and/or changes affecting the health of the RGS instruments. These data are now routinely used to improve the calibration of the CCD offsets.

Telemetry bandwidth limitations can be an issue in observations of very bright sources. In the cases in which the estimated count rate is so high that this problem is expected, the telemetry requirements can be reduced by disabling the download of the diagnostic frames. This is the so-called High Count Rate (HCR) mode. The few cases that would require the use of this mode will be identified and evaluated by the SOC during the proposal enhancement process.

The Spectroscopy mode has been used for almost all observations and is the recommended configuration. For the few 20 brightest X-ray sources, the Small Window mode (§ 3.4.5.1) may be considered.

Some basic characteristics of the RGS science modes are listed in Table 12.

### 3.4.5.1 RGS Small Window Mode

Available first in AO-10, the RGS Small Window (SW) mode allows the effects of pile-up in very bright sources to be mitigated. In RGS Small Window mode only the central 32 of the 128 CCD rows in the cross-dispersion direction ( $\frac{1}{4}$  of the 5 arcmin aperture) are read. The CCD readout time is therefore decreased by a factor 4 compared to Spectroscopy mode.

The RGS SW mode is relevant if wavelengths important for the scientific success of the observation are likely to be affected by pile-up (see §. 3.4.4.8). Using the RGS SW mode, the point-source flux limits for 2% pile-up given in Table 11 increase by a factor 4 if all the eight



CCDs are used, and even more if less than 8 CCDs are read or if one CCD is read more often than the others.

This mode is not intended for routine use or, in particular, where simultaneous estimates of the background spectrum are crucial, as is usually the case. It is designed for the benefit of very bright sources, where both pile-up is expected and the background is negligible.

A number of further considerations must be taken into account in order to decide if the mode could be applied with profit for a given observation.

Due to the high telemetry requirements of the RGS SW mode, both EPIC-MOS cameras must be disabled, and the EPIC-pn maximum available telemetry bandwidth is reduced from 40 to 31 kb s<sup>-1</sup>. Overall, the impact of the telemetry limitations on EPIC MOS and pn is considered to be minor. On one side the upper flux limit to avoid pile-up on the MOS cameras is 35 mCrab (see Table 3). On the other side, the recommended EPIC-pn modes for bright source observations are Timing and Burst, and only the former has telemetry bandwidth limitations (see Table 3). For very bright point sources for which the RGS SW mode may be considered, such as black-hole binaries in outburst, where fluxes of 80 mCrab or more have been recorded, the EPIC-pn camera is likely to be operated in its Burst mode.

Observers considering use of the RGS SW mode should also make an explicit judgement concerning the background. Naturally, in the absence of data from the cross-dispersion edges of the CCDs, the background cannot be estimated in the normal way from those parts of the detector. While this is of little importance for the brightest parts of a continuum spectrum, interstellar absorption at long wavelengths, for example, often reduces the observed intensity towards values near the expected background value. It is conceivable, therefore, that measurements of a variety of interstellar absorption edges, for example, could require a mixed observational approach, using the RGS SW mode at short wavelengths and the normal mode elsewhere, although with some operational constraints, explained below. In general terms, the detailed expected shape of the spectrum and the corresponding observational objectives must be taken into account. This may be especially relevant for very bright line-rich sources (§. 3.4.4.8.1).

There are some operational restrictions on how normal Spectroscopy and SW modes can be combined. The most important ones are summarised here.

- It is possible to request one RGS camera to operate in SW mode while the other is operated in normal Spectroscopy mode. However, the impact on the EPIC MOS and pn telemetry allocations outlined above remains unchanged as long as one of the RGS instruments is in SW mode.
- SW exposures running on both RGS cameras must end simultaneously.
- If the same instrument is required in the two modes, then two consecutive exposures need to be made, taking into account the previous requirement.
- Within a single exposure, it is not possible to read different CCDs in different modes.

### 3.4.5.2 RGS Multipointing Mode (MPM)

Most RGS observations are performed with the target at a central fixed location on the RGS detectors, close to the telescope axes. There are, however, some circumstances in which observers might consider the alternative “RGS Multipointing Mode” (MPM).

A small proportion of defects comprising bad or “cool” columns or pixels are inevitable in CCD detectors. In a dispersive instrument like the RGS, these detector defects, usually one pixel wide, correspond to fixed narrow wavelength intervals of about 10 mÅ (see Tables 13 and 14). These

Table 13: *RGS1 detector defects and corresponding wavelengths for on-axis sources.*

Lambda (Å)	CCD	CHIPX <sup>a</sup>	Type	Lambda (Å)	CCD	CHIPX <sup>a</sup>	Type
6.37	9	171	node gap	22.75	4	171-172	node gap
7.70	8/9		chip gap	22.80	4	167	cool pixel
8.93	8	193	cool pixel	22.97	4	152-153	hot/cool pixels
9.11	8	171-172	node gap	23.40	4	113-115	hot/cool pixels
9.66	8	104	cool pixel	24.12	4	51	cool pixel
10.15	8	44-45	cool pixels	24.29	4	35-36	cool pixels
14.45	6	266-267	hot/cool pixels	24.76	4/3		chip gap
15.25	6	183-187	hot/cool pixels	25.88	3	250	cool pixel
15.33	6	177	cool pixel	26.66	3	186	cool pixel
15.39	6	171-172	node gap	26.85	3	171-172	node gap
15.45	6	165	cool pixel	27.35	3	129-130	cool pixels
15.50	6	160	cool pixel	27.65	3	105	cool pixel
15.84	6	124-125	cool pixels	27.76	3	96	cool pixel
16.43	6	65	cool pixel	28.27	3	54	cool pixel
17.12	6/5		chip gap	28.78	3	12	cool pixel
17.56	5	301	cool pixel	29.01	3/2		chip gap
18.36	5	224-225	cool pixels	30.37	2	237	cool pixel
18.69	5	194	cool pixel	31.22	2	171-172	node gap
18.93	5	171-172	node gap	31.29	2	165-166	cool pixels
18.96	5	168	cool pixel	33.51	2/1		chip gap
19.51	5	115-116	cool pixels	34.02	1	304-307	cool pixels
19.68	5	100	cool pixel	35.85	1	171-172	node gap
19.90	5	79	cool pixel	36.20	1	146	hot pixel
20.81	5/4		chip gap	36.77	1	104	cool pixel
21.82	4	252-253	cool pixels	36.78	1	103	cool pixel
22.19	4	220	cool pixel	37.35	1	62	cool pixel

<sup>a</sup>Pixel position of defect in detector x-coordinates. The conversion to wavelength is given only for on-axis sources.

wavelength defects sometimes coincide with features in the source spectrum that are important for the scientific success of an observation. When these circumstances arise, it is possible to change the spacecraft pointing in order to move the defects away so that more important parts of the spectrum are not affected. Also the small gaps between the CCDs may be filled with data in a similar way using this method.

The RGS Multipointing mode uses five different pointings, with offsets in the dispersion direction of 0,  $\pm 15$  and  $\pm 30$  arcsec, corresponding to 0,  $\pm 35$  and  $\pm 69$  mÅ. In this way, the maximum flux loss in a spectral line is reduced significantly, and it becomes easier to distinguish weak absorption lines from defects.

The user is referred to § 4.6.2 for full details and a discussion of the implications of the use of this mode in the performance of EPIC-pn.

### 3.4.6 RGS specific proposal submission information

In the preparation of RGS observing proposals, the following information should be taken into account.

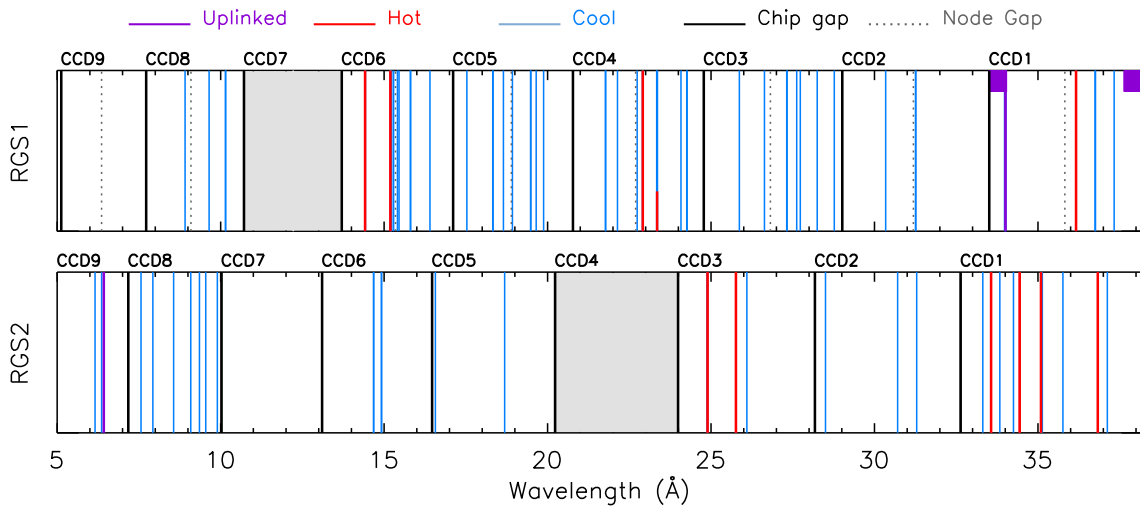


Figure 88: *Scheme of the position of the RGS detector defects in wavelength space.*

Table 14: *RGS2 detector defects and corresponding wavelengths for on-axis sources. Since the introduction of single-node operations, the node gap that applies between the two nodes of the RGS1 CCDs is no longer relevant in RGS2.*

Lambda (Å)	CCD	CHIPX <sup>a</sup>	Type	Lambda (Å)	CCD	CHIPX <sup>a</sup>	Type
6.17	9	130	cool pixel	24.92	3	265-266	hot/cool pixels
6.37	9	103	cool pixel	25.81	3	192	hot pixel
6.43	9	94	hot pixel	26.15	3	164	cool pixel
7.18	9/8		chip gap	28.20	3/2		chip gap
7.59	8	292	cool pixel	28.53	2	316	cool pixel
7.96	8	246	cool pixel	30.75	2	142	cool pixel
8.60	8	167	cool pixel	31.33	2	97	cool pixel
9.12	8	103	cool pixel	32.65	2/1		chip gap
9.38	8	71	cool pixel	33.34	1	291	cool pixel
9.57	8	48	cool pixel	33.60	1	272	hot pixel
9.91	8	6	cool pixel	33.87	1	252	cool pixel
10.01	8/7		chip gap	34.29	1	221	cool pixel
13.10	7/6		chip gap	34.48	1	207	hot pixel
14.71	6	174-175	cool pixels	35.13	1	159	hot pixel
14.95	6	149-150	cool pixels	35.17	1	156	cool pixel
16.47	6/5		chip gap	35.79	1	110	cool pixel
16.58	5	332	cool pixel	36.84	1	33	hot pixel
18.72	5	126	cool pixel	37.12	1	12	cool pixel

<sup>a</sup>Pixel position of defect in detector x-coordinates. The conversion to wavelength is given only for on-axis sources.



**esa**

European space agency  
agence spatiale européenne

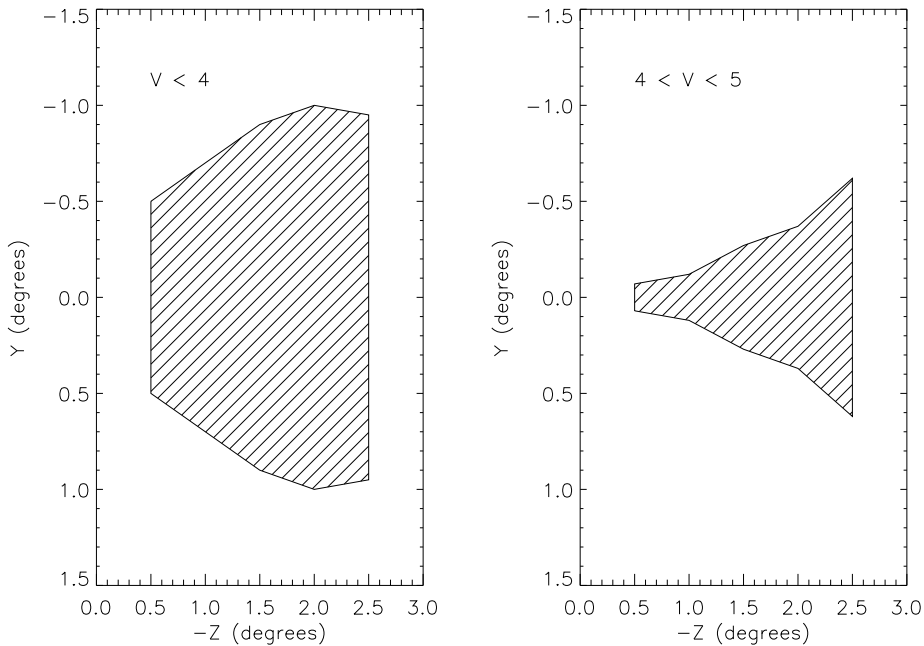


Figure 89: *RGS avoidance angles for sources brighter than 4 and between 4 and 5 optical magnitudes (left and right panel, respectively).*  $-Z$  is the dispersion direction of RGS,  $Y$  is the cross-dispersion direction.

#### 3.4.6.1 RGS avoidance angles

Visual light from bright sources can enter the RGS under certain angles, as displayed in Fig. 89. To prevent contamination of RGS observations, such sources must be avoided.

Observers should be always aware of the potential for what would otherwise be unexpected and unwelcome contributions to their RGS data from other sources that happen to lie along the dispersion axis. The diffraction equation will be satisfied for objects even quite far away in this direction, including those outside the EPIC field-of-view, giving a flux on the RGS CCDs further determined by telescope vignetting. For example, for calibration purposes the brightest source in the sky, Sco X-1, was observed on one occasion 40 arcminutes from the nominal pointing position in order to move light of a particular wavelength onto another CCD. The density of bright X-ray sources is low enough for problems of this type to be extremely rare. In any case, they may be avoided by a judicious choice of position angle.

The choice of position angle is entirely at the responsibility of the Guest Observer. Should an observation become too constrained due to these avoidance angles, GOs may consider violating these regions, depending on the scientific impact on their proposal.

#### 3.4.6.2 RGS flux to count rate conversion

For the conversion of flux to RGS count rates or of count rates from other X-ray satellites to count rates expected for the RGS instruments, we recommend the use of the SAS task '*rgsrmfgen*' to generate a response matrix to be used for simulations, and/or the use of the *PIMMS* software



at NASA's HEASARC<sup>5</sup>.

### 3.4.6.3 RGS spectral quality

Examples of RGS spectra are given in Figs. 90 to 99. A significant fraction of the apparent continuum background measured underneath the Fe-L forest, is due to scattered light. This is included in the response matrix of the instrument, which has to be used to determine the underlying spectral properties.

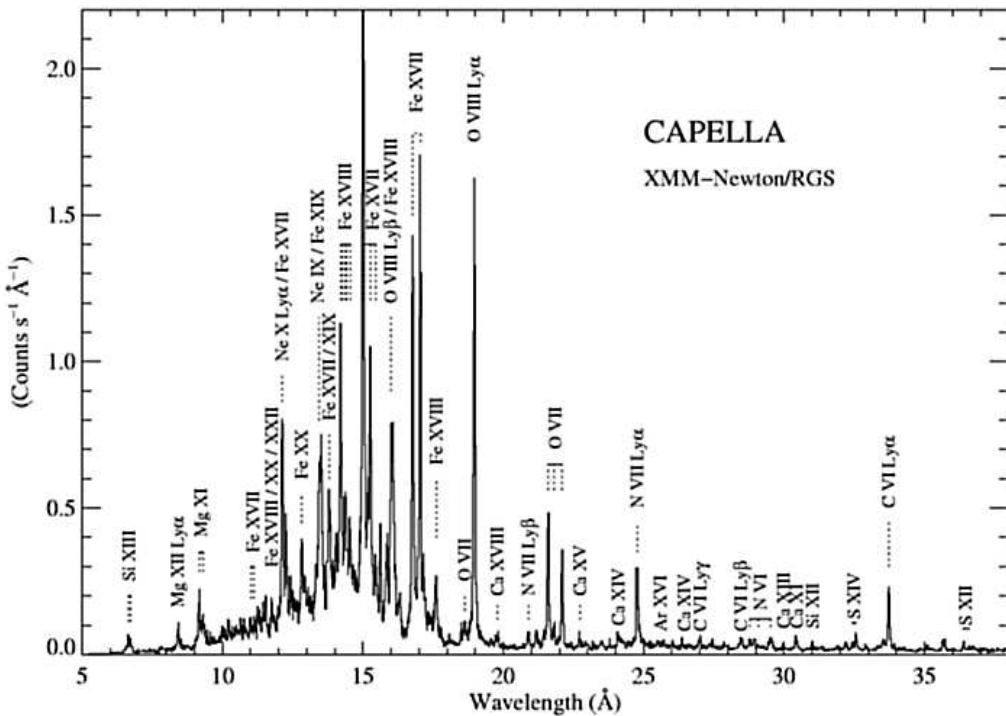


Figure 90: Coronal spectrum of the binary star Capella adapted from Audard et al. 2001, *A&A* 365, L329. The RGS1 first order spectrum is shown with some line identifications. The total exposure time is 53 ks.

<sup>5</sup><http://heasarc.gsfc.nasa.gov/Tools/w3pimms.html>



**esa**

european space agency  
agence spatiale européenne

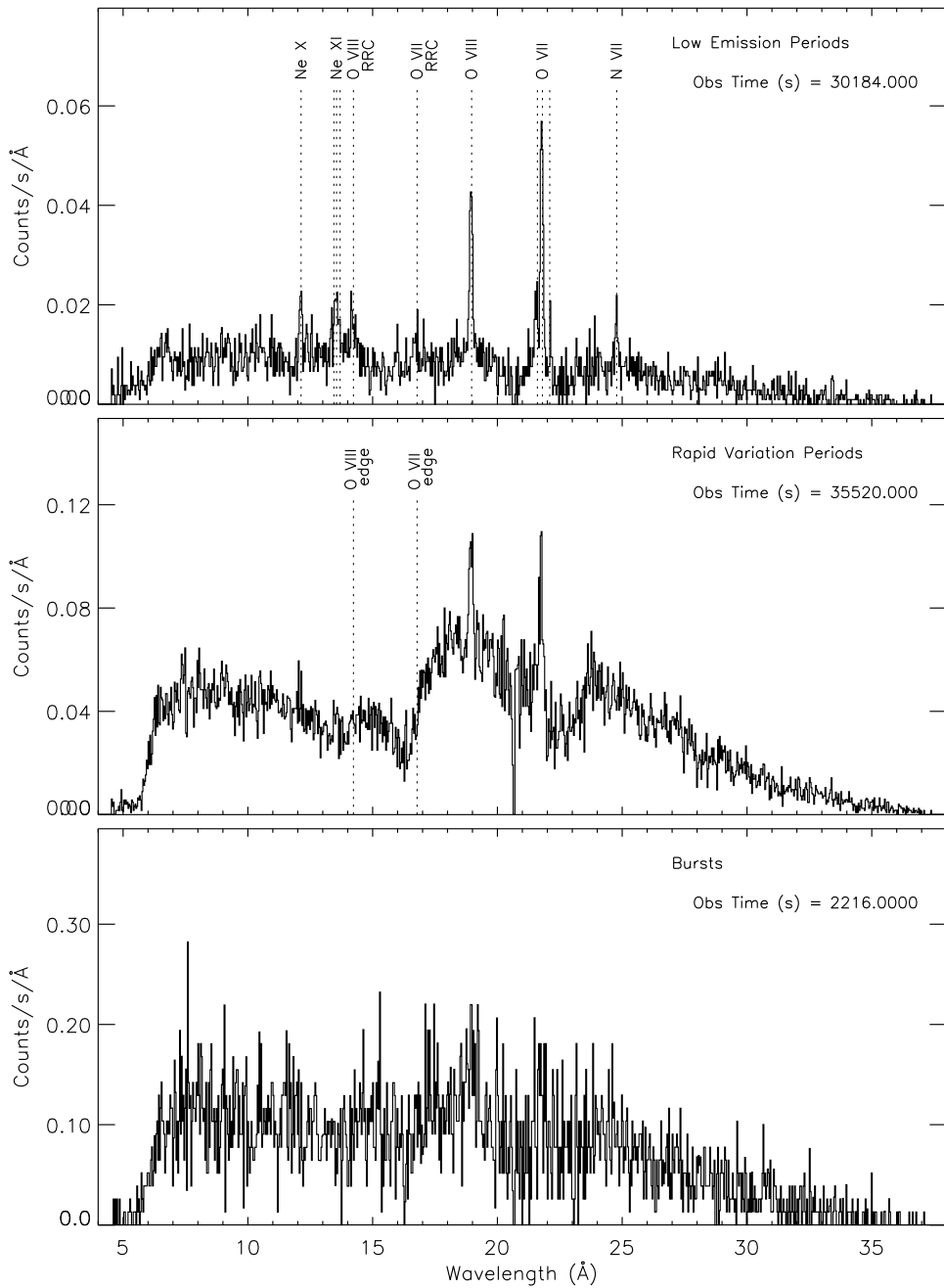


Figure 91: *RGS spectra of the highly variable low-mass X-ray binary EXO 0748-67. The three panels show the spectra for three different activity states: low emission, active variation and burst. The spectra are binned to  $0.035 \text{ Å}$  per bin. The cumulative exposure time for each spectrum is indicated (Cottam et al. 2001, A&A 365, L277).*



**esa**

European space agency  
agence spatiale européenne

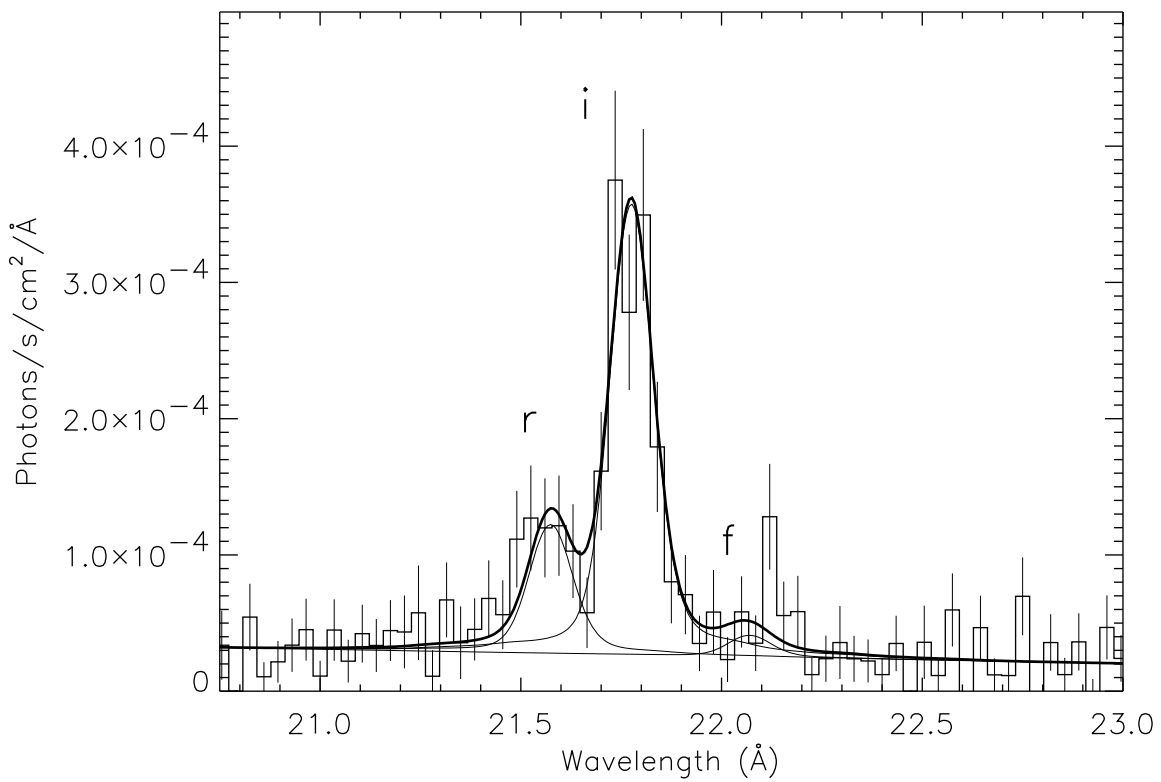


Figure 92: Detail of the EXO 0748-67 RGS spectrum. The O VII He-like lines are shown overlaid with the instrument line spread function, broadened to account for a  $1390 \text{ km s}^{-1}$  velocity field. The contributions from the resonance line (r), intercombination lines (i), and forbidden line (f) are shown with thin lines. The thick line shows the combined fit (Cottam et al. 2001, *A&A* 365, L277).



**esa**

european space agency  
agence spatiale européenne

Document No.: XMM-SOC-USR-MAN-0006

Issue/Rev.: Issue 2.18

Date: 13.07.2020

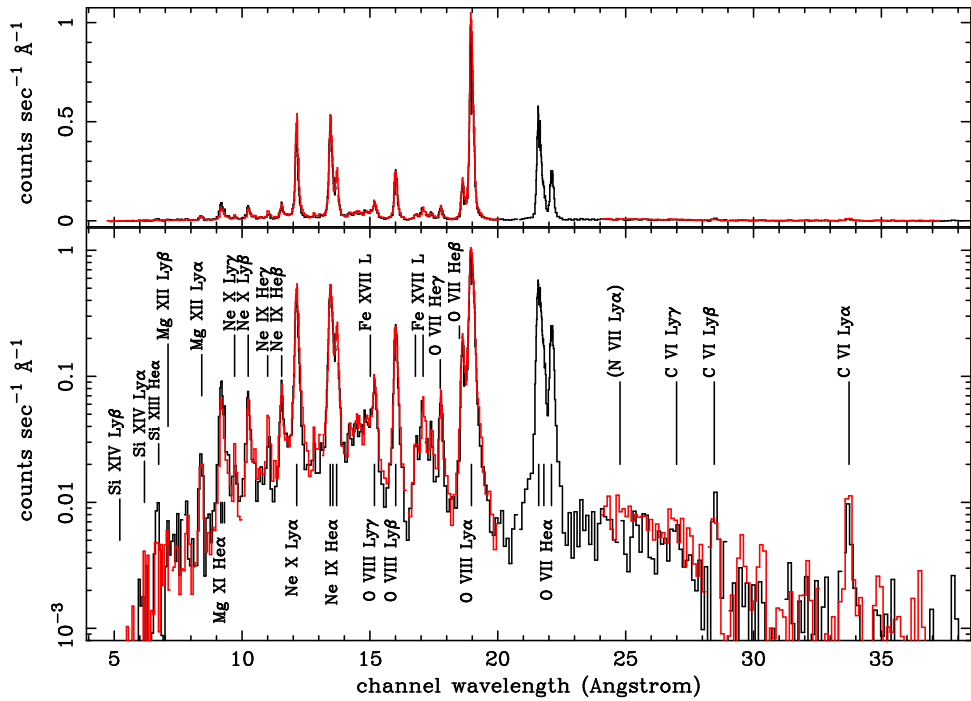


Figure 93: The first order RGS spectrum of the SMC supernova remnant 1E 0102.2-7219. The effective exposure time is 29.7 ks for each RGS after selection of low background periods in a 37.9 ks exposure. RGS1 is plotted in black, RGS2 in red. The data are shown in both linear and logarithmic scales. This figure and the next show that almost the nominal RGS spectral resolution can be achieved even for moderately extended ( $\approx 2'$ ) objects (Rasmussen et al., 2001, *A&A* 365, L231).

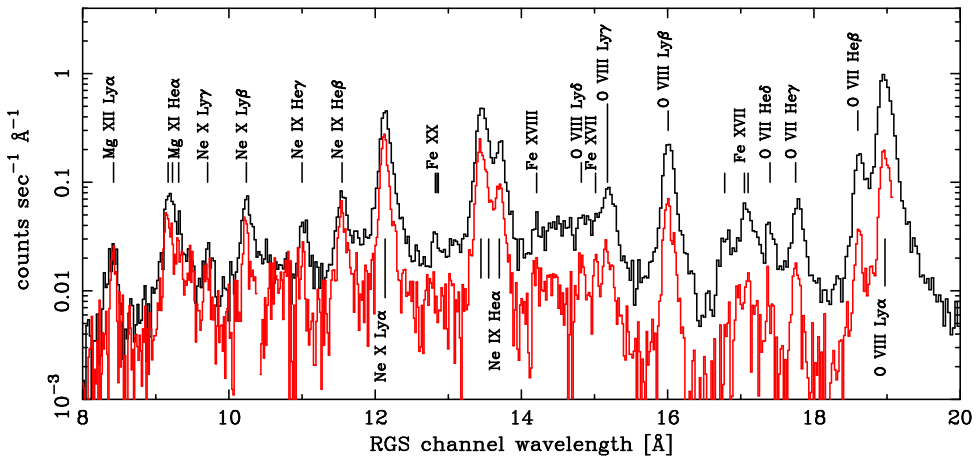


Figure 94: Detail of the 8-20  $\text{\AA}$  region of the spectrum shown in the previous figure. First (black) and second (red) order are plotted separately. The data from the two spectrometers have been averaged for each order extraction. The higher spectral resolution and resilience to source extent is clearly seen in second order, where some line complexes blended in first order are resolved (Rasmussen et al., 2001, *A&A* 365, L231).

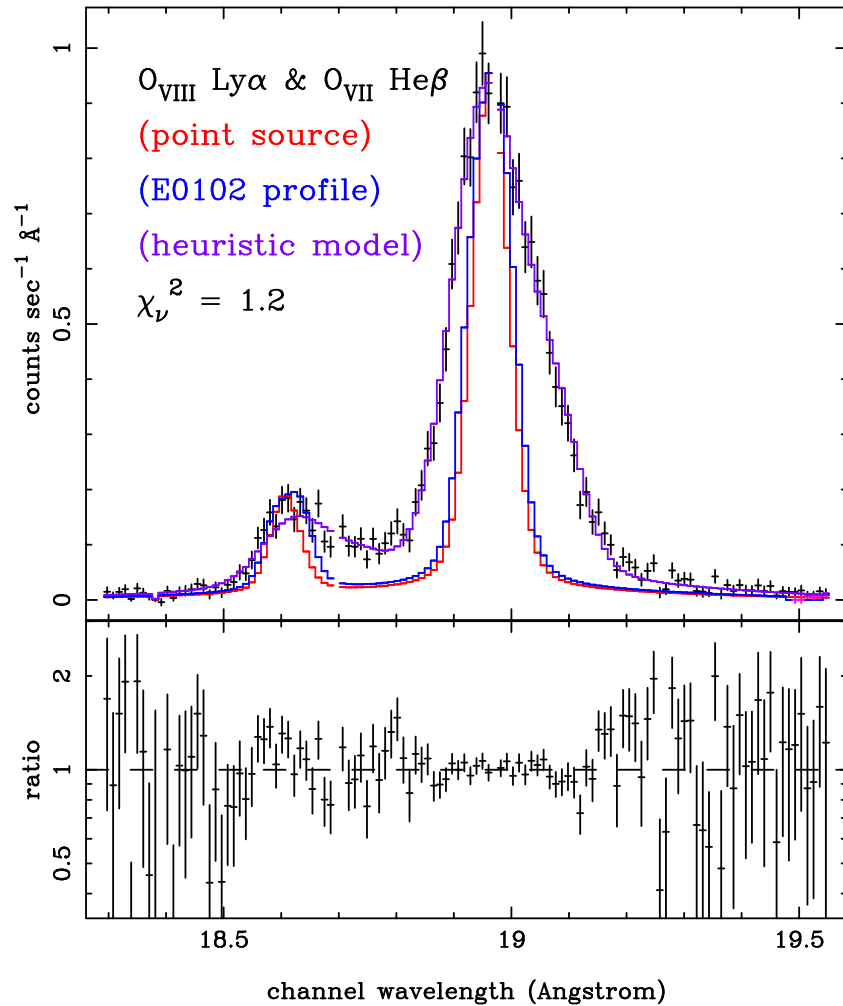


Figure 95: Detail of the Oxygen line profile in the 1E 0102.2-7219 spectrum. The plot compares the point source line spread function for RGS1, the approximate monochromatic line profile based on the target's angular distribution and a heuristic wavelength broadening function that is applied in addition to the angular distribution (Rasmussen et al., 2001, *A&A* 365, L231).



**esa**

European space agency  
agence spatiale européenne

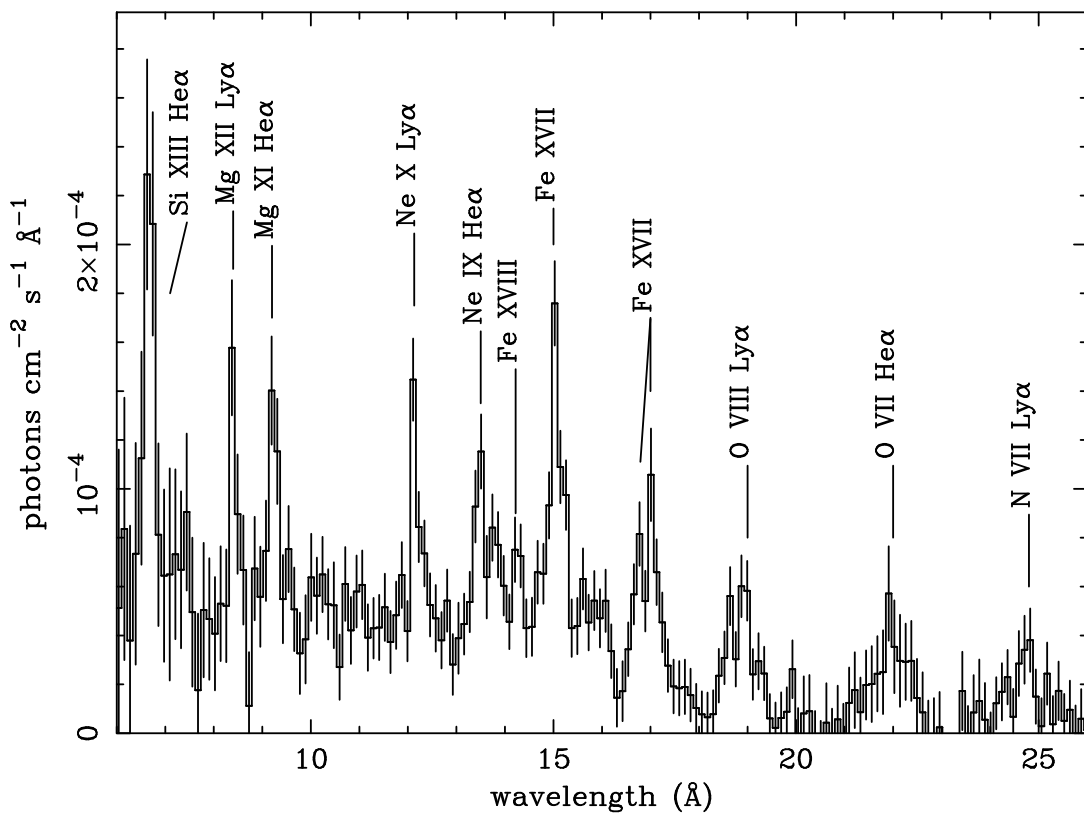


Figure 96: *RGS spectrum of the bright starburst nucleus of the nearby edge-on galaxy NGC 253, binned to  $0.07 \text{ \AA}$  per bin. The effective exposure time is  $\approx 53.4 \text{ ks}$  for each spectrograph, after selection of low background periods. The extraction region is  $1'$  along the minor disk axis. (Pietsch et al. 2001, A&A 365, L174).*



**esa**

European space agency  
agence spatiale européenne

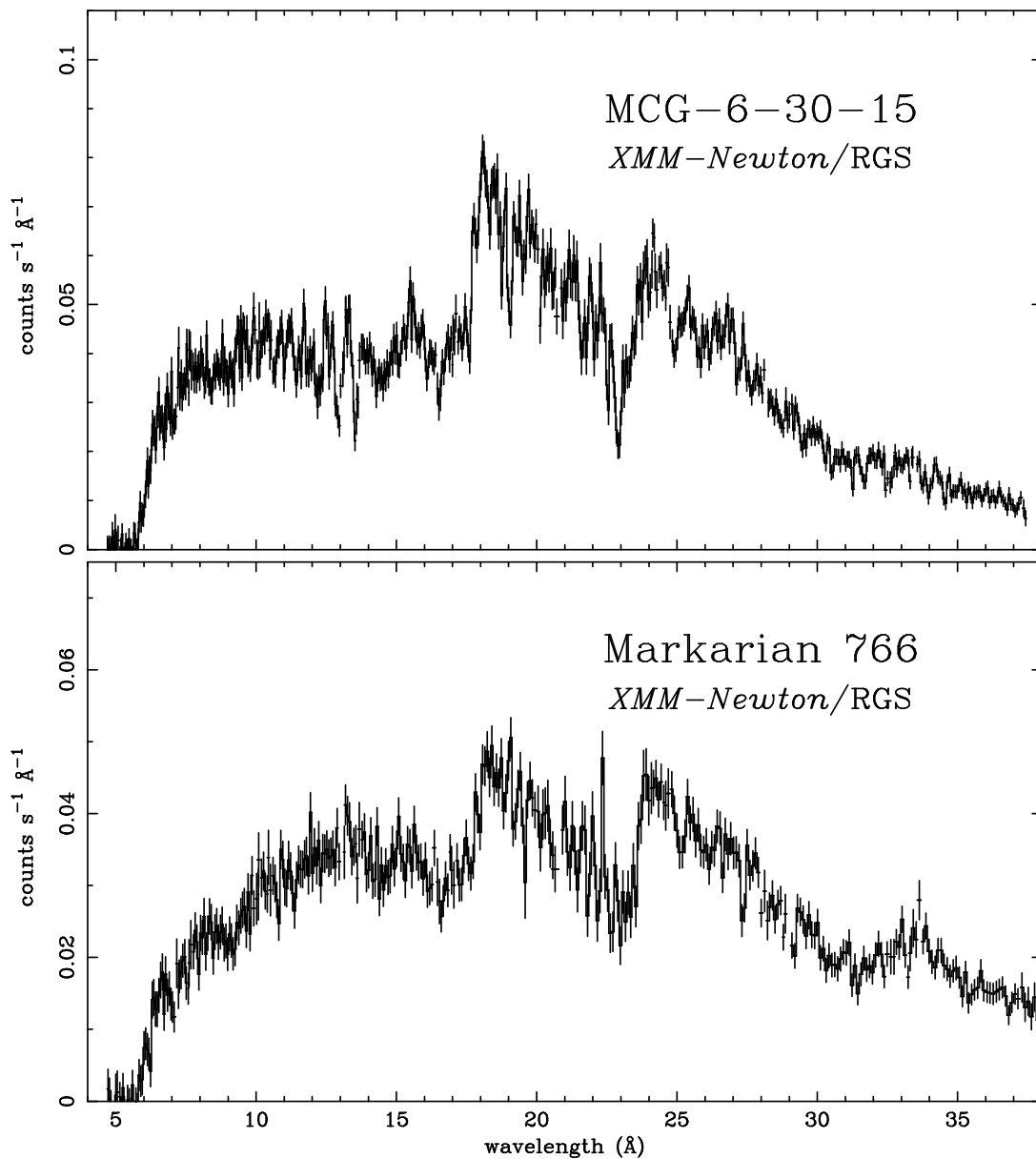


Figure 97: RGS spectra of two bright, nearby, Narrow Line Seyfert 1 galaxies. MCG-6-30-15 (top) was observed for a total of 120 ks while the exposure time for Mrk 766 (bottom) was 55 ks. (Branduardi-Raymont et al. 2001, A&A 365, L140).

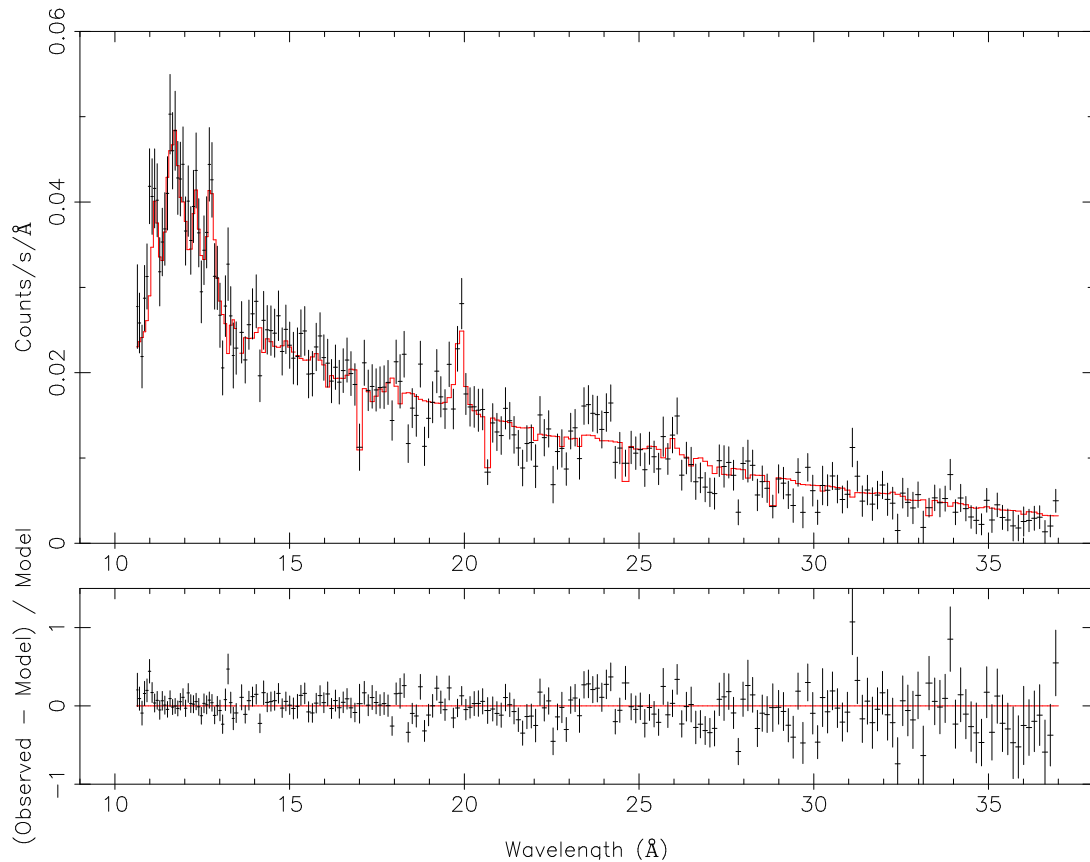


Figure 98: The RGS spectrum of the rich cluster of galaxies Sérsic 159-03 (Abell S 1101). The effective exposure time is 36 ks. The plot also shows in red a fit with a two component cooling flow model. Note the redshifted O VIII Ly  $\alpha$  line at 20.0  $\text{\AA}$  and the Fe XXIV, Fe XXIII and Ne X lines between 11.2 and 12.8  $\text{\AA}$  (Kaastra et al. 2001, A&A 365, L99).

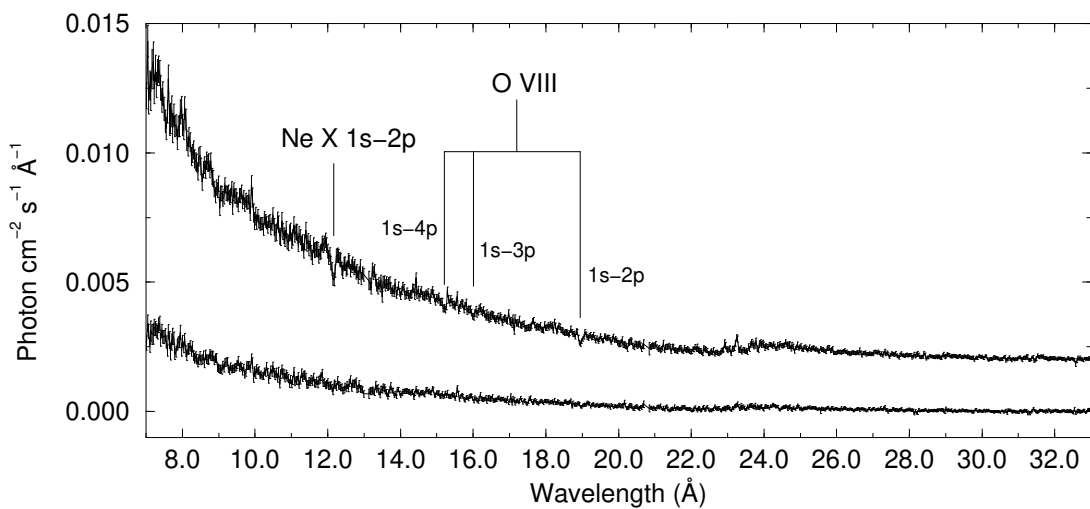


Figure 99: First order RGS spectra of the dipping, transient low-mass X-ray binary MXB 1658-298. The upper curve is the persistent emission spectrum and the lower curve that of the dipping intervals. Narrow absorption lines of O VII and Ne X are visible in the persistent spectrum revealing the presence of a warm absorber (Sidoli et al. 2001, A&A 379, 540).



### 3.5 OPTICAL MONITOR (OM)

Besides its three X-ray telescopes, XMM-Newton also has a co-aligned 30-cm optical/UV telescope (OM), providing strictly simultaneous observations in the X-ray **and** optical/UV regime from a single platform. A summary of OM's salient properties is provided in Table 15. Although small in size, the OM is a powerful instrument because of the absence of atmospheric extinction, diffraction and background. It has three optical and three UV filters over the wavelength range from 180 to 600 nm. Images of the central part of the X-ray field of view with a resolution of ca. 1'' (depending on instrument configuration), low-resolution grism spectra of the optical counterparts of X-ray sources or high time-resolution photometry can be obtained. Due to the extreme sensitivity of the detector, the OM is well suited for observations of faint sources. However, observations of optically bright sources would cause permanent damage to the detector ( $m_V \leq$  ca. 7.4 mag, for an A0 star with the V filter), thus, the OM can not be used if a bright optical source is in the field. The OM is a photon-counting instrument, therefore, as explained below, objects with high photon rates, even within the safety limits, will produce poor quality data.

#### 3.5.1 OM telescope

The OM telescope consists of  $f/12.7$  modified Ritchey Chrétien optics (see schematic in Fig. 100). From the primary mirror, incoming light is reflected onto a secondary from where it is reflected onto a rotatable  $45^\circ$  flat mirror located behind the primary, which can direct the beam onto one of two detector assemblies operated in cold redundancy. See more details of the telescope parts at: [http://www.mssl.ucl.ac.uk/www\\_astro/xmm/om/om.html](http://www.mssl.ucl.ac.uk/www_astro/xmm/om/om.html)

Spectral resolution can be achieved by the use of narrow-band filters contained within the

Table 15: *OM characteristics – an overview*

Total bandwidth <sup>1</sup>	180 – 600 nm
Spectral bandwidth <sup>2</sup>	180 – 600 nm
Sensitivity limit <sup>3</sup>	20.7 mag
Field of view	ca. 17'
Pixel size	0.476513 arcsec/pxl
PSF ( <i>FWHM</i> )	1''.4 – 2''.4
Timing resolution <sup>5</sup>	0.5 s
Resolving power <sup>6</sup>	~ 180
Brightness limit <sup>7</sup>	$m_V = 7.4$ mag

Notes to Table 15:

1) See Fig. 102 for filter bandpasses.

2) Covered by two grisms.

3) 5- $\sigma$  detection of an A0 star in 1000 seconds (B filter; see Table 22).

4) Depending on the filter

5) In the Fast Mode.

6)  $\lambda/\Delta\lambda$  in the optical and UV grisms.

7) Highest magnitude of a star, which can be observed with the OM without exceeding the instantaneous maximum flux. This *brightness limit* is dependent on the filter and the spectral type. The number quoted in Table 15 refers to an A0 star with the V filter; see also Table 25. The *dose limit* is instead related to the total amount of photons detected during a whole observation.



**esa**

european space agency  
agence spatiale européenne

Document No.: XMM-SOC-USR-MAN-0006

Issue/Rev.: Issue 2.18

Date: 13.07.2020

Optical Monitor's filter wheel; there are also two grisms in the filter wheel for low resolution spectroscopy.

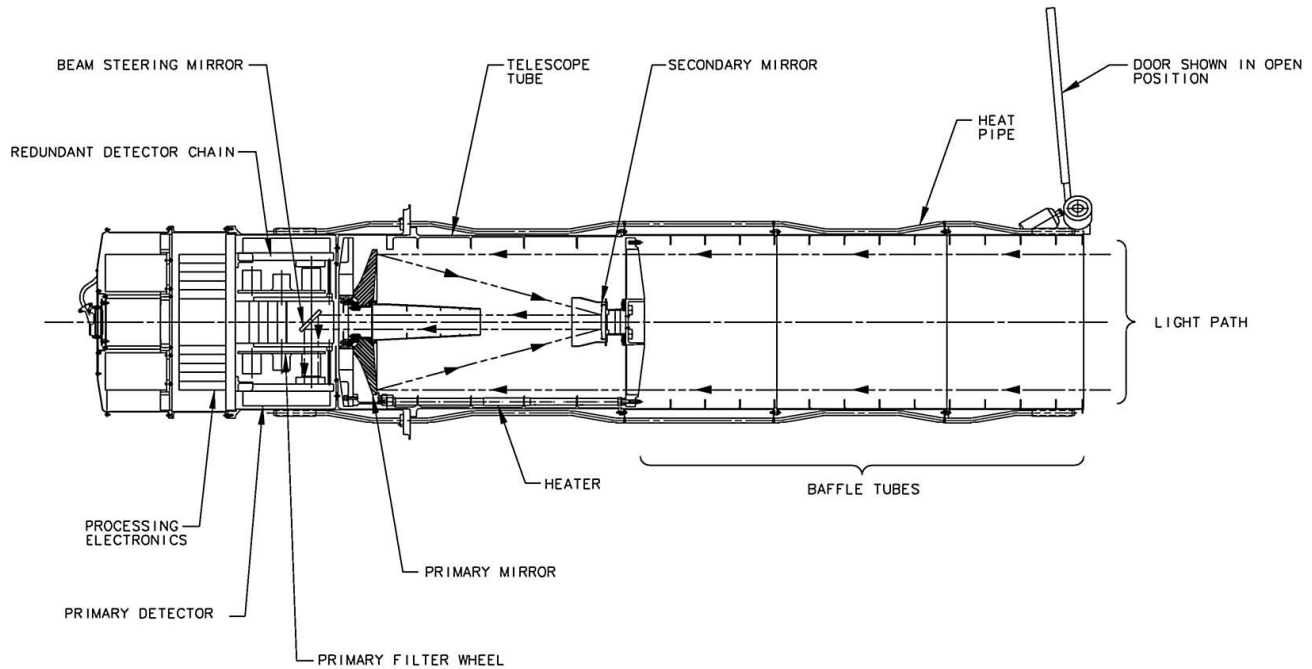


Figure 100: *The light path in XMM-Newton's optical/UV telescope, OM.*

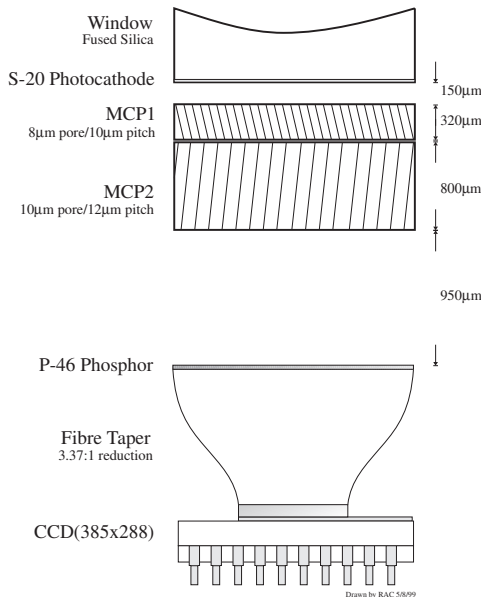
### 3.5.2 OM detector

The OM detector is a compact image-intensified photon-counting instrument. Each of the (redundant) OM detectors consist of a micro-channel plate (MCP) intensified CCD (MICs) with  $384 \times 288$  pixels, 256×256 of which are usable for science observations. Each CCD pixel has a size of about  $4'' \times 4''$  on the sky. Photons coming from the  $45^\circ$ -mirror enter the detector and hit the photo-cathode, from where electrons are pre-amplified by two successive MCPs (Fig. 101). This leads to an amplification of the signal by a factor of ca.  $10^5$ . The detector achieves a large format through a centroiding technique, subsampling the  $256 \times 256$  CCD pixels into  $8 \times 8$  pixels each, as described in the next section. Therefore, the final array has a format of  $2048 \times 2048$  pixels, each about  $0''.476 \times 0''.476$  on the sky. The field of view is therefore  $1024''$  on a side, or  $17' \times 17'$ . The light-sensitive surface is an S20 photocathode optimised for the UV and blue. This provides sensitivity from 180 nm (set by the detector window) to 600 nm.

The internal noise (dark noise) of the detector is extremely low. However, in the UV the Galactic diffuse background amounts to about 7% of the rate seen in darkframes. It can generally be ignored by comparison with other, cosmic sources of background, although it may play a role for diffuse faint sources (*e.g.*: diffuse galactic light).

#### 3.5.2.1 Imaging with OM

As mentioned above and shown in Fig. 101, photons entering the OM detector hit a photo-cathode, which is located at the backside of the detector entrance window. Electrons emanating



Schematic Structure of Detector Head

Figure 101: Sketch of the OM micro-channel plate intensified CCD (MIC) detector.

from the photo-cathode are amplified by the MCPs, creating photon splashes at the location of the OM CCD. The detection of a photon entering the detector is performed by reading out the CCD and determining the photon splash's centre position using a centroiding algorithm, which is part of the onboard software. In the process of centroiding a grid of  $8 \times 8$  "in-memory" pixels is defined, leading to an array of  $2048 \times 2048$  in-memory pixels with an approximate size of  $0''.476$  on the sky. In the resulting images at some level there is always a pattern repeating on an  $8 \times 8$  grid, resulting from a limitation in the algorithm. This spurious pattern can be removed by subsequent processing on ground.

As with all photon-counting detectors, there is a limit to the maximum count rate achievable before saturation sets in. The frame time<sup>6</sup> of the OM detector is about 11 ms at slowest, so a linearity correction must be applied in the offline data processing for count rates above ca. 10 counts/s for point sources. Both *deadtime* and *coincidence losses* contribute to the non-linearity of the OM detector. These effects are corrected by using SAS in the data reduction. Deadtime losses are due to the lack of instrumental response during a frame transfer. Coincidence loss

<sup>6</sup> *Frametransfer time* is the time needed to transfer the charge accumulated on the continuously exposed CCD during an integration time into the storage area. It amounts to  $\approx 0.1740$  ms. The sum of the integration time and the frame transfer time is the *frametime*. The frametime depends on the sizes, shapes and positions of the windows. For a full frame it amounts to about 11 ms. The only time when source photons are not properly recorded by the detector is during charge transfer. Therefore, the *deadtime* is equal to the frametransfer time.



is observed whenever the count rate is such that more than one photon arrive in the same pixel within a given readout frame. Deadtime becomes important for short frametime. On the other hand, longer frametimes are more likely affected by coincidence losses. These effects are quantitatively described in § 3.5.5.

In addition, sources which are too bright can depress the local sensitivity of the photocathode: this is a cumulative effect, so that fainter sources observed for long times have the same effect as brighter sources observed for shorter periods. This places some operational constraints on the instrument. Pointing of bright sources may also yield ghost images in subsequent observations due to fluorescence.

Cosmetically, the OM detectors are good, with few hot or dead pixels, and little global variation in quantum efficiency. Pixel to pixel sensitivity variations on the OM CCD are in some way smoothed by the centroiding mechanism producing the final pixels, as described above. Local sensitivity gradients are negligible on scales up to two minutes of arc.

It should be noted that due to an accidental observation of Jupiter in July 2017, a decreased sensitivity region of about 210 x 120 pixels appeared close to the center of the detector. The highest loss of sensitivity occurs with the V filter ( $\sim 35\%$ ) in the centre of the region. See Sect. 3.5.5 for more details.

### 3.5.3 OM optical elements

The OM is equipped with a filter wheel holding several optical elements that can be moved into the light path. These elements, which are described here, comprise not only lenticular filters, but also two grisms. The complete set of optical elements is collected in Table 16. Their arrangement on the OM filter wheel is indicated by the position number on the filter wheel. **Sequences of exposures using different optical elements must always have increasing filter wheel position numbers.** Observations with the three UV broad-band filters UVW1, UVW2, and UVM2, for example, must always be conducted in the order UVW1, UVM2, UVW2 (positions 7, 8 and 9).

From AO-16 (announced in 2016) it is possible for programmes with specific approval by OTAC to perform several turns of the filter wheel. In other words it is possible to perform series of exposures in which a sequence of filters (ordered in increasing filter wheel position numbers) is repeated several times.

#### 3.5.3.1 OM filter band passes

The OM set of filters covers part of the UV and optical range. The filter throughput curves are displayed in Fig. 102. The plotted quantity is the OM effective area for a given filter including the entire telescope response based on inflight measurements. Aperture radius is 6" for the optical and 17".5 for the UV filters.

The OM effective area has been corrected for time dependent sensitivity degradation. The current throughput in year 2020 is lower due to time dependent sensitivity degradation, about (16, 7, 8, 13, 19, 22) percent for (V, B, U, UVW1, UVM2, UVW2) filters, respectively. The time dependent sensitivity degradation correction for any observing epoch can be found in the corresponding CCF (OM\_PHOTTONAT\_0008.CCF, see XMM-CCF-REL-378 and references therein).

The principal characteristics of the OM filters are listed in Table 17.



Table 16: *OM optical elements*

Filter wheel position number	Filter name
0	Blocked
1	V
3	U
4	B
5	White
6	Grism 2 (visible)
7	UVW1
8	UVM2
9	UVW2
10	Grism 1 (UV)

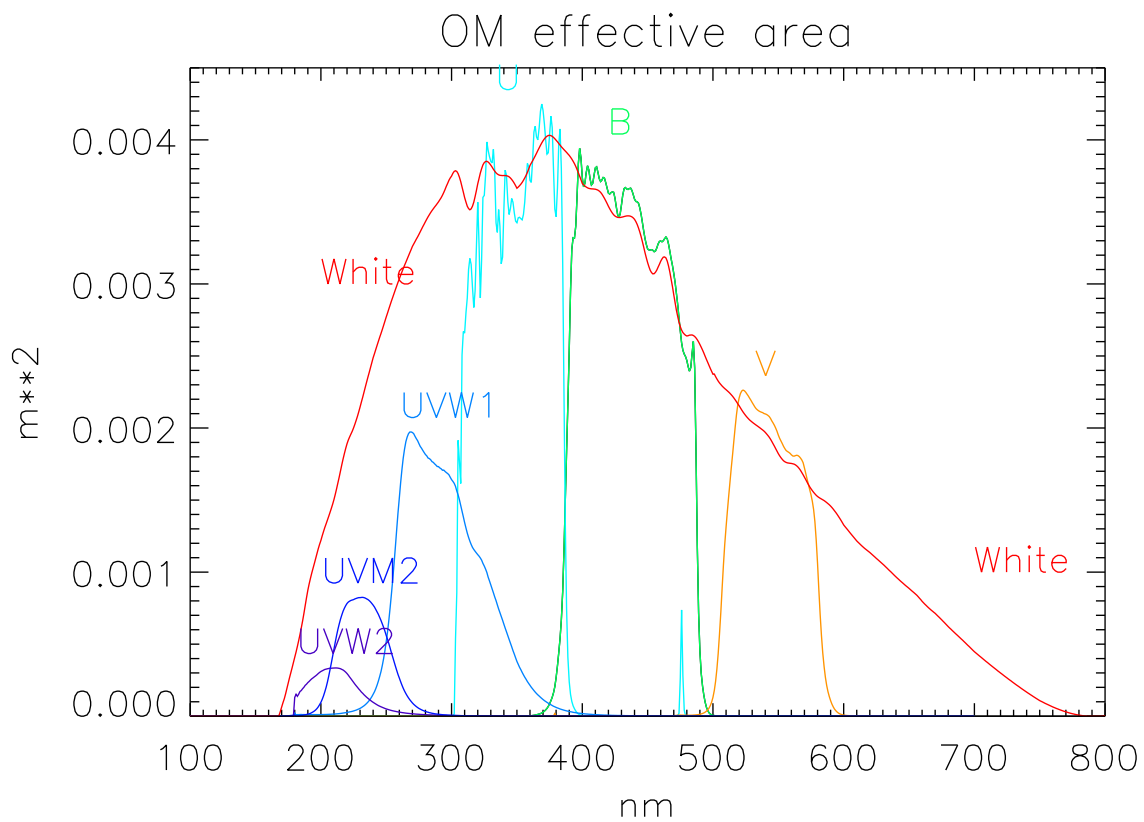


Figure 102: *Throughput curves for the OM filters, folded with the detector sensitivity.*

Zeropoints (by definition the magnitude of an object producing one count per second), have been derived by using, for each filter, the equation:

$$\text{zeropoint} = 2.5 \log_{10}(\text{Countrate}_{Vega}) + m_{Vega}.$$

OM zeropoints have been defined in such a way that Vega has:



Table 17: *OM filters: effective wavelengths, widths and Zeropoints*

Filter	Effective wavelength (nm)	Width <sup>a</sup> (nm)	Zeropoint (magnitudes)	AB zeropoint (magnitudes)
V	543	70	17.9633	17.9230
B <sup>b</sup>	450	105	19.2661	19.0809
U	344	84	18.2593	19.1890
UVW1	291	83	17.2038	18.5662
UVM2	231	48	15.7724	17.4120
UVW2	212	50	14.8667	16.5719
White <sup>c</sup>	406	347	20.2555	20.6900

Notes to Table 17:

<sup>a</sup> The width of a filter with a constant transmission equal to the transmission at the effective wavelength, having the same effective area as the corresponding OM filter.

<sup>b</sup> The effective wavelength of the B filter has been arbitrarily set to 450 nm to avoid the core of the Balmer line H $\gamma$ .

<sup>c</sup> White filter values based entirely on simulations.

$B_{Vega} = V_{Vega} = 0.03$  mag,  $U_{Vega} = UVW1_{Vega} = UVM2_{Vega} = UVW2_{Vega} = 0.025$  mag.

Zeropoints are listed in Table 17. An AB magnitude system has been defined also for OM. Their zeropoints are given in Table 17 as well.

### 3.5.3.2 OM grisms

In addition to the filters, the OM filter wheel holds two grisms. The throughput of the OM grisms depends on wavelength. The Inverse Sensitivity Function (ISF) gives the transformation from count rate in any extracted spectrum to physical flux units as a function of wavelength. The ISFs for both OM grisms are displayed in Fig. 103. Only one grism can be used at any time, because they are mounted together with the other optical elements (see Table 16) on the OM filter wheel.

The angular dispersion of the grisms is almost constant over their wavelength ranges. The UV grism has a dispersion of ca. 0.25 nm per pixel (unbinned), the optical one has a dispersion of 0.5 nm per pixel. The grisms can thus be used for low resolution (resolving power  $\sim 180$ ) optical and UV spectroscopy in conjunction with the X-ray observations. As an example of both grisms flight performances, the flux calibrated spectrum of the white dwarf HZ 2 is shown in Fig. 104. It is compared with the standard flux of this star provided by the HST Calspec database. The flux converted count rates of the star measured with the OM lenticular filters are also shown. An image of the target area taken prior to or after obtaining spectroscopic exposures with a grism can be useful for identification of the spectral sources.

The optical grism is blazed and the zeroth order image is relatively weak. The UV grism is not blazed, however, and ca. 1/3 of the light is expected to go into the zeroth order image, which is expected to be visible near the edge of the FOV when the first order spectrum is centred. Since the UV grism is not blazed, the overlap of the second order on the first one becomes very important above 360 nm, thus limiting the spectral range displayed in Fig. 103.



**esa**

euopean space agency  
agence spatiale europ  ne

Document No.: XMM-SOC-USR-MAN-0006

Issue/Rev.: Issue 2.18

Date: 13.07.2020

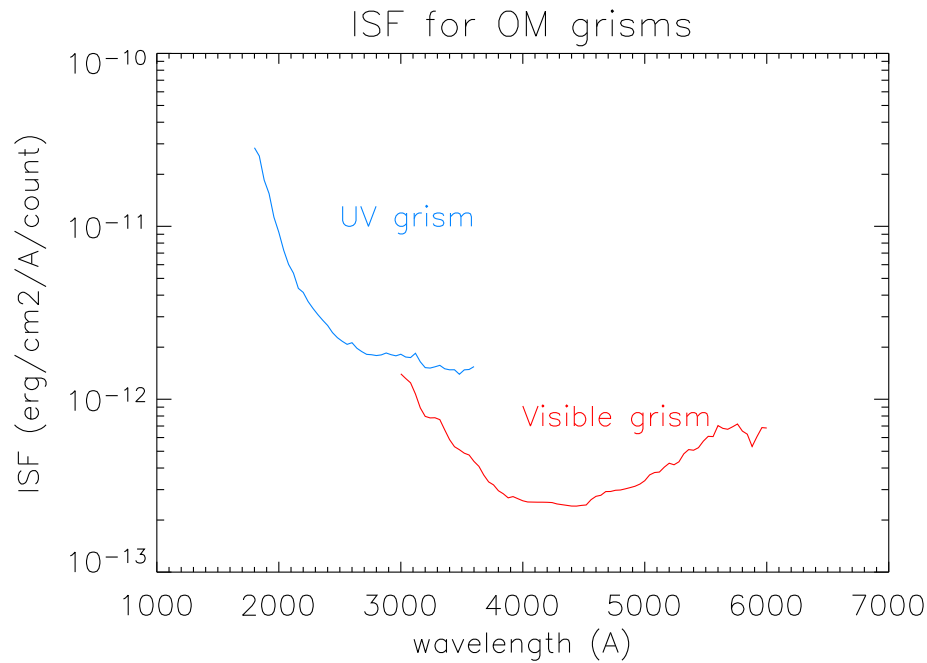


Figure 103: The OM grisms Inverse Sensitivity Functions

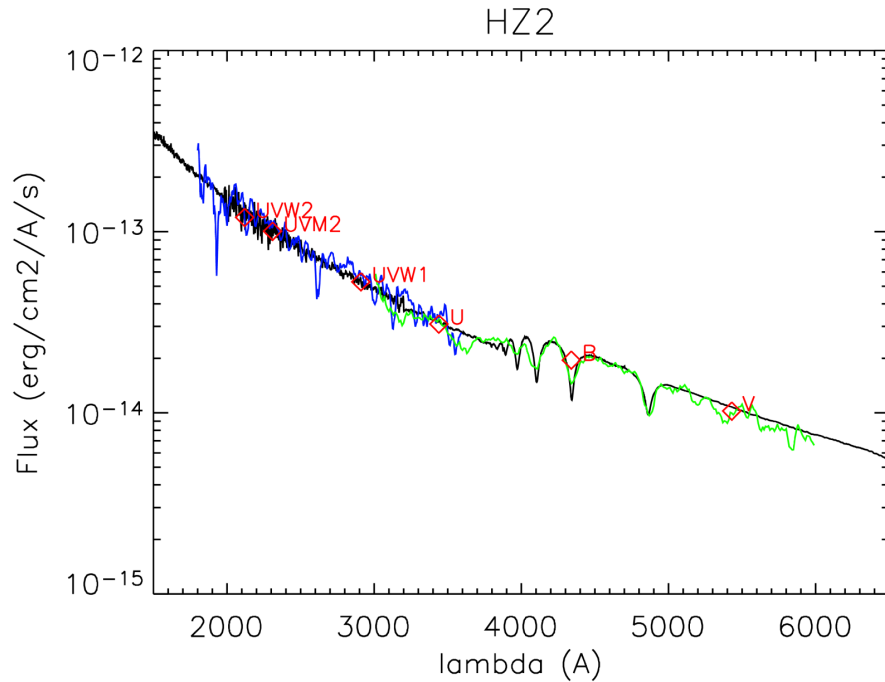


Figure 104: Flux calibrated spectrum of the white dwarf HZ 2, obtained with the OM ultraviolet (in blue) and visible (in green) grisms.



Approximate sensitivity of the grisms in terms of limiting flux that can be reached in typical exposure times is given in Table 18. Flux values in the table refer to the UV grism. The limit for the visible grism is ten times fainter.

Table 18: *OM UV grism sensitivity [detected flux: erg cm<sup>-2</sup> s<sup>-1</sup> Å<sup>-1</sup>] for different detection levels. The Visible grism is one order of magnitude more sensitive than the UV one.*

Detection level	Exposure time (s)	
	1000	5000
<b>1-<math>\sigma</math></b>	$1.0 \cdot 10^{-14}$	$4.6 \cdot 10^{-15}$
<b>3-<math>\sigma</math></b>	$4.0 \cdot 10^{-14}$	$1.6 \cdot 10^{-14}$
<b>10-<math>\sigma</math></b>	$2.4 \cdot 10^{-14}$	$7.0 \cdot 10^{-14}$

It should be noted that because the grisms produce spectra of all objects in the field of view, there may be overlapping of zero and first orders corresponding to other objects that can contaminate the spectrum of the main target. This can be avoided in many cases by properly selecting the observing position angle. The interactive tool in URL:

[http://www.mssl.ucl.ac.uk/www\\_astro/xmm/om/om\\_wintool/om\\_tool2.html](http://www.mssl.ucl.ac.uk/www_astro/xmm/om/om_wintool/om_tool2.html)  
may be helpful to do that.

As with the narrow-band filters, discussed in Sect. /refuhb:par:omfilters, data taken with the grisms suffer from a time-dependent decline in the OM throughput. The decline in each grism is currently characterised in the OM<sub>GRI</sub>S<sub>MCAL</sub>0006.CCF, see *XMM – CCF – REL – 377* and references therein. At 2160 Å, with maximum depth near 2350 Å, while the Visible grism is affected between 3440–4180 Å, being deepest at 4180 Å.

### 3.5.4 Optical/UV point spread function of the OM and tracking

The OM telescope produces images on the detector which are nominally diffraction-limited over the field of view (ca. 0''.35 at 400 nm, decreasing with increasing wavelength). However, this is convolved with the somewhat larger detector resolution. The OM onboard software calculates the spacecraft drift from guide stars in the tracking windows and continually corrects the incoming photons from the detector to register them correctly in the accumulating image (“shift & add” in-memory). This can be done only in steps of an integral number of pixels, so some further broadening (on the scale of another 0''.5) still occurs.

The on-board measurement of the PSF for different filters is shown in Fig. 105 and Table 19. Measurements are based on the observations of the fields of G153, EXO0748-67, LH9 and PSR 0540-69.3. The FWHM values have been obtained after fitting with a Moffat function plus

Table 19: *OM on-board PSF FWHM in different lenticular filters*

Filter	FWHM (")
V	1.35
B	1.39
U	1.55
UVW1	2.00
UVM2	1.8
UVW2	1.98

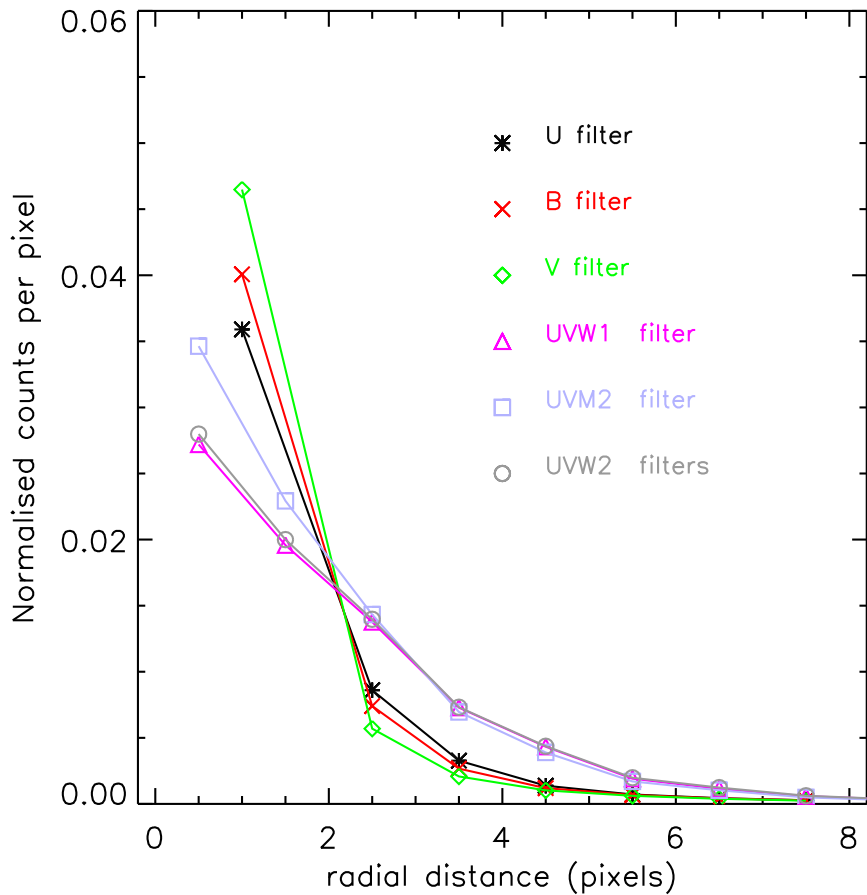


Figure 105: *Optics+detector OM PSF in different filters*

a look up table. The PSF has a slight dependency on the count rate, which is taken into account by the SAS when data are processed.

### 3.5.5 OM sensitivity and detection limits

Both, Fig. 106 and Table 20, provide the expected count rate of the OM, in counts per second, for  $m_V = 20$  mag stars of various types, with the different filters introduced above. These numbers were obtained under the assumption of a perfect detector, i.e., free of deadtime and coincidence loss, and without time sensitivity degradation, and with an aperture radius of 6'' (17''.5) for optical (UV) filters.

The numbers listed in Table 20 can be used to calculate the perfect detector count rates of stars of given magnitude by the formula

$$C_{mag} = C_{20} \times 10^{0.4 \times (20 - b_{mag})} , \quad (3)$$

where  $C_{20}$  is the count rate of an  $m_V = 20$  mag star of the same spectral type as the target, and  $b_{mag}$  and  $C_{mag}$  are the  $m_V$  and the count rate of the target of interest, respectively.



Table 20: *OM count rates [10<sup>-4</sup> counts s<sup>-1</sup>] as function of spectral type for stars with  $m_V = 20$  mag under the assumption of a detector with zero deadtime, no coincidence loss and no time sensitivity degradation.*

Filter	B0	A0	F0	G0	G2	K0	M0	WD
V	1555	1510	1473	1473	1495	1452	1392	1412
B	6190	5272	3805	3010	2577	2289	1337	4454
U	8533	2216	1486	1119	966	444	178	4667
UVW1	5647	958	366	218	182	29.1	17.4	3093
UVM2	2276	316	39.3	8.69	5.54	0.436	0.032	1174
UVW2	950	126	11.1	2.06	1.19	0.112	0.069	561

However, OM deadtime and coincidence losses must be taken into account, for instance using SAS. For the 20th magnitude stars in Fig. 106 and Table 20, OM coincidence losses are negligible. Losses become significant for a point source at a count rate of about 10 counts s<sup>-1</sup> (about 10% coincidence) for a full frame exposure.

The correction is approximated by the following formula:

$$C_{mag} = \frac{\ln(1 - C_{det} * T)}{T_{ft} - T} \quad (4)$$

where  $C_{mag}$  is the count rate of incident photons from equation (3),  $C_{det}$  is the actual measured

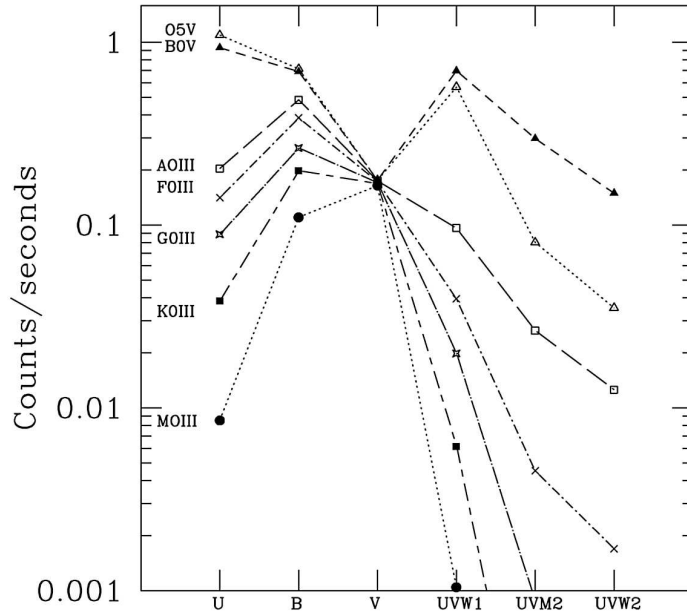


Figure 106: *OM count rates vs. filter selection for stars of different spectral type with  $m_v = 20$  mag.*

**esa**european space agency  
agence spatiale européenne

count rate,  $T$  is the CCD frametime in units of seconds and  $T_{ft}$  the frametransfer time in the same units (0.1740 ms). The frametime is a function of the OM science window configuration, as described in § 3.5.2.

An optimum aperture radius of  $6''$  was found to be the radius at which the loss correction formula is self consistent. At this radius the accuracy of the coincidence loss correction is at a level of 5% between different frametimes.

The validity range of the coincidence loss correction can be obtained from eq. 4 as a function of the frametime, whose maximum value (11.04 ms) occurs for full frame exposures, high or low resolution, where the whole detector is used. In windowed exposures the frametime varies from about 5 to 10 ms. For this reason the maximum measured count rates that can be reliably corrected are in the range of a few hundreds counts per second. Higher rates (1000 cts/s) may not damage the detector, but are scientifically useless.

We give in Table 21 coincidence loss corrected rates for limit high measured rates. The table gives the maximum measurable rate for each given value of frametime (1 count per frametime) and the corresponding corrected values for the maximum rate minus 0.01 and 0.001 c/s. For these high rates we obtain correction factors of 10, and very small differences in count rate produce variations in the corrected rates of more than 20%.

Table 21: *OM coincidence loss corrections for high count rates.*

Frametime (ms)	Maximum measured rate (c/s)	Corrected rate	
		max-0.01 (c/s)	max-0.001 (c/s)
5	200	2052	2531
7	143	1402	1739
9	111	1056	1317
11	91	842	1054

The coincidence loss correction implemented in SAS (from version 14) sets a validity limit at a rate of 0.97 counts per frametime (source+background). Within this limit, the correction error is less than 2%. This corresponds to about 700 and 300 source+background corrected counts for frametimes of 5 and 11 ms, respectively. For values higher than 0.97, the source counts are not corrected by SAS, and therefore, the conversion to magnitudes and fluxes are not applied. The produced source list contains only the measured count rate and position for these sources.

In Fig. 107, a comparison between formula (4) and the inflight instrument performance is shown. In Table 22, an estimate of the limiting magnitudes that can be detected with OM in an integration time of 1000 s at the 5-sigma confidence level is provided. They have been obtained from simulations, taking into account the whole aperture ( $6''$  radius for optical filters and  $17''.5$  for UV) on which the OM photometric calibration is based. If we consider that detections can be obtained in the very few pixels in the core of the PSF, since the total background is then lower, the limit would be about one magnitude fainter.

Table 23 presents the limiting magnitudes derived from the photometric analysis of one of the OM calibration fields (HD5980, also observed from the ground). This can be considered as an extreme case because of the crowdedness of the field which increases the observed background by overlap of the PSF wings. This is why the obtained limits are brighter than the simulations of Table 22.

A detailed study of the background sources in OM can be found in:

[http://www.cosmos.esa.int/documents/332006/623312/MSSLbckgd\\_v6.pdf](http://www.cosmos.esa.int/documents/332006/623312/MSSLbckgd_v6.pdf)



Table 22: *Limiting magnitudes<sup>1</sup> for a 5- $\sigma$  detection in 1000 s*

Filter	Spectral type				
	B0	A0	G0	K0	WD
V	19.8	19.8	19.7	19.7	19.7
B	21.0	20.8	20.2	19.9	20.6
U	21.8	20.4	19.6	18.6	21.2
UVW1	21.1	19.2	17.6	15.4	20.5

Notes to Table 22:

- 1) Numbers obtained adopting as background a zodiacal light level of 100 S10 units, where S10 is the brightness of one  $m_V=10$  mag solar type star per square degree. All magnitudes are in V filter.

<http://www.cosmos.esa.int/documents/332006/623312/OMbackg05.pdf>.

The expected levels of different external background radiation processes in the optical/UV are tabulated in Table 24. The background count rate in the OM is dominated by the zodiacal light in the optical. In the far UV the intrinsic detector background becomes important. Images are regularly taken with the blocked filter and no LED illumination to measure the detector dark

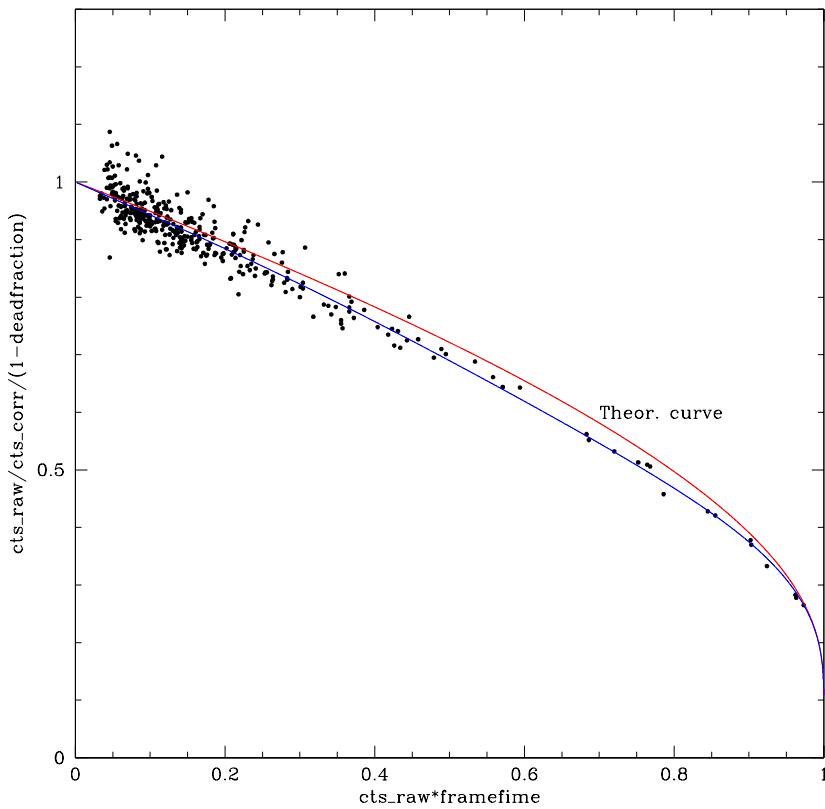


Figure 107: *Theoretical (red line) and empirical (blue line) coincidence loss correction curves superposed to flight data*



esa

european space agency  
agence spatiale européenneTable 23: *Observed limiting magnitudes<sup>1</sup> for a 5-sigma detection (scaled to 1000s)*

Filter	Spectral type range		
	B0/A0	A1/G3	G4/M8
V	19.5	19.4	19.4
B	20.6	19.8	19.3
U	20.2	19.4	18.6

Notes to Table 23:

- 1) Based on OM observations of HD5980 field, obtained with V, B and U filters. Magnitudes are standard V.

counts. The mean OM dark count rate is  $4.0 \times 10^{-4}$  counts s<sup>-1</sup> pixel<sup>-1</sup>. The variation across the detector is  $\pm 9\%$ , with a mainly radial dependence, being highest in an annulus of about 8' radius and lowest at the centre. Variations as a function of time are  $\pm 7\%$ , without any apparent trend. However, if a very bright star is in the field of view, the dark rate can be up to  $\simeq 60\%$  higher than normal, despite the use of the Blocked filter.

Artifacts can appear in the XMM-Newton OM images due to light being scattered within the detector. These have two causes: internal reflection of light within the detector window and reflection of the off-axis starlight and background light from part of the detector housing.

The first of these causes a faint, out of focus ghost image of a bright star, displaced in the radial direction away from the primary image (see Fig. 108). The second effect is due to light reflecting off a chamfer in the detector window housing. Bright stars that happen to fall in a narrow annulus 12'.1 to 13' off axis shine on the reflective ring and form extended loops of emission radiating from the centre of the detector (see Fig. 109).

Similarly, there is an enhanced "ring" of emission near the centre of the detector due to diffuse background light falling on the ring. These features are less prominent when using UV filters, due to the lower reflectivity of UV light.

Figure 110 shows the low sensitivity patch produced by an accidental observation of Jupiter in July 2017. This figure shows also the "ring" mentioned before. The low sensitivity patch is oval with a size around  $210 \times 120$  pix<sup>2</sup>, equivalent to 1.4 square arcmin approximately. The whole field is 17 arcmin in diameter.

Table 24: *Levels of different OM background contributors*

Background source	Occurrence	Count rate range
Diffuse Galactic <sup>1</sup>	all directions	$2.14 \times 10^{-1} - 7.527 \times 10^{-6}$
Zodiacal <sup>1,2</sup>	longitude $90^\circ \pm 20^\circ$	$1.69 \times 10^{-1} - 5.611 \times 10^{-6}$
Average dark count rate <sup>3</sup>	all directions	$4.0 \times 10^{-4}$

Notes to Table 24:

- 1) In units of [counts s<sup>-1</sup> arcsec<sup>-2</sup>].
- 2) In differential ecliptic coordinates, i.e., the angle between the Sun and the pointing position of XMM-Newton. Maximum is for l,b = 70,0 in the white filter, minimum is for l,b = 110,70 in the UVW2 filter.
- 3) In units of [counts s<sup>-1</sup> pixel<sup>-1</sup>]



### 3.5.6 OM brightness and dose limits

To avoid damage of the OM photocathode, the maximum allowed source brightness is set to a count rate of  $\sim 19,000$  photons/s, corresponding to an  $m_V = 7.4$  mag A0 star in the V filter. The equivalent brightness limits for the other filters and optical elements are tabulated in Table 25. For calculating the brightness limits an A0 type spectrum was assumed. Similarly, a maximum count rate of 190,000 photons/s is allowed during the V-filter field acquisition at the start of observation. Moreover, the maximum allowed dose during an OM observation is  $10^9$  photons in the innermost  $3'.5$  and  $5 \times 10^9$  photons outside. This puts some constraints not only on the properties of the sources in the OM field but also on the maximum exposure time. The expected dose can be calculated making use of the count rates listed in Table 20.

The brightness limit for the UV grism is imposed by the zero order. As stated in Section § 3.5.3.2, this grism is not blazed and therefore a lot of energy is concentrated in its zero order. This can make optically bright cool stars not observable, even if they are faint in the UV, because their visible light comes out in the zero order. In other words the limits for the grisms cannot be scaled with the spectral type.

These limits are related to the safety of the instrument. Bright objects, even if they are permitted, can produce poor results due to coincidence losses since the correction applied by SAS becomes uncertain for high count rates (see Section § 3.5.5).

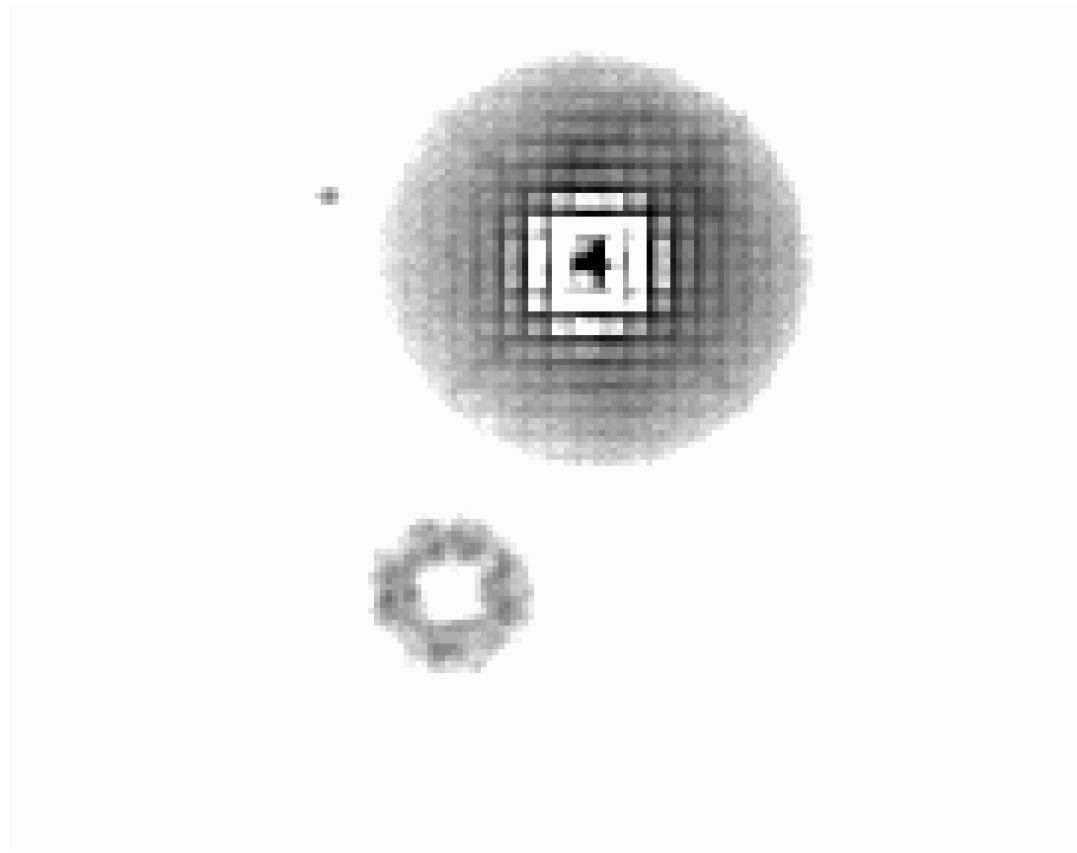


Figure 108: *Out-of-focus ghost image (“smoke ring”) of a bright field star, during a 3C273 observation. Clearly visible is the strong fixed pattern noise around the bright source*



Table 25: *The  $m_V$  brightness limits for all OM filters. An A0 type star spectrum is assumed.*

Filter	Max. $m_V$
V	7.3
U	7.7
B	8.6
White	9.6
UVW1	6.8
UVM2	5.6
UVW2	4.6
Grism 2 (opt.)	9.6
Grism 1 (UV)	8.7

If an optically bright source beyond these limits is anywhere in the OM FOV (not just within an active science window!), users should not include OM exposures in their observation. It is the user's responsibility to check for the presence of such bright sources. The user is recommended to check the Guide Star Catalogue at the URL:

<http://archive.eso.org/gsc/gsc>

The impact of the sources that are present in a given field with respect to the OM brightness and dose limits can be checked through the function "Technical Evaluation" in XRPS.

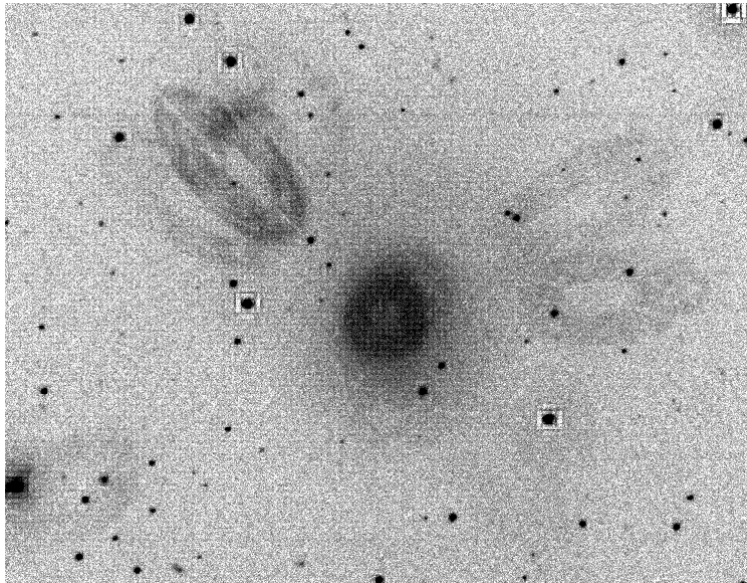


Figure 109: *Straylight ellipses caused by reflection of a star outside the field of view, taken from the PKS 0312 offset 6 field (V filter in use). The average background rate is  $15 \text{ counts pixel}^{-1}$  per exposure; in the bright straylight loop is  $30 \text{ counts pixel}^{-1}$ . The background is also enhanced in the central region due to reflection of the diffuse sky light from outside the field. In the centre it rises to  $\simeq 3$  times the average background rate.*



### 3.5.7 OM distortion

The XMM-Newton OM optics, filters and (primarily) the detector system result in a certain amount of image distortion. This effect can be corrected with a “distortion map”, by comparing the expected position with the measured position for a large number of stars in the OM field of view. A U-filter analysis has been performed on the G153 pointing with 813 stars. The effect of applying this correction is shown in Fig. 111. A positional r.m.s. accuracy of 0.5 – 1.5 arcsec is obtained. The distortion map has been entered into the appropriate CCF file and is used in SAS.

### 3.5.8 OM Field Acquisition

At the start of each science observation a 20 seconds V-filter image is taken to allow proper identification of the field stars with respect to the uploaded guide stars. Shifts are applied on board, whenever necessary, to correct the window coordinates according to the true positions of the stars. This short exposure is called *Field AcQuisition* (FAQ). A correct (*i.e.*: within a few arcseconds) FAQ is indispensable for a proper placing of the Fast Mode windows.

On-flight experience demonstrates that the FAQ is properly working on the overwhelming majority of the fields. However, a few cases have been observed (e.g. very crowded fields or extended objects) where the FAQ fails and consequently no shift is applied.

The XMM-Newton PIs must be aware that no compensation is granted if the FAQ failure yields an impact on the scientific outcome of a given observation.

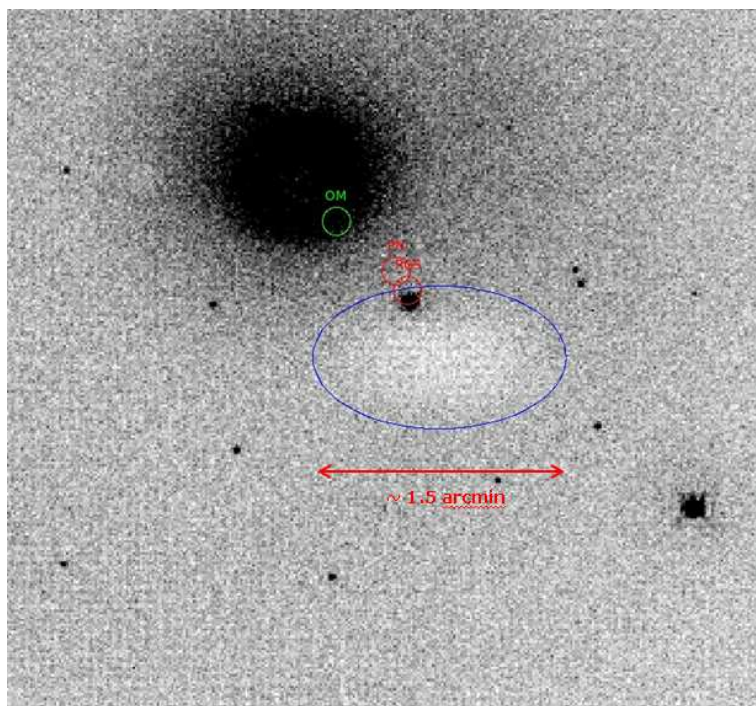


Figure 110: *Image obtained with the V filter showing the depletion patch caused by Jupiter in July 2017. The RGS and EPIC-pn boresights are marked in red.*



### 3.5.9 OM Operating modes and filters configuration

While the OM can access a large part of the field viewed by EPIC, there are limitations on what can be observed in an exposure. These limitations are set in the first place by the amount of on-board memory, and secondly by the telemetry rate allocated to the instrument. Because of constraints on the telemetry rate available, it is not possible to transmit the full data on every photon that the OM detects. Instead, a choice has to be made between image coverage and time resolution. The observer can therefore choose up to 5 “windows”, of which up to two may be operated in the “Fast” mode (see § 3.5.9.1, below). These can be placed where required, with restrictions as identified in § 3.5.10.

In addition to these windows, the instrument assigns itself several small windows for tracking guide stars. The tracking information is included with the other science data.

In general, an observation with the OM will consist of a sequence of exposures in different filters and/or with a sequence of different window setups to cover the full field of view or a defined area around the target.

A set of default OM window configurations is available (§ 3.5.9.2). These will generally be satisfactory for most proposals.

For details on the intricacies of non-default OM window choice and the applicable restrictions, please refer to § 3.5.10.1.

#### 3.5.9.1 OM operating modes

The OM can operate in the two modes listed in Table 26. These allow either imaging or fast photometry or both simultaneously.

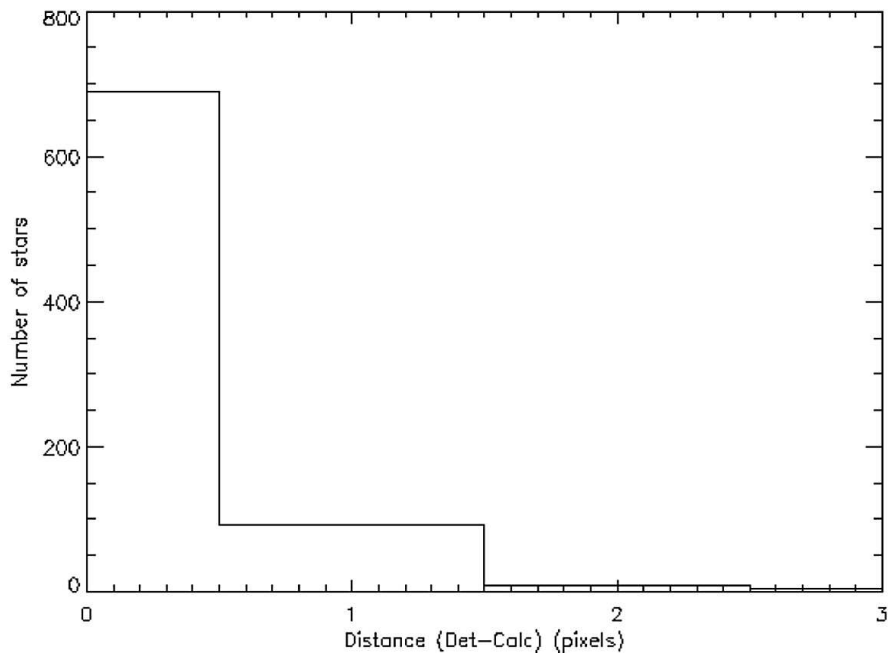


Figure 111: Positional error of sources in a field of view, where the distortion map has been applied. The histogram was made using sources from the 3C273 field corrected for distortion



Table 26: *The science data acquisition modes of OM*

Mode <sup>1</sup>	Special feature
Imaging	Mosaic of 2-D imaging windows with long exposure times ( $> 800$ s)
Fast	High time resolution, providing 2-D time-sliced images over small areas.

Notes to Table 26:

- 1) Both modes can be used simultaneously, as long as total memory capacity and telemetry bandwidth are not exceeded.

- Imaging mode

The *Image Mode* emphasises spatial coverage at the expense of timing information. Images can be taken at the full sampling of the instrument or binned by a factor of 2 to yield a resolution element on the sky of approximately 0.5 or 1.0 seconds of arc. The maximum total size of the science windows is determined by the memory available in the Data Processing Unit DPU. A single Image Mode window binned by a factor  $2\times 2$  can be up to  $976\times 960$  detector pixels, which results in a  $488\times 480$  binned pixel image being stored in the DPU. At full sampling (with no binning) the window can be up to  $652\times 652$  pixels. The trade off is that the images with unbinned pixels take more memory and therefore more telemetry when downloading the data.

**The maximum allowed integration time for an OM imaging mode exposure is 5 ks.** Since the OM in its imaging mode produces accumulated images, there is no timing information attached to individual incoming photons.

Any drift in the pointing direction of the spacecraft is corrected in the image by tracking guide stars.

The operating modes for Imaging consist of a combination of windows (up to five) covering different areas of the detector, or a full frame mode where the whole field of view can be observed.

- Fast mode

The *Fast Mode* emphasises timing information at the expense of spatial coverage. In its Fast Mode, the OM does not produce accumulated two-dimensional images, but instead produces event lists like the X-ray instruments. This mode is useful for monitoring rapidly variable sources, for example Blazars or accreting binaries. Two small windows can be assigned, each of a maximum of 512 pixels only. Thus the maximum size of an approximately square window would be  $22\times 23$  pixels (= 506 total). There is no binning within a Fast Mode window. The pixel locations of individual photons within the window are recorded and assigned a time tag, which has a user-specified integration time of between 500 ms and the tracking frame duration (20 s). No tracking correction is applied to Fast Mode data. This can be applied on the ground, from the drift history supplied by the OM. The data are obtained by default in 0.5 s time slices, each preserving the pixel information. Shorter times are in principle possible, but at the risk of overloading the DPU (*e.g.* when two Fast Mode windows are operated), and are therefore discouraged.

**The maximum allowed integration time for an exposure with one Fast mode window is 4.4 ks,** and 2.2 ks if two Fast mode windows are used simultaneously.



For critical time coverage, it has to be taken into account that during ground station handovers OM exposures are interrupted for 1800 sec.

Fast mode data can be acquired at the same time as image mode data. The default configuration for fast mode includes a large image window, in which the fast mode one is embedded. In case of User Defined windows, it is recommended to include an image mode window of bigger size than the fast mode one that includes the later.

Each mode has a specific **overhead**, *i.e.*, time needed for the instrument set-up, before the actual science exposure can start. For both the above OM modes this overhead includes also the reference frame exposure. In addition, about 1000 s are needed before starting the OM exposures for the field acquisition of the satellite star tracker. The reader is referred to § 4.5.2 for a general discussion of the impact of instrumental overheads on the planning of an XMM-Newton observation, and to the **XRPS User's Manual** at:

[http://xmm.esac.esa.int/external/xmm\\_user\\_support/documentation/rpsman/](http://xmm.esac.esa.int/external/xmm_user_support/documentation/rpsman/) for a detailed description of the **OM overheads**. An interactive web tool is available at the MSSL web page:

[http://www.mssl.ucl.ac.uk/www\\_astro/xmm/om/om\\_tool\\_current.html](http://www.mssl.ucl.ac.uk/www_astro/xmm/om/om_tool_current.html), which may help the user to better handle and understand OM windows and operational overheads.

### 3.5.9.2 OM operating configurations

To ease the use of the OM and to maximise the scientific yield of observations in cases when no particular instrument configuration is requested, OM default configurations have been defined. There is one type of default configuration per OM observing mode, thus one for the imaging mode and one for the Image plus Fast mode (§ 3.5.9.1). Default windows have also been predefined for the V and UV grisms exposures. Moreover, two additional full frame modes are available which allow imaging observation of the whole OM field of view.

The possible configurations are as follows:

1. Science User Defined mode (**Science User Def.** in the RPS)

Up to five windows (two of them in Fast mode) covering different areas of the detector can be defined (see Sect. 3.5.10.1).

2. Full-Frame imaging modes (**Full Frame High/Low Resolution** in the RPS)

It is possible to obtain images of the whole OM field of view in full (high) or  $2 \times 2$  binned (low) resolution. These modes do not allow tracking (see § 3.5.4), and have higher instrumental overheads than the Modes using windows, either User Defined windows or Imaging Mode default. However, they allow homogeneous sampling of the whole OM field of view. They are therefore particularly well suited for survey studies or to obtain multiobject grism spectroscopy in a wide field. These modes have a single window, no other window can be defined (either in image or Fast mode) within the same exposure. Along an observation, Full-Frame imaging modes can be combined with modes using windows that require Field Acquisition (FAQ, see § 3.5.8), particularly Fast mode windows. In this case the Full-Frame exposures must be performed after all the exposures which need FAQ, because Full-Frame modes nullify the results of FAQ.

The lack of tracking in Full Frame mode does not affect the quality of the image because, as experience has shown us, the drift of the XMM-Newton spacecraft is almost negligible (less than one arc sec per hour).

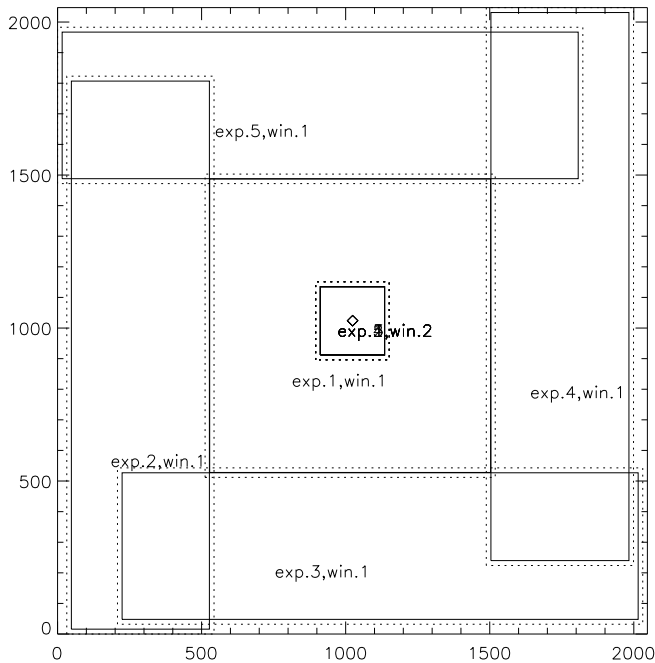


Figure 112: *Setup of OM imaging mode default mode observations consisting of a sequence of 5 exposures. The science windows are indicated by solid lines, the detector windows by dashed lines. A 16 in-memory pixel margin around the science window is allocated to accommodate spacecraft drifts.*

### 3. EPIC/RGS Imaging Mode (depending on the prime X-ray instrument)

- A pre-defined setup of 5 consecutive exposures per filter, covering 92% of the total ( $17' \times 17'$ ) OM FOV. Each exposure having 2 windows.
- In each of the 5 exposures per filter a large fraction of the FOV will be covered by one large window , while the central  $2' \times 2'$  high resolution imaging mode window is observed in all the exposures. The continuous exposure of the central window, ensures continuous monitoring of the prime target (at the centre of the FOV; see Fig. 112).
- The central window has high spatial resolution ( $0''.5 \times 0''.5$ ) while the lateral windows have  $2 \times 2$  in-memory pixel binning ( $1''.0$  pixels)
- Warning: Since each pair of windows has a different frame time, the coincident loss correction can differ for bright sources. This can lead to systematic offsets in corrected count rates (and thus magnitude and fluxes) in each exposure. The User Defined mode with identical windows has always the same frame time is thus more stable for bright sources.

### 4. Fast Mode default (named EPIC/RGS Image Fast in the Remote Proposal System, RPS, depending on the prime X-ray instrument)



**esa**

european space agency  
agence spatiale européenne

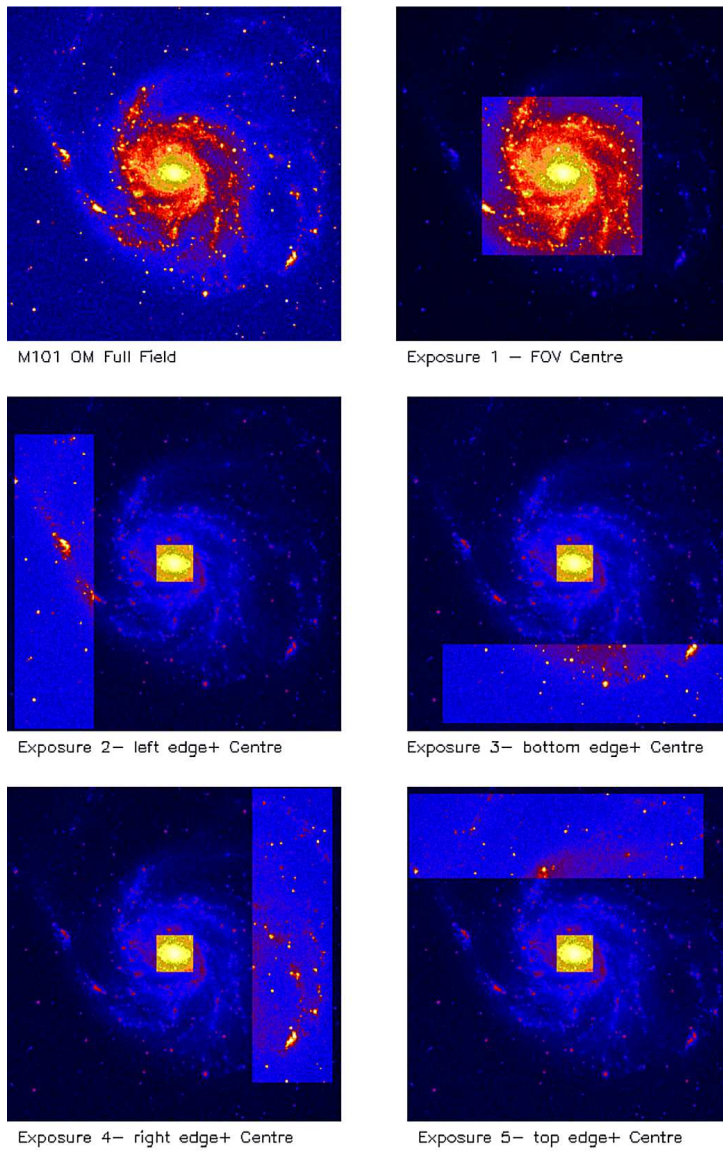


Figure 113: Example of a field imaged with the default Image Mode configuration.

- Image windows configuration as under 3 (i.e. pre-defined Image Mode windows).
- An additional central window is operated in the OM Fast mode. Its size is  $22 \times 23$  in-memory pixels ( $10''.5 \times 10''.5$ ). *It is responsibility of the PI to carefully check the accuracy of the target coordinates, to avoid substantial flux losses.*
- The same warning as in 3 applies for bright sources. It is recommended to select the User Defined mode for variability study of bright sources.

## 5. Default grism configurations

Two standard configurations are available for OM optical or UV grisms:



- a predefined default window, which will contain the spectrum of the target (with its 0th order) at full detector resolution (**Science User Defined mode in RPS**)
- a Full Frame Low Resolution exposure, which provides the spectra of all the targets in the OM FOV, with slightly degraded spatial (and hence spectral) resolution (**Full Frame Low Resolution mode in RPS**)

Examples of the Imaging and Fast default modes are shown in Figs. 112 and 113.

Apart from the configuration of the OM exposures, exposure times and filters have to be specified.

The described Default configurations for Imaging and Fast modes provide a very simple and easy to use set-up aimed at obtaining a good coverage of the main target located at the boresight and imaging at the same time the complete field of view (92% with 5 consecutive exposures).

However, due to the limitations imposed by the coincidence losses in the detector these Default configurations are not recommended in case of bright sources and in variability studies. As explained in section 3.5.5, the coincidence losses (and their correction) depend on the frametime. The different detector windows defined for the five exposures of the Default configuration may have very different frametimes leading, for high count rates, to very large and inhomogeneous corrections and errors. It is better in these cases to select a unique window using Science User Defined mode.

### 3.5.9.3 Integration time for exposures

To achieve the best possible efficiency **an integration time of at least 1 ks for each exposure is required**. With the EPIC/RGS Image Mode configuration of 5 exposures per filter, this leads to 5 ks duration per composite exposure. Note that longer integration times are allowed (§ 3.5.9.1) with the maximum allowed exposure time per exposure of 2.2 ks for the Fast Mode (if two Fast Mode windows are used), 4.4 ks for the Fast Mode (if one Fast Mode window is used), and 5 ks for the Image Mode. Shorter exposure times are limited by the OM telemetry allocation. For the modes EPIC/RGS Image and **Science User Defined** the data are downloaded during the subsequent exposure. Therefore, either the windows must be small, or the subsequent exposure integration time must be long enough to allow the instrument memory to be emptied. This can be critical for crowded fields mainly with the optical filters. The absolute minimum exposure times are: 800 s for the Image Mode and 1200 s for the Fast Mode. **It is strongly discouraged to define a large series of short Image Mode observations. A better way to obtain time information is to use the Fast Mode with longer exposure times and appropriate time binning.**

There are in principle no constraints on the exposure time in Full Frame Low/High Resolution Modes. However, it is forbidden to exceed 5000 seconds, to avoid potential onboard memory corruption after interaction of cosmic rays with the camera, or counter wraparound. Table 27 summarises the integration time constraints.

### 3.5.9.4 Filter choice

It is considered important to take advantage of the unique capabilities of OM in the *ultraviolet* domain, and therefore the recommendation is to use:



1. UVM2 (first choice)
2. UVW1 (second choice)
3. U (third choice)

Although the UVW2 reaches further in the UV, its use is not encouraged because of its low in-flight performance.

A different set of filters for observations in the OM default configurations may be chosen, based on scientific considerations. However, **the sequence in which the filters are used must follow their order in the filters wheel** (see § 3.5.3). For example, the three filters listed above have to be set in the sequence U, UVW1 and UVM2.

### 3.5.9.5 Multiple rotations of the filter wheel

With prior approval by OTAC (see § 3.5.3), it is possible to perform a series of exposures where a filter sequence is repeated, e.g. 'U , UVW1 , UVM2' - 'U , UVW1 , UVM2' - 'U , UVW1 , UVM2',...

The recommended configuration is Science User Defined mode with one window in Image mode and possibly an additional Fast mode window. The minimum exposure time will be 800 s except if Fast mode, which requires a minimum exposure time of 1200 s, is used (see section 3.5.9.3).

### 3.5.9.6 Practical use of OM. Some examples

The choice of a mode or configuration for OM should be driven by a compromise between the time resolution needed and the spatial coverage required for a given pointing. Time discontinuities are due to the **overheads** (see XRPS User's manual for a detailed description) needed to download the data and configure the instrument for the next exposure.

The full frame modes cover the whole FOV, but they have large overheads. If time resolution is needed, then windowed modes provide almost continuous coverage. The maximum time resolution is achieved in FAST mode (up to 0.5 sec). The default image configuration, or IMAGE+FAST, allows the user to cover 92% of the FOV in five successive exposures, obtaining in each of them a small window (less than  $2 \times 2$  arcmin) centred on the pointing attitude and optionally a FAST mode window ( $10''.5 \times 10''.5$ ) centred at the same coordinates. If one needs time coverage on a larger area, one can make several short ( $> 1000$  sec) Science User Defined Mode exposures (image window up to  $7''.6 \times 7''.6$ , if binned). However, for crowded fields, exposures may be lost, and longer exposure times are encouraged.

Field spectroscopy is better achieved using full frame low resolution, while if one wants to monitor spectral variations of the target, there is a pre-defined window configuration for each of

Table 27: *OM exposure time constraints*

Science window configuration	Minimum (s)	Maximum (s)
Only Image Mode windows	800 <sup>a</sup>	5000
Image Mode + 1 Fast Mode windows	1200	4400
Image Mode + 2 Fast Mode windows	1200	2200
Full frame (low or high resolution)	800 <sup>a</sup>	5000

<sup>a</sup> >1000 sec strongly recommended

**esa**european space agency  
agence spatiale européenne

the grisms which is optimally located to encapsulate the target spectrum. Be aware, however, of the issue of the impact of degradation due to the Jupiter patch (see section 3.5.3.2).

### *Examples 1: Imaging*

#### *Example 1a: Science User Defined Mode*

With 10 ks approved observation time, two OM exposures with 4 ks each can be defined in **Science User Def mode**. The overhead is *0.3* ks per exposure, and one can either cover the central  $5' \times 5'$  at high resolution, or  $7'.6 \times 7'.6$  at low resolution ( $2 \times 2$  binning). The total required observing time will be:  $1.3\text{ ks} + 2 \times (0.3\text{ ks} + 4.0\text{ ks}) = 9.9\text{ ks}$ . With the shortest sensible exposure time of 1 ks, the maximum number of exposures that can be defined is six:  $1.3\text{ ks} + 6 \times (0.3\text{ ks} + 1.0\text{ ks}) = 9.1\text{ ks}$ , but note that significantly more overhead time is needed, and such a setup only makes sense if multiple filters are needed. For monitoring of expected variability, please see Example 3. Note, that for best efficiency, the remaining time (in the last case: 900 sec) can be added to one of the exposures, *e.g.*, the last of the six exposures can be defined as 1.9 ks.

It is recommended to increase the exposure time of the exposure that uses the filter with the lowest throughput (see Fig. 102).

#### *Example 1b: Standard Imaging Mode*

Since an EPIC/RGS **image mode** exposure consists of five subexposures, a defined exposure time of, *e.g.*, 1 ks gives a total exposure time of 5 ks for each 1-ks EPIC/RGS **image mode** exposure. The overhead consists of *1.3* ks (overhead times are given with numbers in italic font) at the beginning of the observation (including the star tracker acquisition time) and  $\sim 1.6$  ks for *each* exposure. If, for example, two EPIC/RGS **image mode** are defined, then the total observing time needed is:  $1.3\text{ ks} + 2 \times (1.6\text{ ks} + 5 \times 1.0\text{ ks}) = 14.5\text{ ks}$ . The overhead times are added automatically when entering the data in the RPS tool.

Thus, an approved 10-ks observation allows the definition of only *one* EPIC/RGS **image mode** exposure:  $1.3\text{ ks} + 1.6\text{ ks} + 5 \times 1.0\text{ ks} = 7.9\text{ ks}$ . Conversely, only one filter can be used with this mode. The remaining 2.1 ks can not be used in this mode, because the overhead of 1.6 ks leaves only 500 sec of exposure, shorter than the minimum allowed exposure time of 800 sec.

In order to use the full time, one can either use **Science User Defined Mode** (see below) or increase the defined exposure time by  $2.1\text{ ks}/5=0.42\text{ ks}$ , thus with *one* EPIC/RGS **image mode** exposure with an exposure time of 1.42 ks, we get:  $1.3\text{ ks} + 1.6\text{ ks} + 5 \times 1.42\text{ ks} = 10.0\text{ ks}$ .

#### *Example 1c: Full Frame Low Resolution*

If **Full Frame Low Resolution Mode** is used, in 10 ks we can obtain two exposures of 1.6 ks each, in two different filters:  $1.0\text{ ks} + [2 \times (2.9\text{ ks} + 1.6\text{ ks})] = 10\text{ ks}$  (the FF Low Res. exposure overhead is 2.9 ks). The overhead of the first exposure of the observation for this mode being  $\sim 1.0$  ks.

#### *Example 1d: Multi-filter for longer Observations*

A 28 ks X-ray observation allows four EPIC/RGS **Image mode** OM exposures:

$$1.3\text{ ks} + 4 \times [1.6\text{ ks} + (5 \times 1.0\text{ ks})] = 27.7\text{ ks}.$$

Preferred choice of filters is: U, UVW1, UVM2, UVW2 (in that order). Due to the different throughput of the different filters (see Fig. 102), it is recommended to define longer exposure times for those filters with low throughput. In the above case, if the U filter is not really needed, one might prefer three exposures with  $t_1 = 1\text{ ks}$ ,  $t_2 = 1.5\text{ ks}$ , and  $t_3 = 1.9\text{ ks}$ , yielding:

$$1.3\text{ ks} +$$

$$1.6\text{ ks} + (5 \times 1.0\text{ ks})$$

$$1.6\text{ ks} + (5 \times 1.5\text{ ks})$$

$$1.6\text{ ks} + (5 \times 1.9\text{ ks}) = 28.1\text{ ks}.$$

**esa**european space agency  
agence spatiale européenne

If only a single filter is to be used, it is better to define only one exposure with the maximum exposure time of 5 ks:  $1.3\text{ ks} + 1.6\text{ ks} + (5 \times 5.0\text{ ks}) = 27.9\text{ ks}$ .

***Example 2: Monitoring a variable point source***

It is recommended to use Science User Def mode for variability studies: define one image window plus one additional fast window, both centred on the source coordinates. Choose maximum exposure times (4400 sec) to minimise overhead. The calculation of exposure times is the same as in example 1a. Depending on the expected time scales of variability, the time bin size for the fast window can be adjusted to values between 0.5 and 20 s. For studies of variability it is recommended to use the same filter for all observations. While the use of UV filters is encouraged for imaging, it depends on the scientific aims whether strictly simultaneous X-ray/optical or X-ray/UV monitoring is of higher interest.

### **3.5.10 OM specific proposal submission information**

The XMM-Newton PIs must be aware that if OM can not be used for scientific purposes, OM will be exposed with filter BLOCKED, and that time will be used to perform technical exposures like flat-fields, darks, etc...

In the preparation of OM observing proposals, the following information should be taken into account.

#### **3.5.10.1 Choice of Science User Defined non-default windows**

For OM observations more than one science window may be defined. The different science windows may overlap (as long as they overlap fully) without loss of information in any of these windows. Specifically, a FAST mode WINDOW inside an IMAGE mode WINDOW does not punch a hole into the image, thus, the source will be in the image **and** in the fast window. There are several boundary conditions that limit the user's choice and which **must** be taken into account properly if a non-default window configuration is going to be used.

- Maximum number of windows

Up to five science windows in total (of which up to two in the FAST mode) are allowed.

- Allowed science window locations and sizes

The size of an OM science window must be integer multiples of 16 in-memory ( $0''.5$ ) centroiding pixels, i.e.,  $2 \times 2$  CCD pixels.

Science windows must start at an even pixel number in both the horizontal (x-) and the vertical (y-) direction [*e.g.*: (16,16), (32,32)], and end at (n×16,n×16), where n is an integer number. Starting at pixel coordinate (0,0) is not possible because of the necessity to allocate a 16 pixel wide margin to accommodate spacecraft drift.

The maximum size for a single window in the Sci.User Defined Image Mode is:

- full resolution:  $652 \times 652$  pixels ( $5'.17 \times 5'.17$ )
- $2 \times 2$  binning:  $488 \times 480$  binned pixels ( $7'.6 \times 7'.5$ )



or any rectangular size with a total equivalent number of pixels. If more than one image window is defined, the sum of the number of pixels (binned or not) of all windows should not exceed 432698.

The maximum size of a Fast Mode window is 512 pixels in full resolution, equivalent to  $22 \times 23$  pixels (about  $10''.5 \times 10''.5$ ).

- Science window overlaps

Different scenarios for OM science window configurations are displayed in Figs. 114 and 115. **OM science windows must overlap either entirely or not at all.** This must be true for all satellite position angles allowed by the specifications made during proposal submission.

User defined OM windows should be specified in sky coordinates and angular size. All limitations in size and position are taken into account by the mission planning system after the detailed observation definition, performed in the second phase of

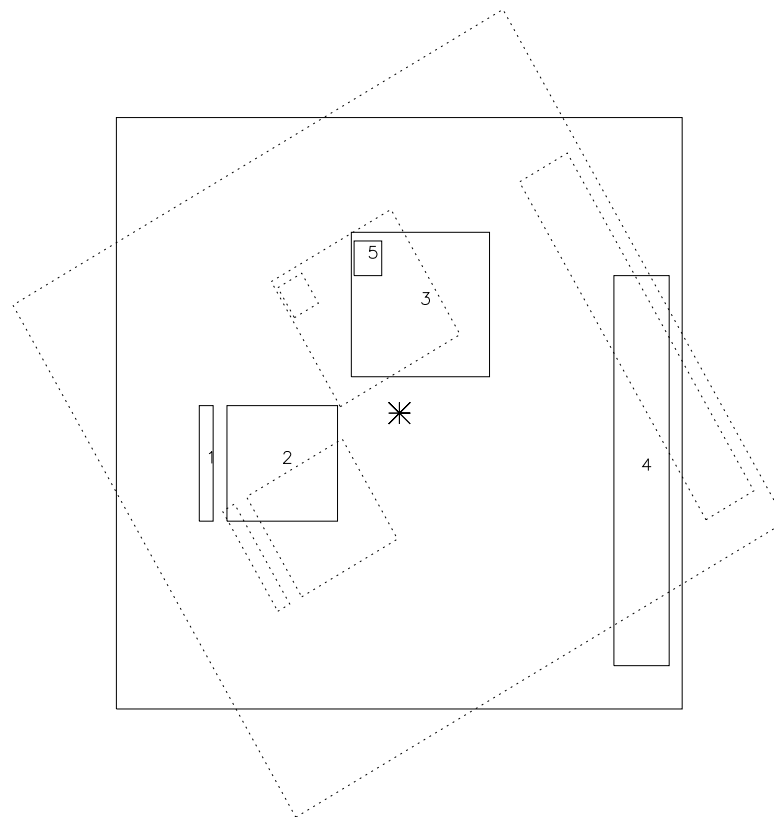


Figure 114: When the boundaries of OM science windows are defined in detector pixel coordinates, the relative location of the windows with respect to each other does not change. However, different areas on the sky are imaged under different position angles.

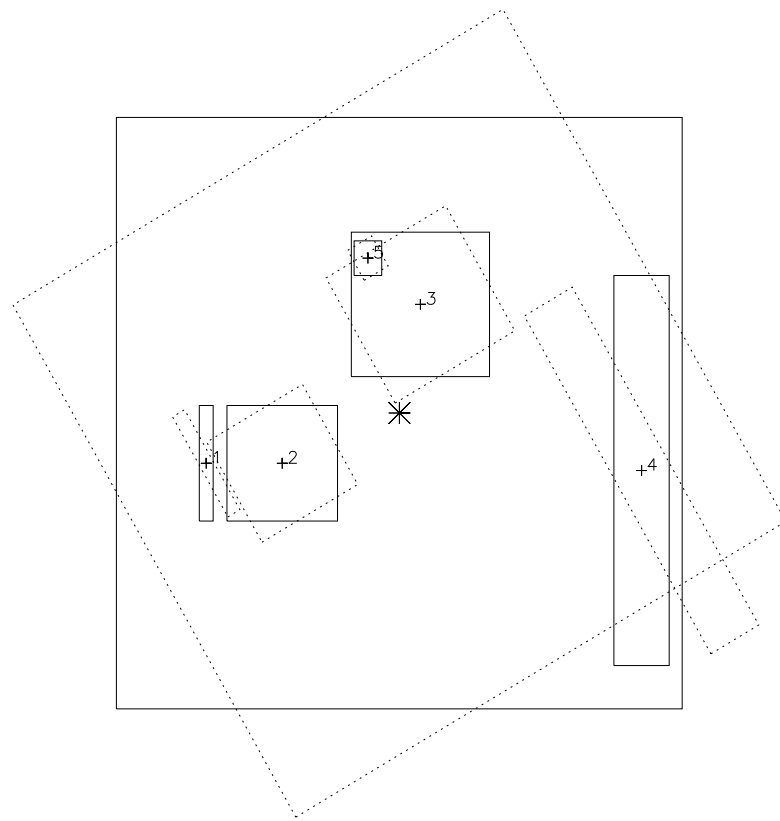


Figure 115: Defining the locations of OM science windows in sky coordinates one makes sure that (approximately) the same area of the sky is imaged under different position angles. However, the OM science windows can change their relative locations. Windows 3 and 5 (which used to be in the upper left corner of window 3, see previous figure) are now partially overlapping, which is not allowed and window 4 is now partly outside the OM FOV (which is also not allowed).

proposal submission.

- Fast Mode slice duration constraints

The minimum Fast mode time slice duration for a Fast mode window is 0.5 s while the maximum duration is the tracking frame duration (20 s).

For a more detailed explanation the reader may refer to the technical note on Constraints on the OM Window Configuration and Definition of the OM Default Configurations (§ 7).

An interactive tool for planning OM observations of point sources is available at the MSSL URL: [http://www.mssl.ucl.ac.uk/www\\_astro/xmm/om/om\\_tool\\_current.html](http://www.mssl.ucl.ac.uk/www_astro/xmm/om/om_tool_current.html)

**esa**european space agency  
agence spatiale européenne

### 3.6 XMM-Newton support instruments

The so-called “non-science” instruments on board XMM-Newton are the EPIC Radiation Monitor System (ERMS) and the Attitude and Orbital Control System (AOCS).

#### 3.6.1 EPIC Radiation Monitor Subsystem (ERMS)

The ERMS registers the total count rate and also basic spectral information on the background radiation impinging on XMM-Newton and its science instruments. This is done not only during science observations, but during the entire lifetime of the mission.

Depending on the mode in which the ERMS is operated, it updates background radiation information once in 512 seconds (slow mode) or 4 seconds (fast mode). The ERMS is normally working in slow mode.

The ERMS data consist of three measurements per readout, two spectra from the High Energy Detectors (HEDs) and one from the Low Energy Detector (LED). 256 spectral bins each will be available in the LED and HED. The HEDs are sensitive to electrons above 200 keV and protons above 10 MeV, while the LED is sensitive to electrons with energies above 50 keV.

The two high energy spectra are the “HE detector spectrum”, with events from either one or both HE detectors, and the “coincidence HE spectrum”, in which only events detected by both HEDs will be recorded.

The data from the ERMS comprise the following quantities:

- one header keyword (warning flag),
- seven broad-band count rates, three from the LED, four from the HEDs,
- LE detector spectrum (256 channels),
- HE detector spectrum (256 channels),
- HE coincidence spectrum.

In this way, the ERMS monitors the total radiation dose that XMM-Newton is exposed to. When the level of radiation intensity exceeds a certain threshold, the ERMS issues a warning to the ground for the Spacecraft Operator to safe the instruments.

ERMS data are not delivered to the PI as part of the XMM-Newton science data but can be obtained from the SOC on request. Note that these data are not properly calibrated and therefore are not suitable for general scientific use.

#### 3.6.2 Attitude & Orbit Control Subsystem (AOCS)

The AOCS determines the attitude of the XMM-Newton spacecraft while in orbit, based on the information from one of XMM-Newton’s two star trackers (which are operated in cold redundancy) and its “Fine Sun Sensors”. During slews and the post-slew phase (comprising attitude determination, trim, and settling of the spacecraft), entries are made into the Attitude History File (AHF) every 10 seconds. Note that during slews the AHF will not contain attitudes reconstructed from actual AOCS telemetry, but the results of a slew time/path predictor, based on the actually observed slew start/end times and attitudes. The accuracy of the attitude reconstruction during slews is expected to be better than 1'.

In the “stable pointing mode” (i.e., after the slews and the post-slew phase), the conditions under which entries into the AHF are made are optimised parameters. An entry is made into



the AHF only in case of Relative Pointing Errors (RPEs) exceeding the programmed limit. The minimal programmable limit (i.e., the smallest programmable deviation from the nominal boresight) is  $1''$ . The minimal time resolution with which entries into the AHF can be made in case of such instantaneous excursions is 2 seconds. For a single nominal pointing entry, only a mean RPE will be provided.

The AOCS attitude information is independent of that from the OM's star tracking windows (§ 3.5.9).

The AHF is a file containing processed AOCS telemetry. Clipped to the start/end times of an observation or slew, the complete AHF for the relevant revolution becomes an ODF or SDF component which is delivered to the observer. For “stable pointing periods” the data records identify intervals of time during which the spacecraft’s boresight did not deviate by more than a configurable limit from the mean boresight during that period. For open loop slews and post-slew attitude trims, the AHF provides the instantaneous boresight at equidistant points in time (typically 10 seconds). It should be noted that attitudes for open loop slews are derived from a “slew model” into which the boundary conditions (actual start/end times and attitudes) have been entered, i.e., the intermediate attitudes provided for slews are not based on sensor data telemetered during the slews.

It should be noted that there is an additional file that holds attitude data, which can be used by the SAS. This is the so called Raw Attitude File (RAF) which provides the attitude information at the maximum possible rate (one entry every 0.5 s). The AHF is in fact a smoothed and filtered version of the RAF. The online documentation of the SAS package *oal* (section on SAS\_ATTITUDE) gives further info on how to select amongst the AHF and RAF source of ODF attitude data.



### 3.7 Comparison with other X-ray satellites

A basic comparison of XMM-Newton's properties with those of *Chandra*, ROSAT, ASCA, RXTE, *Swift*, *Suzaku* and *NuSTAR* is given in Table 28. It is immediately clear that *Chandra* and XMM-Newton have complementary characteristics and that both have constituted a new generation of X-ray missions, with enormously improved capabilities compared to their predecessors ASCA, ROSAT and RXTE.

Table 28: *Comparison of XMM-Newton with other X-ray satellites*

Satellite	Mirror PSF FWHM ["]	Mirror PSF HEW ["]	E range [keV]	$A_e$ at 1 keV [ $\text{cm}^2$ ] <sup>a</sup>	Orbital target visibility [hr]	Energy resolution at 1 keV [eV]
XMM-Newton	6	15	0.15 - 12	4650 <sup>b</sup>	36.7 <sup>c</sup>	4 (RGS)
<i>Chandra</i>	0.2 <sup>d</sup>	0.5 <sup>d</sup>	0.1 - 10	555 (ACIS-S)	44.4 <sup>c</sup>	1 (HETG)
ROSAT	3.5	7	0.1 - 2.4	400	1.3 <sup>e</sup>	500
ASCA	73	174	0.5 - 10	350	0.9 <sup>e</sup>	100
<i>Suzaku</i>	96 - 120	108 - 138	0.2 - 600	1760 (XIS)	0.72 <sup>e</sup>	50
RXTE	n.a. <sup>g</sup>	n.a. <sup>g</sup>	2-250	n.a. <sup>g</sup>	1 <sup>e</sup>	n.a. <sup>g</sup>
<i>Swift</i>	8.8	18 <sup>f</sup>	0.2-10 (XRT)	133.5	~0.8 <sup>e</sup>	70
<i>NuSTAR</i>	18	58	3-79	n.a. <sup>g</sup>	~0.8 <sup>e</sup>	n.a. <sup>g</sup>

Notes to Table 28:

a) Mirror effective area.

b) Note that Figs. 11 and 12 do not just show the mirror effective areas but have the EPIC detector responses included as well.

c) Orbital visibility outside the particle-radiation dominated zone.

d) The *Chandra* High Resolution Camera (HRC) spatial response is well matched to the mirror resolution and the intrinsic on-axis PSF of the HRC is well modelled by a Gaussian with a FWHM of 0.4 arcsec. The spatial resolution for on-axis imaging with the ACIS instrument is limited by the physical size of the CCD pixels (0.492 arcsec) and not the mirrors.

e) Low orbit with Earth occultation.

f) At 1.5 keV.

g) n.av.: not available, n.a.: not applicable.

Some special strengths of XMM-Newton are e.g.:

- Extreme sensitivity to extended emission.
- High-resolution spectroscopy (RGS) with **simultaneous** medium-resolution spectroscopy and imaging (EPIC) and optical/UV observations (OM).
- High sensitivity (EPIC) at high energies.
- Excellent low energy response down to 0.15 keV.
- High time resolution (EPIC).

#### 3.7.1 A comparison of XMM-Newton vs. Chandra

The main difference in instrument operation between XMM-Newton and *Chandra* is that on XMM-Newton all instruments operate simultaneously, unless prohibited by constraints (§ 4.2), while on *Chandra* they are alternated.



**esa**

European space agency  
agence spatiale européenne

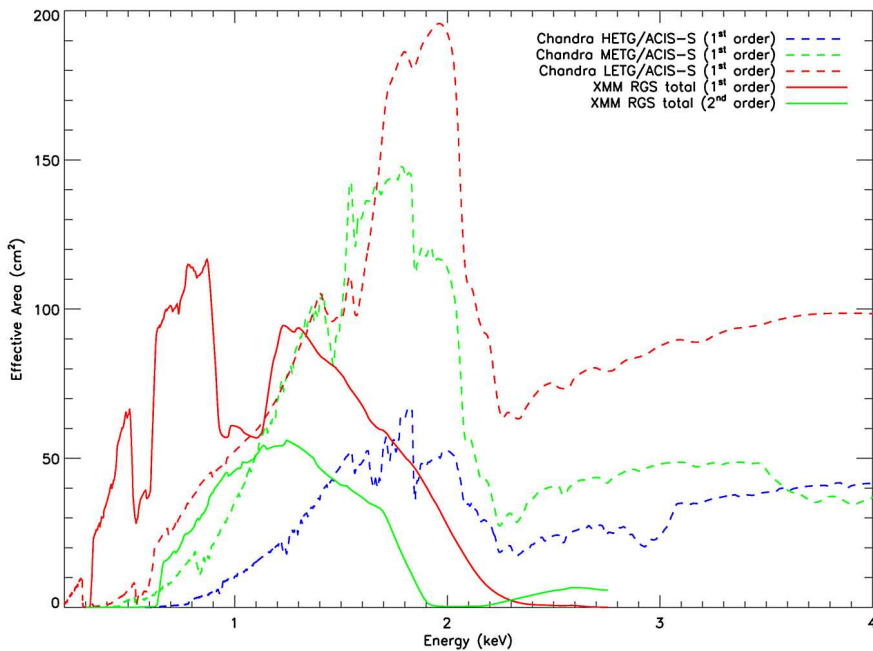


Figure 116: The effective area of both RGS units combined, compared with *Chandra*'s ACIS-S instrument with various transmission gratings. Note that since early after the beginning of the mission, CCD7 in RGS1 and CCD4 in RGS2 are inoperative, thus the effective area in each of the mentioned CCD energy range is reduced by a factor of 2 (see Table 9).

Further differences between *Chandra* and XMM-Newton, in addition to the ones summarised in Table 28, are shown below.

### 3.7.1.1 Effective area for dispersive spectroscopy

Fig. 116 displays the effective area of both RGS units together (from Fig. 84), compared with different *Chandra* instrument combinations. In order to avoid overcrowding the figure, the combination of *Chandra* HRC+LETG is not shown.

### 3.7.1.2 Non-dispersive spectroscopy: an example

For illustrative purposes, Fig. 117 shows a comparison of an XMM-Newton EPIC and a *Chandra* ACIS-I observation of a cluster with a 6 keV thermal plasma spectrum, 0.3 solar metallicity, a redshift of 0.3 and an X-ray flux in the 0.1–10 keV band of  $10^{-12}$  erg cm $^{-2}$  s $^{-1}$  (thus a fairly luminous system). Such a comparison gives a good feel for the capabilities of both instruments for performing studies of faint objects. We simulated the response of the *Chandra* ACIS front-illuminated CCD imaging instrument, using the response matrices supplied for the guest observer proposal submission. With a 30 ksec observation, ACIS is able to measure the temperature of the cluster to about 10% accuracy (assuming only poissonian noise and neglecting systematic effects). Following the same procedure, i.e., up-to-date detector response matrices, input spectrum and observing time, the combined response of the 3 EPIC focal plane cameras on XMM-Newton allows a 2.5% accuracy on the estimated cluster temperature (neglecting systematic effects).



The bottom panel of Fig. 117 also illustrates the different line spectral resolution that XMM-Newton EPIC and RGS and the *Chandra* ACIS instruments can achieve.

The presented count spectra comparisons are based on year 2008 responses. For data of different mission epochs the actual appearance of the count spectra comparisons, especially at the low energies, varies due to the different level of contamination of various instruments at different epochs. The losses of effective areas due to contamination are corrected by the correspondent instrument calibrations.

### 3.7.1.3 XMM-Newton EPIC vs. Chandra ACIS-I pile-up comparison

It has been shown above (§ 3.3.9) how pile-up affects the accuracy of spectral fits and the shape of the X-ray PSF. Figs. 118 and 119 show the fraction of piled-up events for different numbers of counts per CCD frame (in full window imaging mode). One can see in Fig. 119 that pile-up effects for given source fluxes are more severe for ACIS-I by more than an order of magnitude compared to EPIC MOS and even by two orders of magnitude compared to EPIC pn.

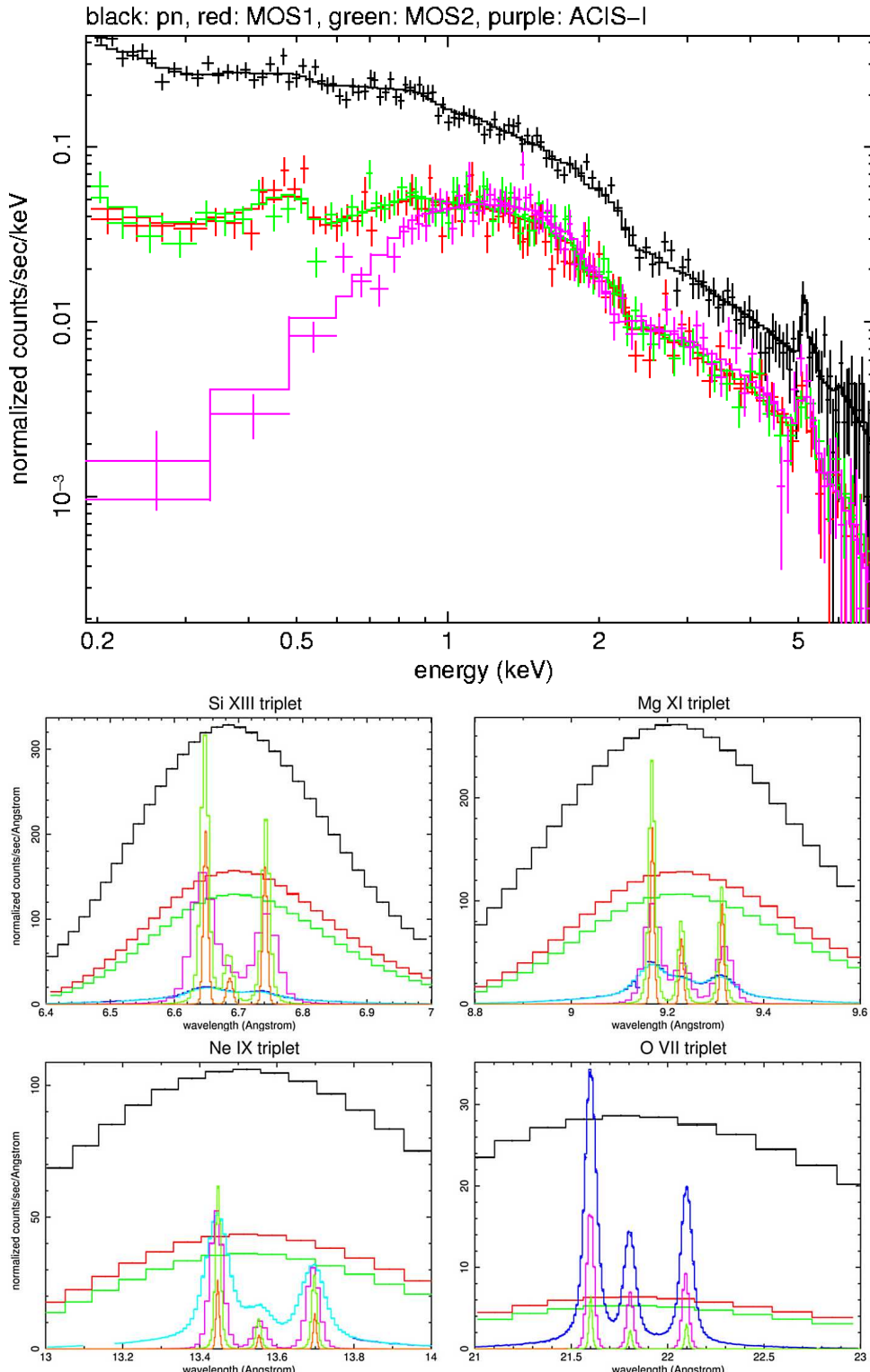


Figure 117: Top: Comparison of a modelled 30 ks observation of a cluster with a 6 keV thermal plasma spectrum with Chandra ACIS-I (purple line) and XMM-Newton EPIC (pn: black, MOS1: red, MOS2: green). Normalised counts are counts per spectral bin. Bottom: Comparison of the spectral response, for several line triplets at different energies, of XMM-Newton EPIC and RGS and Chandra ACIS instruments. Colour codes are: pn: black; MOS1: red; MOS2: green; RGS1/RGS2: dark/light blue; ACIS LEG/MEG/HEG: purple/green/orange.

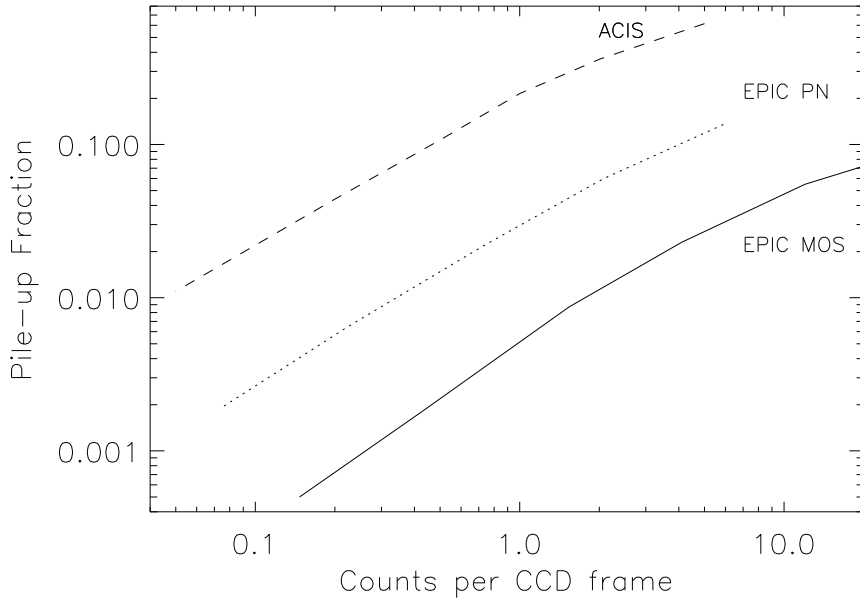


Figure 118: Comparison of Chandra ACIS-I vs. XMM-Newton EPIC (pn and MOS) pile-up for different total frame count rates. The frame times are 3.3, 2.8 and 0.07 seconds for ACIS-I, MOS and pn, respectively.

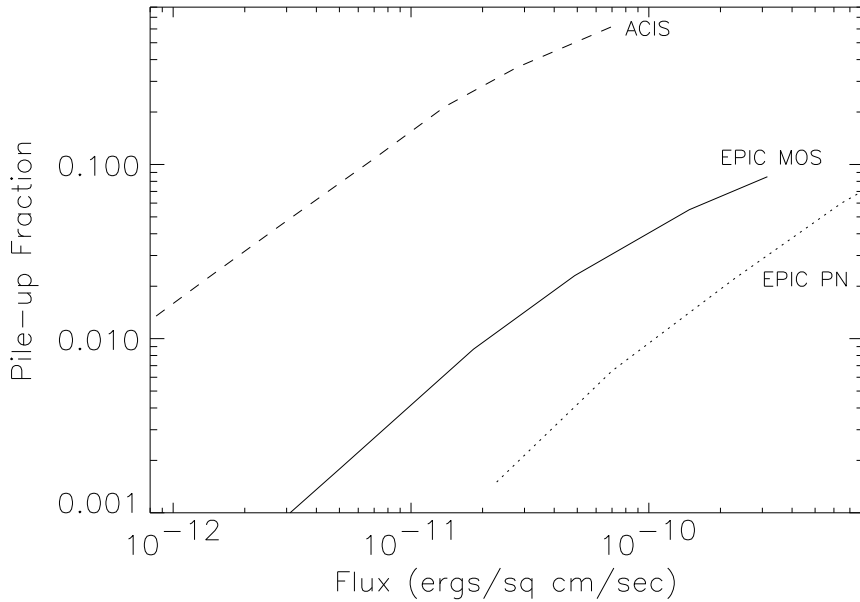


Figure 119: Comparison of Chandra ACIS-I vs. XMM-Newton EPIC (pn and MOS) pile-up for different incident source fluxes, after conversion of counts per frame to flux units, adopting an  $\alpha = -1.7$  power law spectrum with an absorbing hydrogen column density of  $3 \times 10^{20} \text{ cm}^{-2}$ .



## 4 Observing with XMM-Newton

XMM-Newton observes with all instruments simultaneously, brightness limits and other constraints permitting. All instruments can be operated independently (i.e., the exposure times of individual instruments are not coupled to each other) and observers will receive the science data of all science instruments operating during an observation.

When planning XMM-Newton observations, several boundary conditions must be taken into account. The constraining parameters are listed in this section. The available SOC services listed in section 7 aid in planning XMM-Newton observations. The Target Visibility Checker can be used to determine the times of visibility of a given target. To avoid duplications, the Target Search Tool and the list of Pending Anticipated ToO and Triggered Observations can be used to search for performed and planned observations.

Users are encouraged to inspect the outcome of performed observations when planning to apply for new data.

### 4.1 XMM-Newton orbit

XMM-Newton was launched on the 10th December 1999 by an Ariane 5 launcher into a highly elliptical orbit, with an apogee of about 115,000 km and a perigee of ca. 6000 km (Fig. 120). XMM-Newton is operated with three ground stations, located at Yatharagga, Kourou and Santiago de Chile (occasionally also ESAC, Madrid, Spain).

Due to several perturbations, the orbit of XMM-Newton changes with time. In addition, an orbit correction manoeuvre was performed in February 2003 to ensure full ground station coverage during the entire science period. The orbital parameters for May 2021 are listed in Table 29. Such an orbit provides the best visibility in the southern celestial sky (§ 4.2.3).

Table 29: *Evolution of Orbital Parameters of XMM-Newton*

	May 2018	May 2020	May 2022	unit
Inclination	70.0	71.0	70.3	°
Right ascension of ascending node	348.9	322.3	305.8	°
Argument of perigee	95.5	93.1	87.2	°
Apogee height	114.3	108.9	101.2	$10^3$ km
Perigee height	6.8	12.2	19.2	$10^3$ km
Eccentricity	0.82	0.78	0.67	
Period	47.86	47.87	47.86	hours

### 4.2 Observing constraints

For the individual instruments, and also for the XMM-Newton observatory in general, different observing constraints apply, which may affect the schedulability of targets significantly. These are:



**esa**

european space agency  
agence spatiale européenne

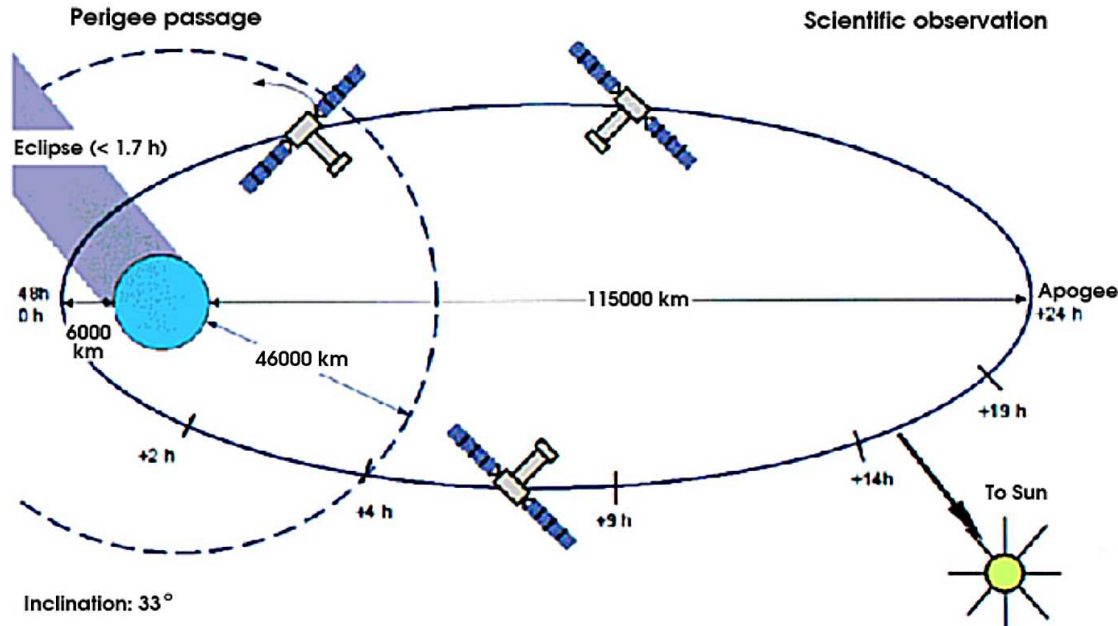


Figure 120: Sketch of the highly elliptical XMM-Newton orbit. Original figure provided by Dornier Satellitensysteme GmbH.

#### 4.2.1 Radiation belts

The radiation background is variable around the XMM-Newton operational orbit, depending on the satellite's location with respect to Earth's magnetosphere. For useful XMM-Newton science observations to be conducted, the minimum satellite elevation is 46000 km. At this height, the EPIC, OM and RGS instruments can start to perform scientific observations, but only if the radiation background is low enough. Otherwise this radiation can damage the detectors. Experience after the first years of XMM-Newton operations shows that it is only from very few minutes to about 3 hours after the correct elevation is reached when it is safe for the X-ray instruments to start the observations. Similarly, X-ray instruments have to be closed from very few minutes to about 3 hours before the satellite elevation goes down to the nominal 46000 km at the end of each orbit. The spacecraft spends 143 ks of the 48-hour orbital period above 46000 km, and because of the radiation background, on average about 132 ks can be used to perform scientific observations with the EPIC and RGS instruments. More details about the expected duration of the science window per orbit are available from the Target Visibility Checker web page.

The particle background outside the belts is dominated by the solar particle emission. The incident flux is therefore coupled to the level of solar activity. During intense solar flares the XMM-Newton payload instruments are switched off.



#### 4.2.2 Celestial constraints

The visibility of sources in the sky depends on several constraints, including avoidance of solar system sources. These are:

- Solar avoidance

A solar aspect angle within the range  $70^\circ$ - $110^\circ$  must be maintained at all times. Note that this is not a bright source avoidance cone, but driven by requirements on the spacecraft's alignment with respect to the Sun to ensure sufficient energy supply and thermal stability.

For the same reasons, the position angle of the observation must be within  $\pm 20^\circ$  of the nominal position angle as defined in § 4.4.2

- Earth limb avoidance

Minimum avoidance angle:  $42.5^\circ$ .

- Lunar avoidance

Nominal minimum avoidance angle:  $22^\circ$ .

Minimum avoidance angle during eclipses:  $35^\circ$ .

#### 4.2.3 Sky visibility during the XMM-Newton mission

Target visibility should **always** be checked using the Target Visibility Checker available at URL <http://www.cosmos.esa.int/web/xmm-newton/target-visibility-tool>.

The Target Visibility Checker allows input of RA and Dec coordinates of a source and find the orbits and times when it is visible to XMM-Newton subject to viewing constraints. The constraints applied in the visibility analysis are actually used for satellite operation. More details on the use of this tool are provided on the Target Visibility Checker web page, especially in the "HowTo" section.

Fig. 121 displays a first-order approximation of the sky visibility during the current AO. It is shown for illustrative purposes and can be used as a rough guideline to assess whether any visibility problem exists, but it is not intended to be used for quantitative statements. An interactive tool based on this figure is available under the link <http://www.cosmos.esa.int/web/xmm-newton/xmm-visibility>.

Fig. 122 shows sky areas for which a certain maximum continuous target visibility is reached within a single revolution in the current AO. Due to the evolution of the XMM-Newton orbit, this diagram is in fact changing with time; the visibility of some sky regions has become better along the XMM-Newton lifetime, while it is now significantly worse in some other regions. The same Fig. 122 has been generated for future AOs (Fig. 123), based on orbit evolution forecast. Absolute numbers on the visibility of a given region must be taken just as rough estimates, but the overall trend is correct: the poorer visibility occurs near the Earth location at spacecraft apogee and this position moves to higher declination and lower right ascension.

We recall that to obtain accurate visibility information for a given target coordinates, the Target Visibility Checker **must** be used.



**esa**

European space agency  
agence spatiale européenne

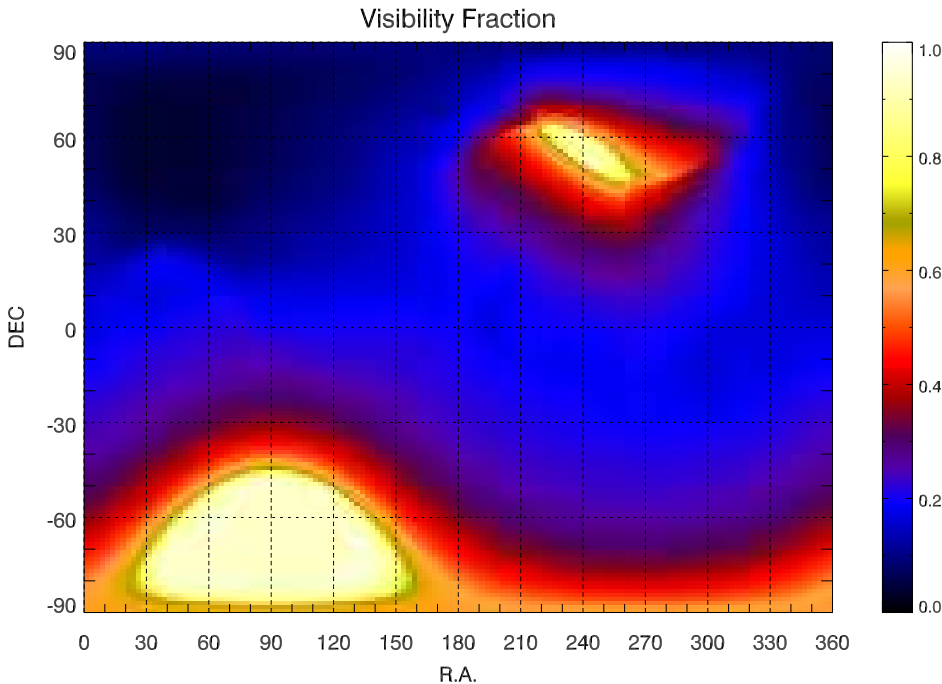


Figure 121: *Approximate sky visibility, as a fraction of the total time available for science*

## 4.3 Points of concern

### 4.3.1 Bright source avoidance

In both the X-ray (EPIC/RGS) and the optical/UV regime (OM) there are restrictions with respect to the brightness of sources within the field of view, albeit of a different nature.

- Star tracker bright optical source avoidance

At present, there is no problem for the star tracker on board XMM-Newton to acquire a requested pointing. However, if a star with V magnitude less or similar to 2 is within  $2.5^\circ$  radius of the aimed target position, special operations that imply longer slew manoeuvres are needed. Anyway, the avoidance of bright sources within the field of view of the star tracker is not a concern to the user.

- OM bright optical/UV source avoidance

With the increasing count rate of a target, the science quality of OM data for that source is compromised by deadtime effects. The effect is of the order of 5% for a source with a count rate of 10 counts/s, increasing to approximately 30% for sources with count rates of 50 counts/s (assuming in both cases a CCD frame rate of 100 Hz).

A different kind of limitation is imposed on science observations by the OM detector photocathode. MCP-based intensifier tubes show localised gain depressions caused by bright point sources. The main cause of the sensitivity loss is related to the defects in the photocathode. From measurements made with OM test tubes, a non-linear relationship between the local sensitivity loss with accumulated count dosage

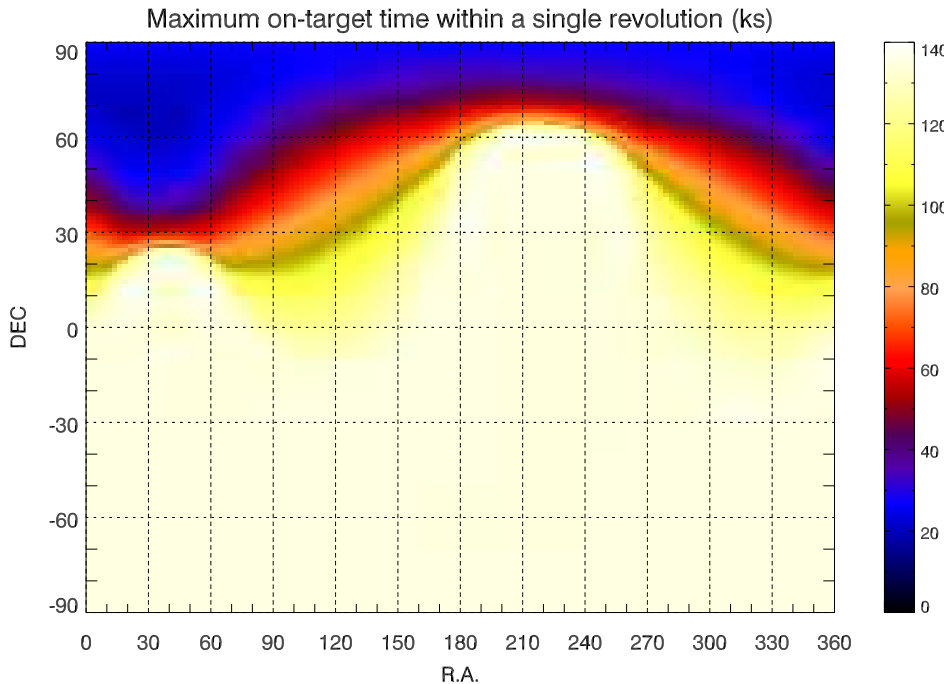


Figure 122: *Maximum target visibility within a single orbit of XMM-Newton during the current AO.*

was established. The brightness limits for all OM filters are tabulated in Table 25 in § 3.5.6.

OM observations of sources beyond these brightness limits are not allowed. **These limits hold for any source in the OM FOV, even if it resides outside an active OM window.**

Since the above refers to point source limits, the quantity to be specified in XMM-Newton observing proposals for extended sources, like e.g. galaxies with active nuclei, is the maximum surface brightness (in most cases of the central object) in V magnitudes per square arcsec. The limits (at the position of the brightest emission) are the same as for point sources (see Table 25).

In addition, the following solar system sources must be avoided by the OM, with avoidance angles as listed:

- Mars –  $3.5^\circ$
- Jupiter –  $4.5^\circ$
- Saturn –  $2^\circ$
- Uranus –  $0.25^\circ$
- Neptune –  $0.25^\circ$

Avoidance of planets will be ensured by the SOC and is thus not a concern to the user. We remark that the planets avoidance only affects OM, but not EPIC or RGS instruments.



XMM-Newton Science Operations Centre

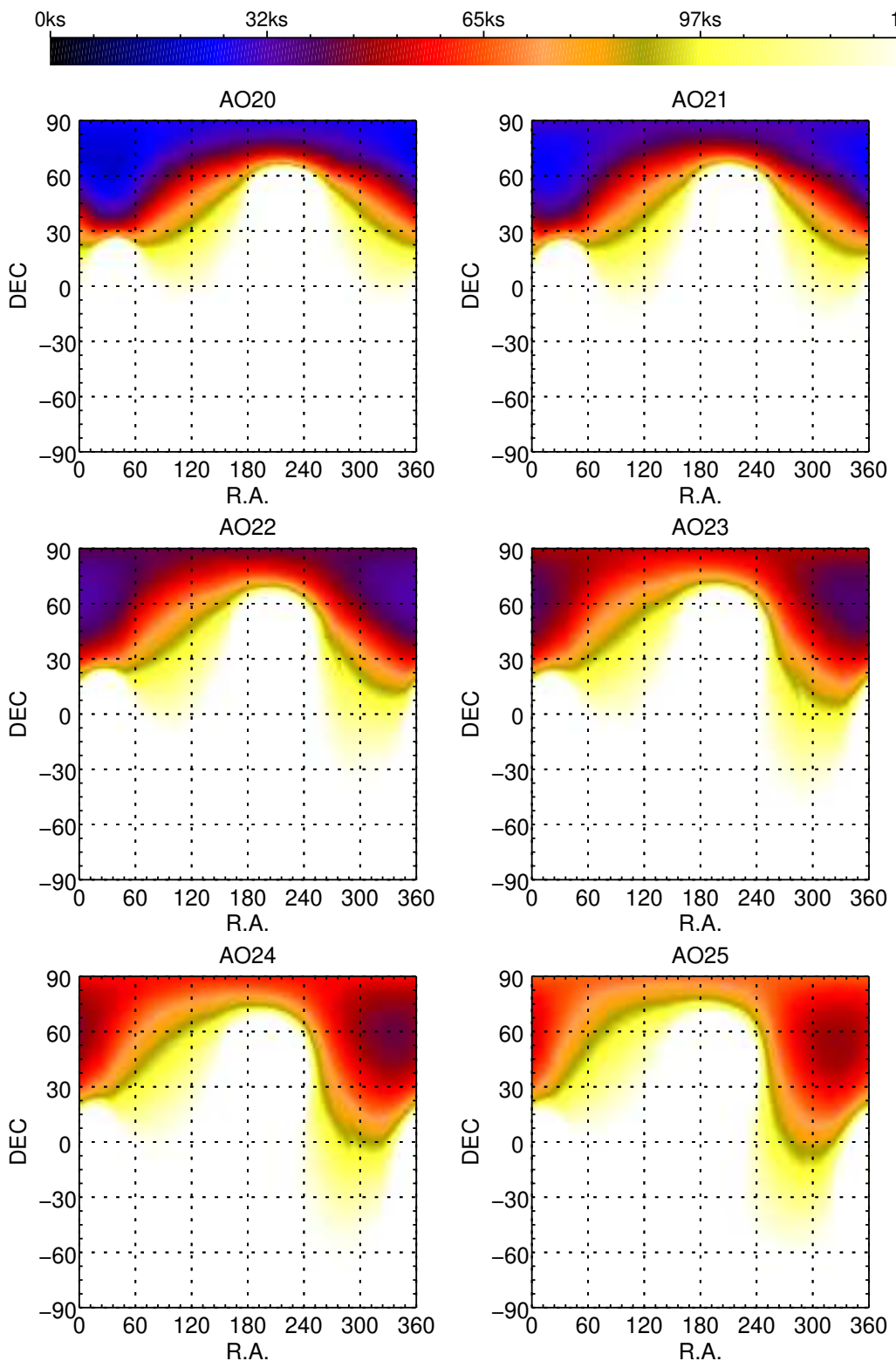


Figure 123: Evolution of maximum target visibility within a single orbit for future AOs



- RGS bright optical/UV source avoidance

Bright optical/UV light entering the RGS under certain angles can deteriorate the quality of the science observations. This is described in § 3.4.6.1.

- EPIC bright optical/UV source avoidance

For the EPIC pn, care should be taken to avoid the presence of a bright optical source located at the same RAWX as the target and at smaller RAWY than the target, i.e. between the target and the CAMEX. Charge would otherwise be transferred over an additional optically generated signal which would alter the CTE in a way which is not modelled, thus adversely affecting the energy reconstruction. This precaution should also be taken for windowed modes, even if the optical source falls outside of the window.

For more details see chapters § 3.3, § 3.3.8 and § 3.3.9.

- EPIC bright X-ray source avoidance

Observations with an expected high level of photon pile-up are not *per se* disallowed, but a special scientific justification is expected stating why and how the scientific goals of the proposal can be achieved despite the expected pile-up (and thus the deteriorated spectral response and PSF quality; §§ 3.3.9 and 3.7.1.3).

Bright optical off-axis objects can leak through the filters and generate false X-ray events that can contribute to the degradation of the telemetry bandwidth. This effect becomes important if the off-axis source is 50 times brighter than the on-axis limit, i.e. 4 or 5 magnitudes brighter.

The EPIC telemetry limits are not hard-wired, making it difficult to provide universal guidelines. For EPIC MOS imaging modes the baseline count rate allowed is about 115 counts/s. For EPIC pn imaging modes, it is about 600 counts/s (over all active CCDs), and therefore observations of single bright point sources at the pile-up limit are not constrained by telemetry. For Timing Mode, a conservative limit can be estimated to be 450 counts/s. Sources at the pile-up limit can still suffer a  $\sim 10\%$  exposure loss due to counting mode. It should be noted that the count rate limits include the background. In Timing Mode the full energy band background count rate measured during the mission is  $< 0.3$  counts per second and column (99% confidence level). In most cases where the source count rate requires the usage of Timing Mode, the source largely dominates the integrated count rate in the EPIC-pn sensitive energy bandpass. It should be stressed that the exact background rate measured during a specific observation is dependent on the position of the source due to the potential confusion of serendipitous point sources as well as of truly diffuse emission, especially along lines-of-sight close to the Galactic plane.

If the total (source plus background) count rate is above a certain limit (a few hundred counts/s), either because of the source being too bright or due to very high flaring background, the EPIC cameras will switch to the so-called ‘counting mode’, a special (non-science) instrument mode where no transmission of information for individual X-ray events occurs.

- No RGS bright X-ray source avoidance

Due to the much smaller effective area of RGS compared to EPIC and the dispersion of the source spectra over many detector pixels, the source count rates per pixel are



much lower. Therefore, photon pile-up in RGS is usually negligible (see however § 3.4.5 for cases where pile-up may occur). Only optically bright sources can impose constraints on RGS observations, as mentioned above. However, radiation of nearby X-ray sources should not fall on the dispersed spectrum of the target source (§ 4.4.2).

#### 4.3.2 Other considerations

Some more parameters that might influence certain XMM-Newton observations, and should therefore be taken into account, are:

- Seam losses between abutted CCDs

Although small, there are gaps between the chips of the different X-ray detectors on board XMM-Newton. The two EPIC MOS cameras are mounted orthogonal with respect to each other, so that in final images, after adding up the data from two X-ray telescopes, the gaps should not be visible after correction for exposure. There will only be a reduced total integration time in areas imaged at the location of chip boundaries. The pn camera has a different chip pattern, leading to minimal losses in other areas of the field of view. It is also offset with respect to the X-ray telescope's optical axis so that the central chip boundary does not coincide with the on-axis position. The inter-CCD gaps of the EPIC MOS chip array are 400  $\mu\text{m}$  (11") wide. Those between neighbouring CCDs within one quadrant of the pn chip array are 40  $\mu\text{m}$  (1".1) wide, the gaps between quadrants about 150  $\mu\text{m}$  (4".1).

The nine CCDs in each RGS also have gaps of about 0.5 mm in between them. Table 9 lists the energies affected by the gaps in the RGSs. The two RGS units have an offset with respect to each other along the dispersion direction to ensure uninterrupted energy coverage over the passband. Due to operational problems with two CCDs there are two additional gaps, one on each RGS unit. The wavelength ranges affected are from 10.6 to 13.8 Å and from 20.0 to 24.1 Å in RGS-1 and RGS-2, respectively.

- “Out of time” events

The XMM-Newton X-ray detectors do not have shutters and are therefore exposed to incoming radiation from the sky at all times . In order to prevent photon pile-up (see § 3.3.9), the CCDs are read out frequently. During readout, photons can still be received. However, they hit pixels while their charges are being transferred to the readout nodes, i.e., when they are not imaging the location on the sky they would normally observe during the exposure. Thus, events hitting them during readout are “out of time” (and also “out of place”; see § 3.3.10). One cannot correct for this effect in individual cases, but only account for it statistically.

The MOS CCDs have frame store areas, which help suppress the effect of out-of-time events. The frame shift times of a few ms are much shorter than the maximum frame integration time of 2.8 s. Therefore, the surface brightness background of smeared photons is only a fraction of a percent divided by the ratio of the PSF size to the CCD column height.

For pn the percentage of “out of time” events is 6.3% for the full frame mode, 2.3% for the extended full frame mode, 0.16% for the large window mode and 1.1% for the small window mode. The large window mode has a smaller fraction of “out of



“time” events because half the image height is used as a storage area, but the reduced smear is penalised by a loss in live time.

- EPIC pn caveat for bright low energy sources

The lower event threshold of the EPIC pn camera constrains its spectral capabilities for sources which show a significant flux below the threshold. These are mostly nearby white dwarfs which have absorption column densities below  $10^{20} \text{ cm}^{-2}$  and temperatures below  $\sim 40 \text{ eV}$ .

This effect is seen in observations of the white dwarf GD 153, that has a temperature of 25 eV, i.e. the bulk of the photons do not directly produce events above the threshold. Spectra of this star taken with various EPIC pn readout modes and filters yield large inconsistencies in the spectra below 0.5 keV. There is a strong correlation between count rates and read-out mode and filters. Slower read-out results in higher count rate and harder spectrum. The medium filter reduces the count rate more than expected from the thin/medium ratio.

The most likely explanation for this effect is pile-up. Three kinds of pile-up at low energies are possible: two source X-ray photons, a source photon with electronic noise and a source X-ray photon with optical photons from the source. Pile-up can bring the energy of sub-threshold events above threshold. Source photons with energies below the threshold (which would nominally not be detected) have a high probability to “gain energy” by fortuitously adding to noise. For weak sources (and/or fast readout) this is most likely the dominant pile-up effect. No calibration is available to correct for this soft pile-up effect.

- EPIC pn frame rejection due to MIPs (Minimum Ionizing Particles)

A certain fraction of EPIC-pn frames are rejected during the standard data processing due to Minimum Ionizing Particles (MIPs, Freyberg et al., 2006, XMM-SOC-CAL-TN-0067). The exact fraction depends on the level of background measured during an observation. It has been observed to be comprised between 3% and 8%. Users are recommended to take this effect into account in their estimation of the requested time.

- EPIC pn timing mode feature

The EPIC pn camera operated in its timing mode shows at `RAWY=19` a bright line in `RAWX` direction. The feature only shows up for bright point sources. Its origin is related to an on-board clock sequence feature whose effect was only noticed after launch.

There is no effect on the scientific quality of the data as long as the integration time for spectra and light curves is longer than 5.9 ms. Care should be taken for pulse phase spectroscopy with bin sizes below 5.9 ms, but only if the pulse period itself is a multiple of the frame time (5.9 ms).

- EPIC MOS1 micro meteorite column

The post-impact offset value in **MOS1 timing mode** is far too large for a meaningful correction to be possible. Users are therefore advised to discard the affected column and the adjacent ones from the accumulation of any scientific products. Please, refer to the SAS watchout web page



<http://www.cosmos.esa.int/web/xmm-newton/sas-watchout>

for a specific recipe on how to calculate effective area files (via arfgen) in this case.

- EPIC-MOS low energy noise in two peripheral CCDs

Two peripheral CCDs of the MOS cameras (CCD4 on MOS1, and CCD5 on MOS2) are frequently affected by a low-energy ( $E < 1$  keV) noise plateau. The cause of this phenomenon is unknown, and currently under investigation. There is a general trend of increasing occurrence rate of noisy CCDs (see Figure 124). There is currently no way to selectively clean the noisy events. As of SASv9.0 a task (emtaglenoise) is available which allows users to tag *all* the events detected in an affected CCD. This issue does not affect the quality of the calibration for the nominal pointed target, and should be taken into account by proposers only with respect to serendipitous point-like sources or for the fraction or large extended diffuse emission falling on the affected CCDs. For more information on "noisy" CCDs users are referred to Kuntz and Snowden, 2008, A&A 478, 575.

- RGA rib scattering

Light scattered off the stiffening ribs of the grating plates of the RGAs produces diffuse ghost images in the EPIC MOS FOV in the  $\pm Y$  direction (i.e., the RGS cross-dispersion direction). The intensity of these images is of the order of  $10^{-4}$  relative to the intensity of the focused image. For off-axis sources at azimuth angles corresponding to the  $\pm Y$  direction, the intensity of the ghost images increases to a few times  $10^{-4}$ .

- OM exposures

When using FAST mode, the target coordinates must be accurate at better than about 2 arcseconds to fit and track the target in the approximately  $10'' \times 10''$  wide windows.

FAST mode OM exposures require a successful Field Acquisition (FAQ). FAQ could fail in crowded fields, where many extended objects are present. This limits the possibility of performing - *e.g.* - high resolution OM timing of active galactic nuclei in clusters.

Ring-like loops due to scattering of out-of-field bright stars (see Fig. 109) can heavily affect the detection of faint or extended sources at the boresight. This effect is mainly due to bright stars that happen to fall in a narrow annulus  $12'.1$  to  $13'$  off-axis.

OM Grisms produce spectra of all objects in the field of view, therefore the spectrum of the target of interest can be contaminated by the zero and first orders from other objects in the field. This problem can usually be avoided by selecting an adequate position angle for the observation.

It has been noted that for bright sources observed in the OM fast mode window, when performed in conjunction with the pre-defined EPIC/RGS Imaging mode configuration (see Section 3.5.9.2), there can be discontinuities in the mean count rate levels of the fast mode time series between each exposure. This stems from the different levels of coincidence loss that occur in each exposure because their different window configurations give rise to differing frametimes. In fact, this effect

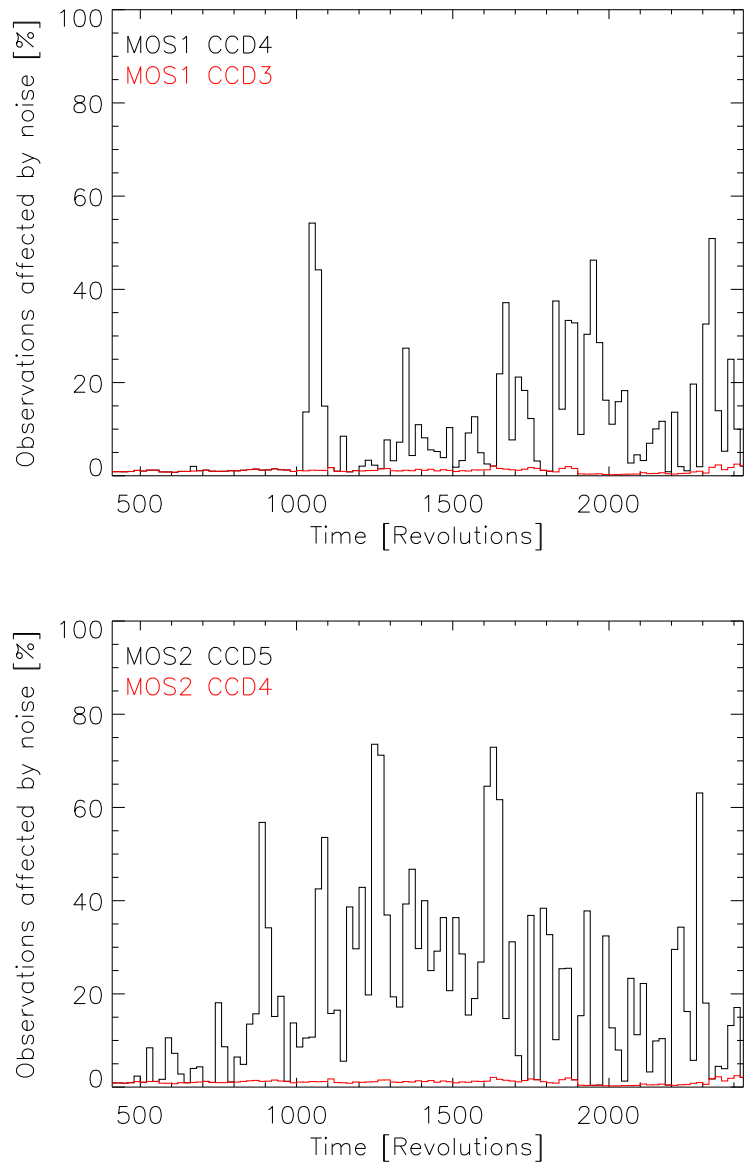


Figure 124: Percentage of observations when the labelled MOS1 (top) and MOS2 (bottom) CCD count rate within the energy range 200-1000 eV is larger by a factor of 4 than the mean of the count rate in the other CCDs (noisy CCD excluded) as a function of the revolution number. In each plot the curves of a "noisy" and of a "clean" CCD are shown.

is also witnessed in the photometry of bright objects observed in the central high-resolution window that is repeatedly (five times) exposed when using the pre-defined EPIC/RGS Imaging mode configuration, for the same reason, regardless of whether



fast mode is operating.

## 4.4 Field of View geometry

### 4.4.1 Instrument alignment

XMM-Newton has three independent X-ray telescopes and an optical/UV telescope, with a total of six science instruments. Neither the telescopes' optical axes nor the centre positions of the detector FOVs are aligned perfectly. Thus, radiation from sources in the spacecraft's boresight direction does not fall onto the nominal on-axis position of all detectors simultaneously.

Starting in AO18, all the observations are performed placing the target at the same position (that corresponding to 'EPIC-pn Prime'), regardless of the instrument selected as 'Prime' in the proposal. This choice does not represent any drawback from the point of view of the RGS spectral coverage, and ensures that the source is located far enough from the edge of the EPIC-pn chip.

The user can always choose an off-axis pointing, but this requires specification of a position angle which implies reduced visibility. The user can use the SAS task 'srcinfov' (which is part of the 'bstools' task package) to determine these choices.

### 4.4.2 Position angle constraints and determination

The orientation of the XMM-Newton instruments is such that the astronomical position angle gives the angular distance of the RGS dispersion axis measured from the celestial North towards East. With regard to the EPIC instruments, their orientations relative to the RGS dispersion axis are shown in Figs. 20 to 22. Examples of the dependence of the EPIC field of view on the position angle can be found in Figs. 17-19. The orientation of the celestial North and East axes over the EPIC-pn detector for a 30° position angle is shown in Fig. 22.

Both RGS and OM with its grisms, can place position angle constraints on observations, if one wants to avoid spatial overlaps of the dispersed spectra of adjacent sources (i.e. to avoid sources to be aligned with the dispersion direction). In the case of RGS, avoidance of bright sources outside the field of view, as described in § 3.4.6.1, can also lead to position angle constraints (see § 4.4.2).

There is no default orientation constraint on XMM-Newton observations. Any constraint imposed on an observation makes it "time-critical" and thereby more difficult to schedule.

Users can check in the Target Visibility Checker possible values of position angles in orbits for which a given target is visible for a minimum observing time. During proposal phase II submission (see XRPS Users Manual), PIs of accepted observations can ask the SOC for enhancement support<sup>7</sup> in the XRPS form in order to optimize the position angle.

## 4.5 Observation overheads

As for all telescopes, XMM-Newton observations are affected by operational overheads. We outline here which overheads apply to XMM-Newton observations. **Some of these overheads need to be taken into account in XMM-Newton observing proposals**, and they will be added on top of the requested science duration as warranted.

There are two categories of overheads:

1. Operational overheads

---

<sup>7</sup>see <http://www.cosmos.esa.int/web/xmm-newton/proposal-enhancement>

**esa**european space agency  
agence spatiale européenne

## 2. Instrument and setup overheads.

### 4.5.1 Operational overheads

XMM-Newton operational overheads are:

- Slew time to move to the target coordinates: variable, depending on the relative target position with respect to the starting spacecraft attitude; the XMM-Newton slew rate is 90°/hour.
- AOCS reference star acquisition time and fine trim to the actual target position after a slew – about half an hour per observation.

**Operational overheads do not need to be taken into account in XMM-Newton observing proposals.**

### 4.5.2 Instrument and setup overheads

The following instrument and setup overheads apply to XMM-Newton science observations. Note that some of them will occur simultaneously, at the start of an observation.

- EPIC setup time is mainly due to the upload (in the case of the MOS cameras) or the calculation and download (in the case of the pn camera) of the offset tables needed to compute the amount of the optical loading of the CCD chips, i.e., the charges that must be subtracted to set the correct zero level for X-ray observations. The overhead of each pn exposure is mode dependent and varies from  $\lesssim 0.5$  to  $\lesssim 1.5$  hours. The overhead of each MOS exposure due to the offset table upload is about 10 minutes.
- The overhead of RGS exposures is about one minute and a half.
- The overheads of the OM exposures are mainly due to the setup of the instrument and the field acquisition driven by the guide star recognition (cp. § 3.5.8).

Instrument and setup overheads need to be taken into account in XMM-Newton observing proposals. A detailed description of the instrument and setup overheads can be found in the **XMM-Newton Proposers Guide and Remote Proposal Submission Software Users Manual** (XRPS). An overview of overheads is given in the overhead table under the link: [http://xmm-tools.cosmos.esa.int/external/xmm\\_user\\_support/documentation/rpsman/overheads\\_table.html](http://xmm-tools.cosmos.esa.int/external/xmm_user_support/documentation/rpsman/overheads_table.html).

### 4.5.3 Special science exposures

Optimal scientific usage of the XMM-Newton instruments sometimes requires special (science) exposures. These are **not** overheads and therefore part of the requested science observing time:

- An OM image with an optical filter may be convenient before using the grisms.
- It is convenient and highly recommended that OM fast mode windows are embedded in an image mode science window. This will help with the fixed pattern noise correction, as it provides a template at the proper count rate level.

Consequently, the observer should specify such additional exposures in the proposal.



## 4.6 Observing modes

### 4.6.1 Mosaic Mode

Along the mission a number of scientific cases have been identified where the goal requires the observation of sky regions larger than the field of view of the EPIC cameras (galaxy clusters, supernova remnants, crowded fields, solar system objects). Since no raster, dithering or tracking modes were included in the original design of XMM-Newton, a target region larger than the field of view can only be achieved by a series of individual, independent observations, each having its own operational and instrument overheads (§ 4.5.1 and 4.5.2). For programmes not requiring long integration times per pointing, these overheads may reduce significantly the observing efficiency, especially for EPIC-pn.

The Mosaic mode has been defined to keep a high observing efficiency when large fields are observed for relatively short integration times. This is done, basically, by suppressing the upload (for MOS) and calculation (for pn) of the EPIC offset tables<sup>8</sup> at every pointing, except in the first one of a series of consecutive, adjacent pointings.

The detailed strategy is as follows: a number of nearby pointings are scheduled consecutively; at the first attitude of the sequence fixed offset tables are uploaded for MOS cameras and an offset table is specifically computed for pn with the filter wheel at the CLOSED position; once the EPIC filters selected by the PI are set, the exposures in all EPIC and RGS instruments are started and continued uninterruptedly until the end of the last pointing of the series.

Since MOS cameras are already operated with fixed offset tables, the new mode has no noticeable effect on the quality of their data products. The offset table computed for pn through the filter CLOSED may result in a degraded spectral resolution for sources producing a non-negligible optical loading. Nevertheless, the effect can be suppressed with the selection of the adequate filter, with the exception of sources extremely bright in the optical. The only restriction to the EPIC filters is that they cannot be changed while completing the pointings series. Different EPIC cameras may use different filters, but they all must be set in Full Frame mode.

Additional constraints exist for the angular distance between consecutive pointings and the duration of individual pointings. The former cannot exceed 1 degree, so that the duration of the re-pointing slews is fixed. On the other hand, the angular distance cannot be shorter than 12 arcsec as required by the accuracy of the slews and of the attitude reconstitution, the pixel size of the cameras and the PSFs of the telescopes. As to the duration of the individual pointings, the minimum and maximum operational efficiency are reached for exposures corresponding to 2 and 15 ks respectively.

As for any other observation, the total duration of any Mosaic observation ( $t_{obs}$ ) is limited to the visibility of the target region within a single orbit.

The total duration of a Mosaic observation made by  $n_p$  pointings each with duration  $t_p$  can be obtained by:

$$t_{obs} = t_{\text{SETUP}} + n_p \times t_p + (n_p - 1) \times t_s$$

where  $t_{\text{SETUP}}$  is the time needed to configure the EPIC cameras at the beginning of the observation and  $t_s$  is total time required for performing slews between consecutive pointings.  $t_{\text{SETUP}}$  includes, among other, the time for computing the pn offset table and uploading the corresponding MOS tables.  $t_s$  is the sum of the time required for a re-pointing slew and for the mapping of

<sup>8</sup>In this section the reader will find two types of “offsets”: “offset tables” for the zero level of charge measurements in EPIC cameras (see § 3.3.6) and “pointing offsets” for the distance between adjacent telescope pointings.



the Star Tracker field of view that follows every slew. Values for these parameters at the time of writing this Handbook are:  $t_{\text{SETUP}} = 4 \text{ ks}$  and  $t_s = 1.2 \text{ ks}$  of which 450 s are for the slew and 750 s are dedicated to the mapping.

When preparing Mosaic observations, the overhead is calculated as the difference between  $t_{\text{obs}}$  and  $n_p \times t_p$ . This means that both  $t_{\text{SETUP}}$  and  $(n_p - 1) \times t_s$  are considered as overhead. It should be noted, however, that the instruments are collecting science data during every re-pointing slew and mapping. During Star Tracker mapping the AOCS operate differently than during stable pointings and the accuracy of the attitude reconstitution has not been fully assessed: for this reason data collected during Star Tracker mapping are considered as overhead. However, the stability of the spacecraft is not significantly worse than during stable pointings, and therefore these data may be scientifically useful.

Astronomers willing to propose for Mosaic observations can justify in their proposals that, in addition to the science data ( $n_p \times t_p$ ), they plan to use data obtained during Star Tracker mapping, should this be valid for their scientific aims. They can therefore argue that for their purposes the true overhead may be smaller than the defined mosaic overhead.

The effective integration time at a given location in the target region depends on the individual pointing duration, but also on the offsets and on the vignetting of the telescopes. All these factors need to be carefully considered in the design of a Mosaic observation.

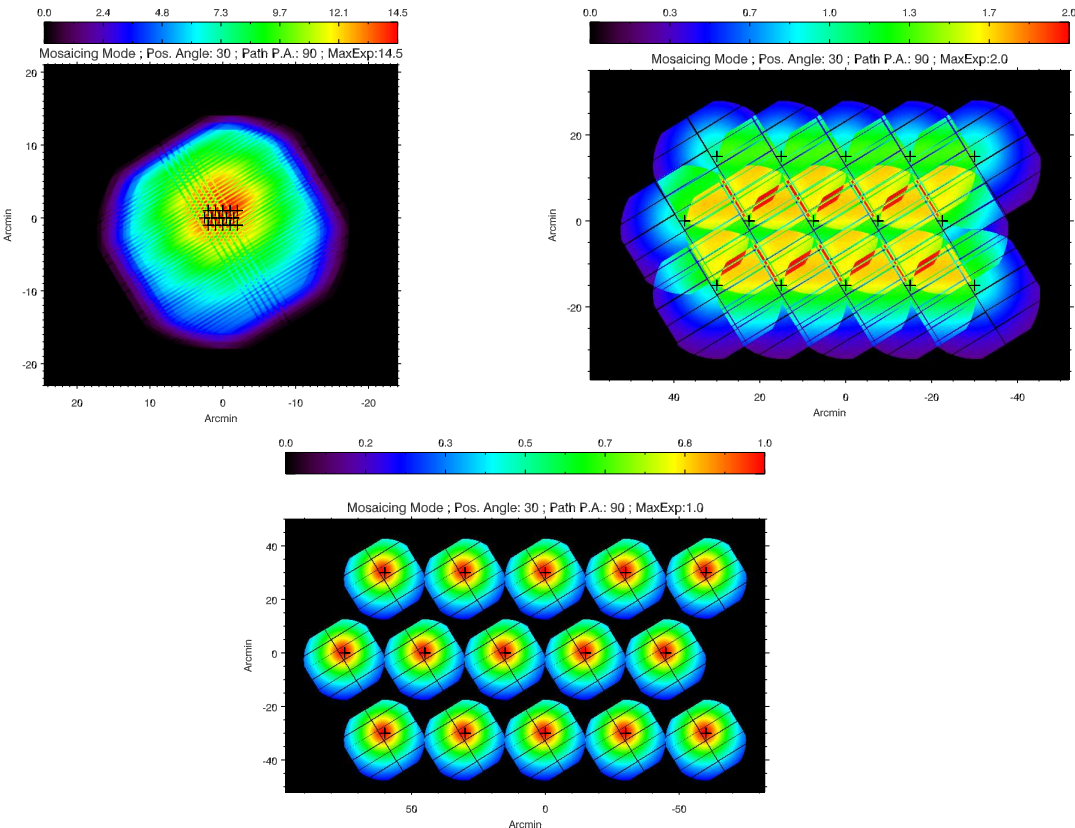


Figure 125: Simulated EPIC-pn exposure maps for a  $5 \times 3$  mosaic observation with pointing offsets of 1arcmin (top-left), 15arcmin (top-right) and 30arcmin (bottom). The colour bar at the top gives the effective exposure relative to the duration of individual pointings.

**esa**european space agency  
agence spatiale européenne

Three examples of Mosaic exposure maps are shown in Fig. 125. When the offsets are small compared to the scale length of the vignetting the result is a sort of blurred exposure map, with the effective exposure time in the core close to the total duration of the observation. If the offsets are similar to the two-folding distance of the vignetting factor, the resulting exposure map becomes relatively smooth on a spatial region larger than the field of view of the cameras. For larger offsets, the exposure map is a combination of snapshots at different attitudes.

An exposure map simulator tool is available under the link:

<http://www.cosmos.esa.int/web/xmm-newton/epic-mosaic>.

In Mosaic mode observations it is possible to include OM exposures, but only during stable pointing periods avoiding re-pointing slews.

It has to be remarked that the Mosaic observing mode is not a new operating mode of the instruments, except for the offset table used in the EPIC-pn exposures. Therefore, the descriptions of the instruments in § 3 are all applicable, including the recommendations, caveats, warnings, alerts and restrictions.

#### 4.6.2 RGS Multipointing Mode (MPM)

A small proportion of defects comprising bad or “cool” columns or pixels is inevitable in CCD detectors. In a dispersive instrument like the RGS, these detector defects, usually one pixel wide, correspond to fixed narrow wavelength intervals of about  $10 \text{ m}\text{\AA}$  per pixel (the RGS line-spread function has a FWHM of about 7 pixels). These wavelength defects sometimes coincide with features in the source spectrum that are important for the scientific success of an observation (see Tables 13 and 14).

One consequence of the pointing stability of XMM-Newton is that point-source photons of a given energy always end up in the same pixel of the detector. If an important spectral feature happens to fall on a defect, up to 20-50% of line flux may be lost depending on the filtering scheme employed. In addition, small defects can be difficult to distinguish from true, weak absorption lines. Further, there are the larger  $70\text{-}100 \text{ m}\text{\AA}$  gaps between the RGS CCDs.

When these circumstances arise, it is possible to change the spacecraft pointing in order to move the defects away so that more important parts of the spectrum are not affected.

The RGS Multipointing mode (MPM) allows the user to make five different pointings, with offsets in the dispersion direction of  $0, \pm 15$  and  $\pm 30$  arcsec, corresponding to  $0, \pm 35$  and  $\pm 69 \text{ m}\text{\AA}$ . In this way, the maximum flux loss in a spectral line is reduced significantly, and it becomes easier to distinguish weak absorption lines from defects. The dispersion step size is limited by the need to keep X-ray sources safely within the EPIC small windows.

For RGS, it is not necessary to start a new observation when slewing to the offset position. The instrument can be left on and useful observation time gained. On the other hand, EPIC pn offset maps must be generated at each pointing leading to a significant loss of EPIC pn exposure time.

A number of considerations must be taken into account in order to decide if the MPM could be applied with profit for a given observation.

- The mode is only relevant if the RGS is the prime instrument.
- The mode is in particular relevant if wavelengths important for the scientific success of the observation are affected by chip defects. This is also important if line positions are unknown in advance, for instance with unknown redshifts of foreground absorbers. Also, the continuum improves, as any small remaining detector defects will be smoothed.



- The mode is designed for high-quality RGS spectra, which is simply a requirement on the number of counts expected. The signal-to-noise ratio should be at least 10 in significant RGS resolution elements of  $\approx 70$  mÅ, equivalent to 100 counts.
- The mode would not benefit sources larger than a few arcmin, such as supernova remnants or the cooling cores of clusters of galaxies, because smoothing of the spectrum would automatically be achieved through the spectral degradation caused by the spatial extent of the source. Only for extended sources with a diameter of 30 arcsec or less is the mode of potential interest.
- For bright sources and relatively small exposure times, a significant fraction of the EPIC pn exposure time may be lost due to the overhead associated with the acquisition of offset tables at every position.
- When time variability of spectral lines is the main scientific driver, the user should carefully consider possible changes of sensitivity during the observation due to the different location of detector defects, versus the time-averaged spectral quality improvement due to the MPM. This holds in particular when the equivalent width or shape of the line vary. For lines with constant equivalent width (e.g. interstellar or intergalactic absorption lines) the MPM can be used without problems.

#### 4.6.3 Slew observations

XMM-Newton conducts EPIC science and/or calibration observations during some slews from one target to another. **Slew observations cannot be proposed.** The data obtained during slews are stored in so-called “Slew Data Files” (SDFs). The latest Slew results can be viewed under the link <http://www.cosmos.esa.int/web/xmm-newton/latest-slew-results>.



## 5 Proposal Submission and Optimisation

The proposal submission process for XMM-Newton is divided into two phases:

In response to the call, principal investigators (PIs) are asked to provide the scientific justification and some basic source and observing parameters, like coordinates, observation duration and observing mode of the prime instrument. This is done using the RPS tool developed by HEASARC.

During the second phase of the process, the PIs of successful proposals must provide the exposure parameters in full detail via the Remote Proposal Submission software (XRPS). After submission each proposal undergoes a technical optimisation (the so called “proposal enhancement”) by SOC personnel. Note that **it is the proposer’s responsibility to ensure that the target coordinates (and, if necessary, the spacecraft position angle) are correct.**

The technical optimisation of the proposals will consider the following points:

- EPIC

1. Expected X-ray counts

Calculating the expected X-ray counts for the specified target for each filter of each EPIC instrument.

2. Expected optical count rate

Calculating the expected optical counts for each specified target for each filter of each EPIC instrument.

3. Telemetry bandwidth

Calculating the expected telemetry bandwidth for each exposure.

4. Science parameters

Calculating for each exposure:

- Expected pile-up

- Counts per frame

- RGS

1. Expected X-ray count rate

Calculating the expected X-ray counts for each specified target for each RGS instrument.

2. Telemetry bandwidth

Calculating the expected telemetry bandwidth for each exposure.

3. Science parameters

Estimating for each exposure, from the expected X-ray count rate, if pile-up may be present.

- OM

1. Count rate estimation

Calculating the counts expected in each window (either imaging or fast) of each OM exposure.

2. Science windows



- Calculating the size in detector pixels of each science window defined by the PI.
- Calculating the number of memory windows required to enclose the specified science windows and their details (position and size), and checking that the proposed configuration is allowed.

### 3. Bright objects

For each observation indicating:

- Whether the observation is possible with the filters specified by the PI.
- Which filters are allowed.

PIs will always be informed about the outcome of the evaluation described above. All changes of observation parameters have to be confirmed explicitly by the PIs.

This is a pre-condition for an observation to be included in the scheduling system (cf.

<http://www.cosmos.esa.int/web/xmm-newton/proposal-enhancement>).

**esa**european space agency  
agence spatiale européenne

## 6 Analysing XMM-Newton data

### 6.1 XMM-Newton analysis software – the Science Analysis Subsystem

In this Section some information related to the scientific analysis of XMM-Newton data are given. The reader is referred to the documentation available on-line for a more detailed description of the XMM-Newton data format and reduction/analysis software.

#### 6.1.1 XMM-Newton data: the Observation/Slew Data Files (ODF/SDF)

XMM-Newton reformatted telemetry is organised in the Observation/Slew Data Files (ODF/SDF). Most of the ODF/SDF files have a FITS format. An ASCII summary file provides the user with some general information on the observation (pointing, proposal, data quality records), as well as an index of the files contained in the ODF. A more detailed ASCII summary file - including a description of the instrumental configuration for all the exposures - needs to be created through the SAS task `odfingest` (cf. the on-line SAS Documentation) prior of any ODF processing. ODF/SDF contain uncalibrated science files, which cannot be directly used for scientific data analysis. Their content is described in the XMM-Newton Data Files Handbook.

#### 6.1.2 The Science Analysis Software (SAS)

The Science Analysis Software (SAS) is the software package to reduce and analyse the XMM-Newton science data. It broadly consists of two main blocks:

- reduction pipelines, which apply the calibrations to the ODF/SDF science files, and produce calibrated and concatenated event lists (for the X-ray cameras) and flat-fielded and calibrated OM sky images, source lists and time series.
- a set of file manipulation tools. Such tools allow also the extraction of spectra, light curves, (pseudo-)images and the generation of source lists, as well as the generation of the appropriate instrument response matrices.

The user is referred to the SAS Users Guide for a general description of the SAS, as well as to the on-line available SAS Documentation.

The SOC is maintaining a SAS Scientific Validation page which contains results of the scientific validation of the currently available SAS version. It reflects therefore the data reduction and analysis software state-of-the-art, and provides additional and frequently updated information on the accuracy of the XMM-Newton calibrations.

#### 6.1.3 XMM-Newton data: the Processing Pipeline Subsystem (pipeline) products (PPS)

The SAS reduction pipelines are run on all the XMM-Newton ODF (see Appendix A). Each dataset is screened to verify its scientific quality and identify potential processing problems. The pipeline (PPS) output includes a wide range of top level scientific products, such as X-ray cameras event lists, source lists, multi-band images, background-subtracted spectra and light curves for sufficiently bright individual sources, as well as the results of a cross-correlation with a wide sample of source catalogues and with the matching ROSAT field.

The PPS products are made available to the PI of an XMM-Newton proposal shortly after the ODF files of her/his observation.



The user is referred to Data Products Interface Control Document and Data Products Specification Document for a detailed description of the PPS products content and format.

#### 6.1.4 Time scale and Reference Time

The Time System used in XMM-Newton is Terrestrial Time or TT (TIMESYS keyword in FITS files headers):

$$\text{TIMESYS} = \text{'TT'}$$

The Reference or zero time used (MJDREF keyword in FITS files headers) has been defined as:

$$\text{MJDREF} = 50814.0 \text{ (Modified Julian Date)}$$

corresponding to:

$$1998.0 \text{ TT} = 1998-01-01T00:00:00.00 \text{ TT} = 1997-12-31T23:58:56.816 \text{ UTC}$$

The conversion from TT to UTC can be found in The Astronomical Almanac. For this reference date it is:

$$\text{TT} = \text{UTC} + 63.184 \text{ sec}$$

The use of this scale for XMM-Newton data gives rise to time values of the order of  $10^8$  s.

Detailed information on time scales can be found, among other references in  
[http://aa.usno.navy.mil/publications/docs/Circular\\_179.php](http://aa.usno.navy.mil/publications/docs/Circular_179.php)

## 6.2 XMM-Newton Calibration data

All the XMM-Newton calibration data are organised in a “Current Calibration File” (CCF). Each constituent of the CCF is uniquely identified by its (progressive) issue number and date of validity. Access to the CCF is based on the Calibration Index File (CIF), which must be generated through the SAS task `cifbuild` at the beginning of an analysis session.

CCF constituents are available from the XMM-Newton Calibration Portal at  
<http://www.cosmos.esa.int/web/xmm-newton/calibration>.

This directory is frequently updated. The XMM-Newton user may consider subscribing to the CCF mailing list, which notifies in real-time all changes in the CCF content, or activating an automatic update of the calibration database on her/his own disk, as specified in the XMM-Newton Calibration Portal.

The user is referred to XMM-Newton Calibration Access and Data Handbook for more information about the calibration files, and the SAS infrastructure to access/visualise the content of the CCF constituents (Calibration Access Layer, CAL). The online version of the XMM-Newton Calibration Access and Data Handbook is available under the link:

[http://xmm-tools.cosmos.esa.int/external/xmm\\_calibration/calib/documentation/CALHB/index.html](http://xmm-tools.cosmos.esa.int/external/xmm_calibration/calib/documentation/CALHB/index.html)

The CCF *release notes* (accessible also through the XMM-Newton Calibration Portal) provide information on the accuracy of the XMM-Newton calibrations. Synthetic documents, summarising the current calibration status and associated systematic uncertainties, are available from the XMM-Newton Calibration Portal as well.



### 6.3 The XMM-Newton data distribution

Once the ODF/SDF files are produced, the SDF files become public immediately and the ODF files are made available to the PI of the XMM-Newton proposal, who can download them from the XMM-Newton Science Archive. At a later stage the PI will get another automatic email notification when the PPS products have been successfully generated and ingested into the XMM-Newton Science Archive. If, for some reason the ODF files are improved during the year of proprietary rights, the PI will be also notified by email.

### 6.4 The XMM-Newton Science Archive (XSA)

The XMM-Newton Science Archive (XSA) became publicly available in April 2002. The XMM-Newton Science Archive content is regularly updated with all the generated ODF, SDF and PPS products and with updated versions of the catalogues of EPIC sources, OM sources and Slew Survey sources, and ancillary info like associated proposal abstract, publications, etc. In 2019 the SSC performed the third bulk reprocessing of all XMM-Newton data obtained since the beginning of the mission in 1999, and all data are thus processed with SAS 18.0 or higher. PIs of XMM-Newton observations can retrieve their own proprietary data using their password-protected XSA account.

Public data can be retrieved through the XSA user interface: <http://nxsa.esac.esa.int/nxsa-web/>. Data can also be retrieved directly from the archive via URL or command line (see examples at the Archive Inter Operability system (AIO) help page: <http://nxsa.esac.esa.int/nxsa-web/#aio>). XSA database tables can be queried using ADQL (Astronomical Data Query Language), see the Table Access Protocol (tap) help page (<http://nxsa.esac.esa.int/nxsa-web/#tap>) for details.

On-the-fly data analysis and processing can be performed from the XMM-Newton Science Archive interface using the Science Analysis System (SAS) without the need of downloading data or software. This is done internally via the Remote Interface for Science Analysis (RISA) server (see the RISA Technical Note,

<https://www.cosmos.esa.int/documents/332006/1361013/SW-TN-0035-1-0.pdf>

and the Interactive Data Analysis help page <http://nxsa.esac.esa.int/nxsa-web/#risaHelp>). To obtain an upper limit from XMM-Newton slew and/or pointed observations at a given sky position, there is an upper limit server available at:

<http://www.cosmos.esa.int/web/xmm-newton/uls>

Of interest may also be the Flix server providing flux limits from images taken with XMM-Newton at:

<http://www.ledas.ac.uk/flix/flix.html>; see section A.3.2.

### 6.5 The XMM-Newton Serendipitous Source Catalogue

With all the sources serendipitously detected in the EPIC field of view of XMM-Newton public observations, the SSC compiles and regularly updates the XMM-Newton EPIC source catalogue (see Appendix A.3). Specific queries on the catalogue can be made using the XMM-Newton Science Archive. The full catalogue can be downloaded from the XSA web page (<https://www.cosmos.esa.int/web/xmm-newton/xsa#download>).



## 6.6 The XMM-Newton OM Source Catalogue

The OM team, under the auspices of the SSC, produces a catalogue of sources detected by the Optical Monitor. The OM catalogue derives from a reprocessing of publicly available OM data using a dedicated pipeline, which includes some additional data that is excluded from the routine XMM data-processing pipeline.

The fourth version of the XMM-Newton OM Serendipitous Ultraviolet Source Survey Catalogue (XMM-SUSS4) was released in December 2018. It includes public data up to July 2017, plus ~30 public ToO and calibration observations up to the end of May 2018.

The catalogue embraces 9749 XMM-Newton observations and contains 8,176,156 detections of 5,503,765 sources, of which 1,035,453 have been observed more than once, thus allowing variability studies.

The XMM-SUSS4 catalogue can be accessed through the XSA search interface. Further, either the complete catalogue or a reduced version of it (the SLIM version) can be downloaded from the XSA.

A new update of the OM SUSS catalogue, SUSS5, is in preparation and its release is anticipated in late 2020.

## 6.7 The XMM-Newton Slew Survey Catalogue

The data acquired during satellite slews are used to build the XMM-Newton Slew Survey Catalogue, which was first released in April 2006 as XMMSL1. Updates were made on a yearly basis culminating in a new version, XMMSL2, which went public in March 2017. All the data contained in XMMSL2 are fully integrated in the XSA. The catalogue has been built by members of the XMM-Newton SOC and the EPIC consortium on behalf of ESA. The description of the catalogue and all relevant documentation, including sky coverage, number of sources and flux limits in different bands can be found in the XMM-Newton Science Archive web page. Further information can be found in Saxton, R. D. et al. 2008, A&A 480, 611 and references therein.



## 7 Documentation

The first point of contact with the SOC is the XMM-Newton HelpDesk

<http://www.cosmos.esa.int/web/xmm-newton/xmm-newton-helpdesk>

Users are always invited to check this web page and get in contact to receive support.  
We compile here links and references of additional sources of information on XMM-Newton.

### 1. SOC services related to observations

- XMM-Newton Phase II Remote Proposal Submission (XRPS)  
[http://xmm-tools.cosmos.esa.int/external/xmm\\_user\\_support/documentation/rpsman/](http://xmm-tools.cosmos.esa.int/external/xmm_user_support/documentation/rpsman/)
- Target of Opportunity (ToO)  
<http://www.cosmos.esa.int/web/xmm-newton/too-details>
- Target Visibility Checker  
<http://www.cosmos.esa.int/web/xmm-newton/target-visibility-tool>
- Target Search Tool (Target search tool for performed or planned observations)  
<http://www.cosmos.esa.int/web/xmm-newton/target-search-tool>
- Observation & Data Processing Status  
<http://www.cosmos.esa.int/web/xmm-newton/observation-data-status>
- SOC Short Term Schedule  
<http://www.cosmos.esa.int/web/xmm-newton/short-term-schedule>
- XMM-Newton Upper Limit Server  
<http://www.cosmos.esa.int/web/xmm-newton/uls>

### 2. SOC services related to the SAS

- SAS  
<http://www.cosmos.esa.int/web/xmm-newton/sas>
- SAS Documentation (including the Users Guide and analysis threads)  
<http://www.cosmos.esa.int/web/xmm-newton/how-to-use-sas>
- SAS Scientific Validation  
<http://www.cosmos.esa.int/web/xmm-newton/sas-validation>
- XMM-Newton Calibration Portal  
<http://www.cosmos.esa.int/web/xmm-newton/calibration>
- EPIC calibration document (XMM-SOC-CAL-TN-0018)  
<http://xmmweb.esac.esa.int/docs/documents/CAL-TN-0018.pdf>
- RGS calibration document (XMM-SOC-CAL-TN-0030)  
<http://xmmweb.esac.esa.int/docs/documents/CAL-TN-0030.pdf>
- OM calibration document (XMM-SOC-CAL-TN-0019)  
<http://xmmweb.esac.esa.int/docs/documents/CAL-TN-0019.pdf>

### 3. Other online SOC services



- XMM-Newton Science Archive  
<http://www.cosmos.esa.int/web/xmm-newton/xsa>
- XMM-Newton Background Analysis page  
<http://www.cosmos.esa.int/web/xmm-newton/background>
- XMM-Newton: A Technical Description  
<http://www.cosmos.esa.int/web/xmm-newton/technical-details>
- XMM-Newton Image Gallery  
<http://www.cosmos.esa.int/web/xmm-newton/image-gallery>
- XMM-Newton Users' Group  
<http://www.cosmos.esa.int/web/xmm-newton/users-group>
- SOC Contact Details & directions on how to get to ESAC  
<http://www.cosmos.esa.int/web/xmm-newton/contact-details>
- Cross-Calibration Review Tool  
<https://www.cosmos.esa.int/web/xmm-newton/cross-calibration>

4. XMM-Newton Mailing lists

- XMM-Newton News Mailing List  
<http://www.cosmos.esa.int/web/xmm-newton/newsletter>

5. Online XMM-Newton documents

- Current Announcement of Opportunity (AO)  
<http://www.cosmos.esa.int/web/xmm-newton/aoannouncement>
- Policies and Procedures  
[http://xmm-tools.cosmos.esa.int/external/xmm\\_user\\_support/documentation/AOpolicy/](http://xmm-tools.cosmos.esa.int/external/xmm_user_support/documentation/AOpolicy/)
- Quarterly Mission Status & Performance Indicators  
<http://www.cosmos.esa.int/web/xmm-newton/quarterly-status-report>
- The Behaviour of the XMM-Newton Background, XMM-SOC-GEN-TN-0014  
<http://xmmweb.esac.esa.int/docs/documents/GEN-TN-0014.pdf>
- XMM-Newton Data Files Handbook  
[http://xmm-tools.cosmos.esa.int/external/xmm\\_user\\_support/documentation/dfhb/](http://xmm-tools.cosmos.esa.int/external/xmm_user_support/documentation/dfhb/)
- XMM-Newton Calibration Access and Data Handbook  
<http://xmmweb.esac.esa.int/docs/documents/CAL-MAN-0001.ps.gz>
- Routine Calibration Plan  
<http://xmmweb.esac.esa.int/docs/documents/CAL-PL-0001.ps.gz>
- ODF/SDF Interface Control Document  
[https://xmm-tools.cosmos.esa.int/external/xmm\\_odf/data/docs/XMM-SOC-ICD-0004-SS.ps.gz](https://xmm-tools.cosmos.esa.int/external/xmm_odf/data/docs/XMM-SOC-ICD-0004-SS.ps.gz)
- Data Products Interface Control Document  
[https://xmm-tools.cosmos.esa.int/external/xmm\\_odf/data/docs/XMM-SOC-GEN-ICD-0001.pdf](https://xmm-tools.cosmos.esa.int/external/xmm_odf/data/docs/XMM-SOC-GEN-ICD-0001.pdf)



- Data Products Specification Document  
[https://xmm-tools.cosmos.esa.int/external/xmm\\_0df/data/docs/XMM-SOC-GEN-ICD-0022.pdf](https://xmm-tools.cosmos.esa.int/external/xmm_0df/data/docs/XMM-SOC-GEN-ICD-0022.pdf)
- Online list of XMM-Newton Papers  
<http://heasarc.gsfc.nasa.gov/docs/xmm/xmmbib.html>

## 6. Documents related to sections of the UHB

- § 3, XMM-Newton – a concise overview:
  - Jansen et al., 2001, A&A, 365, L1
- § 3.2, X-ray telescopes:
  - Aschenbach et al., 2000, in X-Ray Optics, Instruments, and Missions III, J.Trümper and B.Aschenbach, eds., SPIE 4012, p.731
  - Gondoin et al., 2000, in X-Ray and Gamma-Ray Instrumentation for Astronomy XI, K.A.Flanagan, O.H.Siegmund, eds., SPIE 4140, p.1
- § 3.3, EUROPEAN PHOTON IMAGING CAMERA (EPIC):
  - Strüder et al., 2001, A&A, 365, L18
  - Turner et al., 2001, A&A, 365, L27
  - Lumb et al., 2000, in X-Ray and Gamma-Ray Instrumentation for Astronomy XI, K.A.Flanagan, O.H.Siegmund, eds., SPIE 4140, p.22
  - EPIC Calibration Status Report, XMM-SOC-CAL-TN-0018
- § 3.4, REFLECTION GRATING SPECTROMETER (RGS):
  - den Herder et al., 2001, A&A, 365, L7
  - Erd et al., 2000, in X-Ray and Gamma-Ray Instrumentation for Astronomy XI, K.A.Flanagan, O.H.Siegmund, eds., SPIE 4140, p.13
  - RGS Calibration Status Report, XMM-SOC-CAL-TN-0030
- § 3.5, OPTICAL MONITOR (OM):
  - Mason et al., 2001, A&A, 365, L36
  - Constraints on the OM Window Configuration and Definition of the OM Default Configurations  
<http://xmmlweb.esac.esa.int/docs/documents/PS-TN-0026-4-1.ps.gz>
  - OM Calibration Status Report, XMM-SOC-CAL-TN-0019
- Appendix A, XMM-Newton Survey Science Centre (SSC):
  - Watson et al., 2001, A&A, 365, L51
  - Watson et al., 2009, A&A, 493, 339
  - Rosen, Webb, Watson et al., 2016, A&A, 590, A1
- Cross Calibration Report  
<https://www.cosmos.esa.int/web/xmm-newton/cross-calibration>

## 7. External links

- X-ray telescopes at the Max-Planck-Institut für extraterrestrische Physik  
<http://www.mpe.mpg.de/heg/panter>



- EPIC/MOS at the Physics Department, Leicester University  
<http://www2.le.ac.uk/departments/physics-and-astronomy/research/src\//Missions/xmm-newton/instrument>
- EPIC/pn at the Max-Planck-Institut für extraterrestrische Physik  
<http://www.mpe.mpg.de/33319/XMM-Newton>
- RGS at the Space Research Organization Netherlands  
<http://www.sron.nl/missions-xmm-newton>
- OM at the Mullard Space Science Laboratory  
[http://www.mssl.ucl.ac.uk/www\\_astro/xmm/om/om.html](http://www.mssl.ucl.ac.uk/www_astro/xmm/om/om.html)
- SSC: Survey Science Centre  
<http://xmmsc.irap.omp.eu/>
- NASA's XMM-Newton Guest Observer Facility  
<http://heasarc.gsfc.nasa.gov/docs/xmm/xmmgof.html>
- *PIMMS* (HEASARC)  
<http://heasarc.gsfc.nasa.gov/Tools/w3pimms.html>
- *XSPEC* (HEASARC)  
<http://heasarc.gsfc.nasa.gov/docs/xanadu/xspec/>

Additional information on XMM-Newton can always be obtained from other locations under the SOC home page, at <http://www.cosmos.esa.int/web/xmm-newton/>.



## A XMM-Newton Survey Science Centre (SSC)

Due to its large throughput and good spatial resolution, pointed observations with the XMM-Newton EPIC X-ray cameras reach very faint X-ray flux limits ( $\approx$  a few  $\times 10^{-15}$  erg cm $^{-2}$  s $^{-1}$ , 0.2–12 keV, in typical observations). At these fluxes, each XMM-Newton EPIC field at both high and low galactic latitudes contains substantial numbers of “serendipitous” X-ray sources. Typical EPIC observations yield  $\sim$ 70 serendipitous X-ray source detections per field. As XMM-Newton makes of the order 600 observations per year, covering  $\sim$ 100 sq.deg. of the sky, after allowing for overlaps in the sky coverage and observations where EPIC was not used, the number of serendipitous unique sources grows at a rate of  $\sim$ 30,000 sources per year. The XMM-Newton data thus provide a deep, large area sky survey which represents a major resource for a wide range of programmes. The extended energy range of XMM-Newton, compared with previous imaging X-ray missions such as ROSAT and the Einstein Observatory, means that XMM-Newton detects significant numbers of obscured and hard-spectrum objects (e.g. obscured AGNs) which are absent from earlier studies. Pointed XMM-Newton observations thus provide a “serendipitous” X-ray survey (the “XMM-Newton Serendipitous Sky Survey”, see Watson et al., 2001, A&A, 365, L51, Watson et al., 2009, A&A, 493, 339, and Rosen, Webb, Watson et al., 2016, A&A, 590, A1) which, like previous surveys, is making a major impact in a number of front-line areas of astrophysics, a fact that provided one of the original motivations for the SSC concept within the XMM-Newton project. The SSC is responsible for two main aspects of the XMM-Newton Serendipitous Survey: creation of the XMM-Newton source catalogues (section A.3) and the XID Follow-up Programme described briefly below.

The SSC’s XID follow-up programme, designed to ensure that the potential of the XMM-Newton serendipitous survey can be exploited by the community in the context of a wide range of scientific programmes, involves a substantial series of new observations, primarily in the optical and IR using ground-based facilities. The main elements of the programme are a number of complementary sub-programmes to obtain the identifications for well-defined samples of X-ray sources drawn from selected XMM-Newton fields using optical/IR spectroscopy. The programme is also supported by a substantial imaging programme, needed for the selection of the spectroscopic targets, but which is also an important resource in its own right given the large sky area and hence X-ray source sample it covers. One of the principal objectives of the whole programme is to obtain completely identified samples which can be used to characterise the overall XMM-Newton source population sufficiently well that the basic X-ray and optical parameters can be used to assign a statistical identification for a large fraction of all the sources in the XMM-Newton serendipitous source catalogue.

The entire XID Programme is based on samples of serendipitous X-ray sources drawn from pointed XMM-Newton observations that are in the public domain, or are made available to the SSC by the observation PI.

The XID programme is designed to support the community’s access to, and exploitation of, the serendipitous data from XMM-Newton, and as such all the results will be made public. The XID project results are available through a dedicated, searchable database at l’Observatoire Astronomique de Strasbourg.

Most of the XID Programme is now complete. Information on the status of the project, pub-



lications related to the primary source samples, and details of the XID results database are provided at

<http://xcatdb.unistra.fr/xidresult/home>

## A.1 Pipeline processing of XMM-Newton science data

Up to March 1st 2012, the SSC was responsible for systematically processing all XMM-Newton observations to produce data products for the three scientific instruments. Since then, processing responsibilities have been transferred to the XMM-Newton SOC. This processing is done with a pipeline that uses the same SAS software packages that are available for users to interactively analyse XMM-Newton data. However, the pipeline infrastructure used to carry out the processing has been developed by, and has been specific to, the SSC. The SSC was responsible for the pipeline software used until July 2013 when the SOC took over full control, following the transfer of the pipeline used to generate the 3XMM-DR4 catalogue from the SSC to the SOC.

Each dataset processed is subject to a screening procedure by the SSC and SOC teams which aims to verify the quality of the processing and identify any processing problems.

The aim of the pipeline processing is to provide a set of data products which are of immediate value for the XMM-Newton observer as well as for the XMM-Newton Science Archive where they are also stored for eventual public release. The pipeline products, together with the ODF (see § 6.1.1), are distributed to observers by the XMM-Newton SOC via the XMM-Newton Science Archive.

The XMM-Newton data products include calibrated, “cleaned” event lists for all X-ray cameras, which are intended to provide the starting point for most interactive analysis of the data. A number of higher-level products are also provided, such as sky images, source lists, cross-correlations with archival catalogues (performed by the Astronomical Catalogues Database Subsystem (ACDS) at the Observatoire Astronomique de Strasbourg), and spectra and time series of sufficiently bright individual sources. These provide a useful overview of the observation for the XMM-Newton observer as well as constituting key archival resources.

Since late 2010 XMM-Newton slew data have also been pipeline processed to create images, event lists and exposure maps along the slew path.

An outline of the pipeline processing system, information about the pipeline configurations and access to the pipeline software modules, are available at

<http://xmssc-www.star.le.ac.uk/public/pipeline/>

and

<http://www.cosmos.esa.int/web/xmm-newton/pipeline>.

The data products produced by the pipeline are detailed in documents available on the SOC Manuals web page (<http://www.cosmos.esa.int/web/xmm-newton/documentation>).

Up until early 2013 the SSC had the responsibility to perform bulk reprocessings of all XMM-



Newton data from time to time. Bulk reprocessing enables the most up-to-date processing and calibrations to be applied to data and re-imposes uniformity on the archive. The latest bulk reprocessing of all XMM-Newton data took place in December 2012, using a version of the SAS very similar to the public SAS v12.0 and the latest instrument calibrations at that time. This configuration was used for the release of the 3XMM-DR4 catalogue on the 23 July 2013. From this date, both pipeline processing and SAS codes have been updated regularly with no implications on the analysis results. Hence, the XMM-Newton EPIC Serendipity Sources catalogue has been updated from 3XMM-DR4 up to 3XMM-DR8 without the need of a bulk reprocessing.

During 2019 the whole content of the XMM-Newton Science Archive was reprocessed with a new pipeline processing code, using the most recent versions of the SAS software and calibration files. As a result of this re-processing a new version of the EPIC catalogue (4XMM-DR9) has been published in December 2019 and new products made available in the XMM-Newton Science Archive . This new version also includes an update of the stacked catalogue (4XMM-DR9s).

## A.2 Science analysis software development

In collaboration with the SOC, the SSC has made a major contribution to the development of the XMM-Newton Science Analysis System (SAS, see § 6.1) provided by the SOC to the community to enable XMM-Newton data analysis to be carried out by XMM-Newton observers. The SAS provides XMM-Newton-specific software tools for all XMM-Newton science data. It allows the processing of the Observation Data Files (ODFs, see § 6.1.1) sent to the observer through to high-level science products, but does not, in general, aim to provide the high-level analysis tools (e.g. spectral fitting) themselves.

## A.3 The XMM-Newton Serendipitous Source Catalogues

The SSC has been responsible, on behalf of ESA, for the construction of the XMM-Newton Serendipitous Source Catalogues. To date, there have been ten releases of the (EPIC) X-ray catalogue: 1XMM, in April 2003, 2XMMp (an interim version of the more complete and extensive 2XMM catalogue) in July 2006, 2XMM in 2007, and two increments to 2XMM, i.e. 2XMMi in August 2008 and 2XMMi-DR3 in April 2010. 3XMM-DR4 was made public in July 2013, an incremental version, 3XMM-DR5, in April 2015, 3XMM-DR6, in July 2016, 3XMM-DR7, in June 2017, 3XMM-DR8, in May 2018 and the latest release, 4XMM-DR9 in December 2019 which also includes an update to the stacked catalogue (4XMM-DR9s). Production of the catalogues involves collation of archived, processed products (or a bulk reprocessing of all the data when major software and calibration changes have accumulated), the selection of suitable public datasets, screening and verification of the X-ray detections and associated data products, compilation of the catalogue from the source lists of the individual observations and auxiliary information, scientific validation of the catalogue, and making the catalogues and documentation publicly available to the scientific community, in close collaboration with ESA. A number of added-value products, such as image thumbnails and summary web-pages for each source are also generated separately. Each catalogue release uses as many of the publicly available datasets



as possible, though some observations are excluded for various reasons, e.g. very low exposure, or cases with processing or pathological problems.

### A.3.1 4XMM-DR9

New XMM-Newton catalogues are created on a regular basis. The latest 4XMM-DR9 was released in December 2019. 4XMM-DR9 contains 810795 detections or 550124 unique sources drawn from 11204 XMM-Newton observations that were public by February 26th 2019, and covers a unique sky area of 1152 square degrees. 4XMM-DR9 provides approximately one extra year of data compared to 3XMM-DR8. Typical sensitivities in the 4XMM-DR9 catalogue are  $6 \times 10^{-15}$  (0.2-12.0 keV) and  $1 \times 10^{-14}$  erg cm $^{-2}$  s $^{-1}$  (2.0-12.0 keV).

For the first time with 4XMM-DR9, spectral energy distributions (SEDs) are provided for each of the unique 4XMM sources after cross-match with 26 archival catalogues selected to cover the largest sky coverage and widest span in wavelength from UV to radio.

The stacked catalogue (4XMM-DR9s) has been compiled from 1,329 groups, comprising 6,604 overlapping good-quality XMM-Newton observations. It contains 28,191 unique sources, 218,283 of them multiply observed.

XMM-Newton observers may find the 4XMM-DR9 catalogue useful in planning new observation proposals. Further details of each XMM-Newton EPIC catalogue, including available formats, access methods and the Catalogue User Guides, are available through links from the Catalogues home page, at:

<http://xmssc.irap.omp.eu/>.

A paper describing the 4XMM catalogue has been submitted to *Astronomy & Astrophysics* and is under revision at the time of delivering this UHB (). Previous major revisions of the catalogue are also useful to understand the full content of the catalogue and their associated source product (Rosen, Webb, Watson et al., 2016, A&A, 590, A1 and Watson et al., 2009, A&A, 493, 339).

The catalogue can be retrieved from the XMM-Newton Science Archive web page in FITS or CSV format and is fully accessible through XMM-Newton Science Archive user interface.

Other useful interfaces to the 4XMM-DR9 catalogue include

The IRAP catalogue server: <http://xmm-catalog.irap.omp.eu/>

LEDAS at:

<http://www.ledas.ac.uk>,

XCATDB at:

<http://xcatdb.unistra.fr>,

the HEASARC interface at:

<http://heasarc.gsfc.nasa.gov/W3Browse/xmm-newton/xmssc.html>

which are particularly useful for exploring correlations with other catalogues.

### A.3.2 Upper Limit Server

The FLIX utility under the link

<http://www.ledas.ac.uk/flix/flix.html>

can be used to check, for a given sky location, whether XMM-Newton has observed that region of the sky and if so, determine XMM-Newton upper limits, X-ray fluxes, and create image cut-outs.

Alternatively, the XMM-Newton Upper Limit Server can be used:

XMM-Newton Upper Limit Server.



## B XMM-Newton Routine Calibration Programme

In order to monitor the performance of the XMM-Newton science instruments, regular observations of a number of targets are performed.

Such observations are defined in the Routine Calibration Plan (available at <http://www.cosmos.esa.int/web/xmm-newton/calibration-documentation#General>) and are used to update the Current Calibration Files (CCFs, see § 6.2) whenever necessary. Routine calibration targets are also included in the Target Search Tool (at URL: <http://www.cosmos.esa.int/web/xmm-newton/target-search-tool>).

The following monitoring observations are foreseen:

- EPIC

- CTI, Gain and bright Pixel Monitoring: with filter closed or cal-closed during parts of a revolution when scientific observations are not possible due to high background radiation. MOS full frame mode cal-closed data are also collected during slews between adjacent science targets. Longer observations are scheduled in parallel to RGS and OM calibration observations. In addition, diagnostics and noise mode exposures are taken on a regular basis. Regular observations of N132D were reintroduced in 2013 for the same purpose.
- Effective Area, Gain & Offset Monitoring: preferred target is the SNR 1E 0102.2-7219.
- Detector Response and Redistribution Monitoring: the isolated neutron star RX J1856.6-3754 is used to monitor these detector characteristics.
- Monitoring of Spectral Capabilities and Contamination: the Vela SNR is observed. RX J1856.6-3754 is also observed for this purpose.
- Relative and absolute timing Monitoring: based on observations of the Crab pulsar.
- Stability of the boresight: to be monitored on request, for example after an eclipse season.

- RGS

- Confirmation of the Wavelength Scale: with AB Dor and HR1099 (replacing Capella due to reduced visibility, as of mid 2016).
- Long-wavelength calibration: with target PSR B0833-45.
- Monitoring of Effective Area: with target Mkn 421 (replacing PKS 2155-304 as of 2015).
- Gain and CTI monitoring: with Mkn 421 at large cross-dispersion offsets (replacing PKS 2155-304 as of 2015), and (on request) with Sco-X1 on- and off-axis pointings.

- OM



- Monitoring of the Grisms absolute Flux Calibration: observing the spectrophotometric standard targets GD153 and HZ2.
- Monitoring of the Visual and UV Grisms Wavelength Calibration: HZ2 is also used for wavelength scale monitoring of the Visible Grism.
- Monitoring of the Photometric Calibration: targets are BPM 16274 and the standard field SA95-42.
- Engineering Mode Observations: are performed whenever OM does not allow any filter observations but needs to be blocked because of bright optical sources.

- **XMM-Newton Cross-Calibration**

In 2003, a major cross-calibration campaign was started to regularly monitor the internal agreement of the XMM-Newton detectors and the cross-calibration with other facilities, especially with the *Chandra* and *NuSTAR* X-ray observatories.

- As of 2015, the main cross-calibration target is 3C 273, replacing PKS 2155-304. Although on previous occasions 3C 273 had been observed simultaneously by *Chandra*, *Suzaku* and XMM-Newton, in recent years the main cross-calibration target was PKS 2155-304 (Ishida et al. 2011, PASJ, 63, 657 discusses the results of this cross-calibration campaign). The data of these observations are available through the XSA. The blazar 1ES 1553+113 is used as complementary cross-calibration target.

- **XMM-Newton Long-Wavelength Response**

The routine calibration task to monitor RGS and EPIC energy responses is addressed by observations of  $\zeta$  Puppis.

The time needed to fulfil the monitoring requests defined in the routine calibration plan should stay below a 5% margin of the available time for science (cf. Policies and Procedures at [http://xmm-tools.cosmos.esa.int/external/xmm\\_user\\_support/documentation/A0policy/](http://xmm-tools.cosmos.esa.int/external/xmm_user_support/documentation/A0policy/)).